THE UNIVERSITY OF WARWICK

User's Declaration

AUTHOR: **Amna Hassan Ahmed Hassan** DEGREE: **Ph.D.**

TITLE: **Transport properties for pure strained Ge quantum well**

DATE OF DEPOSIT:……

I agree that this thesis shall be available in accordance with the regulations governing the University of Warwick theses.

I agree that the summary of this thesis may be submitted for publication.

I agree that the thesis may be photocopied (single copies for study purposes only).

Theses with no restriction on photocopying will also be made available to the British Library for microfilming. The British Library may supply copies to individuals or libraries. Subject to a statement from them that the copy is supplied for non-publishing purposes. All copies supplied by the British Library will carry the following statement:

> "Attention is drawn to the fact that the copyright of this thesis rests with its author. This copy of the thesis has been supplied on the condition that anyone who consults it is understood to recognise that its copyright rests with its author and that no quotation from the thesis and no information derived from it may be published without the author's written consent."

AUTHOR'S SIGNATURE:……

USER'S DECLARATION

1. I undertake not to quote or make use of any information from this thesis without making acknowledgement to the author.
2. I further undertake to allow no-one else to use this thesis while it is in my care.

DATE SIGNATURE ADDRESS

……

……

……

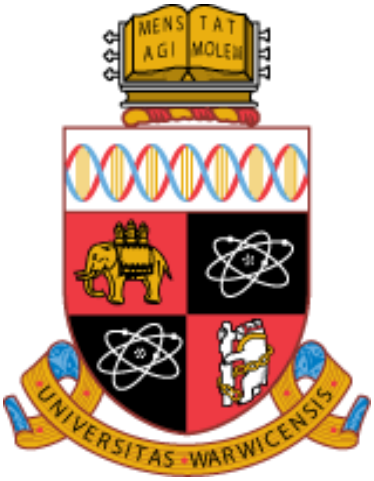

Transport properties for pure strained Ge quantum well

by

Amna Hassan Ahmed Hassan

Thesis

Submitted to the University of Warwick

in partial fulfilment of the requirements

for admission to the degree of

Doctor of Philosophy

Department of Physics

THE UNIVERSITY OF WARWICK

Declaration

This thesis is submitted to the University of Warwick in support of my application for the degree of Doctor of Philosophy. All experimental data presented and simulations were carried out by the author, except in the following cases: sample growth was by A. Dobbie and M. Myronov, XRD was done by A. Dobbie, and AFM by S. Rhead and P. Allred. TEM measured by R. Beanland and one image by J. Halpin, and SIMS by R. Morris and Evans Analytical Group (EAG). Mobility spectrum analysis was carried out by D. Christina and S. Kiatgamolchai. Finally samples 11-289 and 11-284 high field magnetotransport measured by O.A. Mironov, and S. Gabani at the Centre of Low Temperature Physics, Institute of Experimental Physics SAS, Kosice Slovakia, and International Laboratory of High Magnetic Fields and Low Temperatures, Wroclaw Poland, and Hall bar fabrication of sample 11-285 dry etching was with help of C. Morrison.

Dedicated to my lovely husband:

Taher

and my gorgeous daughters:

Alaa, Aya, and Abrar

Acknowledgments

First of all, I would like to Thank my supervisor Prof David Leadley for the Great support and guidance through my PhD, I really appreciate his encouragement that provided me the positive energy I needed for my research. Moreover, I really glad to know him and learn how to be humble and nice even when you achieve great place.

I am also grateful to Oleg Mironov, Richard Morris, and Andy Dobbie for their support and patient during my study they give me grateful advices and bring a lot of knowledge and experience to my scientific acknowledgement.

It is impossible to forget the great personal support that I got from many professors, postdocs and PhD students in Nano silicon group especially Catarina Casteleiro and John Halpin, also Prof .Evan Parker and Prof. Terry Whall, Dr Martin Prest, Dr Stephen Rhead, Dr Chris Morrison, Dr Vishal Shah, and Dr Maksym Myronov.

I am also grateful to technicians Alan Burton and Alistair Julian for their support during experimental work. Finally I would like to thank my great parents and sisters for their encouragements, as well as all my lovely friends Mariam Alemam, Assma Wahra, Omaima Forawi, Badriya Al Hashmi, and Natalia Parzyk.

Publications arising from this work:

A. Dobbie, M. Myronov, R.J.H. Morris, M.J. Prest, A.H.A. Hassan, J. Richardson-Bullock, V.A. Shah, E.H.C. Parker, T.E. Whall and D.R. Leadley, "Ultra-High Hall Mobility (1 x 10^6 $cm^2V^{-1}s^{-1}$) in a Two-Dimensional Hole Gas in a Strained Germanium Quantum Well Grown by Reduced Pressure CVD" International SiGe Technology and Device Meeting (ISTDM 2012), Berkeley, June 4-6, (2012)

A.H.A. Hassan , A. Dobbie, M. Myronov, R. Morris, M. Prest, J. Richardson-Bullock , V. Shah, T. E. Whall, E.H.C. Parker, D.R. Leadley, "Hole Transport Properties in Modulation Doped Germanium Heterostructure" Condensed Matter and Materials Physics, CMMP Edinburgh, 3-7 Sept. (2012)

A. Dobbie, M. Myronov, R.J.H. Morris, A.H.A. Hassan, M.J. Prest, J. S. Richardson-Bullock, V.A. Shah, E.H.C. Parker, T.E. Whall, and D.R. Leadley, "Ultra-High Hall Mobility of One Million in a Two-Dimensional Hole Gas in a Strained Germanium Quantum Well" Applied Physics Letters 101, 172108 (2012)

A.H.A. Hassan, O.A. Mironov, A. Feher, E. Cizmar, S. Gabani, R.J.H. Morris, A. Dobbie, M. Myronov, and D.R. Leadley "Pure Ge quantum well with high hole mobility", Intl Conf on Ultimate Integration on Silicon (ULIS-14) Warwick, March 2013

A.H.A. Hassan, O.A. Mironov, A. Dobbie, R.J.H. Morris, J.E. Halpin, V.A. Shah, M. Myronov, D.R. Leadley, A. Feher, E. Cizmar, S. Gabani, V.V. Andrievskii and I.B. Berkutov, "Structural and Electrical Characterization of SiGe Heterostructures Containing a Pure Ge Strained Quantum Well", ELNANO-2013, April 2013

O.A. Mironov, A.H.A. Hassan, A. Dobbie, R.J.H. Morris, A. Feher, E. Cizmar, S. Gabani, I.B. Berkutov, J.E. Halpin, S.D. Rhead, P. Allred, and D.R. Leadley, "New RP CVD grown ultra-high performance selectively B-doped pure-Ge 20 nm QWs on (100)Si as basis material for post-Si CMOS technology", Phys. Status Solidi C 11, No. 1, 61–64 (2014).

O.A. Mironov, A.H.A. Hassan , R.J .H. Morris, M. Uhlarz, D. Chrastina, J.P. Hague, S. Kiatgamolchai, R. Beanland, A. Dobbie, M. Myronov, S. Gabani, I.B. Berkutov, M. Helm, O. Drachenko, D.R.Leadley "Ultra High Hole Mobilities in a Pure Strained Ge Quantum Well", International Conference on Silicon Epitaxy and Heterostructures (ICSI-8), Fukuoka, Japan, June 2013

O.A. Mironov, A.H.A. Hassan, A. Dobbie, R.J.H. Morris, D.R. Leadley, M. Helm, O. Drachenko, E. Cizmar, S. Gabani, I.B.Berkutov, "Ultra High Mobility 2DHG in Pure 20 nm Ge Quantum Wells with Remote B-doping", Int. Conf. on the Electronic Properties of 2D Systems (EP2DS-20), Wroclaw, July 2013

O.A. Mironov, A.H.A. Hassan , R.J .H. Morris, M. Uhlarz, D. Chrastina, J.P. Hague, S. Kiatgamolchai, R. Beanland, A. Dobbie, M. Myronov, S. Gabani, I.B. Berkutov, M. Helm, O. Drachenko, D.R. Leadley, "Ultra High Hole Mobilities in a Pure Strained Ge Quantum Well", Thin Solid Films (accepted Oct 2013) 10.1016/j.tsf.2013.10.118

A.H.A. Hassan, O.A. Mironov, R.J.H. Morris, A. Dobbie, R. Beanland, M. Myronov and D.R. Leadley, "Anisotropy in the 2DHG mobility measured in a strained Ge quantum well" Applied Physics Letters (accepted!)

O. A. Mironov, M. Myronov, A.H.A. Hassan, A. Dobbie, R. J. H. Morris, V. Shah, M. Prest, I.B. Berkutov, V. V. Andrievskii, and D. R. Leadley, "Effective mass and scattering in ultra-high hole mobility strained germanium", presentation at 6th international conference Materials Science and Condensed Matter Physics September 11-14, 2012, Chisinau, Moldova, 2012.

O. A. Mironov, M. Orlita, A. H. A. Hassan, R.J.H. Morris, A. Dobbie, D. R. Leadley, D. V. Kozlov, and V. I. Gavrilenko "Splitting of the Cyclotron Resonance Lines in p–type Asymmetrically B-doped Pure Ge-QWs with Ultra-high 2DHG Mobility". Ready for publication.

Abstract

Modulation doped heterostructures consisting of a strained Ge (sGe) quantum well on a $Si_{0.2}Ge_{0.8}$ virtual substrate have been used to study enhancement of the transport properties of holes in the sGe channel due to the effective reduction of impurity scattering by placing the doping layer away from the channel.

Electrical and structural analysis was performed for sGe heterostructures produced with a range of growth parameters. The highest hole mobility was 1.34×10^6 cm^2/Vs at 0.5 K for a sGe quantum well in a 'normal' structure (i.e. doped above the channel) at a sheet density of 2.9×10^{11} cm^{-2}, which is the largest hole mobility reported in Ge to date. 'Inverted' structures (doping layer under the channel) were also studied for different sample parameters such as channel thickness, spacer thickness, doping and different temperature growth, with a hole mobility as high as 5.08×10^5 cm^2/Vs at a sheet density of 5.14×10^{11} cm^{-2} at 90 mK.

Simulations of the scattering limited mobility for inverted and normal structures were performed and showed that at low sheet density background impurity scattering limits the low temperature hole mobility. However, as the sheet density increases interface roughness scattering becomes the mobility limiting process, especially in the case of inverted structures where the resistivity and mobility anisotropy is more pronounced.

Magnetotransport measurements revealed the lowest reported effective mass for holes in Ge of 0.063 ± 0.001 m_0 for the normal structure and 0.07 ± 0.002 m_0 & 0.063 ± 0.003 m_0 for two inverted structures, and highest Dingle factors of $\alpha=78$ and 33 for the normal and inverted structures, respectively. The low level of background impurities, high structural quality, and pure Ge channel revealed by structure characterisation are believed to be responsible for these exceptionally high values of mobility.

Contents

List of Figures

List of Tables

List of the abbreviations

2DHG	Two dimentional hole gas
AFM	Atomic force microscopy
BAMS	Bryan's algorithm mobility spectrum
CCC	Closed cycle cryostat
CMOS	Complementory metal oxide semiconductor
CMP	Chemical mechanical polishing
CVD	Chemical vapour deposition
DIW	Deionised water
EMA	Effective-mass approximation
FET	Field effect transistor
FFT	Fast Fourier transform
FWHM	Full width half maxima
HRXRD	High resolution X-ray diffraction
LEPE-CVD	Low energy plasma enhanced chemical vapour deposition
LT	Low temperature
MBE	Molecular beam epitaxy
ME-MSA	Maximum-entropy mobility spectrum analysis
MODFET	Modulation doped field effect transistor
MSA	Mobility spectrum analysis
QHE	Quantum Hall effect
RP-CVD	Reduced pressure chemical vapour deposition
RSM	Reciprocal space maps
SdH	Shubnikov de Haas oscillations
SIMS	Secondary ion mass spectroscopy
SS-MBE	Solid source molecular beam epitaxy
TDD	Threading dislocation density
VdP	Van der Pauw
XTEM	Cross sectional transmission electron microscopy

List of Variables

A	Anisotropy coefficient
A_{eff}	Effective anisotropy
A_{VdP}	Experimental resistivity ratio measured from VdP sample$b$ Variational parameter in Fang-Howard calculation
B	Magnetic field
E_F, K_F	Fermi energy, Fermi wavevector
$f_{\pm}$	Frequency at spin up and spin down sheet densities
F, F_R	Form factors
g_v, g_v	Spin degeneracy, valley degeneracy
l	Depletion width
l_m	Carrier mean free path
L_d, L_s	Thickness of doping layer, spacer layer
m_0	Free electron mass
m^*	Effective mass in transport direction
m_z	Effective mass in confinement direction
N_A	3D density of acceptors
N_{depl}	2D depletion density
p_s	Sheet density
p_{SdH}	Sheet density extracted from SdH oscilations
Q_x, Q_z	In-plane scattering vector, out-of-plane scattering vector
q	2D wavevector
R_H, V_H	Hall coeffecient, Hall voltage
S_0	Screening parameter
$U(q)$	Scattering potential
w	Average width of the hole wavefunction
β	Spin precession (eVm)

ρ	Resistivity tensor
τ, τ_t, τ_q	Scattering time, transport lifetime, quantum lifetime
ω_c	Cyclotron frequency
Ψ	Wavefunction
σ	Conductivity tensor
Δ, Λ	Interface roughness scattering parameters – height, correlation length
μ	Hole mobility
ν	Filling factor

1 Introduction

1.1 Motivation:

In order to scale CMOS circuits below the 22 nm technology node, development of p-channel quantum-well FETs using new materials and new device architectures is an important goal. Compressively strained Ge (s-Ge) grown on a relaxed $Si_{1-x}Ge_x$ virtual substrate (VS) is attracting much attention as a promising candidate for a next generation higher mobility p-type MODFET. Although many 2DHG results have been published regarding the mobility of holes in these structures,[1-8] the highest. hole mobility reported was around 120,000 cm^2/Vs at 2K with carrier density $8.5\times10^{11}cm^{-2}$ [2], also Myronov [9] get 2940 cm^2/Vs at sheet density 5×10^{11} cm^{-2} at room temperature, which suggests germanium as a proper candidate to attain the new technology.

1.2 Germanium Band structure

Germanium is an indirect band gap semiconductor, similar to silicon, with a bandgap of 0.66 eV. In both of these semiconductors the conduction and valence bands consist of a number of sub-bands. In germanium, the conduction band minima lie at the zone boundaries along the <111> direction, or L point, with eight equivalent half valleys while Si has six conduction band minima along the Δ-direction of <100>.

The valence band edge of both silicon and germanium occurs at the zone centre (k = 0). At this point, the valence band consists of two degenerate bands, known as heavy hole and light hole bands, and a split-off band separated in energy from the two degenerate bands due to the spin-orbit interaction Figure 1.1. This spin-orbit splitting energy is 44 meV in silicon and 296 meV in germanium. Germanium is a promising alternative material to Si for electronic devices owing to its higher mobility for both holes and electrons compared to Si [10], see Table (1-1). Since Ge has a lattice spacing which is 4.2% larger than that of Si, Ge (or SiGe)

deposited on Si will be biaxially compressed so as to lattice match in the in-plane direction. However, the out of plane lattice spacing will get longer, to retain Poisson's ratio.

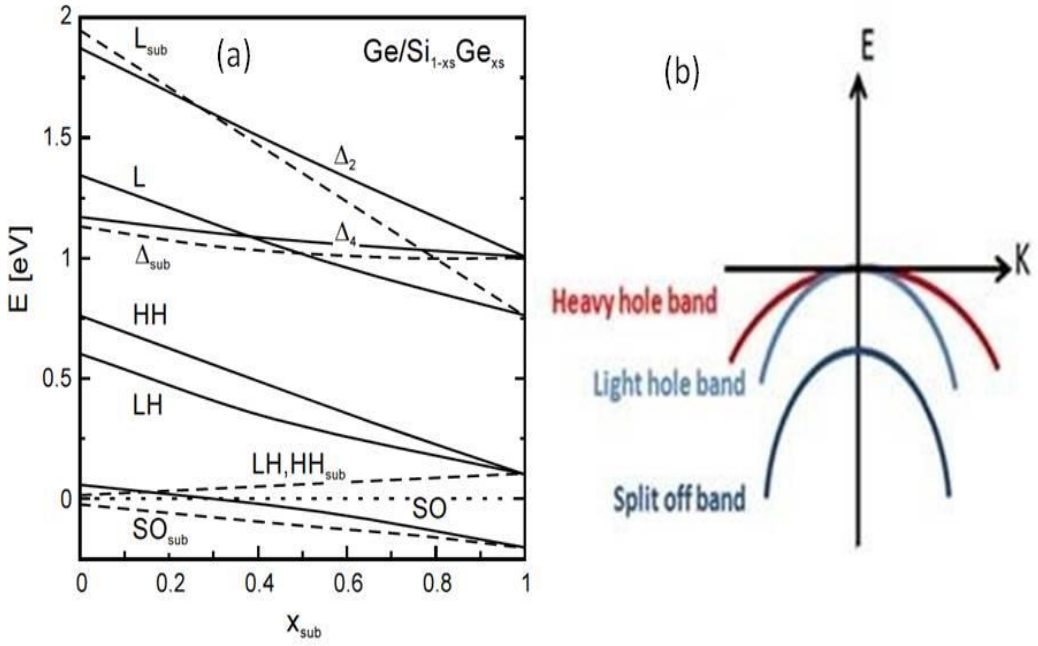

Figure 1.1 (a) Conduction and valance bands of $Ge/Si_{1-x}Ge_x$ heterostructure as a function of substrate composition (X_{sub})[11] (b) Heavy holes, light holes and spin orbit band in the valance band for bulk Ge

Introducing compressive strain Figure 1.2 also leads to a reduction of the hole effective mass [11], due to the heavy hole and light hole bands splitting in which the energy of heavy hole bands raise up and the energy of light hole band reduces leading to "mass inversion" in compressive strain, and results in mobility enhancement.

	Si	Ge
Lattice spacing (nm)	0.5431	0.5658
Electron mobility (cm^2/Vs)	1450	3900
Hole mobility (cm^2/Vs)	505	1800
Hole effective mass of each band	m_{HH}=0.54 m_0, m_{LH}=0.15 m_0, and m_{So} = 0.23m_0	m_{HH}=0.34 m_0, m_{LH}=0.043 m_0, and m_{So} = 0.095 m_0
Electron effective mass	m_{l^*} = 0.98 m_0, m_{t^*} = 0.19 m_0	m_{l^*} = 1.64 m_0, m_{t^*} = 0.08 m_0

Table 1.1 lattice parameters and electron and hole room temperature mobility in bulk silicon and germanium [12]

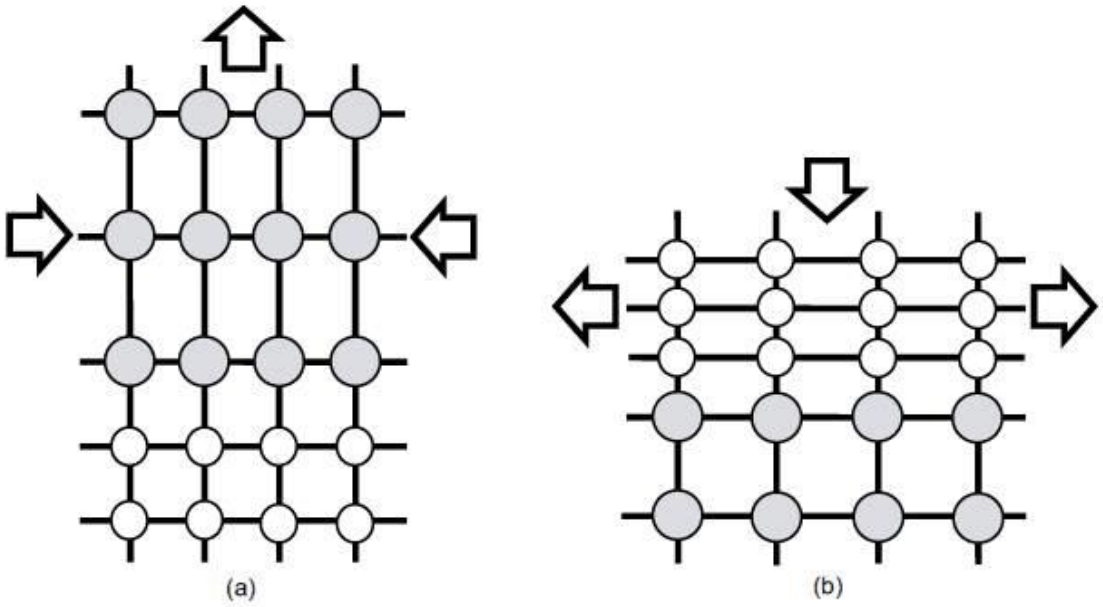

Figure 1.2 the effect of (a) biaxial compressive strain and (b) biaxial tensile strain on the lattice, with the crystal growth direction assumed to be toward the top of the page[13]

According to the lattice constant mismatch between Si and Ge it is difficult to maintain strain for Ge deposited directly on Si. Therefore, it is necessary to consider the limiting strain that could be accommodated without relaxation occurring. This is called the equilibrium critical thickness. For a Ge layer grown on a relaxed $Si_{1-x}Ge_x$ buffer layer, the critical thickness is less as the mismatch between the two layers increases i.e. as the strain is increased the critical thickness of the Ge layer goes down. Exceeding the critical thickness will cause the onset of relaxation and the formation of misfit dislocations which introduce interface roughness that affect the transport properties of the structure.

In order to generate carriers in the channel, doping was previously introduced to the layers where the carriers are required; however, in this case scattering from the impurities limits the mobility of the carriers in the channel. To reduce this effect, People *et al*. introduced doping away from the channel and separated by an undoped spacer layer [14]. This is called 'remote doping' or 'modulation doping'. The major advantage of this technique is separating the carriers from their donors or acceptors leading to reduction of impurity scattering. Another benefit is the confinement of the carriers in two dimensions. Also the carrier density could be varied by changing the spacer layer thickness.

1.3 Epitaxial growth of Ge layers

In search of raising the speed and performance of high mobility devices, scientists have attempted to produce high quality material with as few defects as possible. Different efforts have been made to investigate the most excellent growth technique to give low treading dislocation density, low surface roughness and the highest mobility. There are two main ways of epitaxial growth: molecular beam epitaxy (MBE) and chemical vapour deposition (CVD).

The main characteristic of the MBE growth technique [15, 16] is that it has independent control of growth parameters, low controllable growth temperatures enabling minimisation of solid state out diffusion and auto doping, and low growth rates and shutter control which permits thin, highly uniform layers to be grown. Whilst SS-MBE has demonstrated high wafer uniformity and ultra-sharp doping profiles, the method does have some limitations. A major limitation is the lack of in-line calibration is particularly missed during the growth of thick (several microns) epilayers and arises from the depletion of the solid-source material. Typically, for the growth of SiGe epilayers, the solid atomic sources are evaporated via electron beam impingement. However, as the sources are consumed material flux calibrations are required on a rather frequent basis which is time consuming. SS-MBE is therefore quite a slow growth process and is mainly reserved for research rather than industry.

For CVD [17], a gas containing the material wished to be deposited, known as a "precursor", is passed over a heated substrate. Under the correct conditions the gas will chemically react with the substrate and deposit epilayers. The standard chemical gases used for the SiGe system are silane and germane, which are passed down a furnace tube using a carrier gas, typically hydrogen. This technique offers high growth rates, simultaneous growth of wafers, and it is more stable and reproducible for thick structures. In addition, the growth of thick layers is possible since the gas sources are effectively infinite and the gas ratios can be constantly maintained and monitored throughout the growth via the use of mass flow control units. It is therefore the technique favoured by industry.

Li *et al* [18] investigated a low temperature MBE technique (LT) [18] for $Si_{0.7}Ge_{0.3}$ on Si (001) and found that using this process gives a lower threading dislocation density (TDD) in the order of 10^5 cm^{-2} for a smaller overall layer thickness and smother surface. This development in the quality of the structure was as an excellent motivation for Ueno *et al* [15, 19] who applied a low temperature buffer (LT) ($Si_{0.3}Ge_{0.7}$) for p type sGe channel to examine

this method on the properties of a Ge channel. The growth was in two different ways, using one and two step LT techniques, employing solid source molecular beam epitaxy (SS-MBE). They found that the two step LT buffer produced a single period of surface roughness with a 10 nm amplitude whereas the one step LT technique produced many periods. The one step process resulted in a higher drop of mobility, whilst the two step LT buffer generated a high mobility at room temperature (1700 cm^2/Vs) because of the low TDD (1×10^5 cm^{-2}), small surface roughness (1-3 nm), and almost total relaxation (>95%).

A second technique that has been investigated is low energy plasma enhanced chemical vapour deposition (LEPE-CVD) which is considered as a good choice for a high growth rate 10 nm/s[17]. Strained germanium modulation doped structure grown by LEPE-CVD result in a high hole mobility of 120,000 cm^2/Vs at 2K with a sheet density of $8.5\times10^{11}cm^{-2}$, which was thought to be due to the high quality structure, with low interface roughness compared to other techniques [17]. By optimizing this method (LEPE-CVD) for appropriately chosen plasma densities and substrate temperatures, abrupt interfaces can be achieved on both sides of the Ge channels. Additional hydrogen is supplied to the reactive gases, even for channel widths above the critical thickness for dislocation formation and it ended with high mobility 90,000 cm^2/Vs at sheet density 6×10^{11} cm^{-2} at 4.2 K [20]. In this work, it was established that LT processing below 600˚C is essential for high performance devices due to Si-Ge interdiffusion at high temperature at the Ge/SiGe interface. Annealing at temperatures above 600˚C causes a reduction in mobility and an increase in the sheet density of the structure under study. Moreover, Ge layers beyond the critical thickness easily relax when the annealing temperature is increased above 500˚C.

Another growth mechanism, used by Myronov *et al* [21], is reduced pressure chemical vapour deposition (RP-CVD) with a reverse linearly graded buffer, which improves the rms surface roughness to about 1.5 nm with TDD 2×10^6 cm^{-2} which is nearly the same as by

LEPE-CVD, but the VS thickness is less (3μm to reach 80% Ge), than the thickness of the VS grown by LEPE-CVD (above 10μm to reach 80% Ge).

To enhance the performance of the structure in terms of reduced doping and Ge segregation as well as reduced surface roughness, researchers have also attempted to apply a combination of two LEPE-CVD and SS-MBE techniques [22]. This resulted in a large increase in room temperature mobility, 2700 cm^2/Vs at sheet density $1x10^{12}$ cm^{-2}, as well as a significant improvement in the conductance that is important for device applications.

1.4 Scope of this work

My role in this project is to study the transport properties of strained Ge modulation doped heterostructures by using resistivity and Hall effect measurements, including the quantum Hall effect (QHE) with varied magnetic field. These measurements will yield a range of electrical parameters such as Hall mobility, sheet density, effective mass and so on. Resistivity and Hall effect measurements are reported on square Van der Pauw, 'Greek cross', and Hall bar structures that were fabricated from Ge-on-Si wafers with variation in parameters, such as channel thickness, spacer thickness, doping concentration, and growth temperature. Two different heterostructures are considered either with doping placed above (normal structure) or underneath the channel (inverted structure).

The second chapter of this thesis will illustrate the background theory that is used to analyse the experimental results, while chapter 3 presents the experimental techniques used. Chapter 4 contains an analysis of data from the inverted structure strained germanium, extracted using resistivity and Hall measurement. It also investigates anisotropy in these samples, as well as simulating scattering limited mobility and band edge simulation using $Nextnano^3$ program. Chapter 5 illustrates the analysis of resistivity and Hall effect measurements for the normal structure, together with an anisotropy analysis for high mobility sample (11-289) as well as

scattering limited mobility simulation and band edge simulation using Nextnano^3 program. The sixth chapter presents an analysis of high field magnetotransport result for three samples, one normal structure (11-289) and two inverted structures with different channel thickness (11-284 and 11-285).

2 Basic Concepts and Theoretical Background

2.1 Introduction

Studying the transport properties of holes in the strained Ge quantum wells will require structural and electrical characterization to explain the behaviour. In this chapter, the theoretical background of the techniques used in this research will be explained and then in Chapter 3 the practicalities of the experimental techniques will be discussed. First, the concept of measuring resistivity and mobility in an arbitrary geometry is needed, together with a way to relate a measured anisotropy back to the underlying properties of the holes. Next, the various scattering processes that limit the mobility on the holes are considered These depend on features of the samples such as the number and positions of impurities and dopants, and the surface roughness which in the case of transport in a buried layer is interface roughness that is a particularly important for narrow channels. Simulation methods will be presented for calculating the position of the valance band edge in the complete heterostructures, and hence the distribution of holes within the structure. The simulations account for the position and density of the doping impurities, the alloy composition and strain of each layer for a range of temperatures. Measurements in high magnetic fields reveal effects of quantum transport that can be used to extract values for the hole effective mass and a measure of the carrier scattering lifetime. Finally, the method of mobility spectrum analysis is presented as a way to extract the mobility of carriers in different layers, which is essential since parallel conduction occurs at higher temperatures.

2.2 Resistivity and Hall measurement:

This technique has founded wide application in the characterization of semiconductor materials because it gives the resistivity, the carrier density, and the mobility this part will emphasis all of them in details: A proper method to measure the resistivity is Van der Pauw

(VdP) measurement which allowed measuring the resistivity of a flat sample with arbitrary shape However to use this method it should consider some condition such as the contacts should be sufficiently small according to the size of the sample as well as the sample is uniform and did not contain any hole [23].

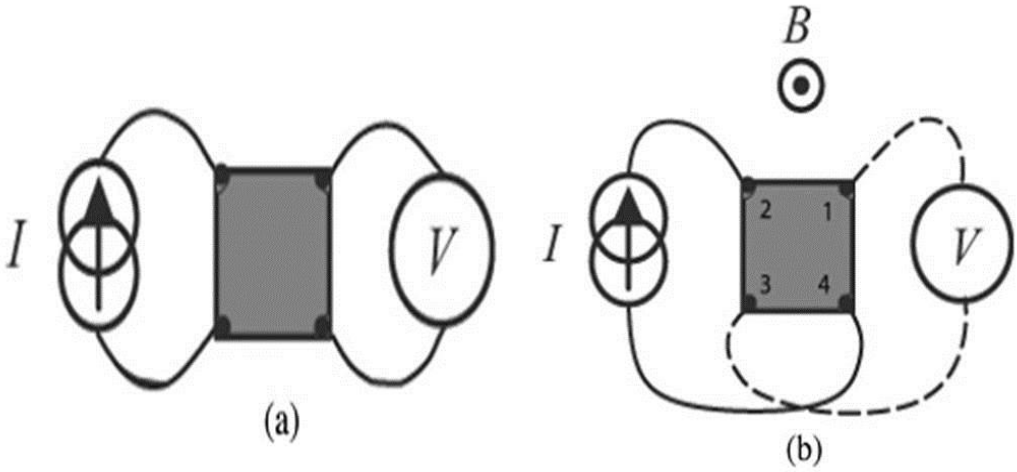

Figure 2.1 Van der Pauw square connection for resistivity and Hall measurement (a) without magnetic field, and (b) with magnetic field

For a square Van der Pauw sample, such as shown in Figure 2.1, the resistance in the vertical and horizontal directions is calculated as follows [23, 24] :

$$R_{12,34} = \frac{V_{34}}{I_{12}}, R_{23,41} = \frac{V_{41}}{I_{23}} \tag{2.1}$$

where

$$R_{12,34} = R_{34,12}, R_{23,41} = R_{41,23} \tag{2.2}$$

Since they related to the sheet resistance by the van der Pauw formula in isotropic case

$$e^{-\pi R_{12,34}/\rho} + e^{-\pi R_{23,41}/\rho} = 1 \tag{2.3}$$

and the sheet resistivity

$$\rho = \frac{\pi}{\ln 2} \frac{(R_{12,34} + R_{23,41})}{2} F \tag{2.4}$$

where F is a form factor determined by the symmetry of the sample; for a symmetric shape, such as circle or square, $F = 1$.

The sheet resistivity is always determined without applying magnetic field [18]. The Hall coefficient is determind from VdP as Figure 2.1 b and from the equation:

$$R_H = \frac{V_H}{IB} \tag{2.5}$$

The sign of the value of Hall coefficient depend on the type of the carrier, since it negative for electrons and positive for holes. Mobility and carrier density could be extracted by the following equations:

$$\mu = \frac{R_H}{\rho} \tag{2.6}$$

and

$$p_s = \frac{1}{eR_H} \tag{2.7}$$

These equations 2.6 and 2.7 assume one type of the carriers in the channel. However, in the case of two type of carriers in the channel the measured sheet density p_{ave} at low magnetic field is the average density between two types, and it expressed by the two carrier model [23]

$$p_{observed} = \frac{\left(p_1\mu_1 + p_2\mu_2\right)^2}{p_1\mu_1^2 + p_2\mu_1^2} \tag{2.8}$$

and the mobility is

$$\mu_{observed} = \frac{p_1\mu_1^2 + p_2\mu_2^2}{p_1\mu_1 + p_2\mu_2} \tag{2.9}$$

For Hall bar devices with uniformly doped sample the Hall mobility is determined by the same equation. However, the sheet resistivity determined by the dimensions of the devices requires the following equation

$$\rho = R\frac{w}{L} \tag{2.10}$$

where w is the width of the Hall bar and L its length between contacts.

In an anisotropic case the anisotropy ratio of sheet resistivity for Van der Pauw in two orientations could be defined as:

$$A = \frac{\rho_{yy}}{\rho_{xx}} \tag{2.11}$$

$$\rho_{xx} = \frac{\pi}{\ln 2}\frac{(R_{12,34} + R_{34,12})}{2}F \tag{2.12}$$

$$\rho_{yy} = \frac{\pi}{\ln 2}\frac{(R_{23,14} + R_{14,23})}{2}F \tag{2.13}$$

However, calculating anisotropy using a square Van der Pauw sample requires some correction. This is because the anisotropy ratio extracted directly from measured voltage and current values will be overestimated for two reasons. Firstly due to geometrical effects of the actual sample size and positioning of the contacts the ratio of the effective anisotropy (A_{eff}) considering geometrical aspect ratio of the VdP structure is [25, 26]

$$A_{eff} = A\left(\frac{L_x}{L_y}\right)^2 \tag{2.14}$$

Secondly, after correcting for geometry, an anisotropic resistance will alter the current flow and electric field distribution in the sample. For example, if the anisotropy coefficient $A > 1$ there will be more resistance in the y-direction than in the x-direction ($R_{23,14} > R_{12,34}$) and so it

is easier for current to flow from contact 1 directly to 2 than to travel around the sample via 2 and 3, hence the measured voltage is even smaller than would naïvely be expected. The full analysis of this was provided by Bierwagen [25], which shows the measured anisotropy of a VdP sample as is

$$A_{VdP} = \frac{\sum_{n=Odd^+} \left[n \sinh\left(\sqrt{A_{eff}^{-1}} \pi n \right) \right]^{-1}}{\sum_{n=Odd^+} \left[n \sinh\left(\sqrt{A_{eff}} \pi n \right) \right]^{-1}} \tag{2.15}$$

In order to get the actual resistivity coefficient (A) from the measured anisotropy ratio (A_{VdP}) a calibration curve based on equation 2.15 is required (Figure 2.2). Note how there can be an extremely large difference in these ratios for highly anisotropic samples. Fortunately for the samples in this thesis the highest measured anisotropy was 9. From the value of A actual resistivity could be defined as $\rho_{xx} = \rho_{ave}\sqrt{A^{-1}}$, and $\rho_{yy} = \rho_{ave}\sqrt{A}$, with the same Hall coefficient in both orientations calculated mobility is defined.

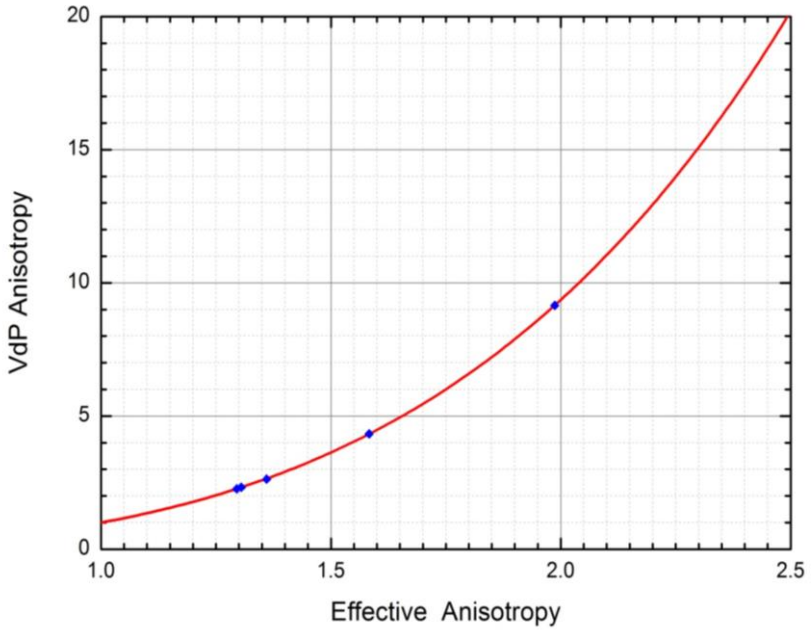

Figure 2.2 Calibration curve between measured anisotropy ratio and actual resistivity ratio for square VdP. Blue points represent data from the inverted structures of Chapter 4

2.3 Scattering limited mobility in Ge:

The main scattering mechanism in bulk high purity p-type germanium is optical and acoustical phonon - hole scattering [27, 28]. The latter reference gives experimental data for the mobility as function of temperature and shows that at low temperature mobility $\mu \propto T^{-1.5}$, which seems to be dominated by acoustical phonon scattering, while at high temperature mobility is limited by both optical and acoustical phonon scattering. This result was in agreement with the theoretical prediction for pure Ge [27]. Moreover, their Hall mobility calculation for Ge and Si was successful for Si and less satisfied for p- type Ge, largely as a result of not having adequate values of acoustic deformation potential parameters.

For a 2DHG in Ge at low temperature, the mobility is limited by three other scattering mechanisms: remote ionised impurity scattering, background impurity scattering and interface roughness scattering, which usually dominate over acoustic phonon scattering at low temperature. Introducing a small amount of impurities will limit the mobility of the 2D carrier gas, for that reason the doping layer is placed away from channel aiming to reduce the effect of impurity scattering on mobility. However, there will still be background impurities at a certain level depending on the cleanliness of the growth system that can have an enormous effect even at unintentional doping levels of $10^{15}cm^{-3}$ and below that are hard to observe in techniques such as SIMS. Even with no background impurities, remote impurities must be ionised in the process of supplying carriers to the channel and the resulting spatially varying electrostatic potential will influence the carriers in the channel. Finally, any imperfections of the interfaces will both locally affect the confinement potential and produce a spatially varying potential leading to scattering or even charge trapped at these interfaces.

Simulation for the mobility at low temperature for sGe normal (doping above the channel) and inverted structure (doping underneath the channel) have been performed for the samples

under study, taking in account remote and background impurities scattering as well as interface roughness scattering.

The variation of sheet density with spacer layer thickness can be calculated following Emeleus *et al* [29], from the equation of valance band offset using the following equation:

$$\Delta E_v = E_0 + E_F + E_A + \frac{e}{2\varepsilon_0\varepsilon_r} N_A l^2 + \frac{e}{\varepsilon_0\varepsilon_r} N_A l L_s \tag{2.16}$$

N_A is the acceptor concentration, N_{Depl} is the depletion charge and l is the depletion width $l = \left(p_s + N_{depl} \right) / N_A$, and E_0 is the energy of the lowest subband, E_A is the boron acceptor energy and is about 30 meV for doping at 2×10^{18} cm^{-3} [30], ε_r is the permittivity of Ge and the Fermi level is given by:

$$E_F = \frac{\pi\hbar^2 p_s}{m_z} \tag{2.17}$$

Only the states near Fermi level contributed to the transport at low temperature and the Fermi wave vector is $K_F = \sqrt{2\pi p_s}$, while the mean free path of the carriers is $l_m = \hbar K_F \tau_t / m^*$.

2.3.1 Remote impurity scattering (RIS):

According to Ando *et al* [31] the wave function for the triangular well is in the Fang–Howard form which goes to zero at the interfaces

$$\Phi(z) = \left(\frac{b^3}{2} \right)^{1/2} z \, exp\left(-\frac{bz}{2} \right) \tag{2.18}$$

where z is the width of the well, z=0 defines the Ge/SiGe interface, b is variational parameter:

$$b = \frac{12 m_z e^2}{\hbar^2 \varepsilon_0 \varepsilon_r} \left(N_{Depl} + \frac{11}{32} p_s \right) \tag{2.19}$$

and m_z is the effective mass in the confinement (*z*-)direction.

At very low temperature, the holes are highly degenerate and behave like a 2D Fermi gas. The mobility is

$$\mu = \frac{e\tau}{m^*} \tag{2.20}$$

Relaxation times τ from multiple scattering mechanisms add according to Matthiessen's rule

$$\frac{1}{\tau_{total}} = \sum_{n=1}^{N} \frac{1}{\tau_n} \tag{2.21}$$

where τ_{total} is the resultant relaxation time and τ_n are relaxation times for n=1 to N scattering mechanisms. For a 2D system the relaxation time is defined by the Stern-Howard formula [31-33]:

$$\frac{1}{\tau_{RI}} = \frac{1}{2\pi\hbar E_F} \int_0^{2K_F} dq \frac{q^2}{\left(4K_F^2 - q^2\right)^{1/2}} \frac{\left\langle \left|U(q)\right|^2 \right\rangle}{\varepsilon(q)^2} \tag{2.22}$$

where τ_{RI} is the remote impurity scattering, $\varepsilon(q)$ is the screening function (equation 2.30), and $\left\langle \left|U(q)\right|^2 \right\rangle$ is the scattering potential, q is a 2D wave number, for remote impurities [33, 34]

$$\left\langle \left|U(q)\right|^2 \right\rangle = n_i \left[\frac{2\pi e^2}{\varepsilon_L q} \right]^2 F_R(q, L_s)^2 \tag{2.23}$$

where n_i is the remote ionized impurity density assumed to be uniform, and $F_R(q, L_s)$ is the form factor for remote impurities for the case of $4K_F L_s \gg 1$ and ideally 2DEG:

$$F_R(q, L_s) = \mathrm{e}^{-2qL_s} \tag{2.24}$$

So, the relaxation time is defined by:

$$\frac{1}{\tau_{RI}} = E_F \frac{n_i}{g_v p_s (2q_F L_s)^3} \tag{2.25}$$

Another approach by different researchers [35, 37] to simulate scattering limited mobility, for modulation doped heterostructure the momentum relaxation time [37] for carriers occupying the first subband is given by

$$\frac{1}{\tau_{RI}} = \frac{e^4 m^* n_i}{8\pi\hbar^3 \varepsilon_r^2 q} \int_0^{\pi} d\theta \frac{\exp(-4qL_i \sin\theta)\sin\theta}{(2q\sin\theta + S_0)^2} \tag{2.26}$$

where at low temperature it should use the degenerate limit where q the electronic wave vector is equal to K_F that is the wave vector on the Fermi surface. S_0 is the screening constant of first subband and it defined as $S_0 = \frac{2e^2 m^*}{4\pi\varepsilon_r \hbar^2}$, and $L_i = L_s + w$ where L_s is the spacer thickness, w is the average width of the hole wavefunction (Figure 2.3). This equation does not take into account the fact that scattering by the acceptors (donors) outside the depletion layer is strongly reduces by screening. However, in reality only the acceptors in a distance range $L_i^{`} = L_s + w + L_d$, where L_d is the width of doping layer, contribute to the scattering, so the relaxation time for remote impurities including this factor is :

$$\frac{1}{\tau_{RI}} = \frac{e^4 m^* n_i}{8\pi\hbar^3 \varepsilon^2 q} \int_0^{\pi} d\theta \frac{\left[\exp(-4qL_i \sin\theta) - \exp(-4qL_i^{`} \sin\theta)\right]\sin\theta}{(2q\sin\theta + S_0)^2} \tag{2.27}$$

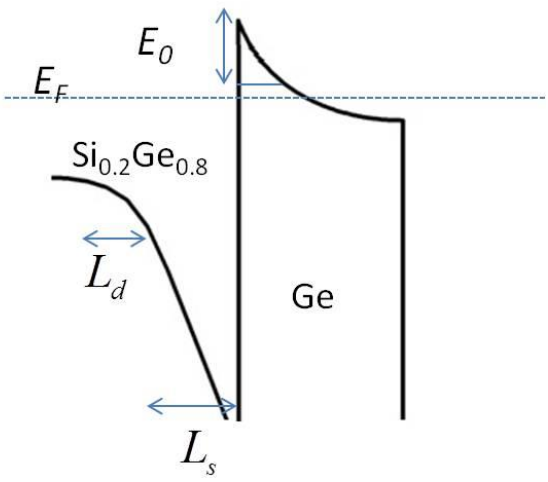

Figure 2.3 Schematic of valance band

At sheet density >10^{11} cm^{-2} and L_i > 5 nm, then $4qL_i$ is larger than one and at low value of θ using screening in the 2D Thomas- Fermi approximation, the relaxation time results in a mobility [29, 36] the mobility at T = 0 K

$$\mu_{RI} = \frac{32(2\pi)^{1/2} e\, p_s^{3/2}}{\hbar N_A}\left(\frac{1}{(L_s+w)^2} - \frac{1}{(L_s+w+l)^2}\right)^{-1} \quad (2.28)$$

2.3.2 Background impurity scattering (BIS):

Scattering from background impurities can significantly affect mobility, especially for higher quality structures with higher spacer thickness to reduce remote impurity scattering. Good quality growth technique has been a target for many researchers to get rid of background impurities, which become the dominant scattering for especially low sheet density samples. The momentum relaxation time due to background impurities using the model given by [36, 37]

$$\frac{1}{\tau_{BI}} = \frac{4e^4\pi m^* d^3 N_B}{\hbar^3 \varepsilon^2 K_F^2}\int_0^{\pi} d\theta \frac{(1-e^{-2K_F \sin\theta})\sin\theta}{(2q_F \sin\theta + S_0)^2} \quad (2.29)$$

where N_B is the background impurity in the Ge channel, which is expected to be very low in our case at less than 10^{14} cm^{-3}, especially for the normal structure, d is the width of the quantum well. This equation was obtained by using degenerate Fermi statics, which might differ in this point from other equations in different references. For example, the model of Gold [38] has been used for Si/SiGe heterostructures, which uses a Fang- Howard wave function and includes Coulomb interaction effects between electrons within the random phase approximation (RPA), modified by local-field correction (G(q)), so the screening is

$$\varepsilon(q) = 1 + q_s\left[1 - G(q)\right]F_C(q)/q \tag{2.30}$$

where $q_s = g_s g_v / a_B$, and $a_B = a_0 \varepsilon_L m_e / m^*$ Bohr radios , $a_0 = \frac{\hbar^2}{m_e e^2}$, q is the wave number, and m_e is electron effective mass. $F_C(q)$ represent the form factor for the Fourier-transformed Coulomb interaction potential $V(q) = {2\pi e^2 F_C(q)}/{\varepsilon_L q}$. This form factor depends on the width of the QW in symmetric doped heterostructures and on the width of the wave function in non-symmetric doped heterostructures [31] and MOSFETs. The carrier scattering simulation used in this thesis [36, 37] considers confinement in the z- direction as well as the screening of charge impurities. The relaxation time of background impurity scattering according to Gold [38] at low sheet density is

$$\frac{1}{\tau_{BI}} = \frac{\pi E_F N_B w F_B(q)}{\hbar p_s g_v (q/q_s)^2} \tag{2.31}$$

where g_v is the valley degeneracy.

2.3.3 Interface roughness scattering

Interface roughness appears between the Ge and SiGe layers and can be the dominant scattering that limits the carrier mobility if the roughness parameters are high. Interface roughness scattering increases as the sheet density increases [39]. Assuming a Gaussian autocorrelation with height Δ and correlation length Λ, the scattering will have a maximum for a roughness length of order $\Lambda = 1/K_F$.

$$\frac{1}{\tau_{IR}} = \frac{\pi e^4 m^* \Delta^2 \Lambda^2}{\pi \hbar^3 \varepsilon^2 K_F^2} \int_0^{\pi} d\theta \frac{\left(2K_F \sin\theta\right)^2}{\left(1+S_0/K_F\right)} \left(N_{Depl} + \frac{p_s}{2} \right) e^{\frac{-q^4\Lambda^2}{4}} \tag{2.32}$$

where: Δ = interface roughness height , and Λ = interface roughness correlation length.

In general, the mobility is affected by both parameters and the mobility increases if Δ decreases and/or Λ increases. In the case of $K_F\Lambda << 1$ then [40]

$$\mu_{IR} = \frac{e\, g_v^3 g_s^3}{192\pi^4 p_s \hbar \left(0.5 p_s + N_{depl}\right)} \tag{2.33}$$

where g_s is the spin degeneracy.

2.4 Simulation of the valance band:

Simulations of the valence band structure were performed with the Nextnano^3 software package[41], using the effective-mass approximation (EMA) and k.p method for single isotropic parabolic bands. The EMA gives an essential insight into the subband structure, which is a good starting point for the 2D hole gas. A more detailed valence band structure can be obtained in the framework of k.p-method. The k.p method is based on a multiband Hamiltonian and assumes non-parabolicity, spin splitting and coupling between heavy holes (HH) and light holes (LH), as well as spin split off (SO) holes. The program of Nextnano^3 has an extended database, where all the parameters of the material are included. The input file

contains detailed information for the structure, which is connected with the database for the materials introduced in the input file, each layer is assigned to specific grid point, which requires all layers to be inserted with their widths and material type. Then, the strain is calculated. Only pseudomorphic growth can be considered, where the in-plane lattice constant matches to the substrate and the out-of-plane is extended or compressed. For a predefined "quantum region", typically the quantum well and its close neighbourhood, the Poisson equation and the Schrodinger equation are solved self-consistently, and the strain assumed to be homogeneous, elsewhere only electrostatics are considered. More information about this software, and some detailed examples, can be found on the webpage [41].

2.5 Magnetotransport in high magnetic field:

2.5.1 Landau Levels

The eigenstate energy for three dimensional (3D) carriers can be found from the solution of the Schrodinger equation:

$$-\frac{\hbar^2}{2m}\nabla^2\psi + V\psi = E\psi \tag{2.34}$$

where ψ is the wave function. However, by applying a magnetic field new eigenstates will form and in 2D the Schrödinger equation is modified and 2DHG energy levels for single subband occupancy are split into Landau levels (LLs) that are due to quantisation of motion in the xy directions. The energy of these levels depends on the magnetic field and is given by

$$E_n = \hbar\omega_c(n+\frac{1}{2}) \quad n = 0,1,2,..... \tag{2.35}$$

$\omega_c = eB/m*$ is the cyclotron frequency. The number of the levels occupied with carriers depends on the magnetic field. As the degeneracy of the LLs increases with field, at higher magnetic field fewer LLs need to be filled for constant carrier density. The filling factor, which defines the ratio of hole density to the number of LLs, is [42]:

$$\upsilon = \frac{hp_s}{eB} \tag{2.36}$$

As the magnetic field increases, E_n increases and the position of the Fermi Energy E_f within the LL structure will change. At higher fields the separations between LLs get larger and so the number of LLs with energy below the Fermi energy, and hence populated, will reduce. In the experimental case, the LLs are broadened due to scattering by $\Gamma = \frac{\hbar}{2\tau_q}$, where τ_q is the quantum scattering time. In order to resolve the LL structure in an experiment the condition $\omega_c \tau \geq 1$ must be satisfied, which means that an electron (or hole) has to survive long enough without scattering to complete at least one cyclotron orbit.

2.5.2 Shubnikov de Haas Oscillation:

Shubnikov de Haas (SdH) oscillations and QHE occur in the same conditions which mean the energy separation between LLs should be larger than the LLs width. These oscillations are periodic in inverse magnetic field 1/*B*. Oscillation in the longitudinal resistance can be expressed as [43-45]

$$\frac{\Delta\rho}{\rho_0} = C\, R_s \sum_{s=1}^{\infty} \frac{\psi}{\sin h\psi} \exp\left(-\frac{\pi}{\omega_c \tau_q}\right) \cos\left(\frac{2\pi s \epsilon_0}{\hbar\omega_c} - s\pi\right) \tag{2.37}$$

where $\Psi = \frac{2\pi^2 k_B T}{\hbar\omega_c}$ and *s* is Fourier harmonic index, R_s is associated with Zeeman splitting.

The constant *C* could be at 2 or 4 which depends on the behaviour of resistivity with the density of states n_{2D} [46, 47]. If the intercept is at 2 that means the resistivity is dependent on n_{2D}, while if it is 4 that means the conductivity is proportional to the square of the density of states. The value of *C* determines the intercept of the Dingle plot that will be explained in next section.

SdH oscillations depend on the sheet density of the 2DHG. So it is useful to use these oscillations to deduce the hole sheet density of the channel by plotting the oscillations as a function of 1/*B* where they should have a constant period defined by the cosine term. By determining $\Delta\left(\frac{1}{B}\right)$ the sheet density is given by

$$p_{SdH} = \frac{g_s g_v e}{h\Delta(1/B)} \tag{2.38}$$

With one subband occupation analysis of the SdH oscillations is relatively simple; however, if two levels are occupied the analysis becomes more complicated, since two different periods of oscillation will be superimposed as a result of different values of sheet density for each subband [48]. Beating could also occur when two types of carriers pocket appear in the channel or zero field spin splitting is presented. The sheet density for each frequency in the case of zero spin splitting occurs in the FFT analysis of SdH oscillation calculated using the following equation

$$p_{\pm} = \frac{e}{h} f_{\pm} \tag{2.39}$$

Where $f_{\pm}$ the frequencies observed in FFT of SdH oscillation due to the beating pattern , and $p_{\pm}$ is the spin subband densities(spin up sheet density and spin down sheet density) [49].

2.5.3 Effective mass and ratio of transport to quantum life time

The SdH oscillations can be used to extract the effective mass and Dingle ratio α (ratio of the transport scattering time and the quantum scattering time) [50-52]. The transport lifetime τ_t is the time needed to relax the transport of the charge carried by the holes i.e. their momentum and so it depends on the scattering angle of an event; it can be extracted from classical resistivity and Hall measurement equation (2.20) [10]. The quantum lifetime τ_q is the relaxation time between any scattering process, irrespective of scattering angle, and it can be extracted from the damping of SdH oscillations [53]. The Dingle ratio allows us to identify the scattering mechanism that limits the mobility, because each scattering processes contributes differently to τ_t and τ_q. Background impurity scattering has the same contribution to the two scattering times, because all scattering angles are equally likely, while remote impurity scattering produces smaller angle scattering and leads to a factor $(1-\cos\theta)$ difference between the two scattering times. Therefore the ratio of transport to quantum lifetime α can be used as a measure of the relative importance of the two scattering processes. Generally, very high mobility material requires very low background impurity levels, so the Dingle ratio tends to be very high [54-56].

Both the effective mass and Dingle ratio are revealed by the method introduced in the reference [57]. The resistance amplitude of the SdH oscillations is first measured at each integer filling factor (i.e. for the various magnetic field at which a peak appears) for a range of temperatures. Then, assuming some value of m^*, a graph is plotted of $\ln\left(\frac{\Delta R}{R}.\frac{\sinh\psi}{\psi}\right)$ vs $(\mu B)^{-1}$ for various temperatures, as shown in Figure 2.4(a). Different effective mass values are tried until this graph is a straight line with an intercept at 1.38, which shows the correct value has been found for the mass, and from the slope $(-\pi\alpha)$ the Dingle ratio can be

determined. This value of α is next used to plot $\ln\left(\frac{\Delta R}{R}\right)$ against $\ln\left(\frac{\sinh\psi}{\psi}\right)-\left(\pi\alpha/\mu B\right)$ over a range of temperatures. The gradient of this plot confirms the choice of effective mass if it is unity. A poor Dingle plot, with a non-linear distribution of the points, indicates that the sample is inhomogeneous, with more than one sheet density present in different regions of the sample. This can appear in the SdH oscillations as beating if the regions are well defined or, more usually, as a smearing out of the oscillations. In addition, the Dingle plot could be quadratic, not linear, which is a sign that there is general spread of densities [54]. Finally, if the line of the Dingle plot intercepts at a point less than ln4, this can indicate two subband occupation or a parallel conduction contribution.

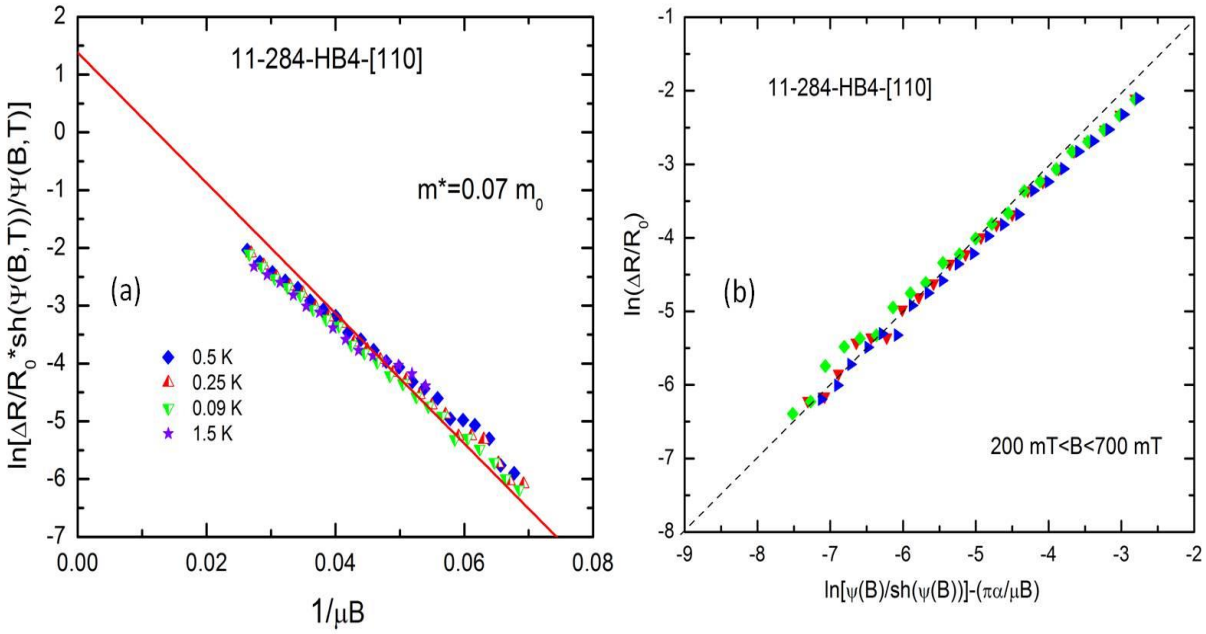

Figure 2.4 Example Dingle plot and α extraction curves. Each set of symbols correspond to a different temperature. In both plots, all the data should lie on a single straight line with a fixed intercept of 1.38 in (a) and a unity gradient in (b).

2.6 Mobility spectrum analysis

Semiconductor heterostructures can have several layers populated with charge carriers that conduct in parallel channels. The mobility and sheet density values extracted from Hall effect measurements are a result of the contribution of carriers in all these layers. This is a particular issue at room temperature, when all can contribute, whereas as the temperature is reduced some of the channels 'freeze out' (because the carriers are localised and no longer free to move). Carrier freeze-out at low temperature has been observed in many 2D heterostructures [58-60] and will be seen in the results chapters of this thesis as the number of carriers saturating at low temperature to just represent the carriers in the quantum well.

In order to extract the number of the carriers in the quantum well at room temperature, two slightly different implementations of mobility spectrum analysis will be introduced in this section and applied by two different people for our structure. Several researchers have used these methods to defined channel mobility and sheet density at room temperature for sGe heterostructures [4, 8, 22, 61-64]. The first use of mobility spectrum analysis (MSA) was by Hock *et al.* [65]. The idea of MSA is to record the magnetoresistance components for the sample over a wide magnetic field range and then to solve the inverse problem of finding an arrangement of carriers with particular mobilities that would produce these curves. Solving the inverse problem is the difficult bit and was improved by Kiatgamolchai *et al* [66] into what they called maximum-entropy mobility spectrum analysis ME-MSA. This method obtains a stable mobility value and does not require any assumptions Figure 2.5. Mobilities at room temperature found in previous MSA studies were in the range 1300-3000 cm^2/Vs [4, 19, 22, 59, 61, 62, 64]. However, it has been estimated that the room temperature hole mobility in Ge can reach 5000 cm^2/Vs [59]. For that reason, and according to the high mobility observed at low temperature in our structure, room temperature mobility becomes more interesting especially because of its priority in device application.

2.6.1 Maximum-entropy mobility spectrum analysis (ME-MSA):

The minimum resolvable mobility in MSA will be an inverse of magnetic field. The nature of the calculation is that with more iterations, peaks become sharper and the relative error is reduced. The magnetoconductivity tensor components σ_{xx} and σ_{xy} are obtained from the relations:

$$\sigma_{xx}(B) = \frac{\rho_{xx}(B)}{\left|\rho_{xx}(B)\right|^2 + \left|B.R_H(B)\right|^2} \tag{2.40}$$

$$\sigma_{xy}(B) = \frac{B.R_H(B)}{\left|\rho_{xx}(B)\right|^2 + \left|B.R_H(B)\right|^2} \tag{2.41}$$

These equations can also be written in an integral form in terms of the carrier mobility spectrum

$$\sigma_{xx}(B) = \int_{-\infty}^{\infty} \frac{s(\mu)}{1+\left(\mu.B\right)^2} d\mu \tag{2.42}$$

$$\sigma_{xy}(B) = \int_{-\infty}^{\infty} \frac{s(\mu).\mu.B}{1+\left(\mu.B\right)^2} d\mu \tag{2.43}$$

where the generalized conductivity function or mobility spectrum is $s(\mu) = n_s(\mu)e\mu$. This definition of the mobility spectrum contains the implicit assumption that the number and mobility of each carrier type do not vary with magnetic field. The experimentally measured magnetoresistance and quantum resistance are related to the conductivity tenser by the following equations:

$$\rho_{xx} = \frac{\sigma_{xx}}{\sigma_{xx}^2 + \sigma_{xy}^2} \tag{2.44}$$

$$R_H(B) = \frac{\rho_{xy}}{B} = \frac{1}{B}\frac{\sigma_{xy}}{\sigma_{xx}^2 + \sigma_{xy}^2} \tag{2.45}$$

This method considers the mobility spectrum as a probability distribution of several events p_i accompanied with discrete values of mobility, where p_i is the probability of a set of partial conductivities s_i and it is supposed to be positive:

$$p_i = \frac{s_i}{\sigma_0} \tag{2.46}$$

σ_0 is the conductivity at zero magnetic field. Since many probability distributions agree well with the data, the concept of entropy appears as a proper solution to find the best p_i. The entropy of a mobility spectrum *H* is defined as:

$$H(s) = -\sum_{i=1}^{N} p_i \ln(p_i) \tag{2.47}$$

which represents a positive weight for each event and for the maximum entropy that is used here, $p_i \geq 0$ should be satisfied, so no negative results appear.

These equations could be also written in a form where:

$$Kp = \sigma^{tot} \tag{2.48}$$

$$K_{ji} = \frac{1 + \mu_i B_j}{1 + (\mu_i B_j)^2} \tag{2.49}$$

$$\sigma_j^{tot} = \sigma_{j\ xx}^{xx} + \sigma_j^{xy} \tag{2.50}$$

The probability of maximum entropy of mobility spectrum is achieved using Langrange multipliers [67]

$$p_i = \exp(-\lambda_0 \sum_{j=1}^{M} \lambda_j K_{ji}) \tag{2.51}$$

where

$$\exp(\lambda_0) = \sum_{i=1}^{N} \exp(-\sum_{J=1}^{M} \lambda_j K_{ji}) \tag{2.52}$$

and

$$\sum_{i=1}^{N} p_i = 1 \tag{2.53}$$

Using equations (2-51), (2-52) and (2-48), it found:

$$\sum_{i=1}^{N} \left[\left(K_{ji} - \sigma_j^{tot} \right) \exp\left(-\sum_{j=1}^{M} \lambda_j K_{ji} \right) \right] = 0 \tag{2.54}$$

which is *M* nonlinear equations with *M* unknown Lagrange multipliers.

$$\lambda_j^{new} = \lambda_j^{old} - B\left(\sigma_j^{tot} - \sum_{i=1}^{N} K_{ji} p_i \right) \tag{2.55}$$

where *B* is an adjustable parameter help to repeat the solution between equations (2-51) and the last equation until p_i converge. The maximum entropy mobility is then achieved.

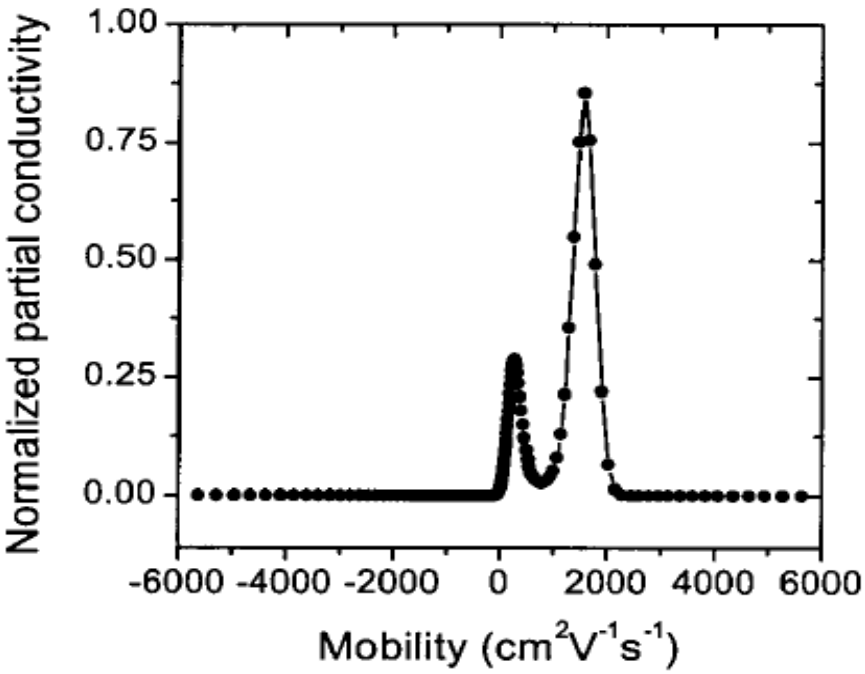

Figure 2.5 ME-MSA spectrum of two carrier peaks representing two layers in the structure and their mobility shown in x axes while sheet density could be calculated from the width of the peak.

2.6.2 Bryan's Algorithm Mobility Spectrum (BAMS):

BAMS uses a maximum entropy method to find out the least-squares fit of the mobility spectrum *s*(μ) [68]. It is performed on the inverse of total conductivity in order to find *s*(μ) for a range of values of the parameter α which controls the balance between the minimization of the least-squares fit and the maximization of the entropy, and then calculates the average of the probability *s*(μ) related to α. Much iteration could be performed to get the best result and minimizing *Q* for many α value and average the results weighted by their probabilities. Where $Q = \chi^2 - \alpha H(s)$ where H(s) is the entropy represented in equation 2-47, and χ is the least squares fit. The conductivity is calculated using the following equation

$$\sigma(B) = \sigma_{xx}(B) + \sigma_{xy}(B) = \int_{-\infty}^{\infty} \frac{1+\mu B}{1+\mu^2 B^2} s(\mu) d\mu \qquad (2.56)$$

3 Experimental Methodology

3.1 Introduction

This chapter will describe the structure of the samples studied in this work. The process of fabricating them into devices for electrical measurements at a range of temperatures will be described, along with the cryostat systems used. Finally, a description will be given of the structural measurement techniques used to determine important parameters of the material that affect the hole transport, such as impurity and dopant distribution, layer thickness and strain, and surface roughness.

3.2 Sample structure:

Many strained Ge quantum well (QW) structures have been grown in Warwick with different parameters see table 3.1. This thesis will specifically concentrate on "normal" modulation doped heterostructure (NH) 11-289 (i.e. with doping above the sGe channel), and a number of "inverted" ones (i.e. doping underneath the sGe channel (IH)) Figure 3.1, that have different parameters such as doping, channel thickness, different growth temperature, and spacer thickness. All these samples were grown in an ASM Epsilon 2000 reduced pressure chemical vapour deposition (RP-CVD) chamber. The normal heterostructure (sample 11-289) contain a 20 nm fully-strained germanium (sGe) channel, equivalent to 0.65% lattice mismatch with respect to the underlying $Si_{0.2}Ge_{0.8}$ buffer. This strain tuning buffer [69] is grown at 400˚C without any chemical mechanical polishing (CMP) [70, 71], and the structures have a very low threading dislocation (TDD ~ 4×10^6 cm^{-2}) [72]. The doping layer thickness of 13 nm, as calculated from a SIMS profile using full width half maxima (FWHM), is placed above an undoped spacer layer of 30 nm nominal thickness. (The actual thickness will be discussed in chapter 5.). The structure is capped by a 30 nm $Si_{0.2}Ge_{0.8}$ layer followed by a 2 nm Si layer, which are grown at 500 °C to avoid strain relaxation [73].

Investigations of the Inverted structures will start from the control sample 11-284, which contains a 20 nm sGe channel followed by a 20 nm thick undoped spacer. Next, the doping layer was designed to be 10 nm as a nominal thickness; however, as will be shown by SIMS in section (4-2-3), it was 18 ± 2 nm. Furthermore, other inverted structures were produced that were designed to have one parameter change in each sample: Sample 11-285 differs from control sample by having a 10 nm channel thickness and 11-286 has a 40 nm thick channel; Sample 11-287 has a smaller spacer thickness of 10 nm and 11-288 has a higher doping density which is 4×10^{18} cm^{-3}. For the last two samples: 11-290 had the active region grown at 450°. Table 3.1 shows all the samples and their parameters.

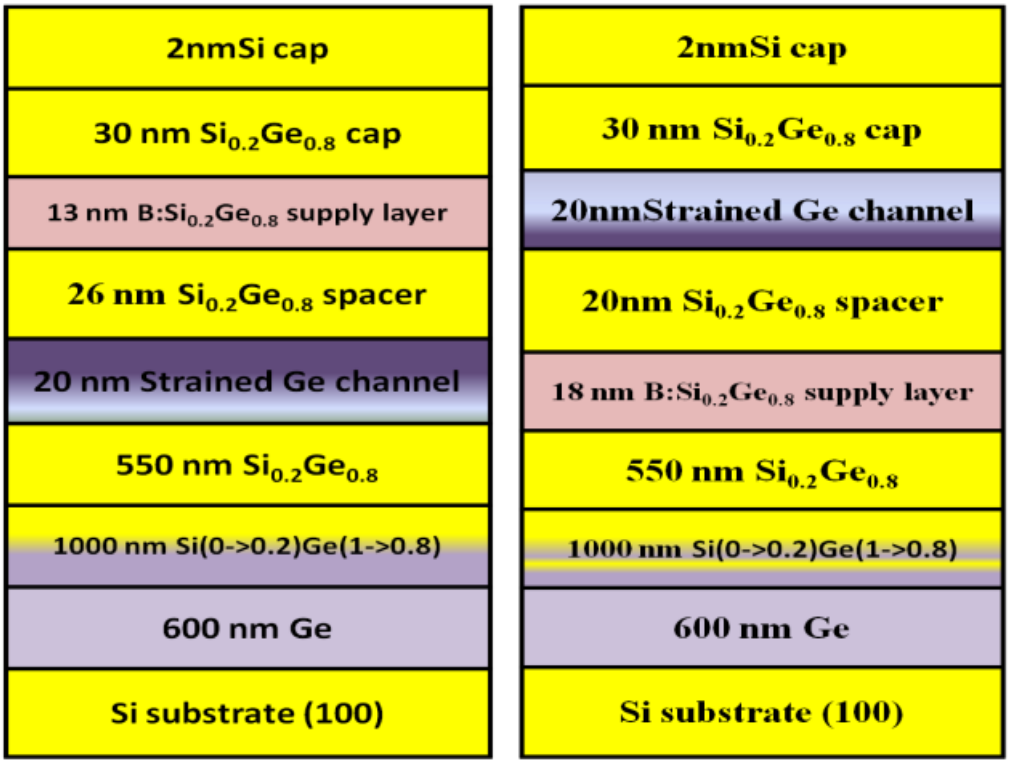

Figure 3.1 Schematic diagram of the strained Ge QW heterostructure, (a) normal structure 11-289, (b) inverted structure 11-284

Wafer	sGe Growth Temperature (C°)		Channel Thickness (nm)			Spacer Thickness (nm)		B Doping (1×10^{18} cm^{-3})		Doping place		Si Cap (nm)	
	400	450	10	20	40	10	20	2	4	NH	IH	0	2
11-284	*			*			*	*			*		*
11-285	*		*				*	*			*		*
11-286	*				*			*			*		*
11-287	*			*		*		*			*		*
11-288	*			*			*		*		*		*
11-289	*			*			*	*		*			*
11-290		*		*			*	*			*		*

Table 3.1All samples with their nominal structure parameters and NH represents normal heterostructure, and IH represents inverted heterostructure.

3.3 Electrical transport measurements

3.3.1 Sample Fabrication Process:

The first type of sample used was a simple Van der Pauw cleaved in a square (8×8 mm^2) and with the corners scribed using a diamond pen before applying InGa contacts using brush to the corners. The scribing was necessary to ensure contact was made to the buried sGe channel. Finally, the middle and the edge of the sample were cleaned carefully by acetone to ensure no short has applied between contacts by mistakes Figure 3.2 The second type of sample was fabricated by hand as a ‘Greek cross’. Firstly, the samples were cleaned using a 2% HF dip for 30 sec and rinsed by deionised water (DIW). Ohmic contacts to the cleaved sample were arranged by thermal evaporation of aluminium dots through a mask with 1 mm

holes, and black wax is painted onto the surface as cross covering the contact as illustrated in Figure 3.3 (a), after 30 min, which is the time needed to ensure the wax was dried, the sample was etched for 2-3 sec using a solution of HF:HNO3:CH3COOH in the ratio 3:5:3. The process ended by removing the black wax using xylene and rinsing with deionised water Figure 3.3 (b). The samples were annealed at 425 ˚C for 20 min to activate the contacts before measuring.

Hall bar fabrication was performed using standard photolithography procedure Figure 3.4 and either wet chemical etching or dry etching. The procedure for the wet method is illustrated in Figure 3.4. In this method the contacts are formed first and then the body of the Hall bar is made in a self-aligned way. After the wafer had been cleaned with 2% HF and rinsed with DIW, the contact metal layer was deposited by thermal evaporation of Al. Photoresist (S1818) was coated on the sample using a spinner in the clean room (3000 rpm, 35 sec), and baked for 1 min at 115˚C. The sample was then aligned with the Hall bar mask Figure 3.5 and exposed for 4.5 sec to UV-light. The unexposed area was removed using a developer solution and rinsed with DIW. Out of the clean room, the Al was removed from places outside of the mesa then etched using the same etching solution as in the previous method for 2 sec and rinsed by DIW. The resist was removed by acetone and the sample is ready for the next step which is contact fabrication. The same steps were repeated with another photoresist (AZ5214E) spun on at 4000 rpm for 35 sec, after which the sample was baked for 1 min at 110˚C. The sample was aligned with a different mask and exposed for 2 sec to UV- light, then the sample was baked for 2 min at 120˚C before flood exposure of the whole sample for 8 sec, rinsing with developer and Al etching followed and in the end resist stripped using acetone. All the samples were annealed for 20 min at 425˚C before measuring. For the dry etching process, instead of using chemical solutions plasma ashing at 100W RF for 1 min was

employed first to determine the contact and for 12 min by Corial ICP/RIE to define the devices. Dry etching is believed to be a better process to reduce current leakage.

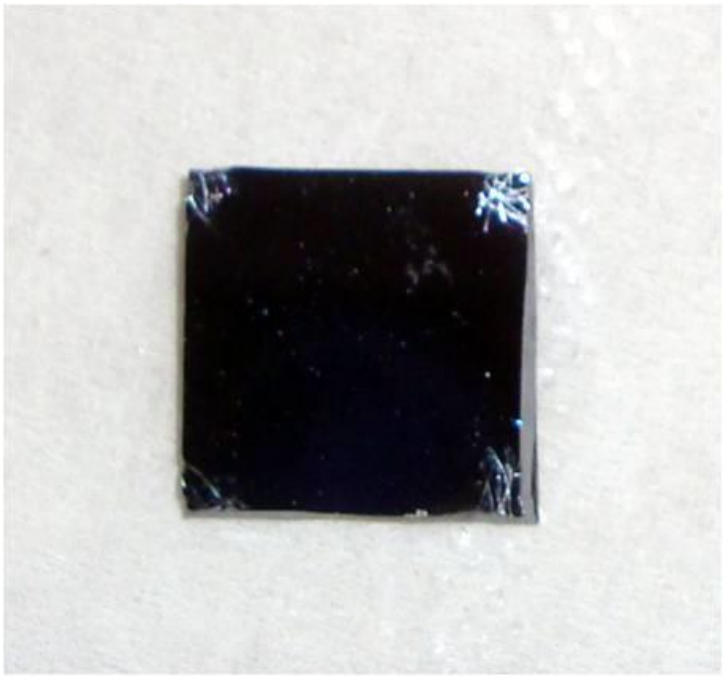

Figure 3.2 Squared Van Der Pauw with InGa contact.

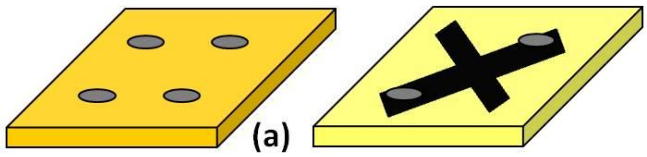

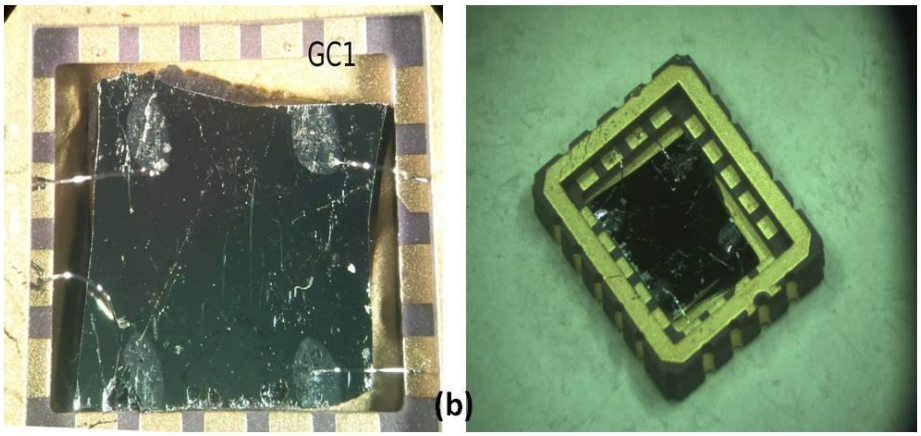

Figure 3.3 (a) Greek cross fabrication process, and (b) image for Greek cross sample 11-289.

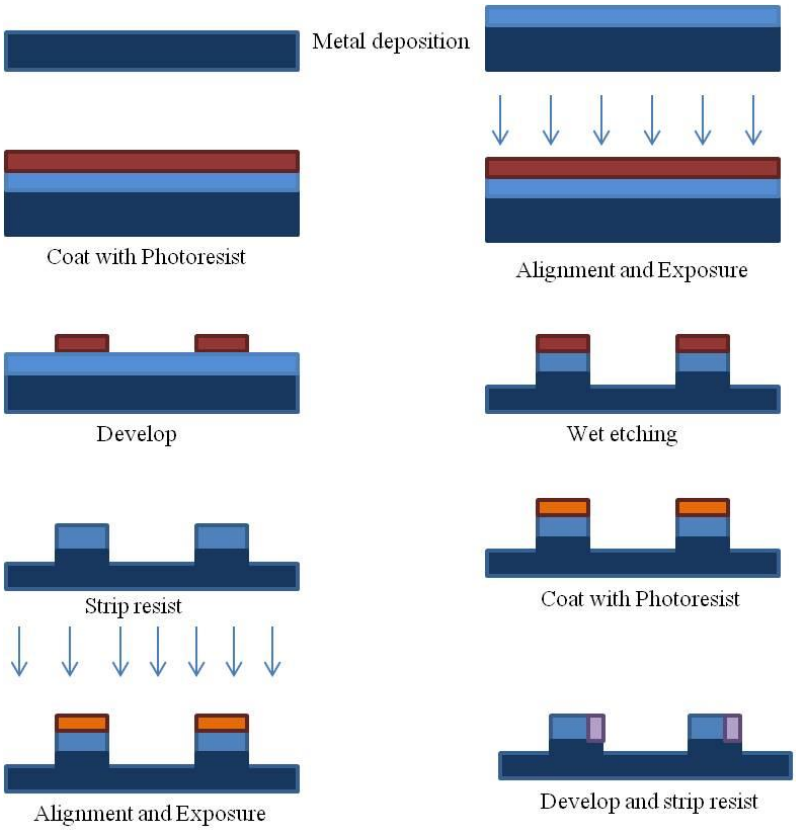

Figure 3.4 Hall bar fabrication process using wet etching

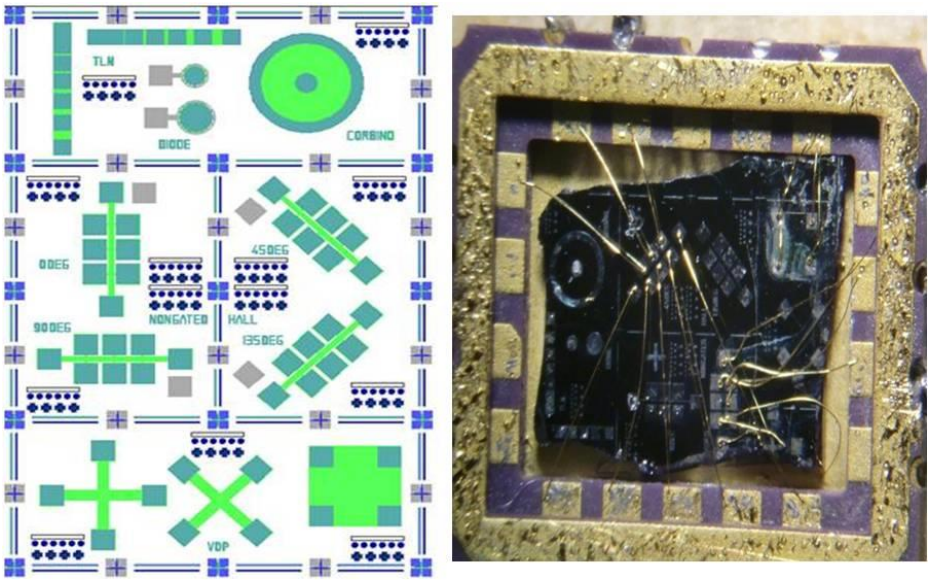

Figure 3.5 Lithography mask and image for Hall bar.

3.3.2 The Closed Cycle Cryostat (CCC)

A closed cycle cryostat system was used for resistivity and Hall effect measurements for all the samples in this thesis over a range of temperatures 10 K-300 K. A schematic diagram of the closed cycle cryostat is shown in Figure 3.6. The refrigeration system depends on compressor and an expander module, linked by flexible high pressure tubing. The expander module was insulated by a vacuum casing and used motor driven valves to allow a controlled two stage expansion of the helium gas. The gas expansion cooled a copper block at the end of the module, to which was attached a temperature diode and a resistive heater. Samples were mounted on a holder which was screwed into the end of the copper block. A Lakeshore DRC-91C temperature controller read the diode voltage and varied the heater current to allow temperatures to be set between 10 K and 300 ± 1 K. Magnetic fields were supplied by an electromagnet which could produce fields of up to 1.2 T (Figure 3.7).

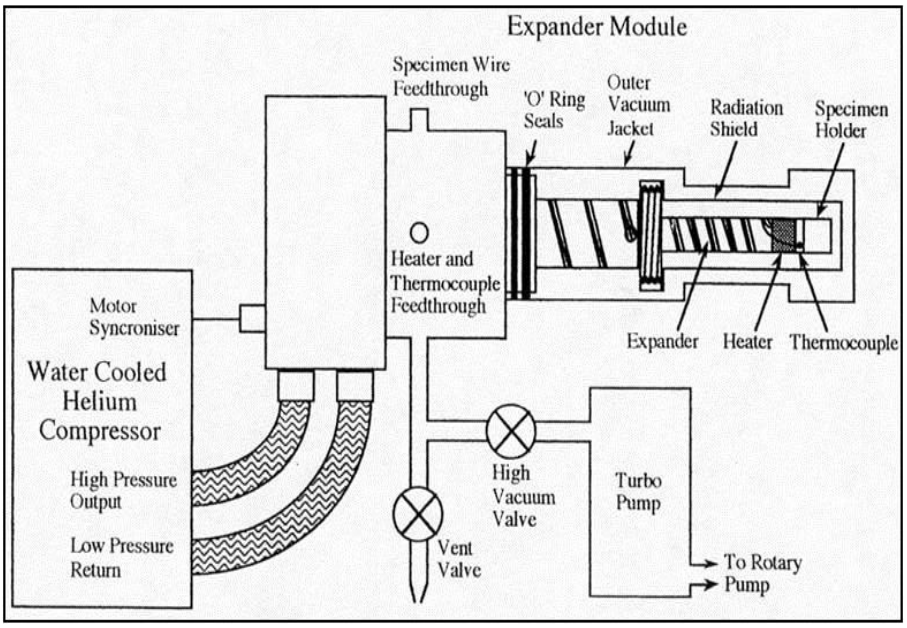

Figure 3.6 Schematic diagram of close cycle cryostat.

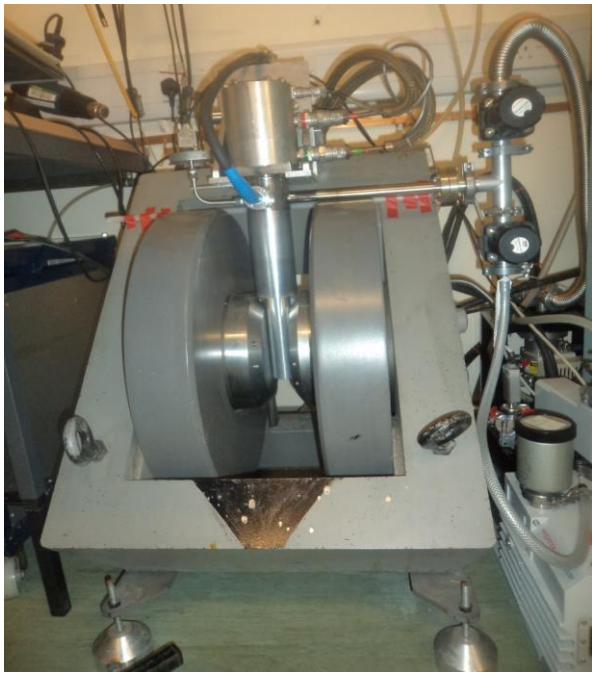

Figure 3.7 Image of closed cycle cryostat used in the Nano-Silicon lab.

Figure 3.8 Image of 300 mK, 12 T cryomagnetic system (Heliox)

3.3.3 Cryomagnetic system:

Measurements in high magnetic fields of up to 12 T over a range of temperatures 0.35-300 K were performed using an Oxford instrument dry ^{3}He cryomagnetic system Figure 3.8. A lock in amplifier was used to generate currents of 100nA-1µA and measure longitudinal (V_{xx}) and Hall voltages (V_{xy}) continuously while the magnetic field was swept.

3.4 Structural Measurements

3.4.1 Secondary Ion Mass Spectroscopy (SIMS)

SIMS determines the concentration of both the matrix and dopant materials as function of depth from the top surface, which both confirms the intended structures were grown and provides a way to accurately measure the thickness of each layer and the concentration of dopants. High and low energy SIMS have been performed in this study. High energy SIMS was performed by in a secondary ion mass spectrometer with a caesium (Cs^+) ion beam of energy 14.5 keV, which provides a depth resolution of approximately 5 nm, while low energy SIMS was performed using near a normal incidence (O_2^+) primary beam at 250 eV [74] which provides sub-nanometre depth resolution. The high energy SIMS utilised in this study was performed at Evans Analytical Group (EAG). The low energy SIMS was performed by Dr. Richard Morris within the Analytical Science Projects group at the University of Warwick.

The reason for using high energy SIMS was to detect a lower dopant concentration 10^{15} cm^{-3} and also to detect more materials such as O_2, H_2, and C that are not detected by low energy SIMS with an O_2^+ source.

3.4.2 High Resolution X-ray Diffraction (HRXRD)

Figure 3.9 shows a schematic diagram of the XRD system, which consists of sample stage, X-ray source and detector. A copper source was used with 40 kV acceleration to produce an X-ray beam wavelength of 1.5406 Å. This beam passes through a Ge crystal and a high intensity, monochromatic X-ray beam is produced. The X-rays diffracted from the sample are counted using the detector. It is shown in the figure that ω is the angle between the sample

plane and the incident X-ray beam, while θ is the angle between the sample plane and the diffracted beam making 2θ the angle between the incident and diffracted beams. Rocking curves were measured with ω kept constant while 2θ is scanned around a specified reflection. On the other hand, a reciprocal space map (RSM) is a composition of many rocking curves with different ω values.

Sharp (Bragg) peaks appear in the diffraction pattern, due to constructive interference of X-rays scattered from sets of parallel lattice planes, when the relationship between the crystal spacing and the incident radiation satisfies Bragg's equation

$$n\lambda = 2d\sin\theta$$

where n is an integer (0, 1, 2, 3…), λ is the wavelength of incident radiation, d_{hkl} is the inter-planar spacing with Miller indices hkl, and θ is the grazing angle of incident radiation (Bragg angle). The conditions of Bragg law are met when the reciprocal lattice points lies on the limits of the Ewald sphere [75], where the scattering vector Q is equal to the inverse distance between planes $Q = \frac{1}{d}$, and $\sin\theta = \left(\frac{|Q|}{2}\right)\left(\frac{1}{\lambda}\right)$.

Strain and composition have been determined using a Philips X'pert MRD Pro single crystal high resolution x-ray diffractometer. The characterisation required two types of RSM measurement: about the symmetric $[004]$ and asymmetric $[224]$ Bragg peaks. The $[004]$ RSM enables the out-of-plane lattice spacing to be directly resolved; however, changes in this spacing can be due to both strain and alloy composition changes. The $[224]$ scan allows values of both the in-plane and out-of-plane components of lattice spacing to be found which assists in extracting the in-plane lattice parameters by the help of the $[004]$ scan and means the effects of strain and composition can be separated.

The data was analysed using X'pert Epitaxy software, which calculates the lattice parameter in the growth direction from the [004] reciprocal space map that is inversely proportional to the distance in reciprocal space. Moreover, the layer relaxation can be calculated by comparison with the equivalent reciprocal lattice point in the [224] reciprocal space map.

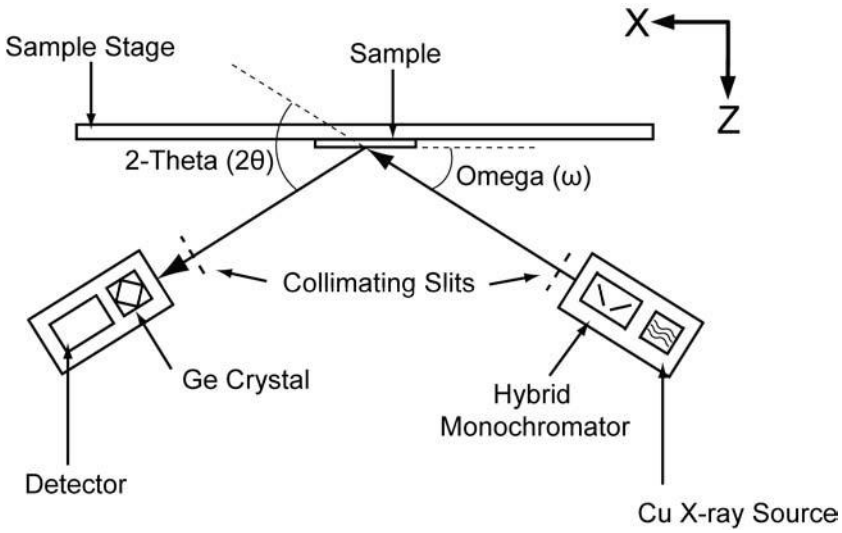

Figure 3.9 A schematic diagram of the XRD system used in this study

3.4.3 Atomic Force Microscopy (AFM)

Sample imaging was performed using a Digital Instruments Nanoscope III AFM in contact mode, which is suitable for mapping out the surface topography of materials of uniform hardness. The results were digitally recorded and analyzed using Digital Instruments' Nanoscope software. The sample was mounted on a piezoelectric stage then the tip lowered and moved on the sample. Depending on the force between the tip and the surface the cantilever will bend according to Hooke's law and by the help of the software the height was recorded as the tip moved across the sample. The data was then analysed to extract the roughness parameters.

4 Structural and electrical properties of strained Ge heterostructures doped below the channel

4.1 Introduction:

Asymmetrically doped strained Ge heterostructures have been used to study the transport properties of the charge carriers (holes) confined in a quantum well. While placing the doping layer above the channel (which is termed a “normal” structure) has an advantage of avoiding the dopant atoms segregating to the channel, placing the doping underneath the channel (“inverted” structure) can be more effective in reducing the effect of interface roughness scattering on the mobility of the carriers. Inverted structures can also reduce the gate leakage, since the doping will not segregate to the surface.

This study aims to investigate both types of structure for high purity strained Ge channels, starting with the Inverted structure in this chapter and followed by the Normal structure in the next chapter. Results will be presented for structural and electrical properties on a number of different samples, involving classical resistivity and Hall measurements together with theoretical simulations of the valance band edge and simulation of the scattering limited mobility at low temperature.

4.2 Structural characterization of inverted sGe QW structures:

Intensive structural analysis has been key in explaining the remarkable behaviour of the transport properties of holes in these samples. A range of techniques have been used, such as HR-XRD, XTEM and SIMS.

4.2.1 X-ray Diffraction (XRD) analysis for inverted structure sGe/SiGe

The alloy composition and degree of strain in each layer of these strained Ge structures (see section 3.2.1) has been determined using a Phillips PW1835 high-resolution x-ray diffraction HR-XRD. The out of plane and in plane lattice constants were obtained from (004) and (224) reciprocal space maps (RSM). Figure 4.1 shows the five different layers in our structure, two peaks for nominally $Si_{0.2}Ge_{0.8}$ appear here as a result of the different Ge composition in the buffer (0.79) and the cap (0.82). The buffer was found to be slightly over relaxed with respect to the Si substrate, which is typical of reverse-graded buffers and is due to the differential contraction of Si and Ge when cooled down from the elevated growth temperature [70, 76]. The strained Ge layer was expected to be 0.84% strained with respect to the $Si_{0.2}Ge_{0.8}$ buffer. However, from XRD it appears to have a 0.65% lattice mismatch.

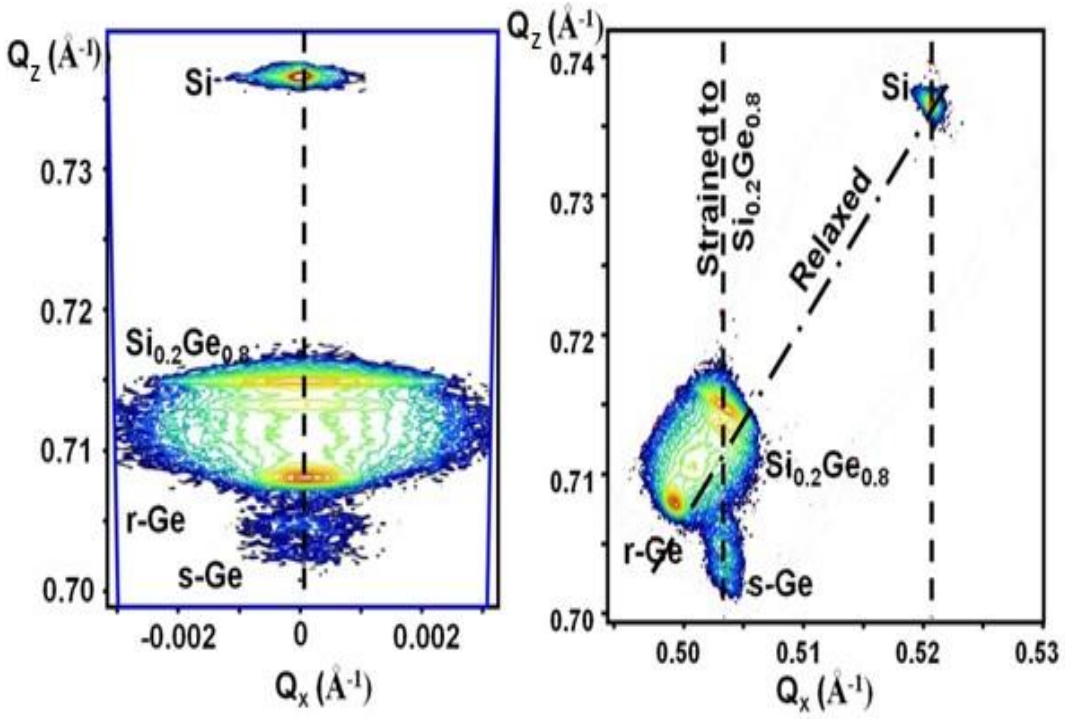

Figure 4.1 XRD for sample 11-284 Inverted structure (a) (004) symmetric reflection (b) (224) asymmetric reflection. Peak intensity in the RSMs is colour coded on an arbitrary scale, with red as most intense.

XRD rocking curves performed when the value of ω was kept constant and $\omega/2\theta$ scanned across the diffracted beam, and it confirms that the s-Ge channel remains fully strained. In Figure 4.2, the multi-layer structure makes it difficult to fit a simulated rocking curve to the experimental data due to the large number of variable parameters and additional fringes are present from the low temperature $Si_{0.2}Ge_{0.8}$ and Si cap layers. However, a reasonable fit can be made by using the strain and composition already determined from the RSM and the nominal growth thickness of each layer as the initial values when modelling the thickness of the channel using the PANalytical X'pert Epitaxy software. In this way, for a s-Ge channel thickness of 20 nm (nominal growth thickness), a thickness 20±1 nm was obtained by fitting to the X-ray data, in corroboration with the other measurement techniques for inverted structures.

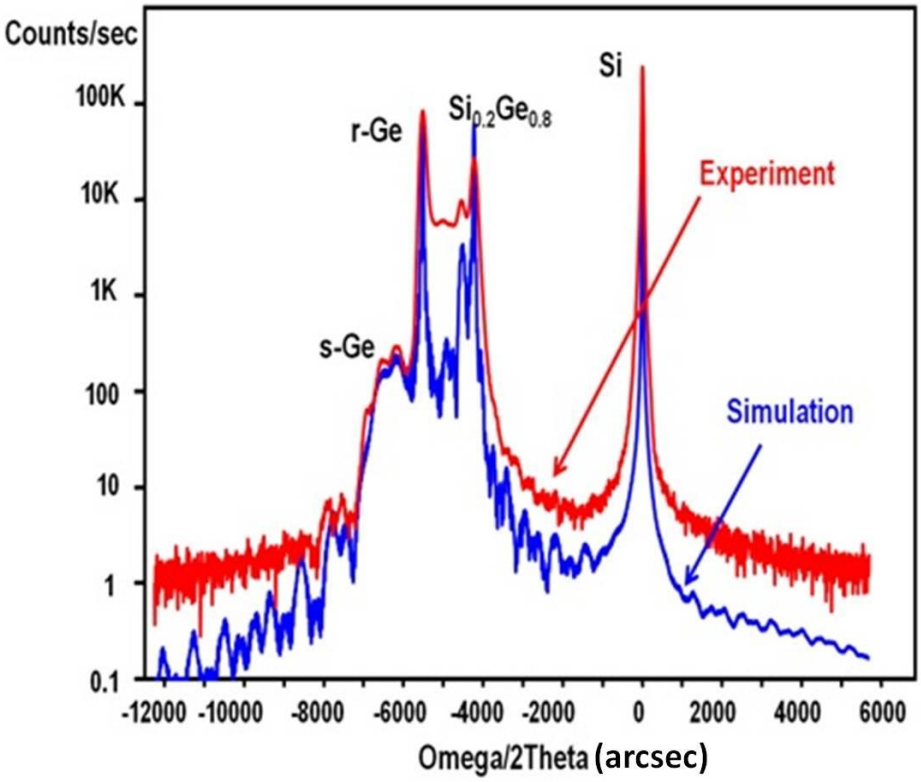

Figure 4.2 Rocking curve for sample 11-284 inverted structure.

4.2.2 TEM analysis for sGe/SiGe inverted structures:

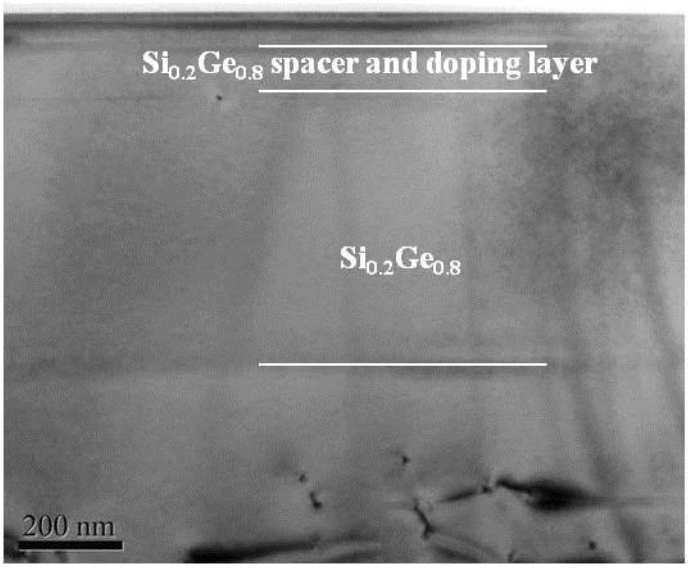

Figure 4.3 XTEM bright field 004 for inverted structure (11-284).

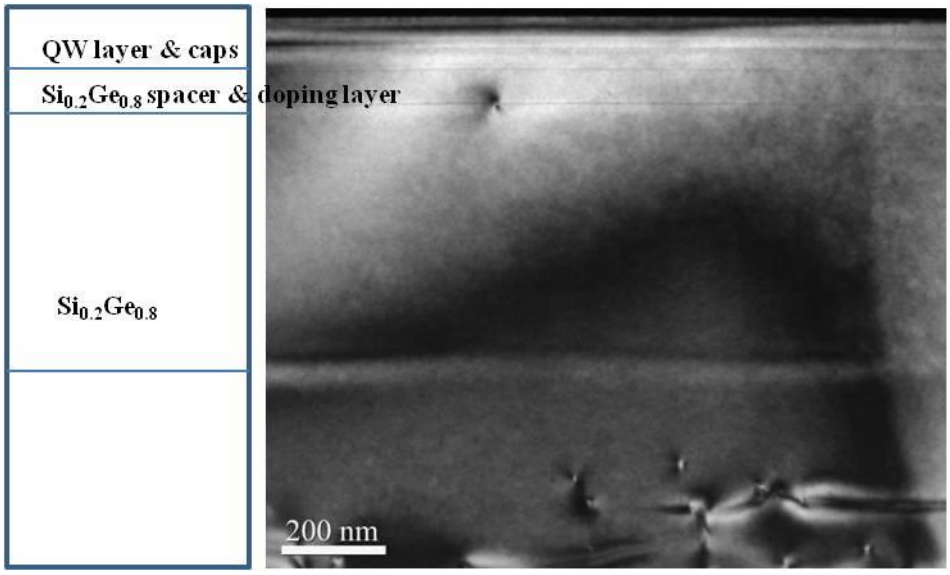

Figure 4.4 XTEM dark field 004 image for inverted structure (11-284).

The first sample analysed by TEM was the control sample 11-284. The structures were viewed in cross sectional TEM (XTEM) using a JEOL2100fx TEM microscope. XTEM bright field images Figure 4.3 and the dark field image Figure 4.4 show the top of the buffer layer and the active layers for sample 11-284, with a nominal channel thickness of 20 nm.

There is a dislocation close to the active layers at the lower dark line, lying parallel to the beam direction (upper left).

Figure 4.5 is a more highly magnified dark field (004) image of the active region. The central image is laterally compressed by 10×, which makes it easier to see any interfacial roughness. In this case the roughness is extremely low and could not be measured, demonstrating the good quality of the structure in this sample.

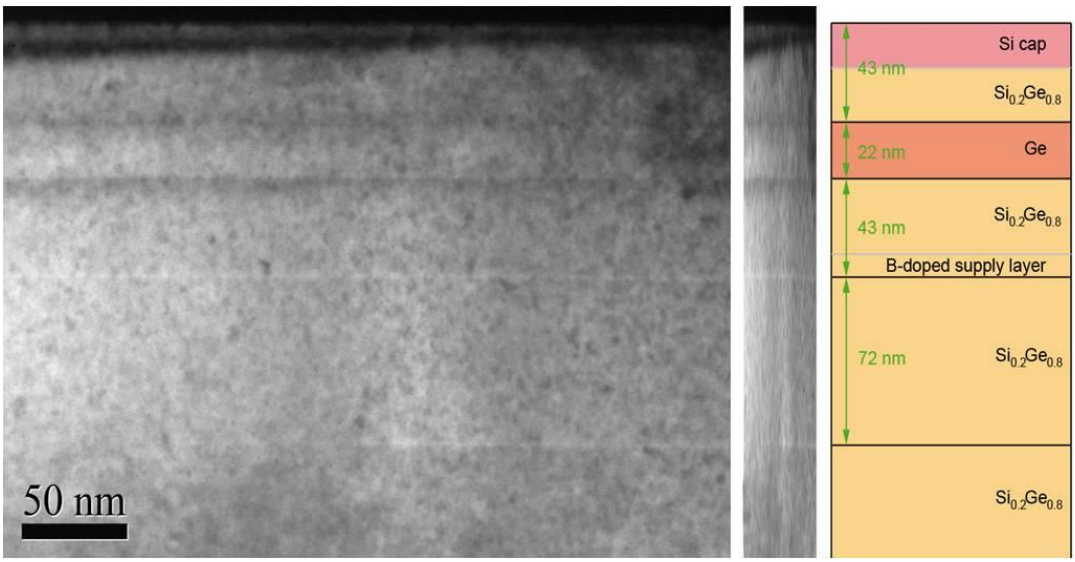

Figure 4.5 XTEM dark field 004 image of the active region in the inverted structure 11-284, with ×10 compressed figure in the central pane to emphasis any interface roughness and, on the right, a schematic diagram of the structure with measurements taken from this

The layer thicknesses have been measured from Figure 4.5, as shown in the right hand image pane. The two thin bright lines under the channel within the $Si_{0.2}Ge_{0.8}$ region arise from pauses in the growth and should essentially be ignored. The B-doped layer gives no contrast, so it is included in the 43nm distance with the spacer thickness. This doping will, however, be revealed in the SIMS measurements and shown later. The Ge channel can be seen in the dark field image Figure 4.5, but is much clearer in the bright field image Figure 4.6 taken from a specimen prepared in the perpendicular direction. The Ge channel thickness was 23±1

nm, which is 2 nm higher than the nominal thickness. The interface between the $Si_{0.2}Ge_{0.8}$ cap and Si is unclear in the dark field image, but again can be seen much more clearly in the bright field image from which a Si cap thickness of 4±1 nm and $Si_{0.2}Ge_{0.8}$ cap of 41±1 nm can be measured. Both orientations have extremely low interface roughness that it is difficult to measure from these 300 nm wide images.

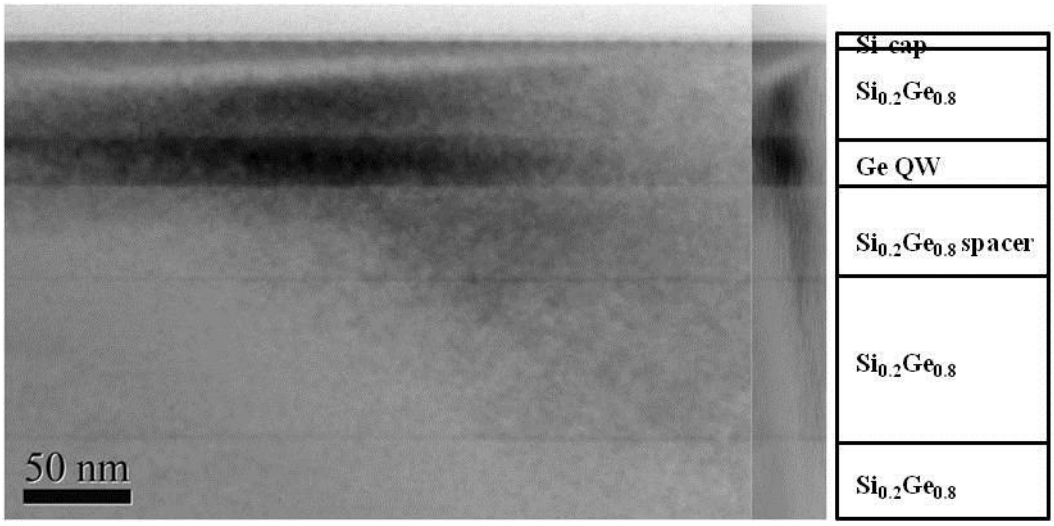

Figure 4.6 Bright field (004) XTEM showing the active region for inverted structure 11-284. The compressed figure on the right shows the interface roughness more clearly in the perpendicular direction. .

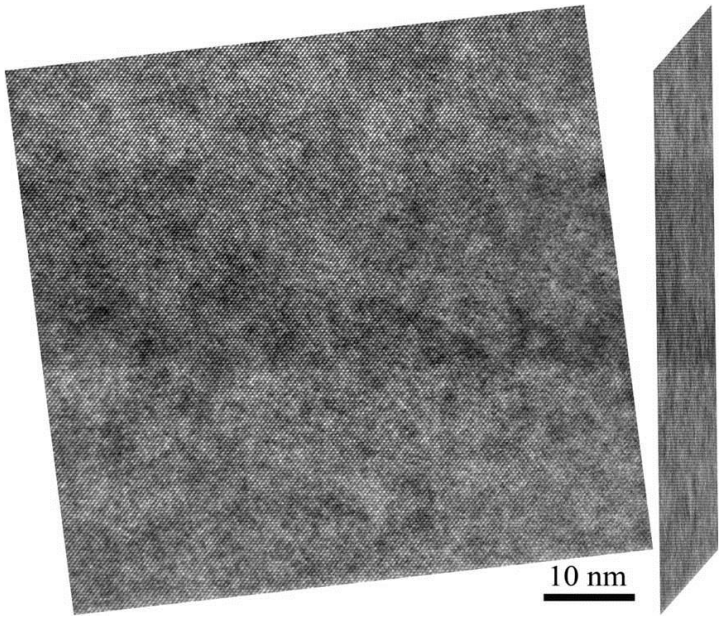

Figure 4.7 HRTEM shows Ge channel of the inverted structure 11-284 with compressed image in the right to illustrate the interface roughness.

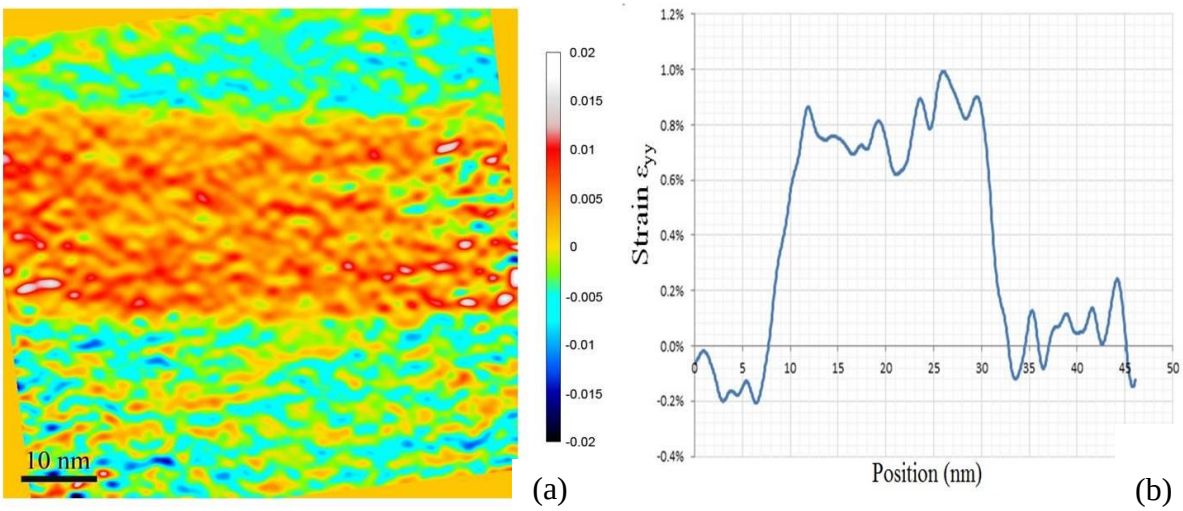

Figure 4.8 (a) Strain map of inverted structure 11-284 shown in false colour on a HRTEM image, with red showing up to 1% enlargement of the lattice parameter perpendicular to the growth direction (meaning biaxial compressive strain in the channel) and blue showing relatively smaller perpendicular lattice parameter. (b) Curve, formed by summing data across the image, that shows the strain in the Ge channel was 0.8±0.2

More focus on the channel by higher resolution TEM (HRTEM) in Figure 4.7 indicates smooth interfaces. From this HRTEM image it is possible to construct a map of the strain component perpendicular to the interface, Figure 4.8. The measured strain is 0.8±0.2%, which agrees with the expected value of 0.84%. It is about 0.15% higher than the strain extracted by XRD, but these values are consistent within the limits of experimental uncertainty. It should be noted that the measurement is affected by surface contamination, which arises whilst preparing the extremely thin sample required for HRTEM and adds noise to the image and is to a large part responsible for the experimental uncertainty in strain mapping. Nevertheless, the strain map does show an extremely abrupt shift in strain between the channel and surrounding layers, as well as providing further clear evidence for the smoothness of the channel walls and general homogeneity of the channel material both of these features are crucial in obtaining high mobility hole transport through the Ge channel.

The bright field 004 TEM image in Figure 4.9 illustrates the active layers for sample 11-285 and their thickness. For this sample the channel thickness is measured to be 14±1 nm, which is 5 nm greater than the nominal thickness. The spacer with doping layers has a thickness of 41±1 nm, while the Si cap is 4±1 nm and the $Si_{0.2}Ge_{0.8}$ cap is 41±1 nm. The distance between growth interrupts of 66±1 nm is slightly smaller than that for sample 11-284. Figure 4.10 shows the perpendicular orientation active layer with extremely low interface roughness and same layers as previous orientation.

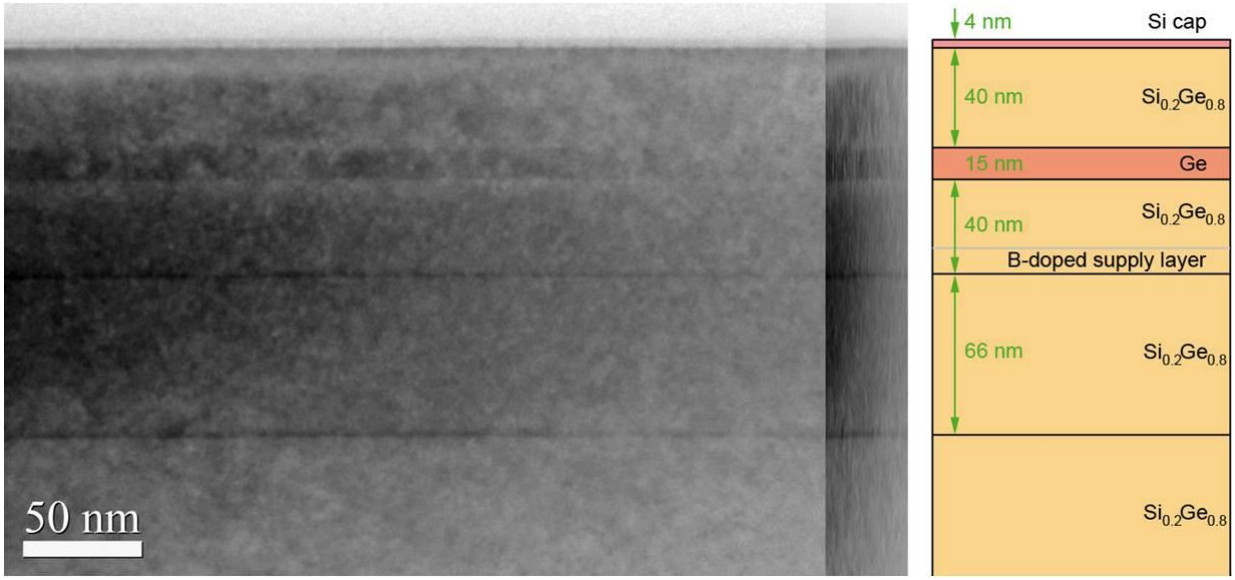

Figure 4.9 Bright field 004 image shows active layers for the sample 11-285 and clearly indicated the thickness of the layers.

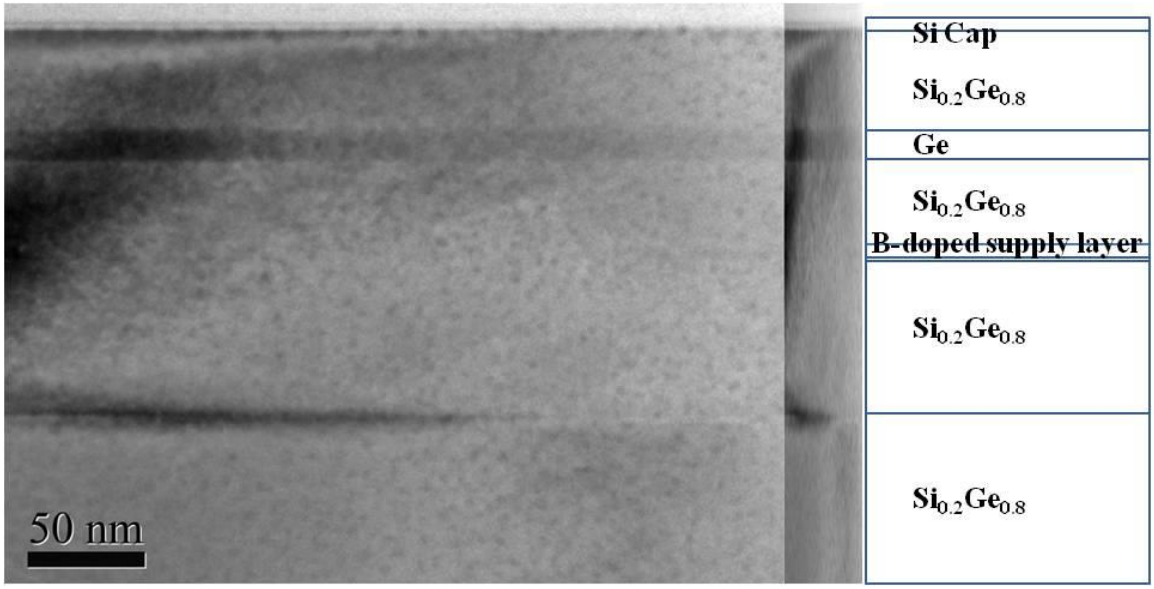

Figure 4.10 XTEM (004) image for inverted structure 11-285 with compressed figure in the right to show the interface roughness for perpendicular direction.

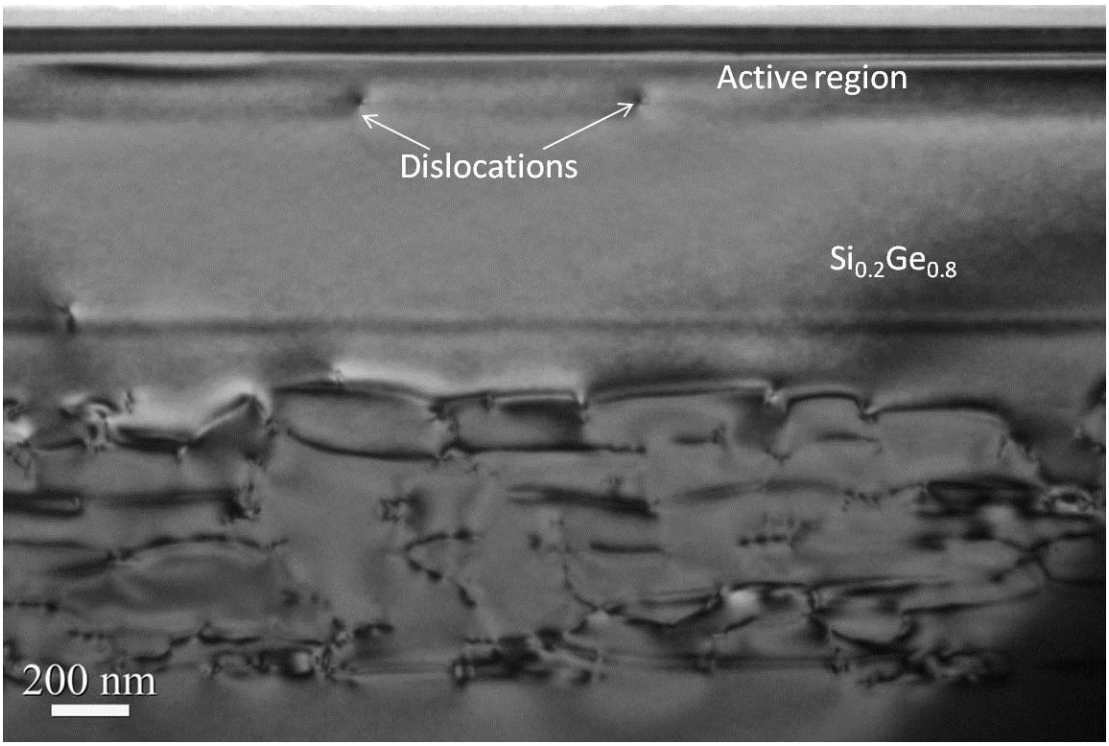

Figure 4.11 Bright field 004 image showing top of the buffer layer and upper part of the structure (active region) sample 11-286

The nominal channel thickness of 40 nm for sample 11-286 is much wider than for the two previous samples 11-284, and 11-285. The bright field 004 TEM image of Figure 4.11 shows the top of the buffer layer, with its complex network of strain relieving dislocations, and the upper part of the structure which is almost perfectly clean; however, two dislocations can be clearly seen next to the active region, which could have serious detrimental effects on the transport properties of this sample if repeated at a similar density in other parts of the wafer.

The layers thicknesses for sample 11-286 are indicated in the right hand schematic diagram of Figure 4.12, with all thicknesses measured from the left hand image. The Ge channel thickness of 40±2 nm is 5% different than the nominal thickness, and the spacer and doping layers were 41±2 nm together with no proper distinction between them, as previously. The distance between growth interruptions was 72±2 nm which is similar to sample 11-284. The

Si cap was measured to be 3.5±0.5 nm; the $Si_{0.2}Ge_{0.8}$ cap is 45±1 nm. Bright field 004 image from the perpendicular orientation (Figure 4.13) illustrated the active layers with small curvature of the layers is visible in the compressed version, similar to sample 11-285.

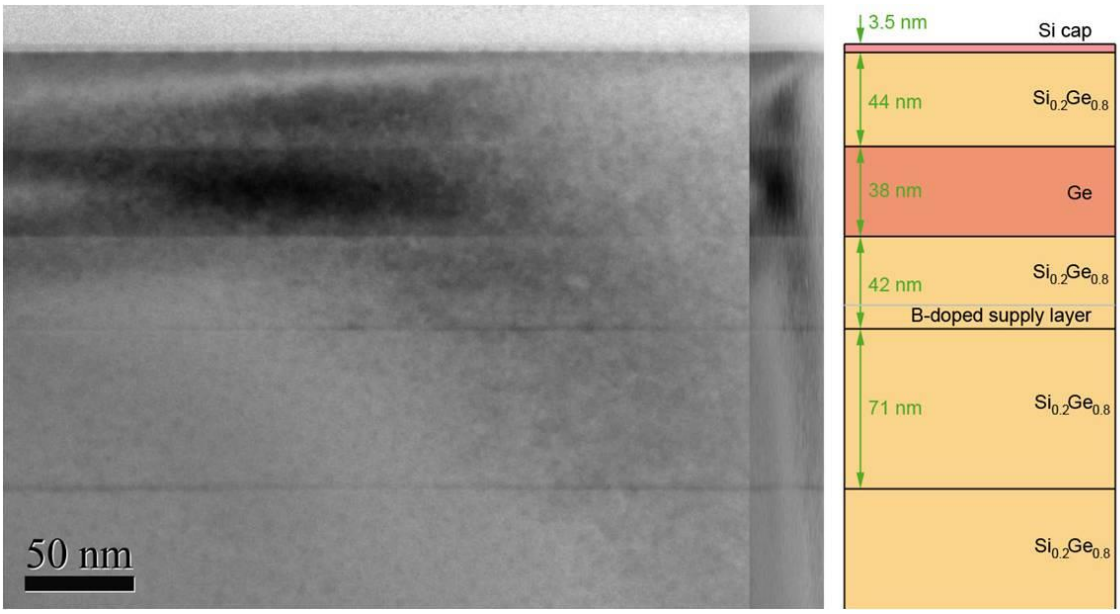

Figure 4.12 Bright field 004 image showing active layers of the sample 11-286

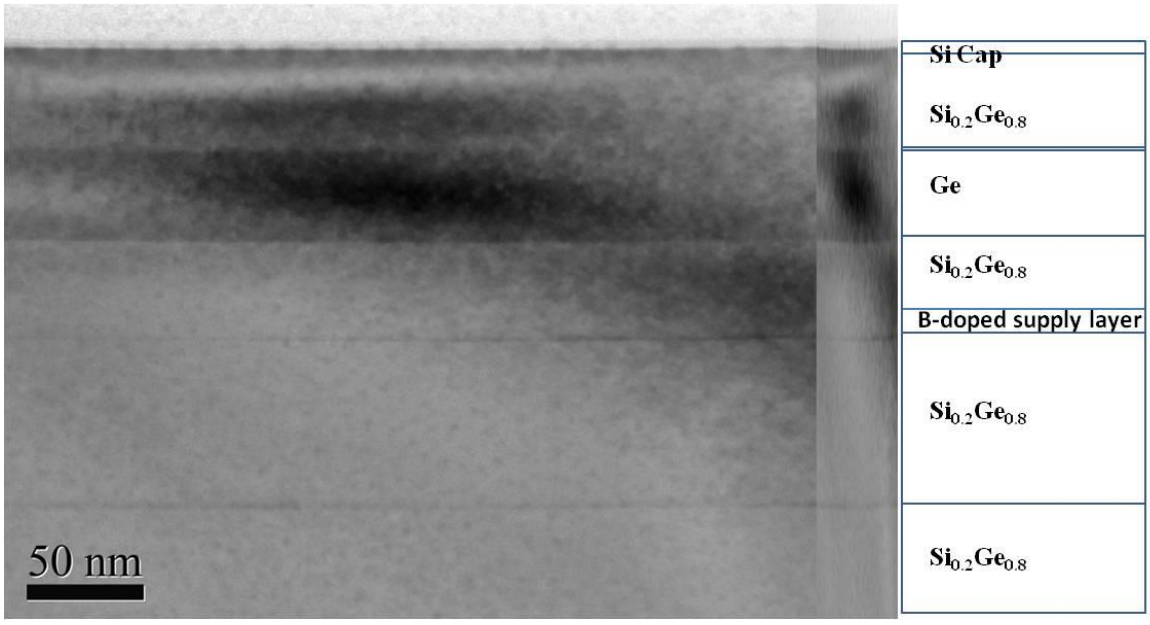

Figure 4.13 Bright field 004 image from the perpendicular section showing active layers of sample 11-286.

Another inverted structure sample that has been characterized by TEM is 11-290, which was grown at the higher temperature of 450°C rather than 400°C. The bright field 220 TEM image in Figure 4.14 has the sample tilted so that the layers are not seen edge-on. The horizontal lines at the top are thickness fringes, from the specimen tilt. Short vertical lines at the top are unknown but maybe misfit dislocations at the Si cap/$Si_{0.2}Ge_{0.8}$ interface. A misfit dislocation at the bottom interface of the Ge layer is visible top centre, which could be the reason for the low mobility of this sample that will be discussed in section (4.3.1). Underneath that, the dark horizontal line is a misfit dislocation lying in the interface marked by the lower dark line. Bottom right shows a threading dislocation coming from the buffer layer. In dark field 220 TEM images, Figure 4.15 shows the end of the horizontal misfit dislocation at the lower dark line, while Figure 4.16 illustrate the threading dislocation from the buffer layer reaching the top surface.

Figure 4.17 indicates the layer thicknesses for sample 11-290, with the channel thickness of 25±2nm, and both the spacer and the doping layers thickness 40±1nm. The distance between growth interruptions was 68±2 nm, while there are 3±0.5 nm Si cap illustrated in the images, and finally the $Si_{0.2}Ge_{0.8}$ cap is 41±1 nm.

In general, it is obvious that almost all the samples have smooth channel interfaces, which indicates high structure quality that improves the electrical transport of the carriers in the channel.

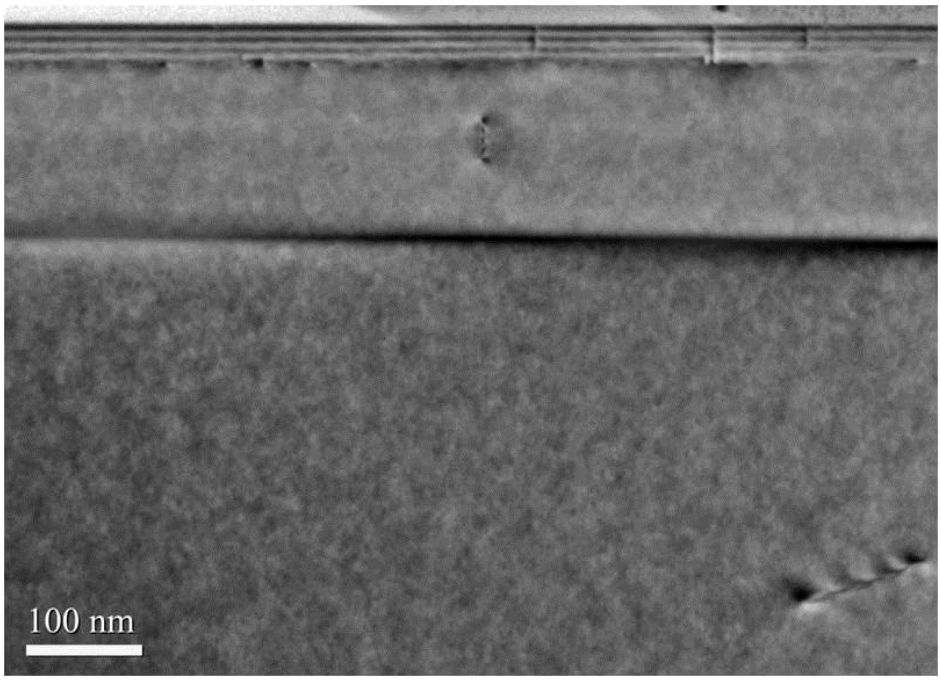

Figure 4.14 Bright field 220 XTEM image for the sample 11-290 represents sample tilted and thickness fringes in the top of the structure, also threading dislocation shown in the bottom right.

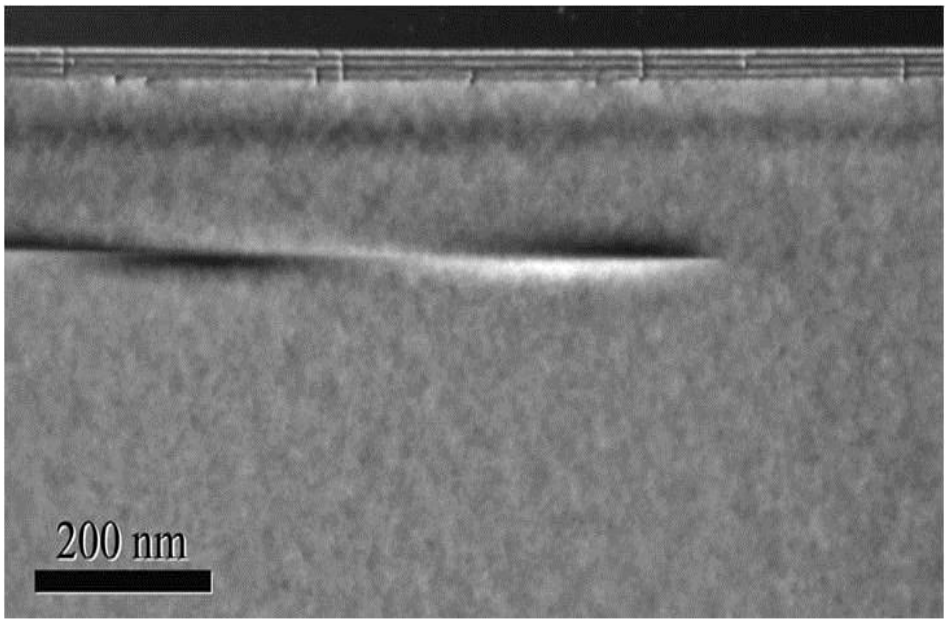

Figure 4.15 Dark field 220 images, the end of the horizontal misfit dislocation at the lower dark line.

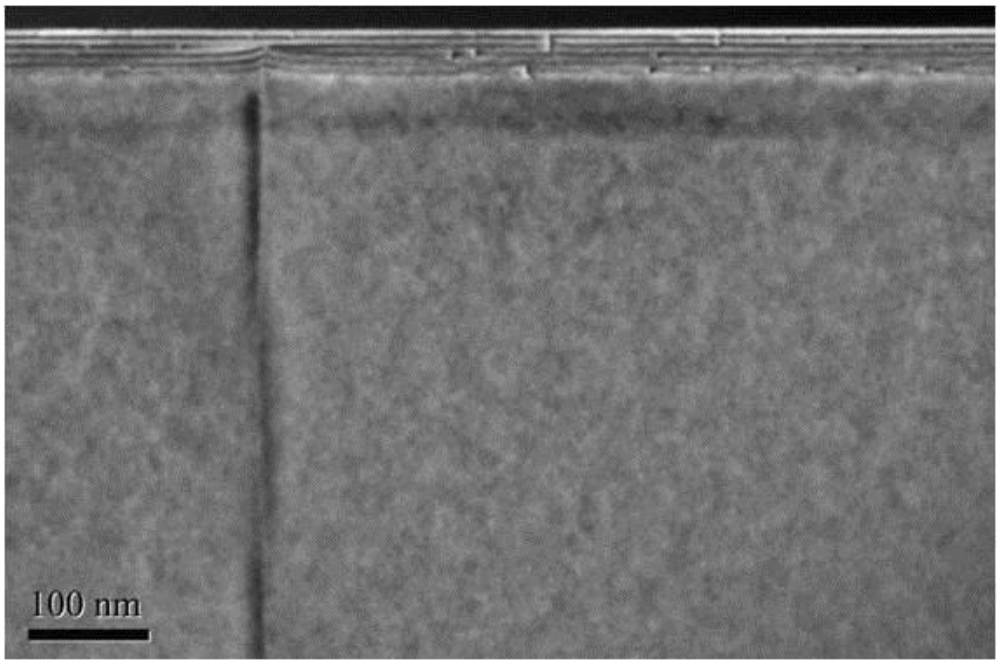

Figure 4.16 image for a threading dislocation from the buffer layer reaching the top surface.

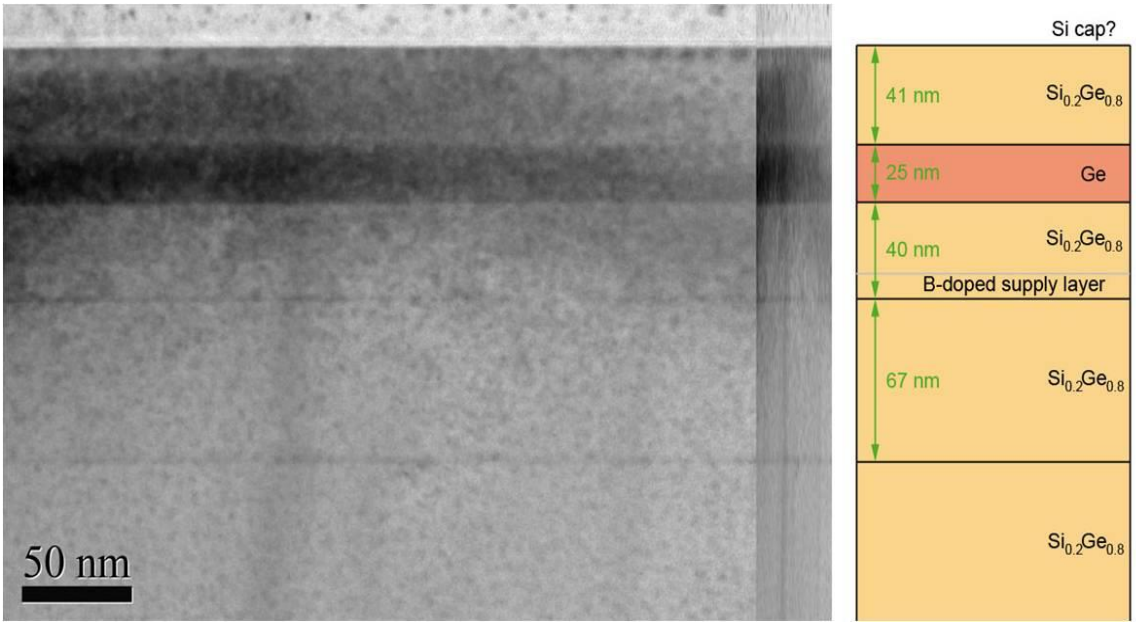

Figure 4.17 Bright field 004 image showing active layers and it indicated the layer thickness of the sample 11-290

4.2.3 High-resolution TEM analysis:

Silicon wafers are prepared by slicing from a large boule of material, which can sometimes mean the wafer surface is not precisely normal to the [001] direction, but is "off-cut" by a small angle towards a particular direction. Later in the thesis (Section 4.5) an anisotropy will be reported in the mobility measured for the inverted structure in the perpendicular [110] and $[\bar{1}10]$ orientations. This anisotropy could arise from a difference in off-cut angle that will affect both the terrace height and length, and hence the scattering rates, in the two orthogonal directions. Therefore, this substrate off-cut angle was investigated by HR-TEM, using an aberration corrected microscope. The result does appear to show a significant difference in substrate off-cut angle between the two orientations i.e. [110] and $[\bar{1}10]$ of up to 1º (see Table 2, Figure 4.18 and Figure 4.19). The values reported are averages of at least three measurements per sample direction with an uncertainty of ±0.3º coming from the spread in measured slopes.

11-287-$[\bar{1}10]$	1.5° ± 0.3º
11-287-[110]	0.3°± 0.2º
11-288-$[\bar{1}10]$	0.9°± 0.3º
11-288-[110]	0.4± 0.2º

Table 4.1 Off-cut angles towards $[\bar{1}10]$ and [110] measured from HRTEM images.

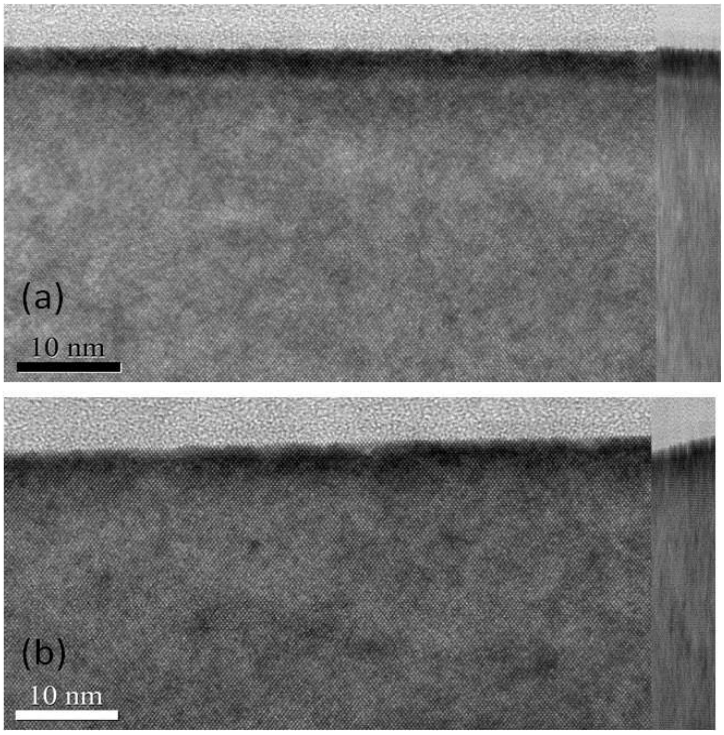

Figure 4.18 HRTEM for sample 11-287 for two perpendicular orientation, showing the substrate off cut more clearly in the compressed image to the right

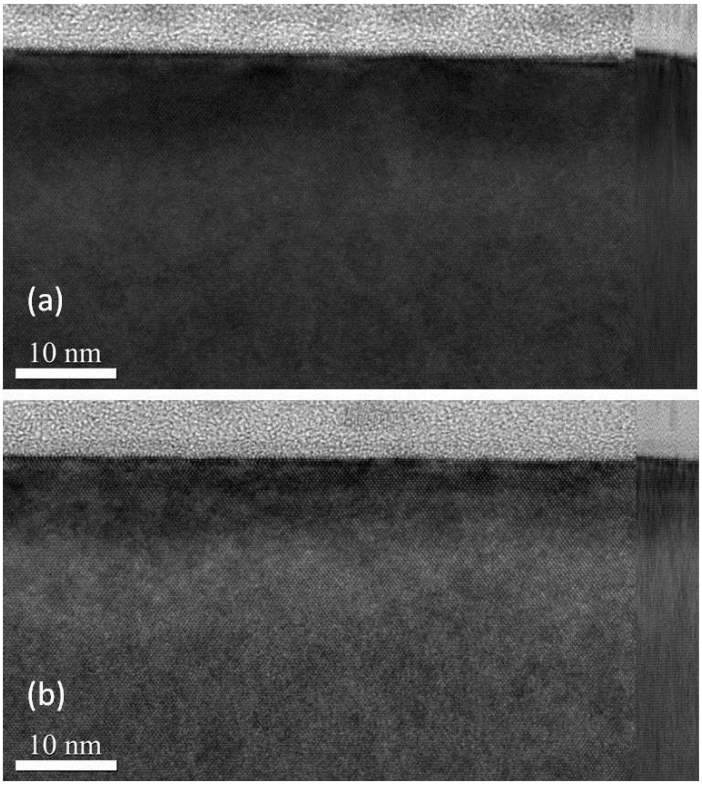

Figure 4.19 As Figure 4.18 for sample 11-288.

4.2.4 uleSIMS analysis for inverted structure sGe/SiGe:

Starting with the control sample 11-284, the inverted structures have been assessed by SIMS depth profiles, using a near normal incidence O_2^+ primary beam at 250 eV. Although the doping layer in the inverted structures is not separately observed from XTEM, the SIMS measurements Figure 4.20 clearly show its presence with a boron concentration of up to 10^{18} cm^{-3}. The thickness of the doped region is not straightforward to evaluate from the SIMS profiles, due to the profile not being square. The shape of the doping profile recorded is a combination of both the SIMS measurement process and actual segregation or diffusion of dopants in the sample. The thickness of the doped region in 11-284 deduced from the SIMS profile is 18±2 nm, which is obtained at a fixed doping level (average doping concentration) about 2 times higher than the expected value. Determination of the spacer thickness for the inverted structure 11-284 is complicated by dopant segregation. However, it is 20±2 nm from the edge of doping layer where the doping is below the average doping concentration to the onset of the channel. The thicknesses of all other layers are illustrated in Table 4.1 and, in general, the XTEM images in Figure 4-5 confirm these dimensions.

The average boron concentration, measured from the SIMS profile in Figure 4.20 for the inverted structure is ~ 7×10^{17} cm^{-3}. Significant segregation of the B-doping in the spacer is seen, which has given a larger doped region than intended. High doping at the surface is also observed for all the samples. For the first 1 nm this might be an artefact of the SIMS measurement, but the fact that it extends into the sample suggests that it seems there is some high surface doping. This may cause high gate leakage if gated devices were to be fabricated on these samples. These SIMS profiles also confirm the purity of the Ge channel for this sample, with a Si concentration in the centre of the channel below 0.015 at %. This value is much lower than in previous Ge channels reported [77].

For sample 11-285 a smaller channel thickness is expected, which was 12±2 nm from the SIMs profile in Figure 4.21. The spacer thickness was 23±2 nm, which is 13% different from the intended thickness. The average concentration of boron doping was 8.55×10^{17} cm^{-3}.

Figure 4.22 indicates a channel thickness of 39±3 nm for sample 11-286, and the thickness of the spacer was 20±2 nm. Other layer thicknesses are indicated in Table 4.1. The spacer thickness in this sample was much similar to the control sample 11-284, while the difference in doping layer thickness is 0.14% compared to the control sample.

The aim in sample 11-287 was to reduce the spacer thickness, to achieve a higher change sheet density in the channel. The SIMS profile indicates a spacer thickness of 12±2 nm, which is 1.5 times lower than spacer for the control sample 11-284. The average boron concentration in this sample was $1\times10^{18}cm^{-3}$ Figure 4.23, which is 2 times less than it is nominal value. The thickness of the Ge channel is 20±2 nm, and the doping layer was 19±1 nm, which is estimated from full width half maxima (FWHM) method.

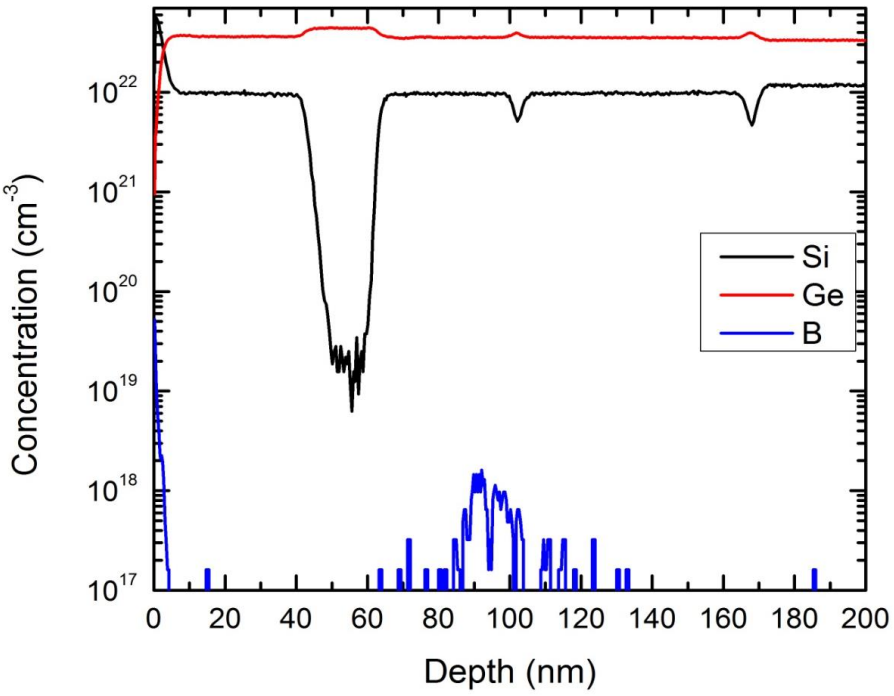

Figure 4.20 Si, Ge and B SIMS profiles for the inverted structure 11-284.

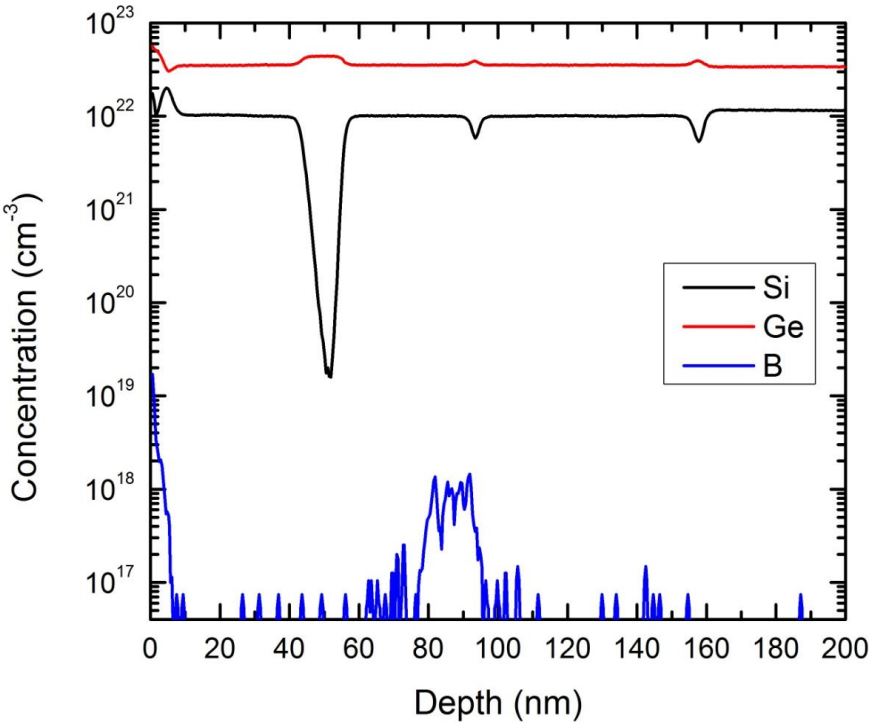

Figure 4.21 Si, Ge and B SIMS profiles for the inverted structure 11-285

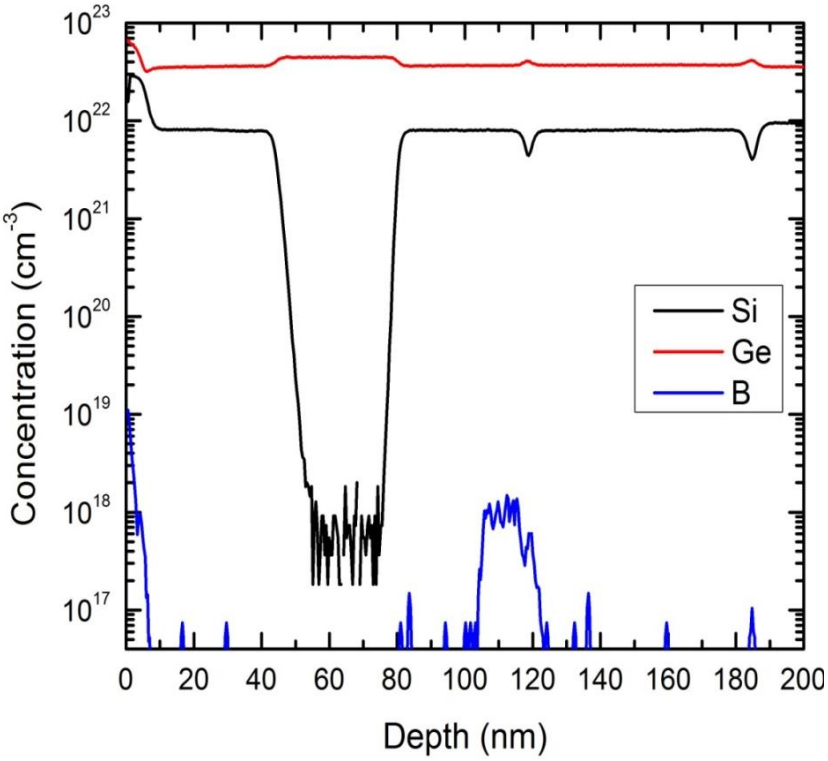

Figure 4.22 Si, Ge and B SIMS profiles for the inverted structure 11-286.

The last inverted structure sample investigated by ule-SIMS was 11-288 Figure 4.24 shows that the channel thickness is confirmed to be 20±2 nm, and the spacer thickness is 24±2 nm; all layer details are in Table 4.1. The average doping concentration is 1.79×10^{18} cm^{-3}. This sample spacer and doping layer thickness is much similar to sample 11-285.

	SIMS					TEM		
	Si cap (nm)	SiGe Cap (nm)	Channel (nm)	Spacer (nm)	Doping layer (nm)	Cap (Si+SiGe) (nm)	Doping layer+spacer (nm)	Channel (nm)
11-284	2±1		20±2	20±2	18±2	43	43	22
11-285	2±1	38±2	12±2	23±2	13±2	4 (Si cap) + 40 (SiGe cap)	40	15
11-286	2±1	38±2	39±2	20±2	21±3	3.5 (Si cap) + 44 (SiGe cap)	42	38
11-287	3±1	42±2	20±2	12±2	19±1	-	-	-
11-288	3±1	41±2	20±2	24±2	15±2	-	-	-
11-290						41	40	25

Table 4.2 Layer thicknesses for all the inverted structure samples from SIMS and XTEM characterization.

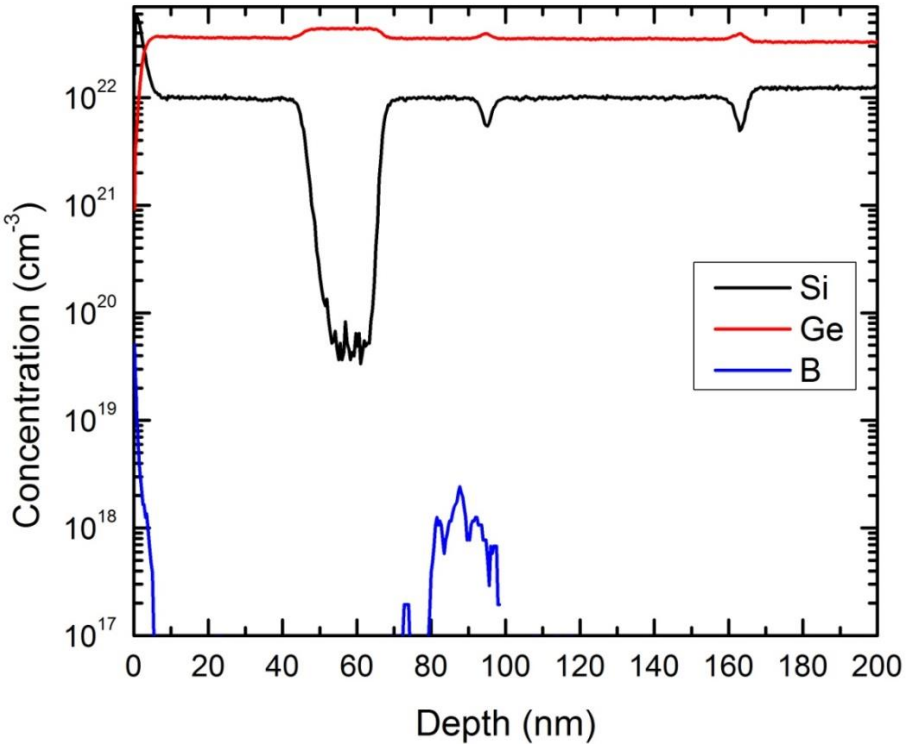

Figure 4.23 Si, Ge and B SIMS profiles for the inverted structure 11-287

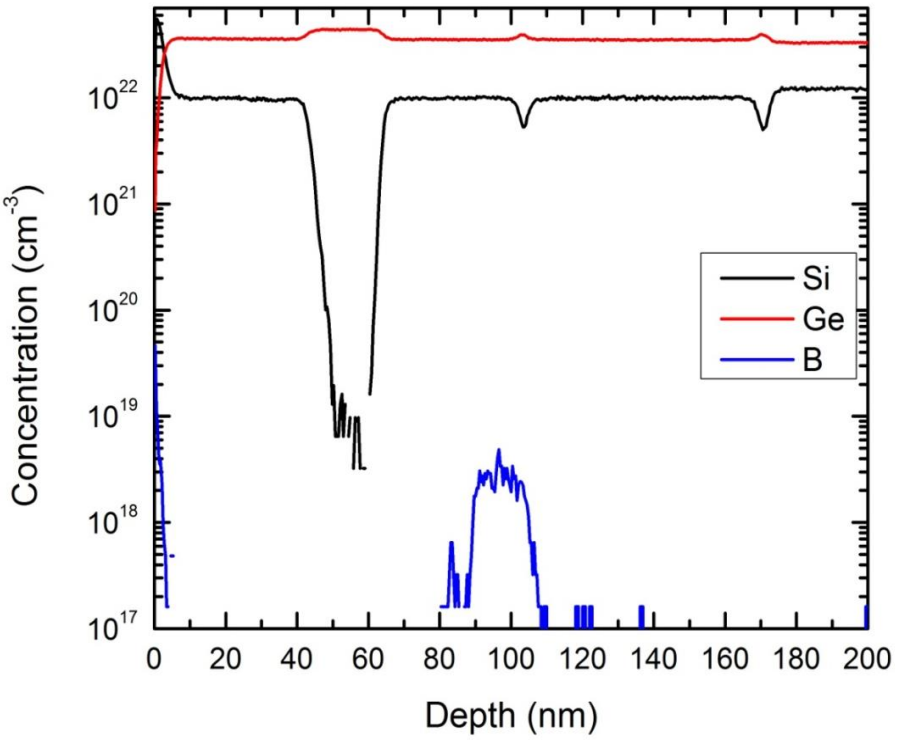

Figure 4.24 Si, Ge and B SIMS profiles for the inverted structure 11-288

4.2.5 AFM analysis for inverted structure:

AFM images allow high resolution of 0.2 nm in the vertical scan and 4 nm horizontal scan resolution for the epitaxial layer. Figure 4.25 was recorded using Digital Instruments Nanoscope software in contact mode operation. It shows that sample 11-284 has low threading dislocation, and that the root mean square (rms) height of the roughness is 1.9±0.4 nm, when measured in the [110] direction (horizontal in Figure 4.25). This indicates a very good quality sample, as confirmed by other structural characterization techniques. On the other hand, measuring the roughness along the orthogonal $[\bar{1}10]$ direction (vertical in Figure 4.25) yields an rms of 2.1±0.4 nm. Although these two values do agree within the experimental uncertainty the small difference could be a reason for the anisotropy in Hall mobility, discussed later. It is believed that the direction with lower rms roughness has higher mobility which is the [110] orientation

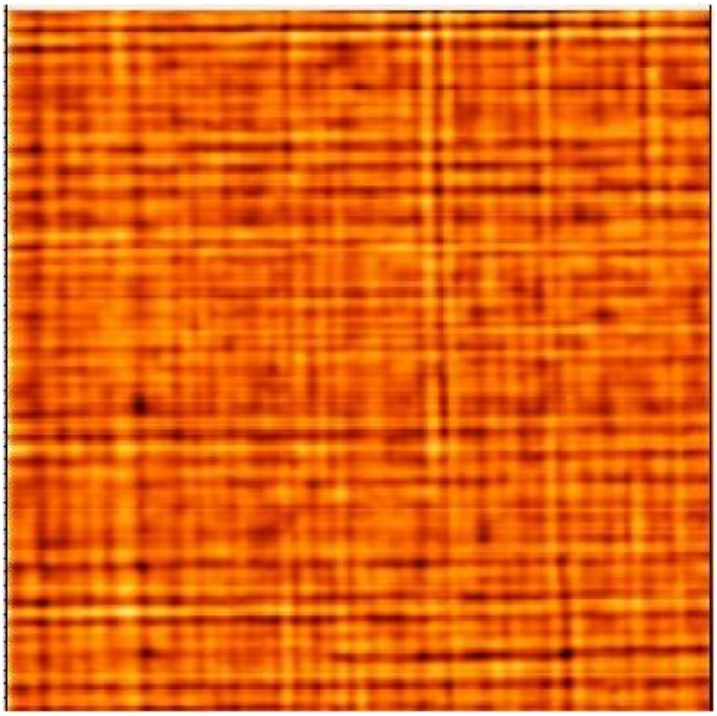

Figure 4.25 AFM images for Cross hatches of sample 11-284.

4.3 Electrical characterization of inverted structure s Ge QW

Standard resistivity and Hall effect have been performed on all the inverted structures using square Van der Pauw samples, with InGa contacts, and Greek cross (GC) samples with Al contacts. Hall bars with Al contact have also been measured for samples 11-284, 11-285 and 11-286. All details of the fabrication process were mentioned in Chapter 3. Electrical measurements were performed at temperatures between 12 K and 300 K using a lock-in amplifier operating at a frequency of 13 Hz. Low-field Hall effect measurements were carried out in both forward and reverse perpendicular magnetic fields with the field strength (B) reaching 1.2 T. All the measurements were performed in the dark with excitation currents between 0.2 μA and 20 μA. One measurement, for sample 11-284, used 20 nA to investigate whether self-heating was affecting the measurements at higher current.

4.3.1 20 nm strained Ge channel, sample 11-284

The temperature dependence (10 K - 300 K) of the Hall mobility and sheet density for sample 11-284, the 20 nm channel thickness sGe heterostructure, are presented in Figure 4.26 for measurements on a square Van der Pauw sample with InGa contacts. The graph confirms the 2DHG behaviour at low temperatures, where the mobility and sheet density saturated with a low temperature hole mobility at 10 K of 1.79×10^{5} cm^2/Vs at a sheet density of 5.7×10^{11} cm^{-2}. However, the mobility of 357 cm^2/Vs and sheet density of 2.36×10^{14} cm^{-2} extracted at nearly room temperature is not just for the Ge channel; there is also a contribution from other carriers in parallel conduction layers. This contribution seems to affect all the data above 30 K, while at lower temperatures the mobility and sheet density saturated, which means the carriers in other layers are frozen out. The sheet resistivity and Hall coefficient, shown as a function of temperature in Figure 4.27 illustrates a resistivity of

61 Ohms/sq at 10 K that is high compared to other device geometries. The Hall coefficient was 1094 m^2/C at 10 K.

A Greek cross structure, with Al contacts, was also measured. This data, in Figure 4.28, appears to show a smaller contribution to the parallel conduction, especially at low temperature, with carriers freezing out at a higher temperature (about 100 K) than the previous structure. The mobility of 2.9×10^5 cm^2/Vs is 1.6 times higher than the mobility measured in the Van der Pauw square, and the sheet density of 5.0×10^{11} cm^{-2} at 10 K is some 15% less. The low temperature sheet resistivity of 43 Ohms/sq was 1.4 times lower than for the InGa contacted square sample (Figure 4.29).

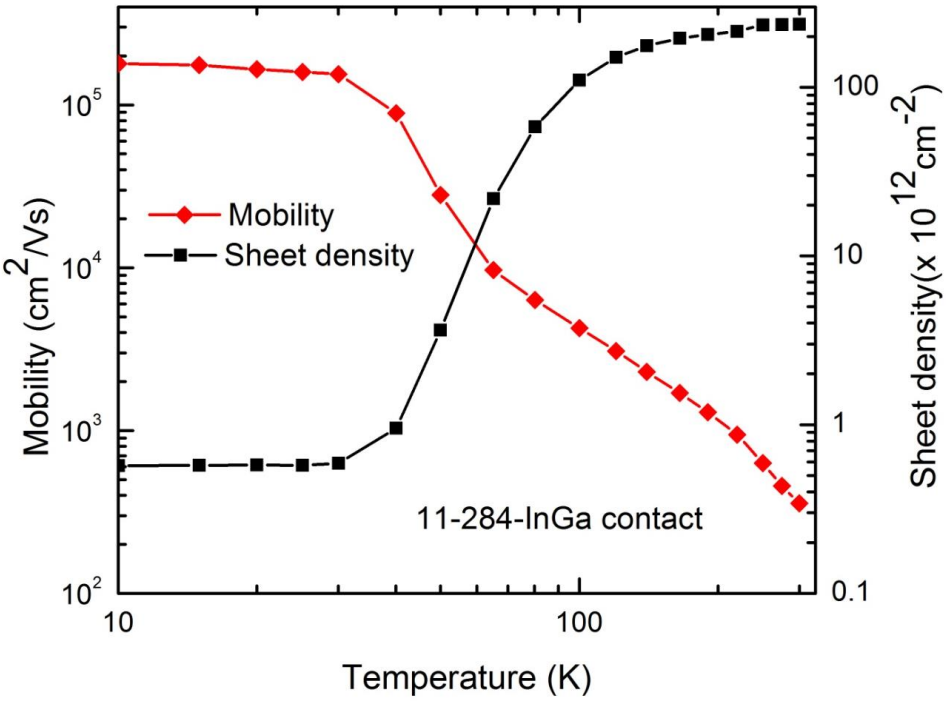

Figure 4.26 Mobility and sheet density as function of temperature for sample 11-284 measured on a Van der Pauw square with InGa contacts

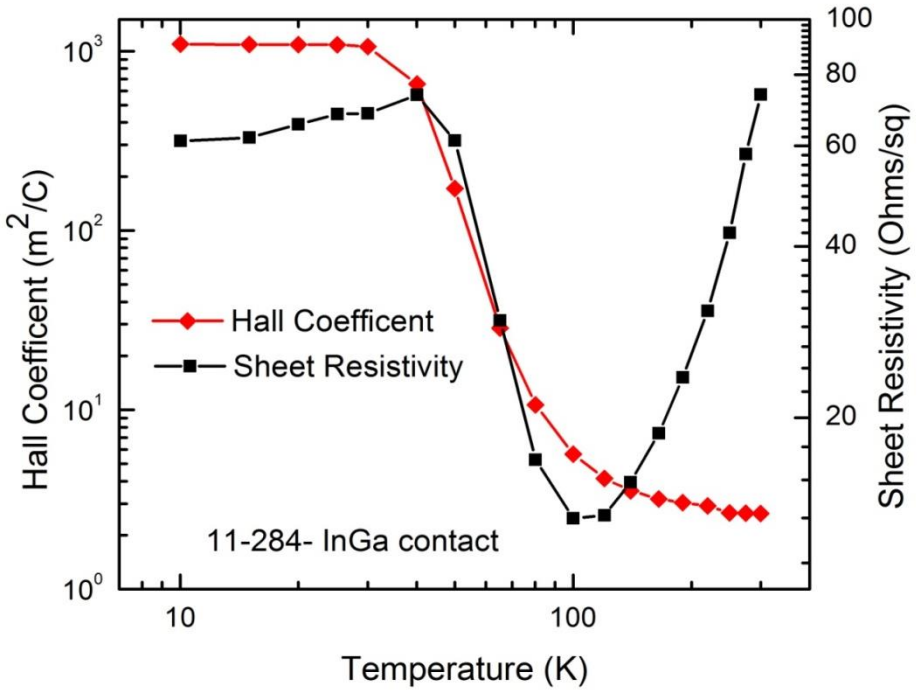

Figure 4.27 Resistivity and Hall coefficient as function of temperature for inverted 20 nm channel thickness for square VdP with InGa contact.

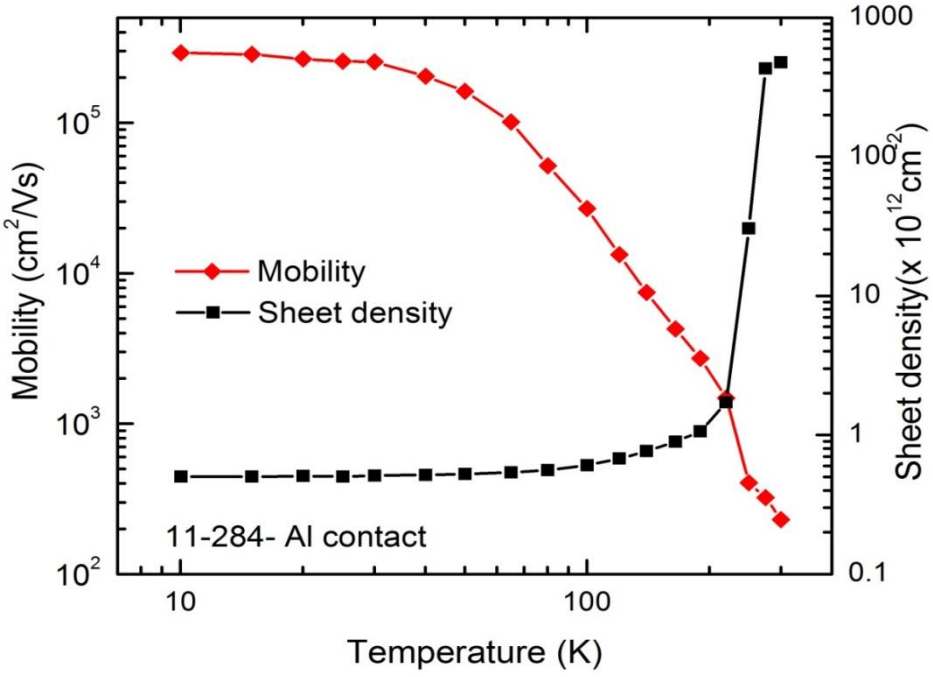

Figure 4.28 Mobility and sheet density as function of temperature for Greek cross with Al contact.

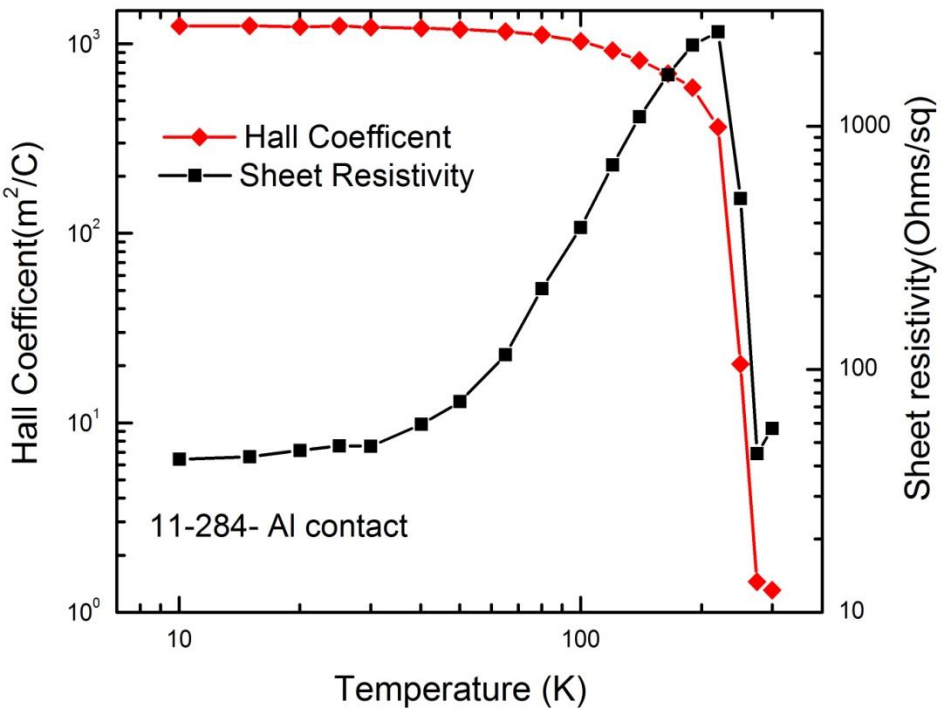

Figure 4.29 Resistivity and Hall coefficient as function of temperature for inverted 20 nm channel thickness GC with Al contact.

Finally, Hall Bar structures have been measured for this wafer, which should give a more accurate result due to the well-defined path for the current. The Hall bars were fabricated with current flowing along different crystallographic directions to determine any mobility anisotropy. In particular, the Hall bar along $[\bar{1}10]$ will be referred to as 0Deg orientation and that along $[110]$ as 90Deg orientation. These Hall bars have also been used to study carrier self-heating by varying the measurement current. The results are presented Figure 4.30 to Figure 4.32, and summarised in Table 4.3.

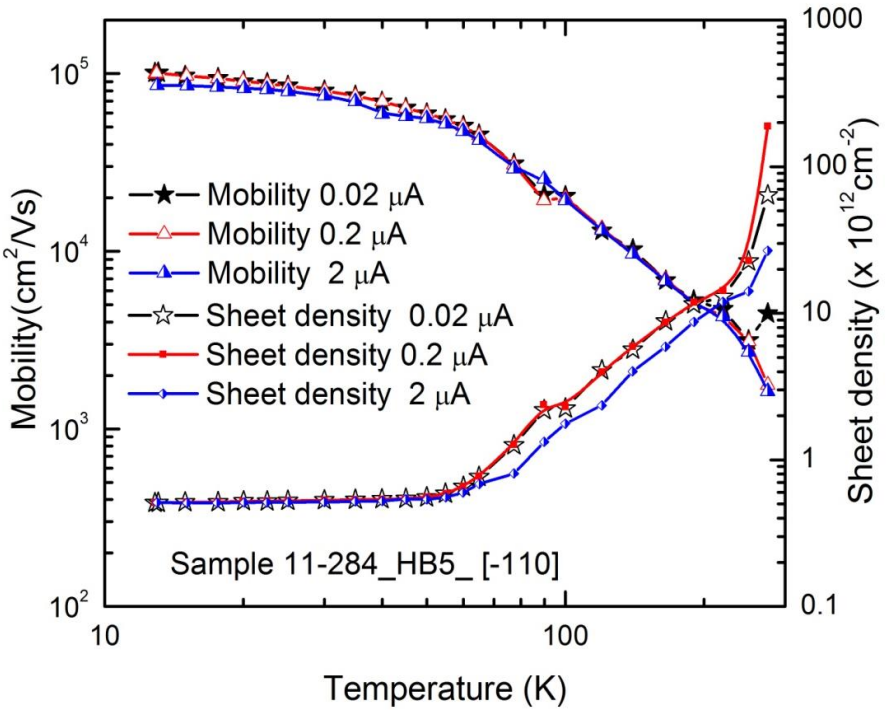

Figure 4.30 Mobility and sheet density as function of temperature for Hall bar in $[\bar{1}10]$ orientation (0 DEG) for currents of 20 nA, 200nA and 2μA

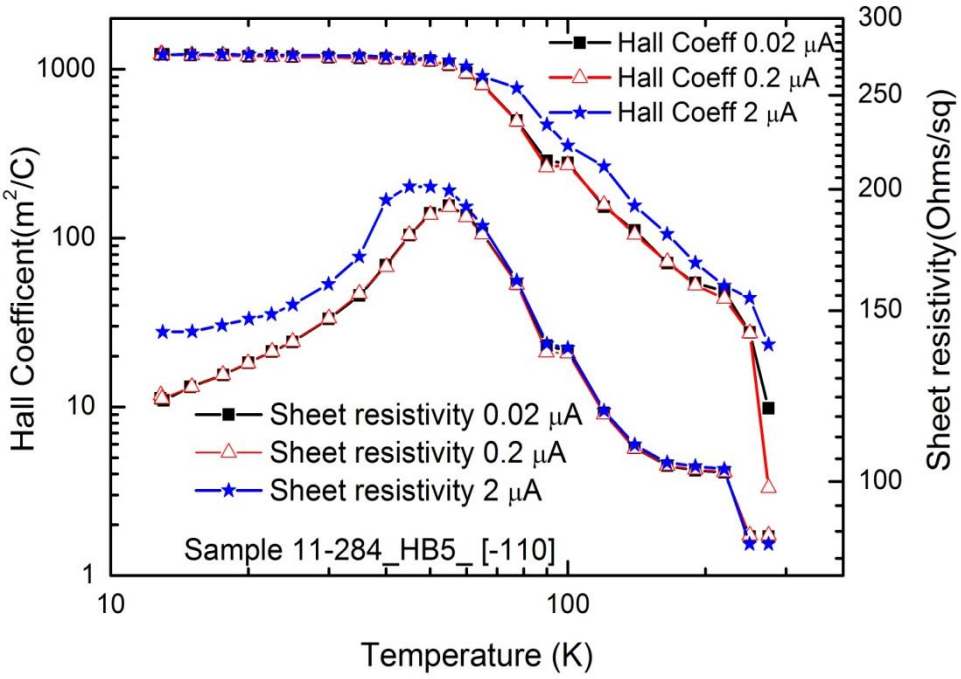

Figure 4.31 Resistivity and Hall coefficient as function of temperature for inverted 20nm channel thickness for Hall bar in $[\bar{1}10]$ orientation for current 20nA, 200nA and 2μA.

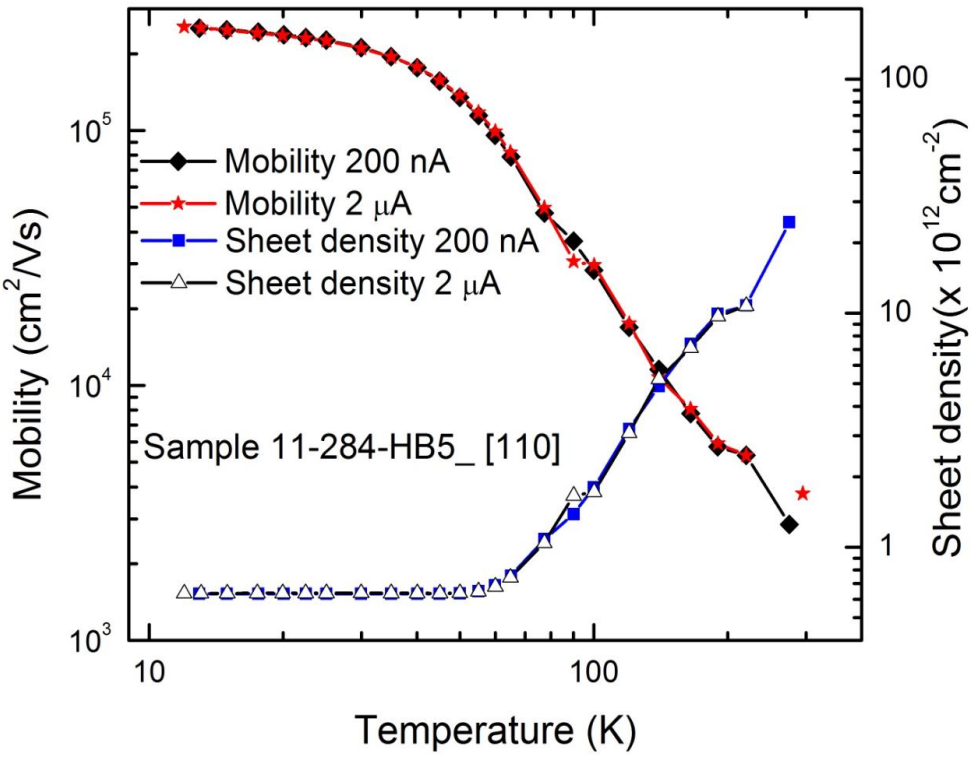

Figure 4.32 Mobility and sheet density as function of temperature for Hall bar in $[110]$ orientation for currents of 200 nA and 2 μA

Orientation	Current (μA)	ρ (Ohm/sq)	Hall Coeff (m^2/C)	p_s (12K) ($\times 10^{11}$ cm^{-2})	Mobility(12K) ($\times 10^5$ cm^2/Vs)
HB- 0 DEG $[\bar{1}10]$	2	145	1225	5.09	0.86
HB-0 DEG $[\bar{1}10]$	0.2	123	1224	5.1	1.00
HB-0 DEG $[\bar{1}10]$	0.02	122	1226	5.09	1.01
HB-90 DEG $[110]$	2	43	986	6.33	2.27
HB-90 DEG $[110]$	0.2	39	983	6.36	2.55
Greek cross GC	19	37.4	1015	6.15	2.72
Greek cross GC	2	37.9	1022	6.11	2.69
Greek cross GC	0.2	37.9	1024	6.09	2.69

Table 4.3 Parameters of Hall measurement of sample 11-284-HB5 in two orientations with different current values applied to the devices at 12 K.

From Table 4.3 it can firstly be seen that the size of the measurement current has some effect on the results obtained. Particularly in the $[\bar{1}10]$ case, some self-heating is evident for a current of 2 μA which has raised the sample resistivity by almost 20% compared to the lower currents, where no difference is seen between 0.02 μA and 0.2 μA. This affects the mobility value extracted to a similar degree, but has no effect on the Hall coefficient since the carrier sheet density is of course unchanged. Consequently in all subsequent low temperature mobility measurements a current of 0.2 μA has been used to minimise noise whilst avoiding self-heating. There is less of an issue at high temperature where Figure 4.31 shows the resistivity is independent of measurement current (lower than 2 μA).

There is a clear difference in the results between the two orientations of Hall bar; the [110] orientation shows a 12K mobility of 2.6×10^5 cm^2/Vs that is more than twice as large as seen for $[\bar{1}10]$. There is, however, a difference in the sheet density observed for these two Hall bars, 6.4×10^{11} cm^{-2} for [110] compared to 5.1×10^{11} cm^{-2} for $[\bar{1}10]$, which could partially account for an increase in mobility, but this 25% difference in density is unlikely to fully account for a mobility difference of 2.5 times. This issue of anisotropy will be returned to in Section 4.4 after examining data from the other similar wafers.

It should be noted that the heating effect was also examined for the Greek cross for sample 11-284 at 12K and the result is mentioned in Table 4.3. This indicated that because the size of the Greek cross is much bigger than hall bar the heating effect measured from the Greek cross sample is much lower than from the Hall bars.

4.3.2 15 nm strained Ge channel, sample 11-285

Mobility data for sample 11-285, which has a thinner Ge channel than 11-284, are presented in Figure 4.33 to Figure 4.35 Again three types of sample have been examined. Modulation doping characteristics are clearly observed at low temperature, with the sheet density settling

to a temperature independent value once all the parallel conduction in the doped layers has been completely frozen out. The exact temperature at which freeze out occurs seems to vary between 70K and 100K depending on the contact metal used. From a square sample with InGa contacts, the low temperature 2DHG sheet density is measured to be $7.76\times10^{11}cm^{-2}$ with mobility as high as 2.07×10^{4} cm^2/Vs at 10K. From a Greek cross with Al contacts, which is expected to produce more accurate results, the 2DHG sheet density is $6.09\times10^{11}cm^{-2}$ and mobility is 3.88×10^{5} cm^2/Vs. Finally, data from a Hall bar, orientated along the expected high mobility [110] direction, yields a sheet density of $5.2\times10^{11}cm^{-2}$ and mobility of 2.65×10^{5} cm^2/Vs.

The scatter in sheet density and mobility values recorded on the three different samples is similar to that seen for sample 11-284, which suggests there is some significant inhomogeneity across these wafers and/or in the fabrication process. Nevertheless, the overall picture is of a mobility that is much higher in 11-285 than in 11-284. This is not what was expected, because reducing the channel thickness should increase the influence of surface roughness scattering and lead to a reduction in mobility. That points to high quality interfaces without mobility limiting roughness. It is still a question why this sample has higher mobility than 11-284 especially with higher sheet density. However, it is known from SIMS that the layer thicknesses and doping density are not quite the same in both samples and that the undoped spacer thickness in 11-285 is larger than in 11-284, which will reduce the effect of remote impurity scattering in 11-285.

In the same way as for 11-284, the sheet density increases rapidly towards room temperature as parallel conducting channels are populated, resulting in a measured room temperature mobility of 238 cm^2/Vs at a sheet density of $4.5\times10^{14}cm^{-2}$ from the square sample, and similar values for the other devices. The actual density and mobility in the QW can be extracted from magnetic field dependent transport measurements using a technique of MSA.

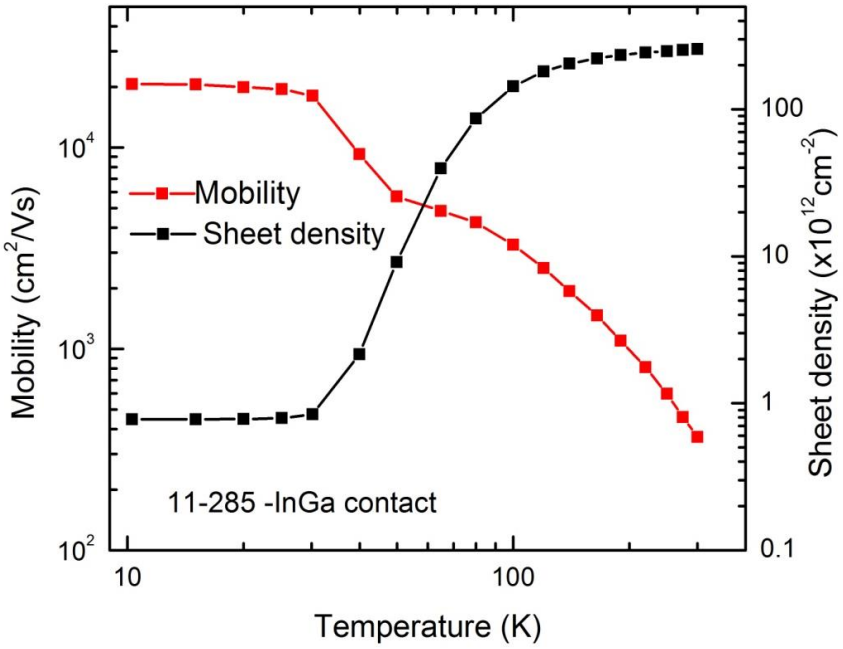

Figure 4.33 Mobility and sheet density as function of temperature for 15nm sGe channel thickness for square VdP with InGa contact

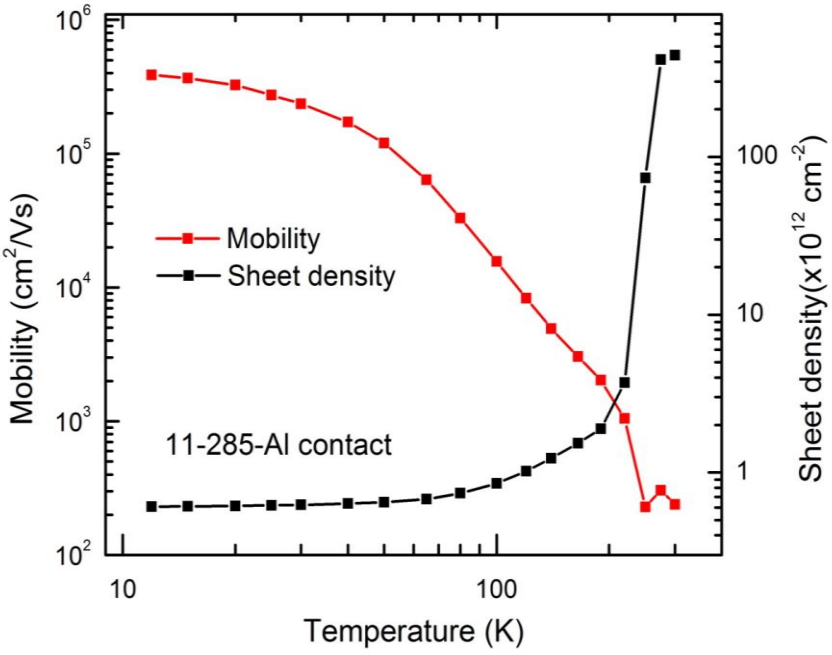

Figure 4.34 Mobility and sheet density as function of temperature for 15nm sGe channel thickness for Greek cross with Al contact

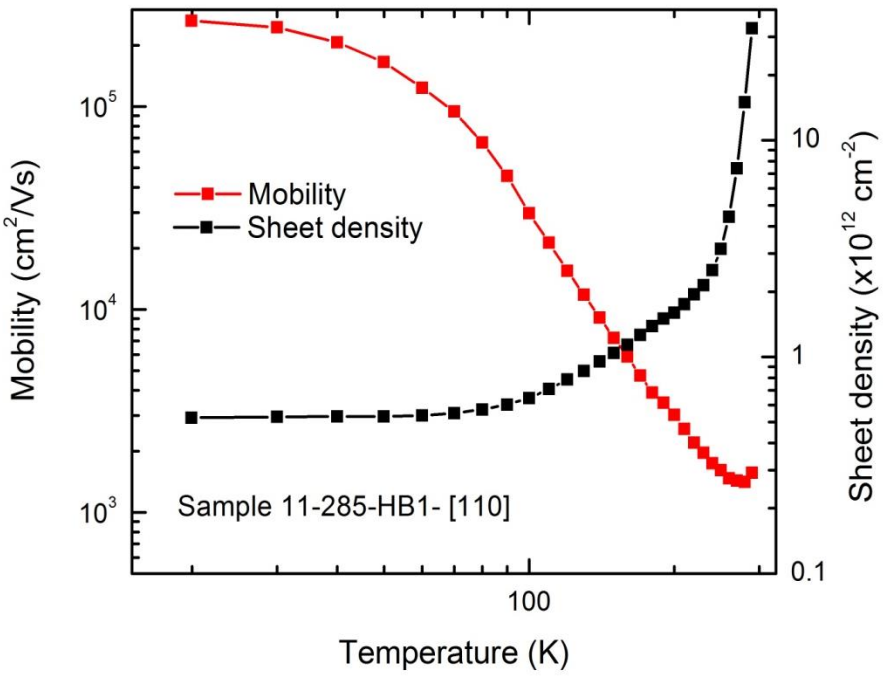

Figure 4.35 Mobility and sheet density as function of temperature for Hall bar sample 11-285.

4.3.3 38 nm strained Ge channel, sample 11-286

Figures 4.36 to 4.38 show temperature-dependent Hall mobility and sheet carrier density data from the 2DHG in the wider QW sample 11-286. Overall these again follow a similar pattern to the two preceding wafers, showing evidence for a modulation doped structure with almost constant carrier density at low temperatures and an increase in mobility with decreasing temperature. In this case the low temperature mobility reached 2.0×10^5 cm^2/Vs at a sheet density of 4.35×10^{11} cm^{-2}, for the InGa contacted square; 3.04×10^5 cm^2/Vs at sheet density 6.7×10^{11} cm^{-2} for the Al contacted Greek cross; and 2.65×10^5 cm^2/Vs at sheet density of 5.35×10^{11} cm^{-2} for a [110] orientated Hall bar. Apart from the square sample, which seems to give less reliable data, these values are quite similar to those observed for 11-285 which again suggests that scattering from the QW interfaces is not the process limiting the low temperature mobility.

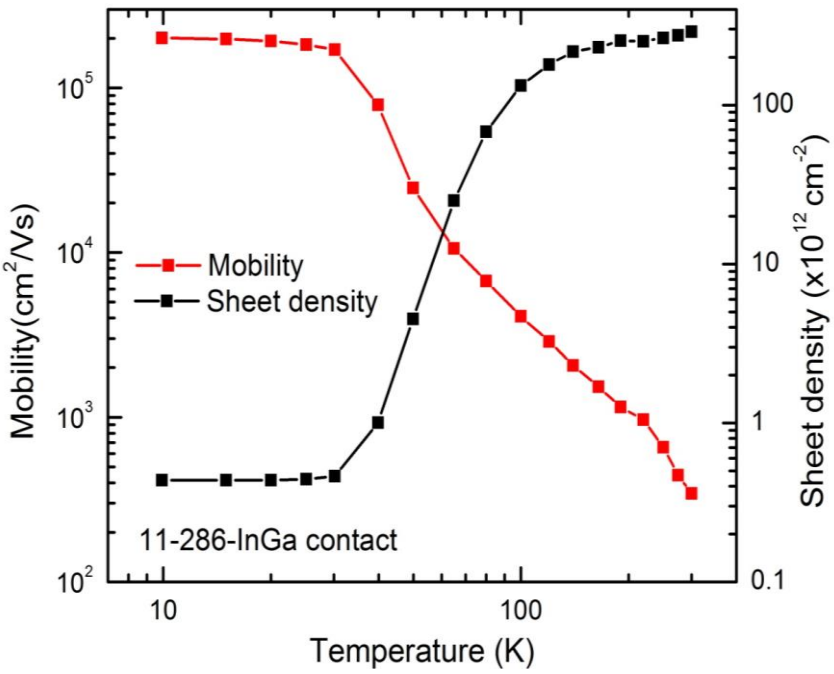

Figure 4.36 Mobility and sheet density as function of temperature for sample 11-286, with a 40 nm thick sGe channel and InGa contacts.

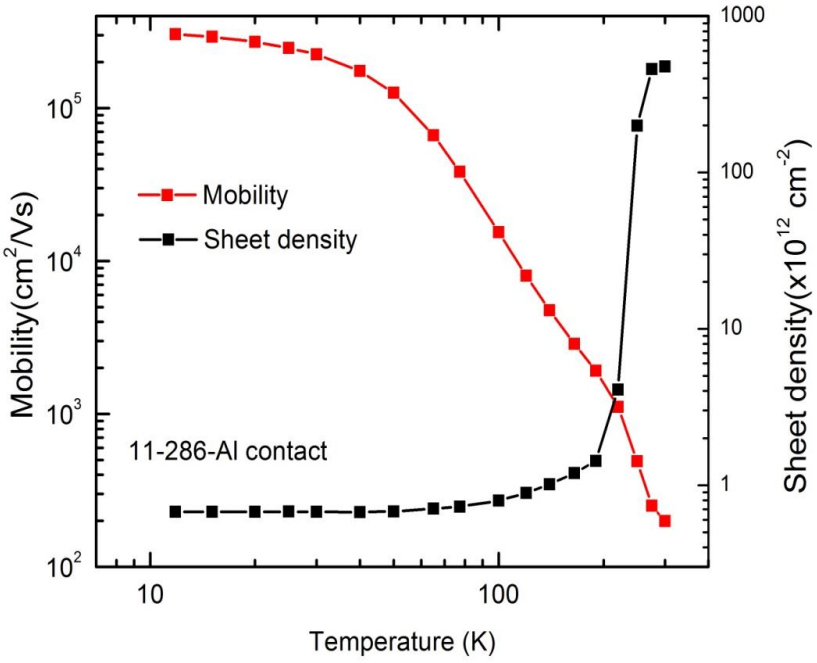

Figure 4.37 Mobility and sheet density as function of temperature for sample 11-286, with a 40nm thick sGe channel and Al contacts

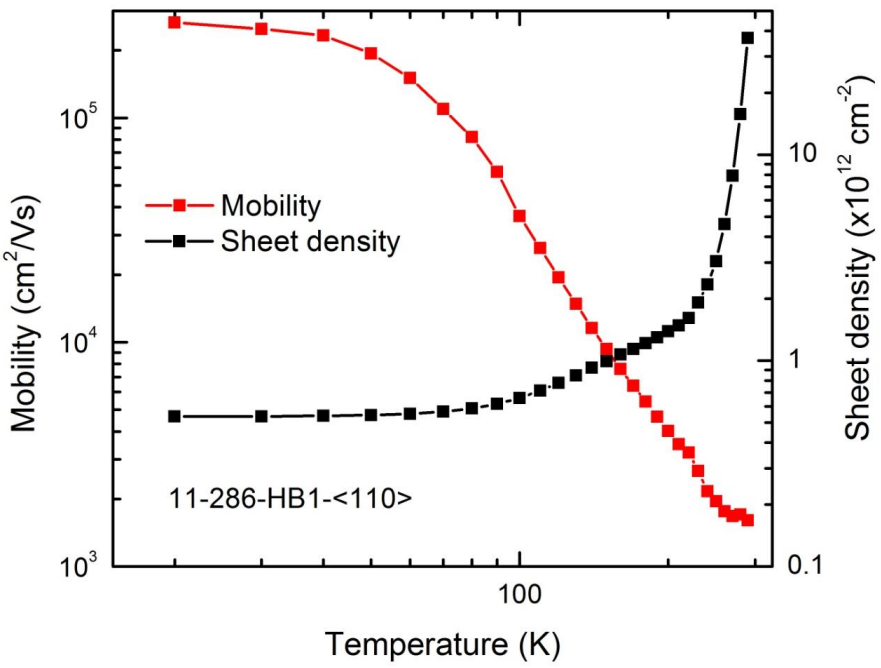

Figure 4.38 Mobility and sheet density as function of temperature for a Hall bar of sample 11-286

4.3.4 20 nm strained Ge channel, sample 11-287

Sample 11-287 differs from the previous three in that it has a much thinner undoped spacer layer, of 10 nm rather than 20 nm nominal thicknesses which was confirmed by SIMS. For that reason the sheet density at low temperature is expected to be much greater. It is measured as 9.32×10^{11} cm^{-2} in the square Van der Pauw sample with InGa contacts (Figure 4.39). The mobility at 10 K is much lower at just 0.22×10^{5} cm^2/Vs. For this measurement, it appears that parallel conduction effects start to be seen from as low as 35K. The mobility was considerably low compared with the other samples and gives an indication that increasing the sheet density in the channel reduces the mobility. Hall measurements from the Al contacted Greek cross structure show a higher mobility of 1.46×10^{5} cm^2/Vs at a sheet density of 8.74×10^{11} cm^{-2}, with a less dramatic onset of parallel conduction (Figure 4.40) that suggests this result is more reliable than that from the square sample and more in line with the observations from the previous wafers.

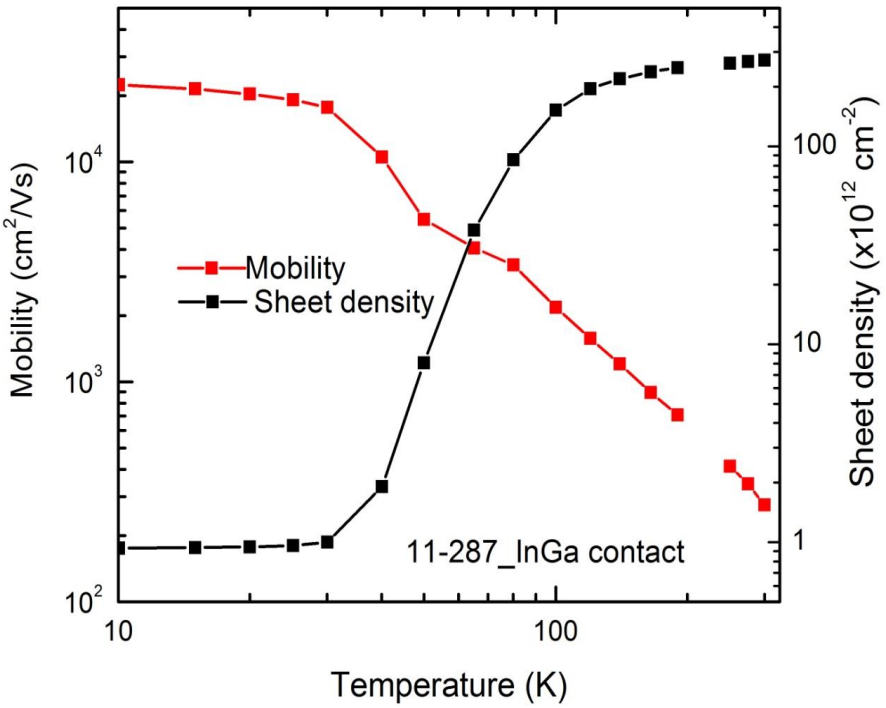

Figure 4.39 Mobility and sheet density as function of temperature for sample 11-287, with a 10 nm spacer thickness and InGa contacts.

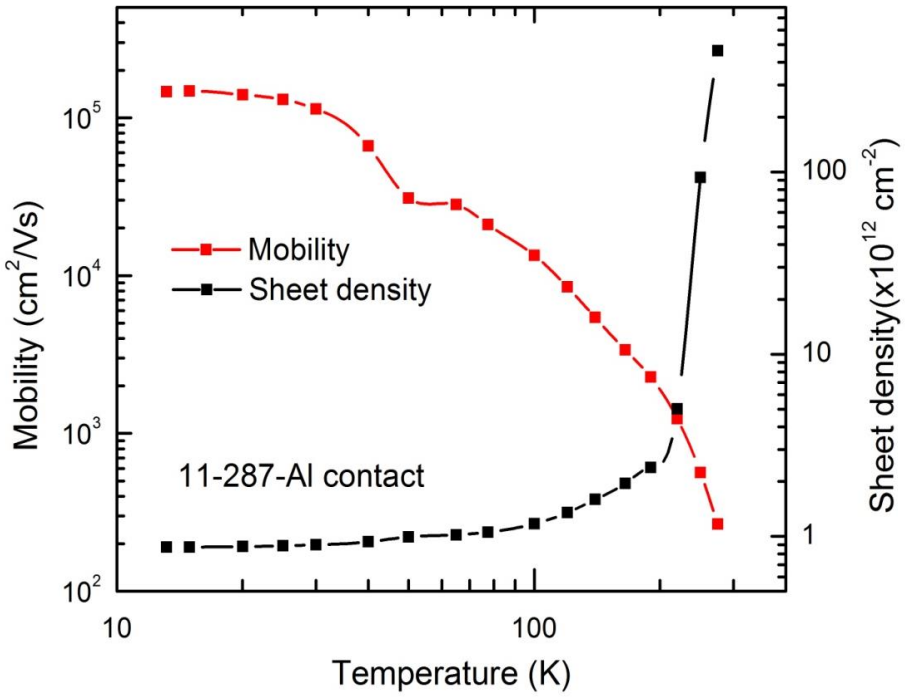

Figure 4.40 Mobility and sheet density as function of temperature for sample 11-287, with a 10 nm spacer thickness and Al contacts.

4.3.5 20 nm strained Ge channel, sample 11-288

With regard to the higher doping density sample (11-288), it is expected that the sheet density will be higher than for 11-284 with the same 20 nm doping set back distance. The same procedures were applied to this sample which was measured firstly with InGa contacts to ensure the modulation doped behaviour Figure 4.41. The 10K mobility was measured as 0.83×10^5 cm^2/Vs at a sheet density of 8.45×10^{11} cm^{-2}. As in sample 11-287, parallel conduction effects start to be observed above about 35 K and the mobility seems to be anomalously low compare to the other samples. More investigation were performed using the Greek cross with Al contacts, Figure 4.42, that illustrates a mobility and sheet density of 1.91×10^5 cm^2/Vs and 6.12×10^{11} cm^{-2} at 12 K.

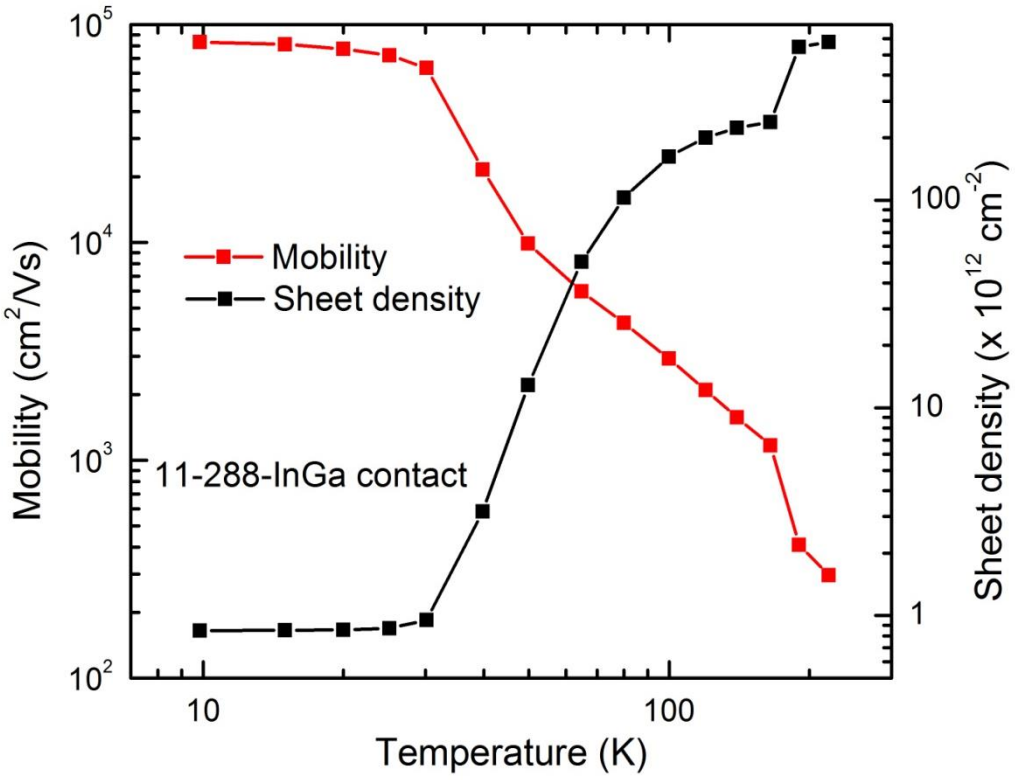

Figure 4.41 Mobility and sheet density as function of temperature of sGe channel with InGa contact (11-288).

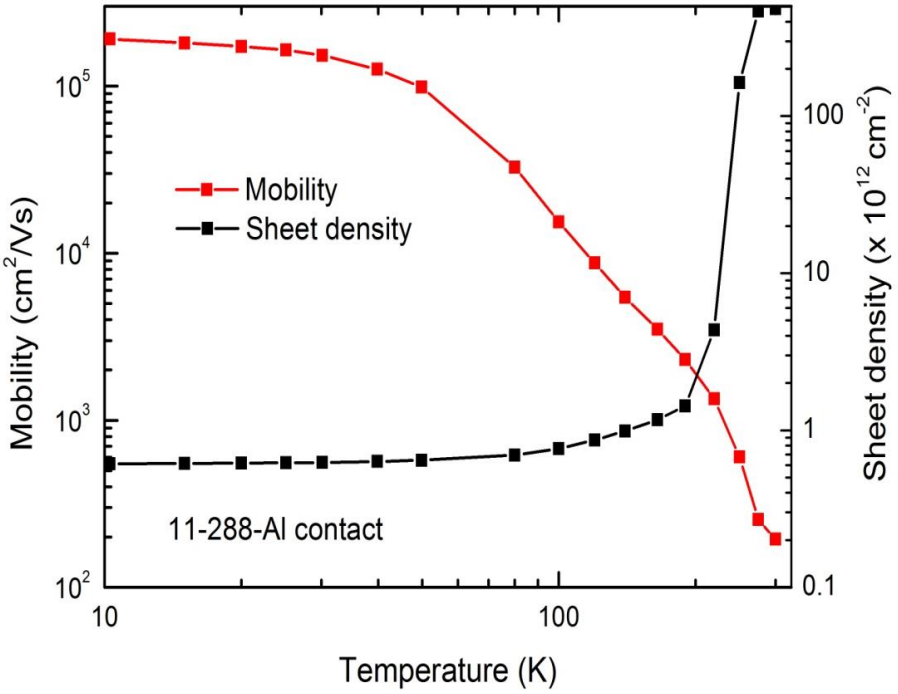

Figure 4.42 Mobility and sheet density as function of temperature of sGe channel with Al contact (11-288)

4.3.6 25 nm strained Ge channel, sample 11-290

Sample 11-290 had a nominally identical structure to 11-284, but was grown at the higher temperature of 450 °C, which was shown by the TEM analysis in Section 4.2.2 to cause more structural defects and would be expected to result in a reduced mobility. Resistivity and Hall measurement were performed first on Van der Pauw square with InGa contact and present mobility of 8000 cm^2/Vs at a sheet density of 9.57 $\times 10^{11}$ cm^{-2} at 10 K (Figure 4.43). Secondly, the Greek cross structures with Al contacts performed and showed a mobility of 2.00×10^5 cm^2/Vs at a sheet density of 6.19 $\times 10^{11}$ cm^{-2} at 15K (Figure 4.44). This is about half the mobility measured in Greek cross structures for 11-285 and 11-286 at a similar density and represents a similar mobility reduction to that shown by 11-288.

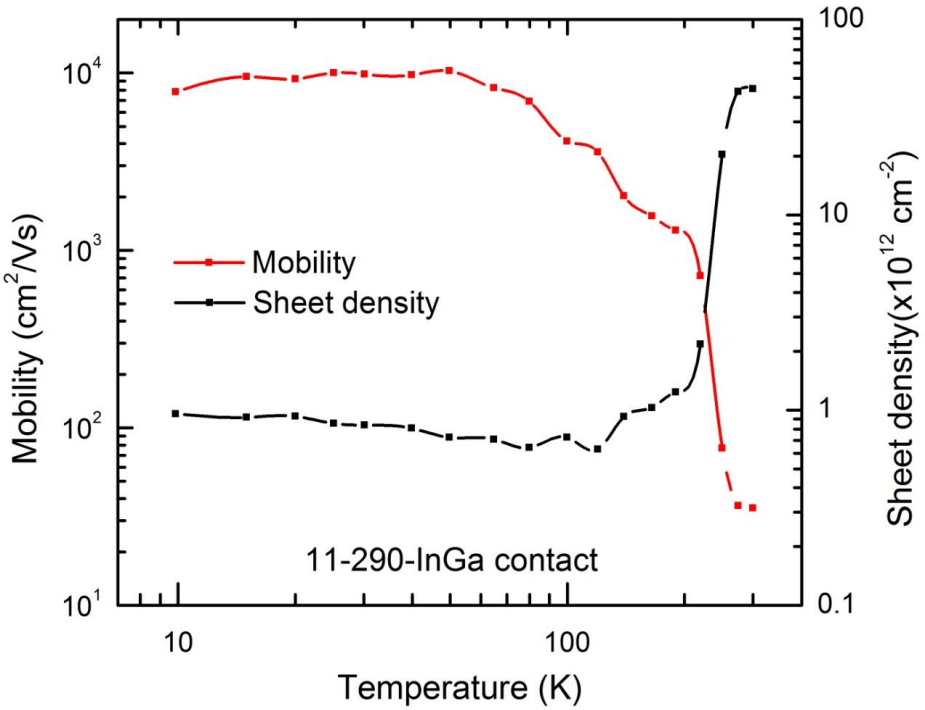

Figure 4.43 Mobility and sheet density as function of temperature of sGe channel with InGa contact (11-290)

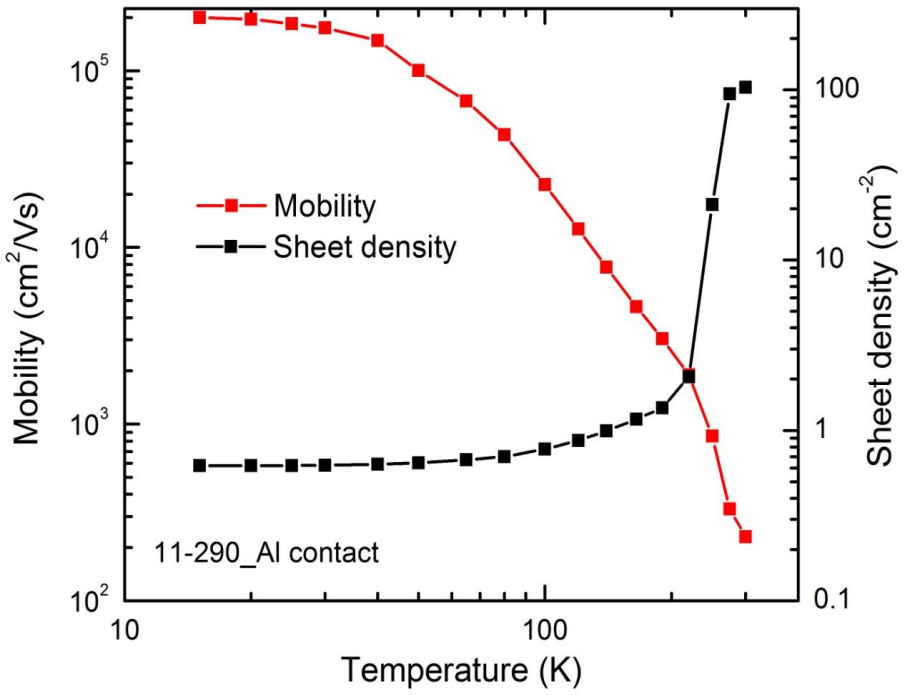

Figure 4.44 Mobility and sheet density as function of temperature of sGe channel with Al contact (11-290)

The measured low temperature mobility and sheet density values from the whole batch of samples is summarised in Figure 4.45. At low sheet density, up to ~6×10^{11} cm^{-2}, the mobility increases with hole density. It then remains fairly constant until starting to decrease again at higher sheet densities above ~8×10^{11} cm^{-2}. At low sheet density the mobility is expected to be limited by background impurity scattering, for which it should increase with carrier concentration, and at higher sheet density it is expected to be dominated by interface roughness scattering and to decrease with sheet density.

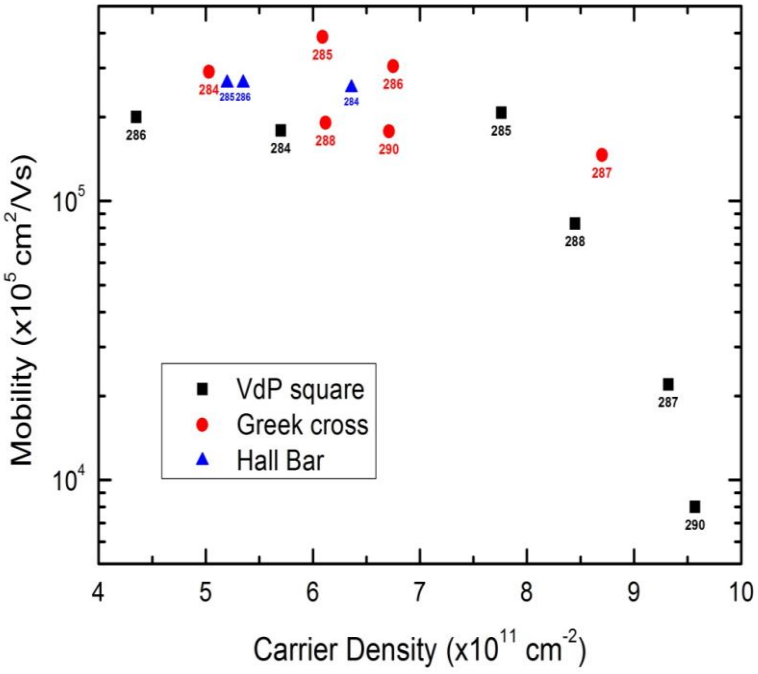

Figure 4.45 Mobility as function of sheet density for all inverted samples with different configuration square van der Pauw, Greek cross and Hall Bars at 10 K

That different sample configurations have different mobility and sheet density values could be a sign of non-uniform wafers. The three device configuration illustrate similar mobility for samples 11-284, 11-285 and 11-286 using the square VdP configuration. The fact that the sample with the lowest channel thickness (11-285) has the highest mobility compared to all the samples demonstrates that the effect of interface roughness is not dominating the mobility for these samples which is normally observed in previously reported sGe samples [6]. On the

other hand, at higher sheet density than 6.9×10^{11} cm^{-2} a clear reduction in mobility is observed resulted from interface roughness scattering, as will be seen in next section.

4.4 Theoretical Simulation of scattering limited mobility:

The hole mobility at low temperature is limited by remote (RI) and background impurity (BI) scattering as well as interface roughness scattering (IR), as outlined in section 2.1. However, due to the high quality structure of these samples, interface roughness scattering is believed to have less impact on mobility at low sheet density. Figure 4.45 shows that reducing the channel thickness did not reduce the mobility of the carriers, whereas usually this would cause a big reduction due to the increased contact with the interface in a narrower channel [6] As it mentions in section 4.2.2, the TEM imaging did not illustrate any roughness in the channel interfaces as well. For that reason, only background and remote impurities scattering included in the first simulation Figure 4.46. However, to fit experimental data ionized remote impurities up to 1×10^{18} cm^{-3} or more should be included, which is not possible according to the amount of sheet density measured at low temperature for these samples.

A small amount of interface roughness scattering is included in the revised simulation of Figure 4.47, with a small height of 0.28 nm (two atomic layers of germanium, or half the lattice constant) and a correlation length of 8 nm. This simulation fits the experimental data with a remote impurity density of 4×10^{17} cm^{-3} and background impurity concentration of 5×10^{14} cm^{-3}, which are much more reasonable values. SIMS profiles for these samples did not show us significant background impurities above 1×10^{17} cm^{-3} that is the resolution limit of the particular SIMS used. At higher sheet density more mobility data points would be needed for accurate simulation. However, it could be seen that interface roughness limits the mobility for sheet densities greater than 7.5×10^{11} cm^{-3}.

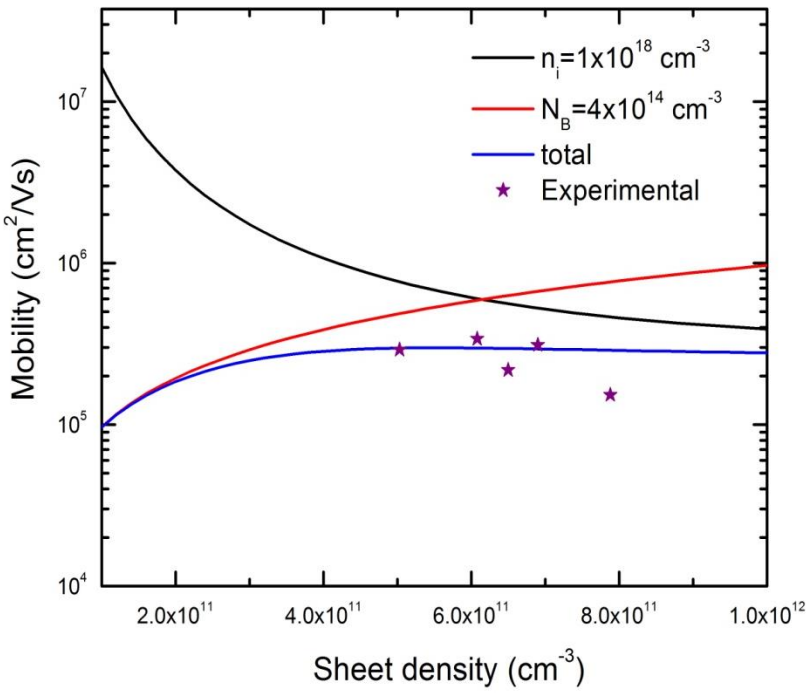

Figure 4.46 Background and remote impurity scattering limited mobility simulation in respect of sheet density..

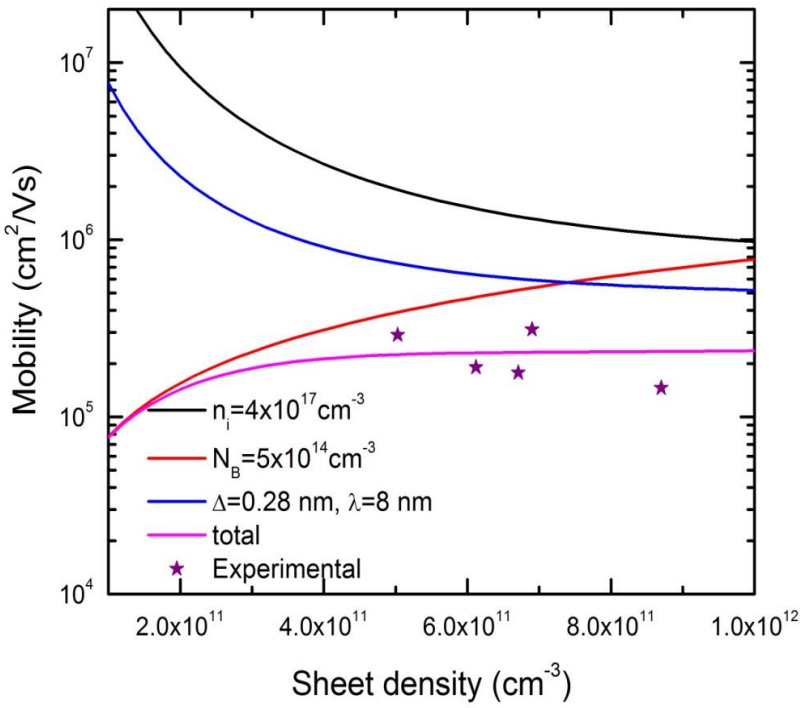

Figure 4.47 Simulation for background and remote impurity scattering, and interface roughness scattering limited mobility in respect of sheet density.

4.5 Anisotropy study in inverted structures:

Mobility anisotropy has been observed in all the samples with an inverted doping structure. Therefore, careful treatment was needed for all the data obtained from Hall measurements for all the devices fabricated. As reported in the literature, the Hall bar configuration is preferred, which accurately reflects the resistivity in the direction of the bar. Unfortunately, there was not enough time during the period of this PhD to fabricate and measure Hall Bars for all the samples. Another way is to analyse anisotropy using a square Van der Pauw configuration, as mentioned in [25], and this was used to better understand the transport properties of holes in these sGe heterostructures

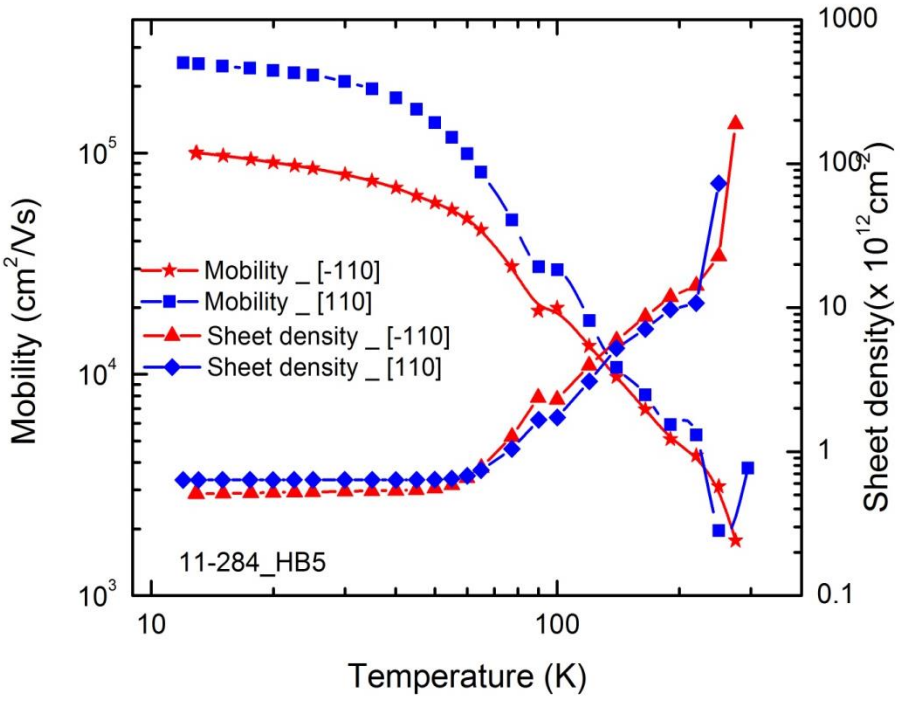

Figure 4.48 Mobility and sheet density as function of temperature for two orientation $[110]$, and $[\bar{1}10]$

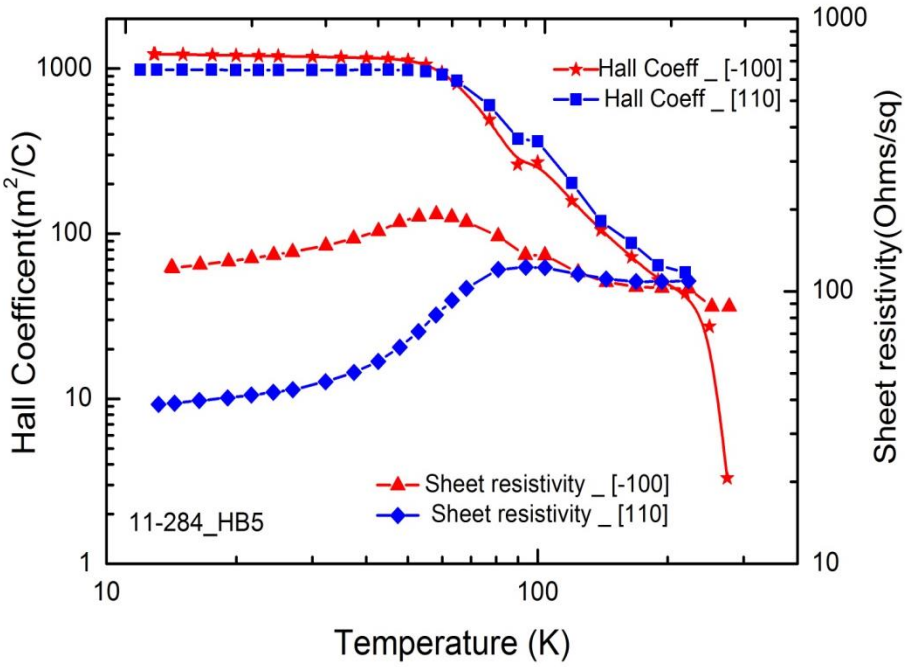

Figure 4.49 Resistivity and Hall coefficient as function of temperature for two orientations $[110]$ and $[\bar{1}10]$.

This section will present anisotropy analysis for different samples configurations square VdP, Greek cross, and Hall Bar devices. Data from a Hall bar device (for sample 11-284), in Figure 4.48 and Figure 4.49 clearly shows mobility and resistivity anisotropy between the $[110]$ and $[\bar{1}10]$ orientations.

The resistivity is about 3.2 times higher in the $[\bar{1}10]$ orientation than for the $[110]$ orientation. The anisotropy ratio increased by lowering the temperature which is also observed for other configurations. Table 4.3, already noted the huge anisotropy in this sample, but it also shows that there is a difference in sheet density of 20% between the two orientations. These measurements were from different Hall bars on the same piece of the wafer, which shows wafer uniformity is an issue here that may mask actual anisotropy. By contrast a measurement on a Van der Pauw device will be sampling the same material in two directions, so should not suffer from carrier density non-uniformity.

The experimental resistivity ratio A_{VdP} for all the samples measured in a Greek cross configuration is presented in Figure 4.50 over a range of temperatures 10 K – 300 K. It shows that the anisotropy ratio increased at lower temperatures in each case. Significantly, at lower temperatures the mobility will be more affected by interface roughness scattering that is potentially anisotropic due to different roughness profiles in the in two orientations. At high temperature the dominant mechanism is expected to be phonon scattering,[78] which should be isotropic; indeed the measured room temperature anisotropy ratio is around one for almost all the samples except 11-284 and 11-288, which reflects a pronounced geometric effect in the anisotropy for these two samples only.

All the samples were found to have 2DHG sheet densities in the range 5.03 - 7.89 × 10^{11} cm^{-2} and corresponding mobilities of 5.26 - 7.78×10^5 cm^2/Vs when measured along the [110] direction using standard Van der Pauw square and Greek cross geometries at T = 12 K. For the $[\bar{1}10]$ direction, the sheet density were found to be the same, but the mobility varied between 2.01 - 8.49 × 10^4 cm^2/Vs which is significantly lower. Figure 4.51 represents the experimental resistivity ratio for the square Van der Pauw configuration. The resistivity ratio in almost all the samples increased towards lower temperature, except samples 11-284 and 11-286 where it could again be the result of a geometric effect.

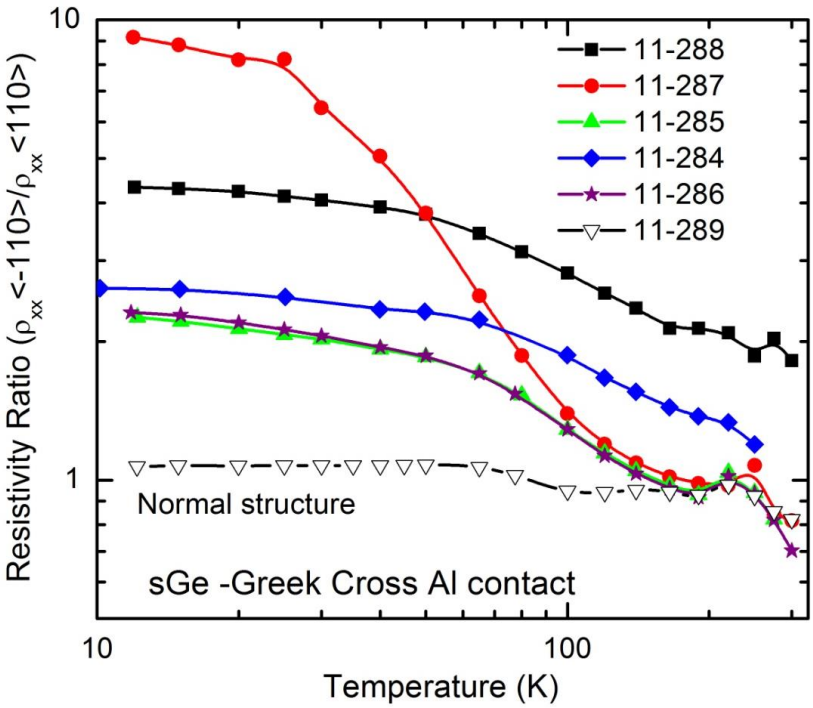

Figure 4.50 Resistivity ratio as function of temperature for Greek cross samples

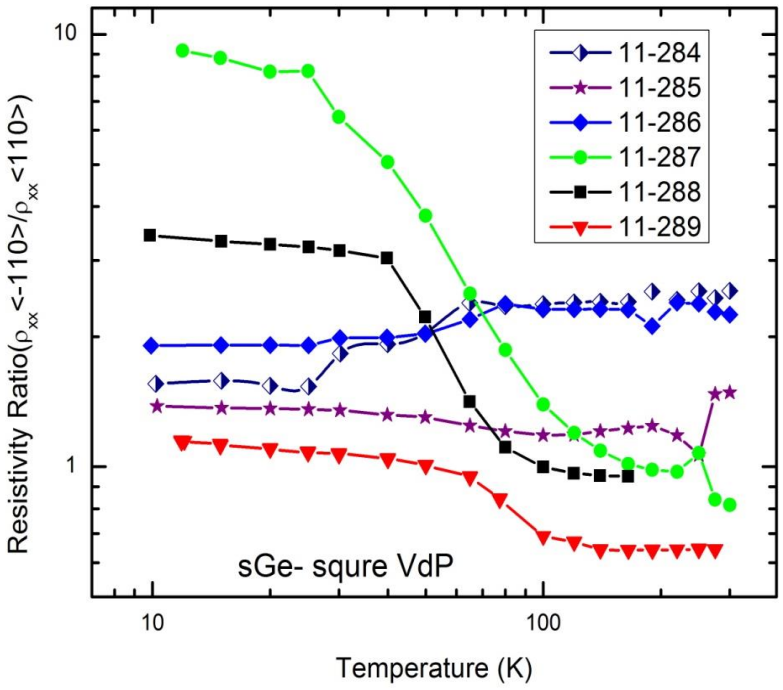

Figure 4.51 Resistivity ratio as function of temperature for inverted samples for square VdP samples

The experimental ratio of resistances overestimates the actual resistivity anisotropy for VdP geometries, but can be converted to the more accurate ratio *A* by the method outlined in Section 2.1. The result is presented in Figure 4.52 and shows the anisotropy ratio calculated for the Greek cross and VdP configurations. Generally, it could be seen that the anisotropy increased with sheet density, and as reported before [31] the influence of interface roughness scattering also increases with carrier density, and roughness can vary with orientation. It is therefore reasonable to investigate whether interface roughness scattering is responsible for the anisotropy that we see increasing with hole density. Indeed a previous study on GaAs [39] did attribute a mobility anisotropy that increased with sheet density to interface roughness or substrate off-cut. [79-81]. We have therefore calculated the mobility contributions from these various scattering mechanisms to compare with the experimental values as will be seen in the next section. Sample 11-289 with the lowest sheet density has the lowest anisotropy in both VdP and Greek cross configurations, while sample 11-287 with the highest sheet density has the highest anisotropy of 1.92 for the VdP configuration and 1.99 for Greek cross Table 4.3 summarizes the calculated 12 K Van der Pauw (Greek cross) mobility and sheet density found for all the samples and for the $[\bar{1}10]$ and [110] orientations.

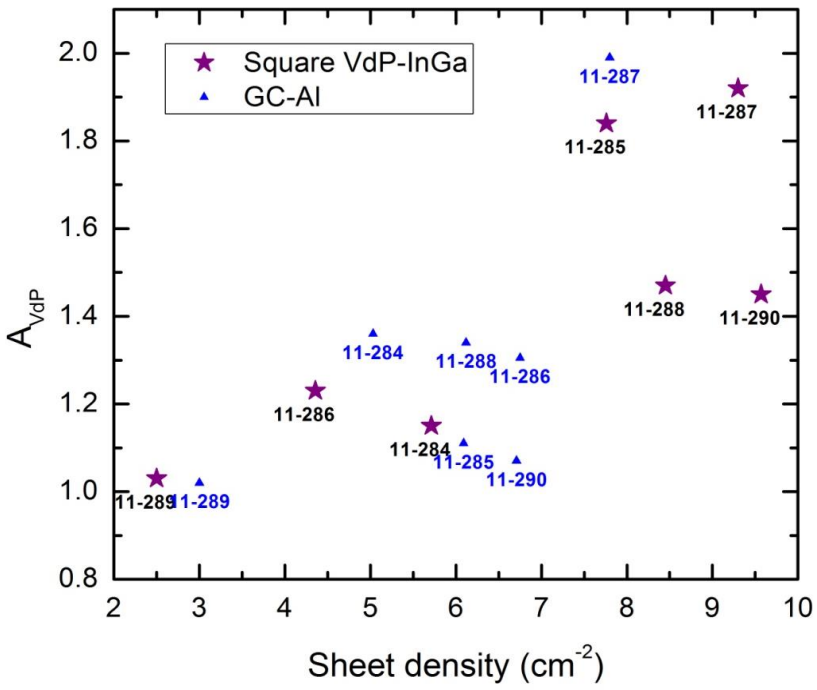

Figure 4.52 Calculated anisotropy ratio for all sGe samples with VdP and Greek cross configurations at 12 K.

Sample	ρ_{xx} (Ω/sq)	p_s ($\times 10^{11}$ cm^{-2})	μ ($\times 10^5$ cm^2/Vs)
11-284-$[\bar{1}10]$	50	5.03	2.47
11-284-[110]	36		3.36
11-285- $[\bar{1}10]$	33	6.90	2.74
11-285-[110]	25		3.57
11-286-$[\bar{1}10]$	35	6.75	2.65
11-286-[110]	27		3.48
11-287-$[\bar{1}10]$	70	7.89	1.12
11-287-[110]	37		2.15
11-288- $[\bar{1}10]$	54	6.51	1.77
11-288- [110]	34		2.81

Table 4.4 Theoretical calculation of resistivity and mobility for inverted structure.

4.6 Simulation of scattering limited mobility:

Scattering simulations at low temperature have been performed for all the inverted structures in two orientations, [110] and $[\bar{1}10]$, to understand the scattering limited mobility in these directions. Figure 4.53 shows that background impurity density of $2\times10^{14}cm^{-3}$ and an ionized remote impurity density of $3\times10^{17}cm^{-3}$ is determined from the simulation. Interface roughness scattering has a lower impact in the [110] orientation than for $[\bar{1}10]$, for which direction it can be seen to dominate the mobility at higher carrier density.

The total mobility in each direction has been determined by fixing the same values of remote and background impurities and changing the parameters of interface roughness scattering. The background and remote impurity densities in this simulation are slightly lower than the previous one for average mobility. The height of the roughness was equal to 3 monolayers (Δ=0.42nm) in the $[\bar{1}10]$ orientation, while it is 2 monolayers (Δ=0.28nm) for [110]. The change in the roughness period (or correlation length) from λ= 4 nm to λ=7 nm could double the mobility of the holes in these strained Ge inverted structures. At much higher density the effect of IR scattering starts to depress the mobility significantly as indicated in Figure 4.53.

The reason for the anisotropy observed in this work is believed to be from the 3 monolayer high steps along $[\bar{1}10]$, due to an off-cut (θ ~1.0 ±0.5°) of the starting (100) Si substrates in this direction. This would also result in shorter terraces in the $[\bar{1}10]$ direction than in the perpendicular direction to the off-cut. It is believed that this treatment of each orientation separately results in more realistic values.

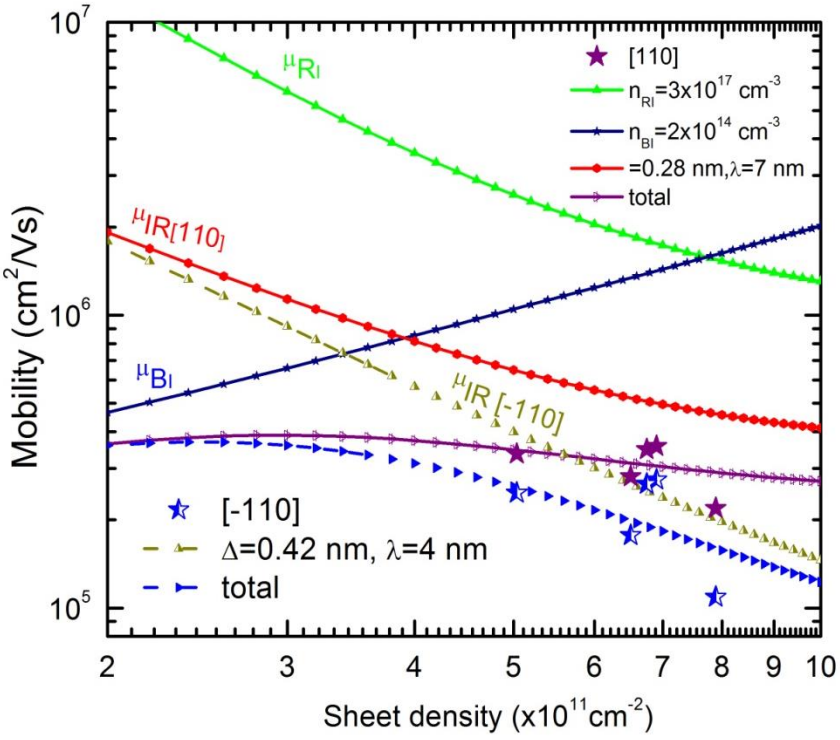

Figure 4.53 Simulation of the scattering limited mobility at low temperature at two different orientations, with the experimental result referred as stars.

4.7 Nextnano[3]Simulationof the Valance-band structure:

This section will present simulations for the heavy hole valance band edge using two approaches: the effective mass approximation (EMA) and a 6×6 k.p method, both implemented by the Nextnano[3] program. More details about this program were presented in section 2.4. The first approach within the EMA is helpful to get a first approximation about the band edges starting from the nominal layer thicknesses and assuming completely abrupt interfaces with no Ge segregation or diffusion. Figure 4.54 represents the heavy hole band edges at a temperature of 4K for sample 11-284. Note that the valance band edge energy axis has been rescaled with respect to the Fermi level E_F, which is defined as E = 0 meV (black line). It has been assumed that the boron in the doping layer is fully ionised and that there is no additional doping at the surface and that the Ge concentration was 0.79 in the buffer and

spacer layers. The doping concentration was taken from the SIMS profile in Figure 4.18 as the average concentration shown there in the doping layer. The hole concentration in the channel is also illustrated in Figure 4.54, showing a 2D sheet density of $4.52\times10^{11}\text{cm}^{-2}$ in the quantum well, which is 8% lower than the sheet density extracted from Hall measurements.

A more accurate method for calculating valance band edges is to use a 6×6 **k.p** perturbation method. Figure 4.55 shows the heavy hole band edge and hole concentration calculated this way, using actual layer thicknesses and doping density extracted from the SIMS measurements. The 6×6 **k.p** simulation results in a single subband occupation, with a sheet density of $5.83\times10^{11}\text{cm}^{-2}$, that is now 16% larger than measured. In this case the hole density is much more realistically spread across the quantum well, which is the reason for its higher value.

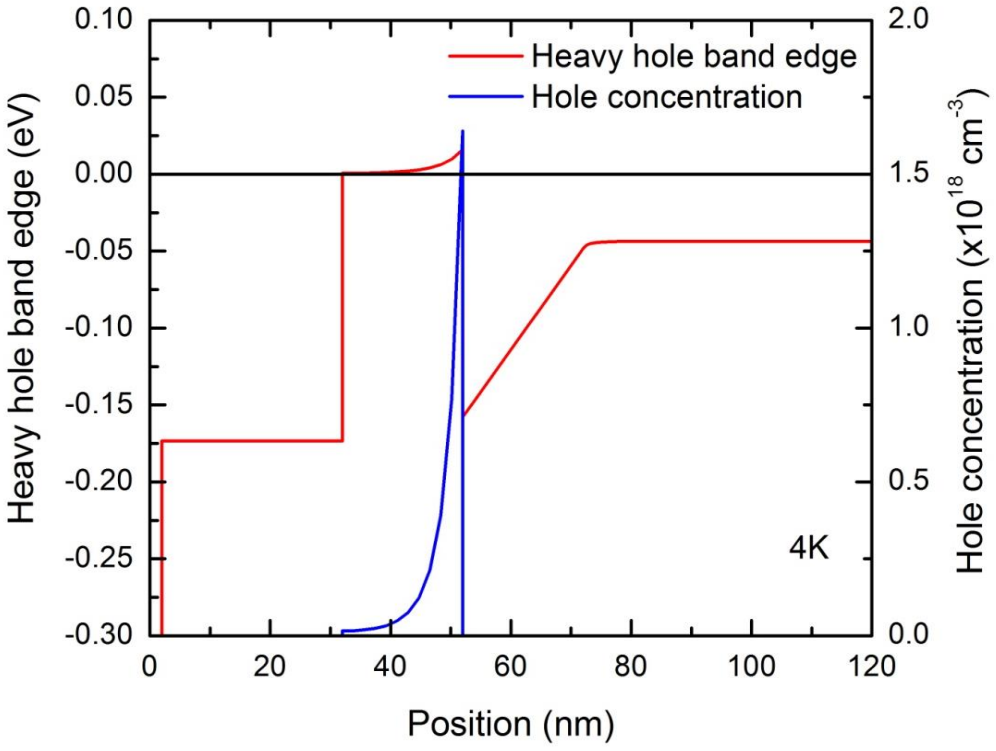

Figure 4.54 Heavy hole band edge and hole concentration calculated by EMA using Nextnano[3] for sample 11-284. The black line at 0 eV shows the Fermi energy, found by matching the chemical potential of each layer.

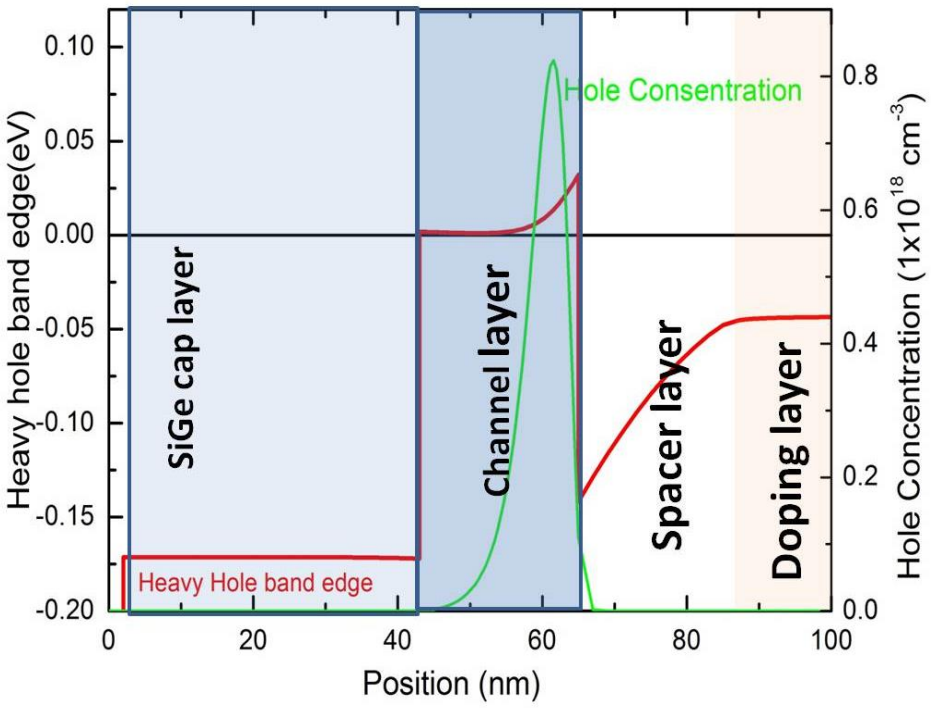

Figure 4.55 Hole band edge and hole concentration calculated by 6×6 **k.p** using Nextnano[3] for sample 11-284.

Finally, the high doping at the Si cap observed in uleSIMS images for all the samples under investigation must be considered. We assume that it may affect the transport properties due to significant changes to the band bending. Therefore, another simulation has been performed that includes Boron doping with a concentration of $1\times10^{18}\,\mathrm{cm}^{-3}$ in Si cap layer. The result is illustrated in Figure 4.56 and shows two pockets in the quantum well, which means two kinds of carriers in the channel. The sheet density calculated for the combination of the two carrier types was $4.44\times10^{11}\,\mathrm{cm}^{-2}$ that is now 11% lower than experimental sheet density. It should be noted that the carriers in the two pockets could have different mobilities, because they are scattering off different rough interfaces and are in regions of different vertical electrical fields. This might be expected to show up as two distinct carrier types in magnetotransport measurements (see Chapter 6).

Although, none of the simulations exactly matches the experimental sheet density it should be remembered that these calculations make a number of assumptions, including uniform background doping in all parts of the sample and completely abrupt interfaces. In reality, the smearing of the interfaces due to segregation and diffusions will change the actual subband energies and hence the distribution of charge carriers. The non-uniformity of doping will mean that, even within a relatively small area of the measured device, there will be variations in carrier density so that a resistance measurement will average over these regions. Nevertheless the simulations do allow for greater understanding of the carrier distribution in these samples.

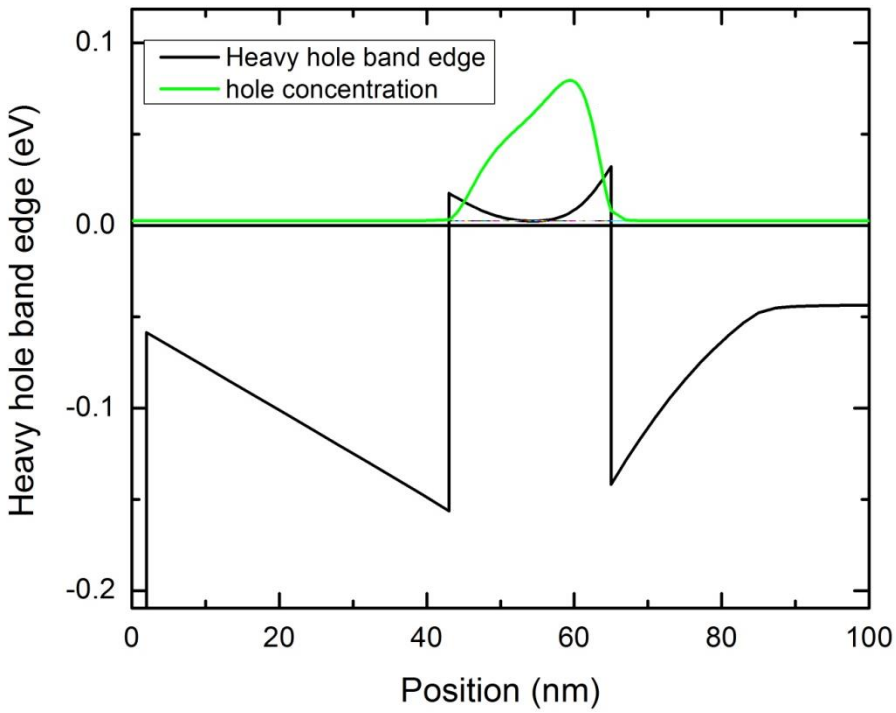

Figure 4.56 Nextnano simulation for the sample 11-284 using 6×6 **k.p** method applying doping in Si cap.

4.8 Summary

This chapter has shown that sGe heterostructures with doping underneath the channel have significantly improved transport properties of the holes in the channel compared to previous reported studies. The reason behind that high mobility is the high quality of the structure with very low interface roughness, as proven by TEM for all the structures as well as the high purity of the sGe channel, with less than 0.015 at % of Si in it, as seen by the uleSIMS depth profile. In addition, the low level of background impurities $< 1\times10^{16}$ cm^{-3}, as shown by SIMS and simulated to be 2×10^{14} cm^{-3}, which is comparable to the background impurities of 2.3×10^{14} cm^{-3} simulated to the highest sSi electron mobility revealed recently [82].

These inverted structure samples showed a pronounced resistivity anisotropy which was extracted by Hall measurement using Van der Pauw devices. The resistivity anisotropy is overestimated using Van der Pauw and it is better to extract using a Hall Bar, where possible, but the underlying mobility anisotropy can still be extracted from VdP data using a calculated correction to obtain the real anisotropy coefficient. The anisotropy coefficient was in order of 1.3 to 2 which is considerably high. The explanation for this anisotropy is found to be a result of substrate off-cut which is confirmed in high resolution TEM images.

Using the relaxation time approximation for isotropic remote impurity scattering, background impurity scattering and anisotropic interface roughness scattering, it was found that the difference in mobility could be modelled by varying the interface roughening scattering parameters between the two orientations. For the [110] and $[\bar{1}10]$ orientation, the interface roughness is mobility limiting, with approximately double the roughness height Δ and half the correlation length in $[\bar{1}10]$ orientation. Initial XTEM results appear to indicate this interface roughness variation is from a significant difference in off-cut angle between the [110] and $[\bar{1}10]$ orientations that arise from the starting (001) Si substrate.

5 Structural and electrical properties of strained Ge heterostructures doped above the channel

5.1 Introduction:

This chapter will focus on sGe quantum wells having a 'normal' structure, with doping placed above the channel to avoid doping segregation to the channel during epitaxial growth. Samples with different growth situations have been examined electrically using classical resistivity and Hall effect measurements as well as structurally with a range of characterization techniques such as TEM, XRD, SIMS and AFM. The electrical properties of these samples will be shown to depend strongly on the growth conditions. Most effort is devoted to sample 11-289 that, as will be seen in section 5.4, has the highest hole mobility reported to date.

5.2 Structural characterization of normal structures

5.2.1 XRD analysis for normal structure sGe/SiGe:

The composition and macroscopic degree of relaxation of all the layers were determined using a Phillips PW1835 HR-XRD. The out-of-plane and in-plane lattice constants for all layers were obtained from RSMs taken around the symmetric (004) and asymmetric (224) reciprocal lattice points, which is shown in Figure 5.1 for sample 11-289. The RSM shows five well-defined peaks which correspond to the Si substrate, the relaxed Ge layer at the bottom of the buffer, the thick relaxed $Si_{0.2}Ge_{0.8}$ buffer layer, the strained Ge channel, and the thin $Si_{0.2}Ge_{0.8}$ layers above the channel. The two distinguishable peaks around the $Si_{0.2}Ge_{0.8}$ layer region arise because the Ge composition in the layers above the channel was slightly higher (0.82) than the layer at the top of the high temperature buffer (0.79).

The region of the RSM between the relaxed Ge and the $Si_{0.2}Ge_{0.8}$ peaks corresponds to the graded region of the buffer. Analysis of the RSMs indicated that the buffer was slightly over relaxed (i.e. under tensile strain) with respect to the Si substrate. This is typical of reverse-graded buffers and is due to the differential contraction of Si and Ge when cooled down from the elevated growth temperature [70]. The strained Ge layer was determined to be fully strained with respect to the underlying $Si_{0.2}Ge_{0.8}$ buffer, equivalent to 0.65% lattice mismatch. This is lower than the expected value of 0.84% if the $Si_{0.2}Ge_{0.8}$ buffer was not under tensile strain. Finally, the thickness of the channel was ascertained to be 20±1 nm from the thickness fringes observed in (004) ω-2θ rocking curves.

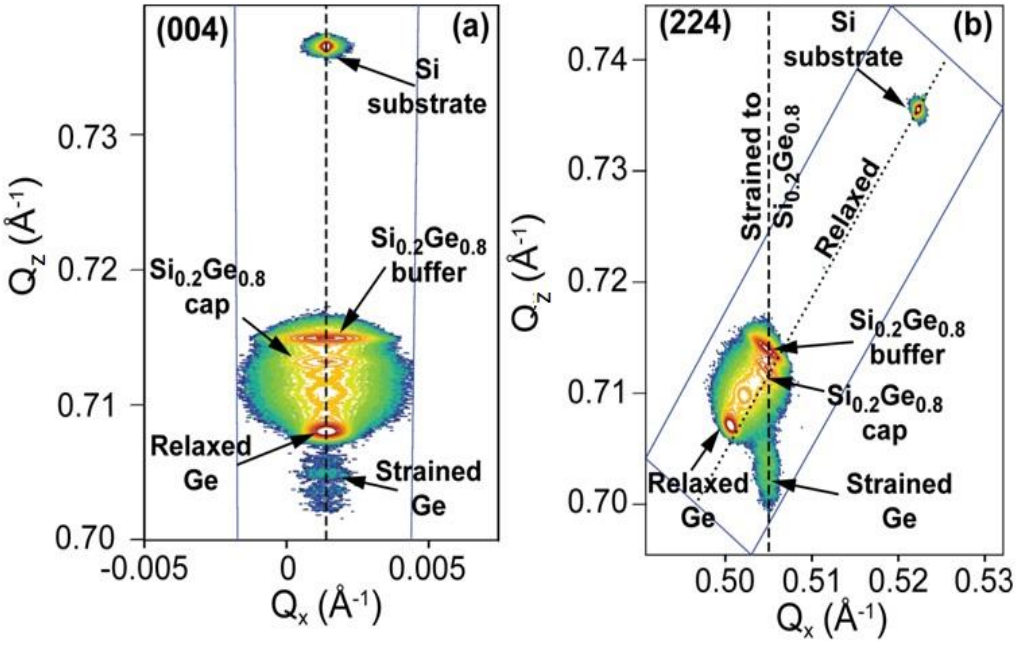

Figure 5.1 XRD for normal structure (a) (004) symmetric reflection (b) (224) asymmetric reflection. Peak intensity in the RSMs is colour coded on an arbitrary scale, with red as most intense.

5.2.2 TEM analysis for sGe/SiGe normal structures:

The structures were viewed along the (110) planes in cross sectional TEM (XTEM) using a JEOL2100fx TEM microscope by Richard Beanland in the Microscopy Group at the University of Warwick. The sample under investigation is 11-289 which has the highest mobility compared to all other samples in this study.

Figure 5.2 shows a bright field (004) image of the active region for a piece of sample from the edge of the wafer. Layers thicknesses were measured from Figure 5.2, starting from the lowest part, as: distance from growth interruption to the channel is 61±2 nm; channel thickness 20±1 nm, undoped spacer 26±1 nm, doping layer 13±1 nm (from SIMS), SiGe cap 35±1 nm, and finally Si cap 2±0.5 nm. The full extent of the doped layer is not clear in the TEM, although the growth interrupt at the end of the doping can be seen.

Although we get high mobility from the centre of the wafer, the mobility was reduced significantly near the edge. The TEM image in Figure 5.3 shows a remarkable interface roughness near the channel that is most clearly illustrated in compressed image on the right. This may explain the drop in mobility, the curvature appear in the middle comes from virtual substrate. Another TEM picture was performed for a piece of the sample from near the centre part of the wafer and is presented in Figure 5.4, showing a smooth interface in the Ge channel.

Substrate off-cut has a significant role in the resistivity and mobility anisotropy of these samples, as illustrated in the previous chapter for the inverted structures. HRTEM confirmed a 1º off-cut in the wafer towards the $[\bar{1}10]$ direction. For the sample 11-289 (normal structure) Figure 5.5 presents substrate off-cut of 0.1˚ in $[110]$ orientation, while it is again 0.9˚ in the $[\bar{1}10]$ orientation.

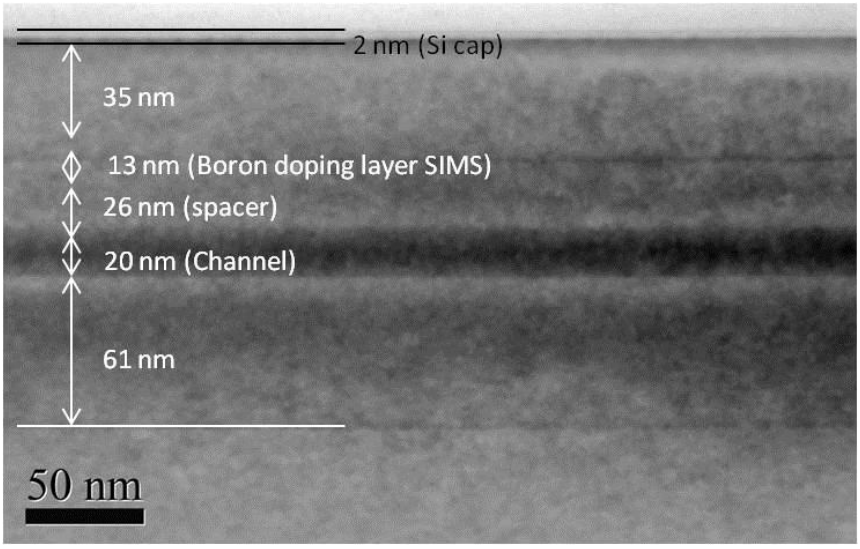

Figure 5.2 XTEM images bright field (004) for the active region of the sample 11-289 from the edge of the wafer.

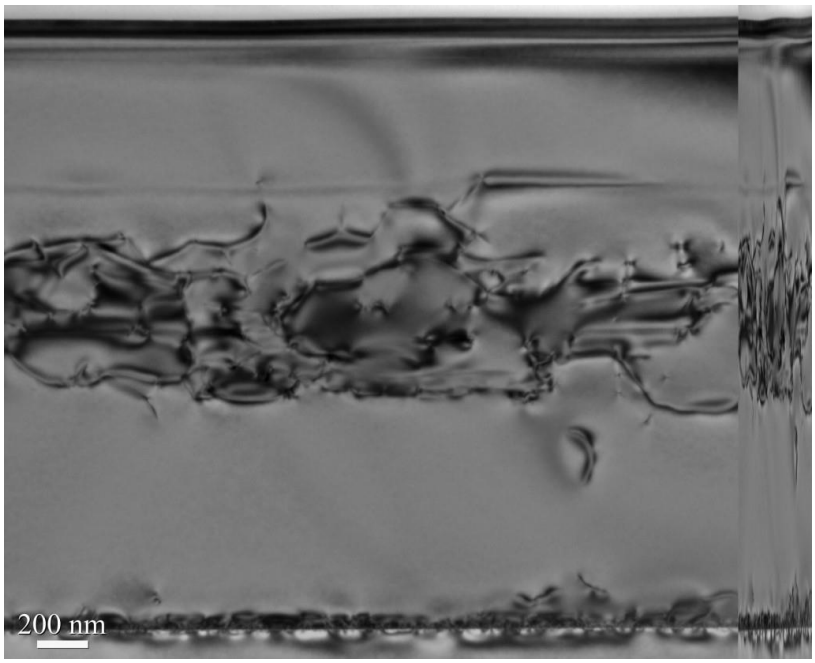

Figure 5.3 XTEM image bright field (004) for the sample 11-289 from the edge of the wafer shows pronounced interface roughness.

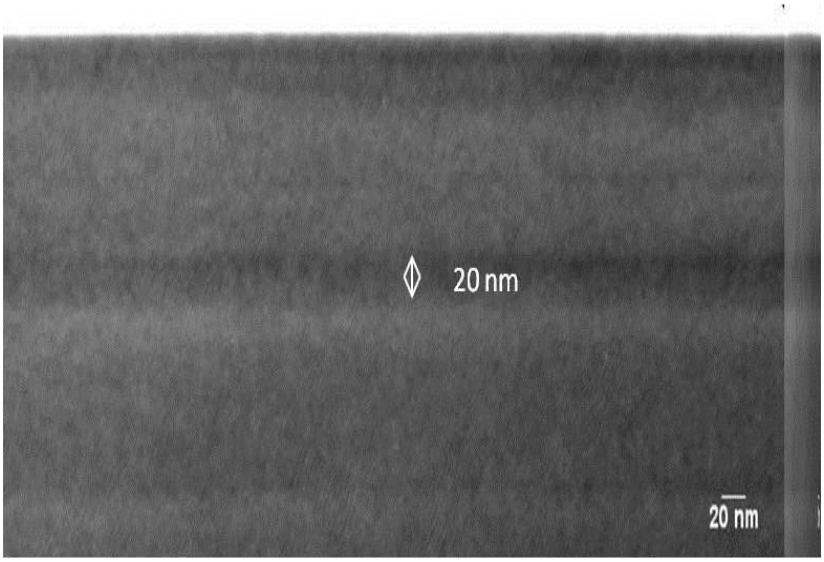

Figure 5.4 XTEM image bright field (004) from a near centre part of the sample 11-289.

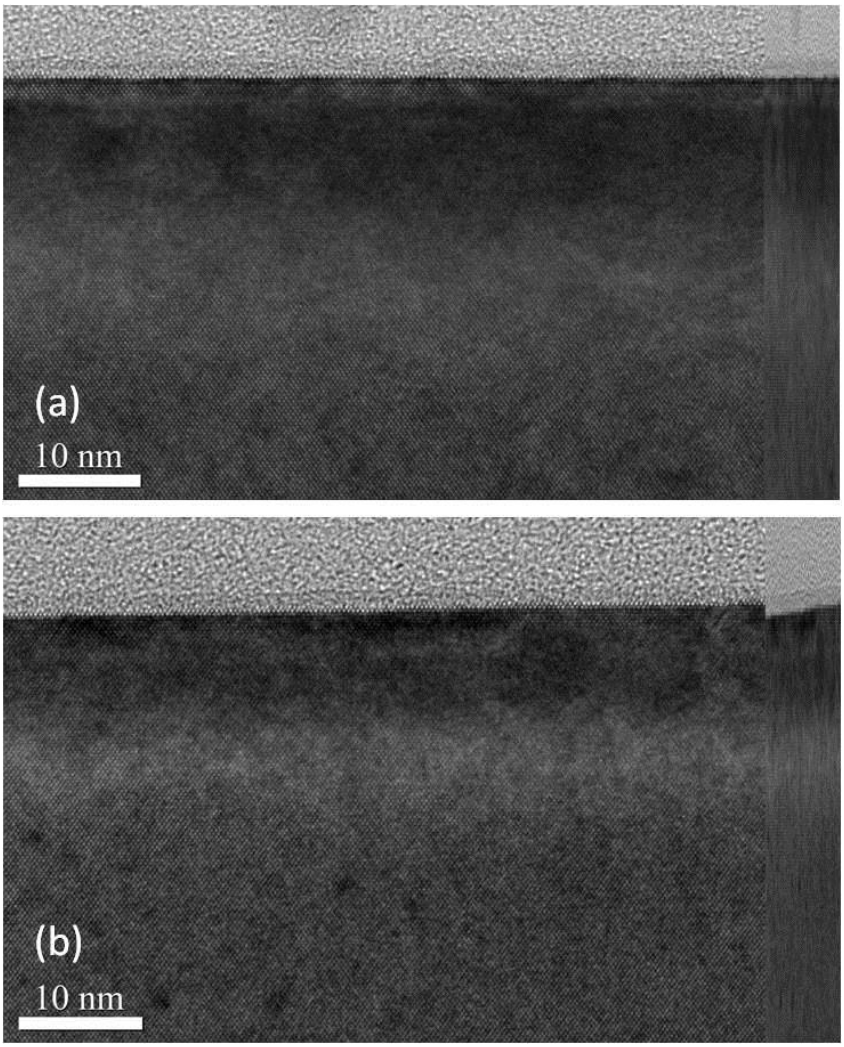

Figure 5.5 HREM of the sample 11-289 in perpendicular orientations to show substrate off cut.

5.2.3 uleSIMS analysis for normal structure sGe/SiGe:

SIMS depth profiles using a near normal incidence O_2^+ primary beam at 250 eV, has previously been shown [74] to offer an accurate quantification of nanometre scale $Si_{1-x}Ge_x$/Ge heterostructures. The depths of the upper and lower interfaces of the supply layer were estimated from the full width half maximum (FWHM) values of the average boron concentration within this layer to give a supply layer thickness of around 13 nm. The spacer thickness was found to be 26±1 nm as the distance from the lower interface of the supply layer to the point where the Ge alloy concentration at the top of the channel reached 0.9.

Figure 5.6 also shows the Ge and Si depth profiles, which are in excellent agreement with the results obtained from HR-XRD experiments. The two peaks in the Ge signal observed at depths of 55 nm and 180 nm are real features and occur as a result of a brief interruption in the epitaxial growth for purge steps in order to change one or more growth parameters prior to deposition of a subsequent layer. The uleSIMS measurements also showed that the Si concentration in the centre of the strained Ge channel was less than 0.01 at. % Figure 5.7 and that both interfaces were abrupt. This confirmed that the low temperature epitaxy approach had achieved a high purity Ge channel and that there had not been significant Si-Ge inter-diffusion.

One of the issues associated with low temperature growth is the gas quality, since the oxygen and moisture contamination are critical for epilayers quality. For that reason SIMS profiles for oxygen, carbon, hydrogen and phosphorous were obtained, using a Cs^+ primary ion beam, to indicate their level of concentration in the structure. Figure 5.7 shows the oxygen level in 11-289 was lower than 1×10^{18} cm^{-3}, although a spike appears at each growth interruption that indicates some contamination in the chamber. However, the oxygen concentration of these spikes is not more than 6×10^{18} cm^{-3}. More details about the effect of oxygen contamination on the structure will be mentioned in section 5.3.

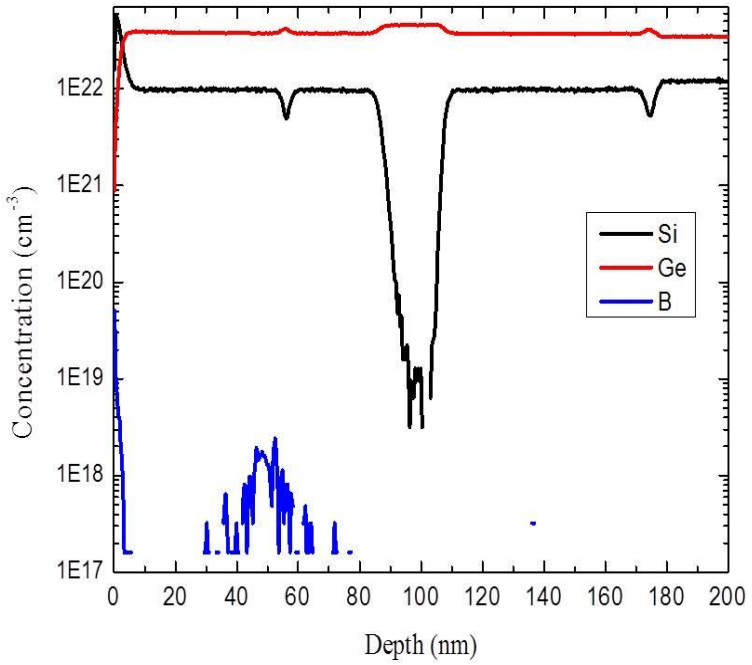

Figure 5.6 SIMS depth profile for Si, Ge and B from the normal structure (11-289) using an O_2^+ primary beam.

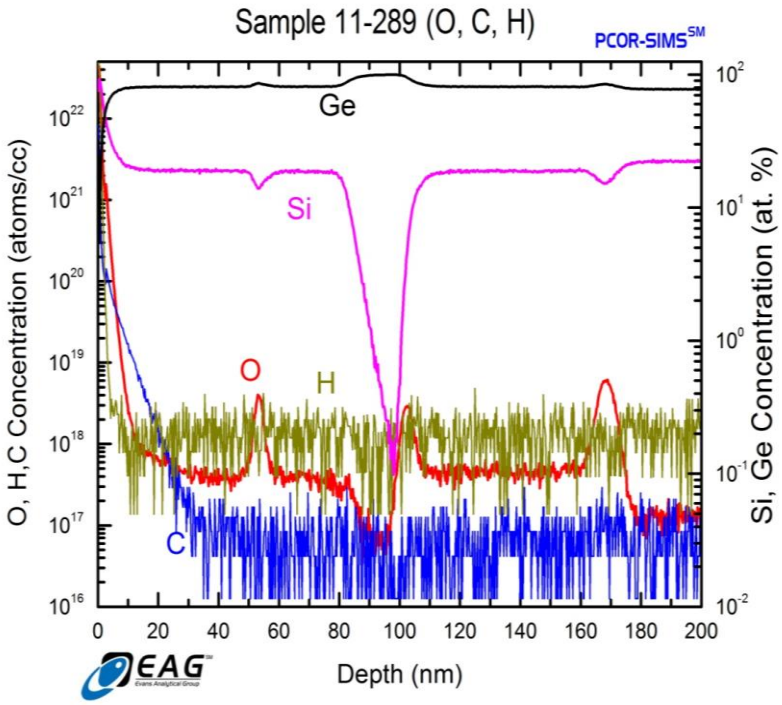

Figure 5.7 SIMS depth profile of Si, Ge, P, H, C, and O from the normal structure (11-289) using a Cs^+ primary ion beam

5.2.4 AFM analysis for normal structure

AFM was performed using contact-mode AFM and the results were digitally recorded and analysed using Digital Instruments' Nanoscope software with help from Stephen Rhead. The 50 μm x 50 μm AFM image (Figure 5.8) shows few defects, which means a very low threading dislocation density, and revealed an rms roughness value of 2.0±0.2 nm for this structure which is very low and confirms the high quality of the structure.

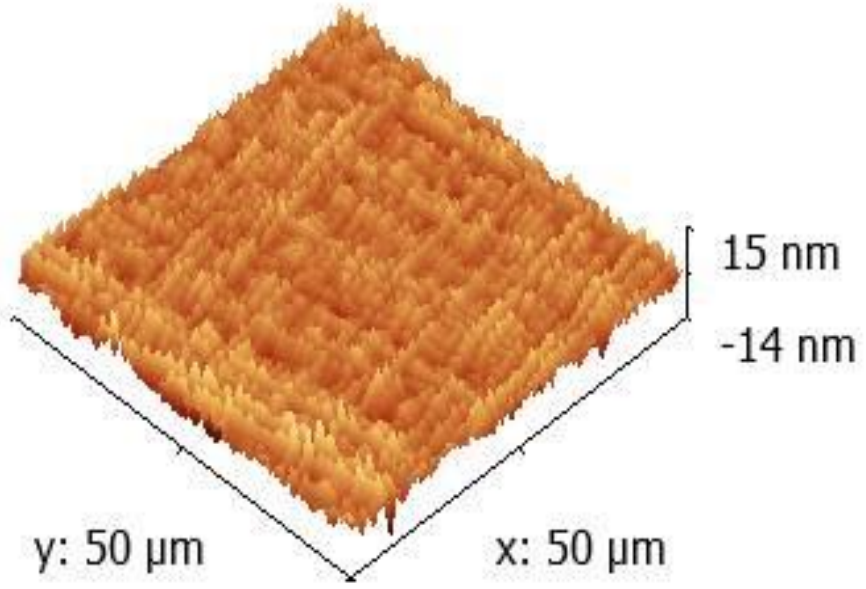

Figure 5.8 AFM image for the normal structure sample 11-289. (The large values on the z-axes in this image are an artefact due to tip being far away from the surface at the start of the measurement.)

5.3 Oxygen contamination effect on structural and electrical characterization:

Following the discovery of very high hole mobility in sample 11-289 a further batch of nominally similar samples (12-010 to 12-013) were grown with variation to the B-doping level and spacer layer thickness. However, as will be seen in section 5.4, the mobility dropped significantly below the level recorded in sample 11-289, so an intensive structural

investigation was made to find the reason. SIMS and XRD were performed to confirm the basic structure properties, such as thickness of the layers and strain, remained the same as sample 11-289. The SIMS profiles for 11-289 and 12-010 are overlaid in Figure 5.9, and similarly for the XRD rocking curve in Figure 5.10. (The RSM for 12-010 shown in Figure 5.11 can also be compared to Figure 5.1). These data clearly show that the two wafers are almost structurally identical, with similar crystalline quality. Therefore, differences in strain relaxation change in alloy composition, change in layer thickness, differences in the B supply layer doping, and B diffusion can all be ruled out as being responsible for any change in mobility.

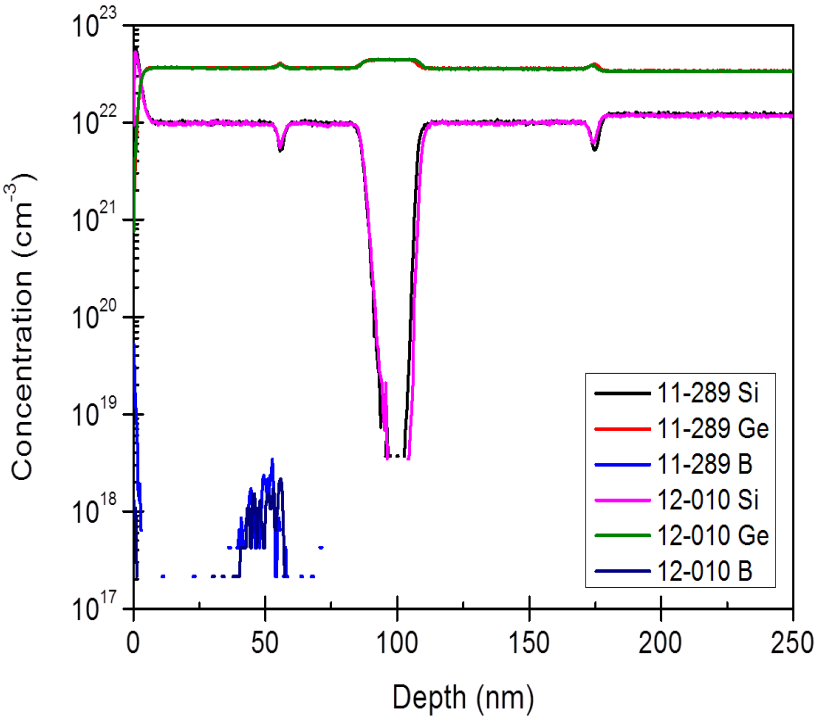

Figure 5.9 SIMS depth profile concentration from 12-010 and 11-289.

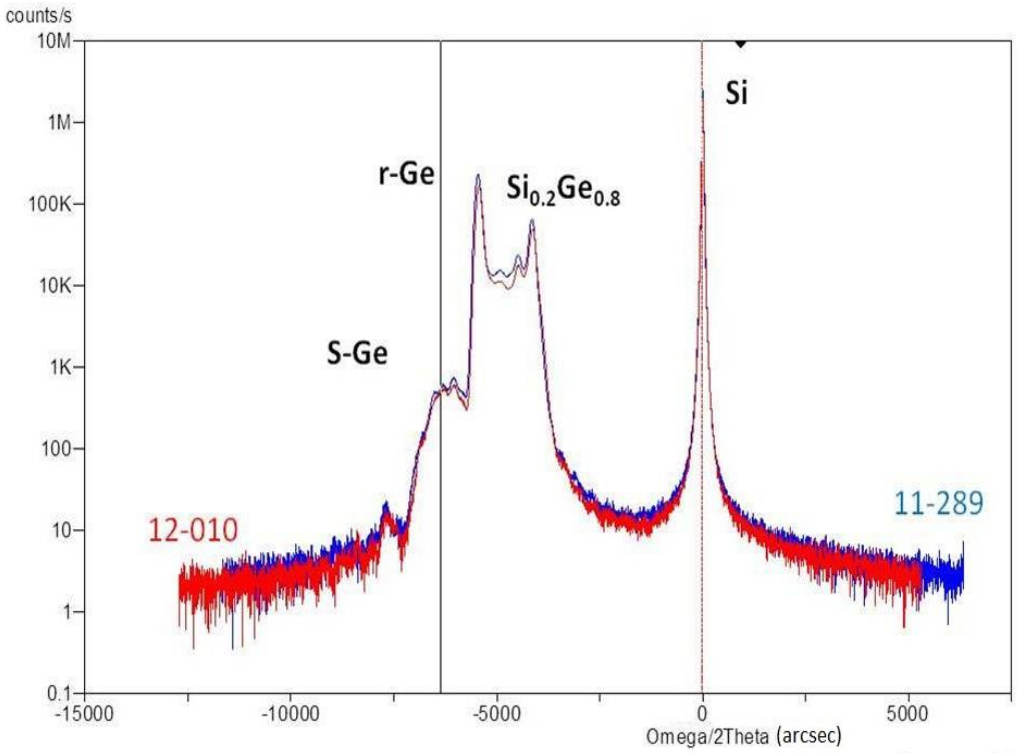

Figure 5.10 X-ray rocking curves for samples 11-289 and 12-010 indicating same lattice constant and strain

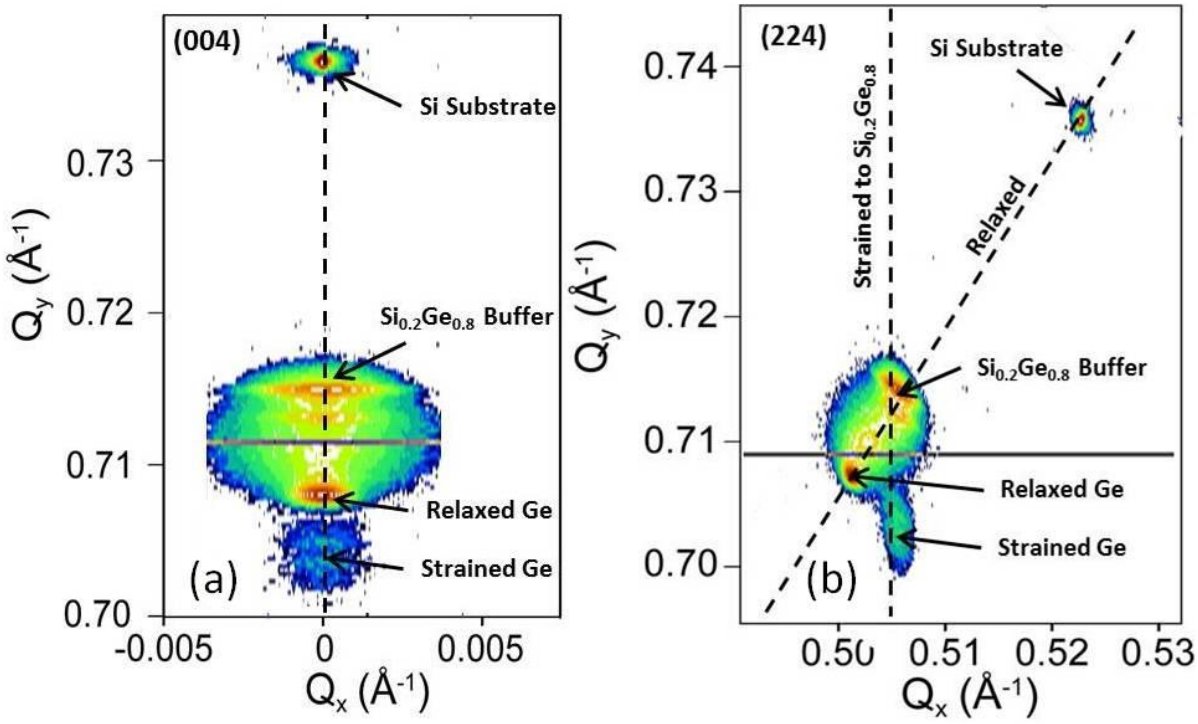

Figure 5.11 XRD 004 and 224 for the sample 12-010. Peak intensity in the RSMs is colour coded on an arbitrary scale, with red as most intense.

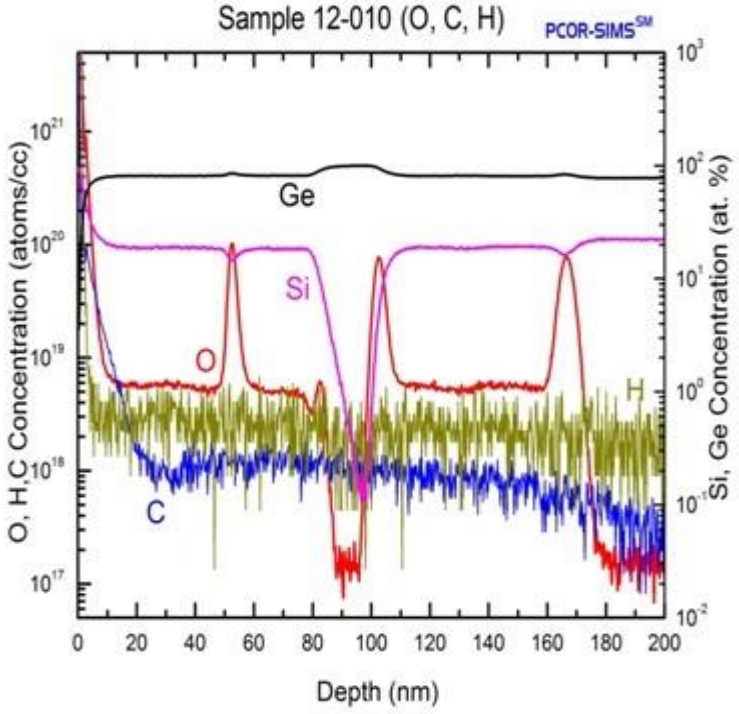

Figure 5.12 SIMS depth profile of Si, Ge, P, H, C, and O from the normal structure (12-010) using a Cs^+ primary ion beam.

A further detailed SIMS depth profile was performed to study oxygen, carbon and hydrogen concentration in sample 12-010, Figure 5.12. By contrast to sample 11-289, the SIMS profile for sample 12-010 shows a background oxygen content of more than 5×10^{18} cm^{-3}, and spikes at the growth interrupts reaching 10^{20} cm^{-3}. Also the C levels in the Si, SiGe and Ge layers are 1×10^{18} atoms/cc, which 10 times higher than its level in the sample 11-289, and hydrogen level is considerably higher about 5×10^{18} atoms/cc; however, these high concentrations that are seriously depressing the mobility do not appear to have a big effect on the layer structure. One last possible cause of mobility degradation is due to interface roughness that results from very small oxide islands that form when there is contamination from oxygen and/or water vapour, especially at low growth temperature. Reference [83] mentions that a low oxygen background, below 5×10^{16} cm^{-3}, is preferred and that above this level could cause interface

roughness. A theoretical simulation will be presented in section 5.8 to investigate the possibility of this suggestion.

For the other samples in this 12-01x batch, with different spacer thicknesses, only the in-house SIMS depth profile for Si, Ge and boron concentration were performed, as seen in Figure 5.13, Figure 5.14 and Figure 5.15. For sample 12-011 the average concentration of boron is 7.3×10^{17} cm^{-3}, the thickness of the Ge channel is 20±2 nm, the spacer thickness is 15±2 nm, and the doping layer width was 17±2 nm. The structure was capped with 31± 2 nm $Si_{0.2}Ge_{0.8}$ and 5±1 nm Si. Sample 12-012 had an average boron concentration of 5.9×10^{17} cm^{-3}. The spacer layer of 34±2 nm is 2.3 times larger than for the previous sample, while the doping layer thickness is almost the same at 15±2 nm. The channel thickness was 18±2 nm, which are a few nanometres less than sample 12-011. The last sample characterized by uleSIMS was Sample 12-013, for which the boron doping concentration was 5.4×10^{17} cm^{-3}, while the doping layer thickness was 17±2 nm. This sample has the highest spacer thickness which was 56±2 nm, and 20±2 nm was the width of the channel as measured by SIMS. All this thickness values are presented in Table 5.1.

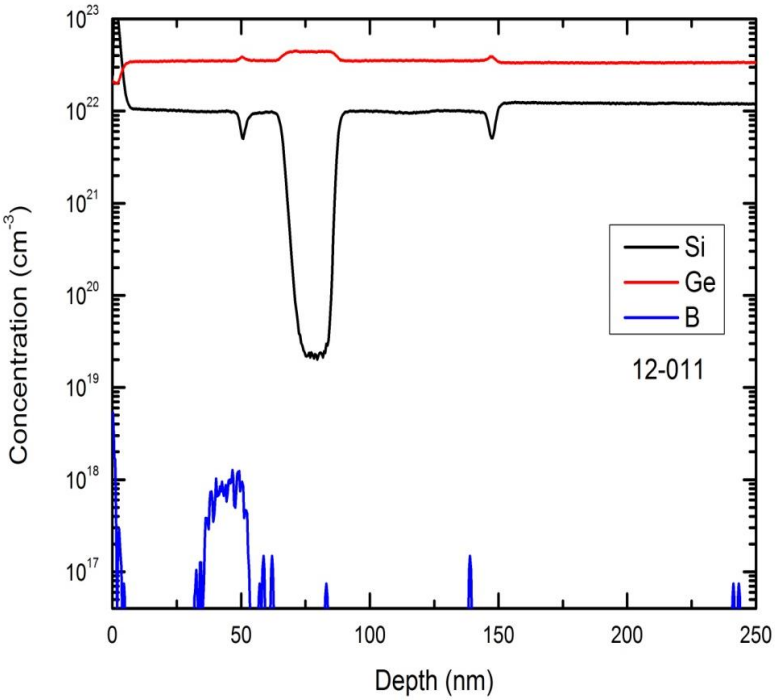

Figure 5.13 SIMS depth profile for Si, Ge and B from the normal structure (12-011) using an O_2^+ primary beam.

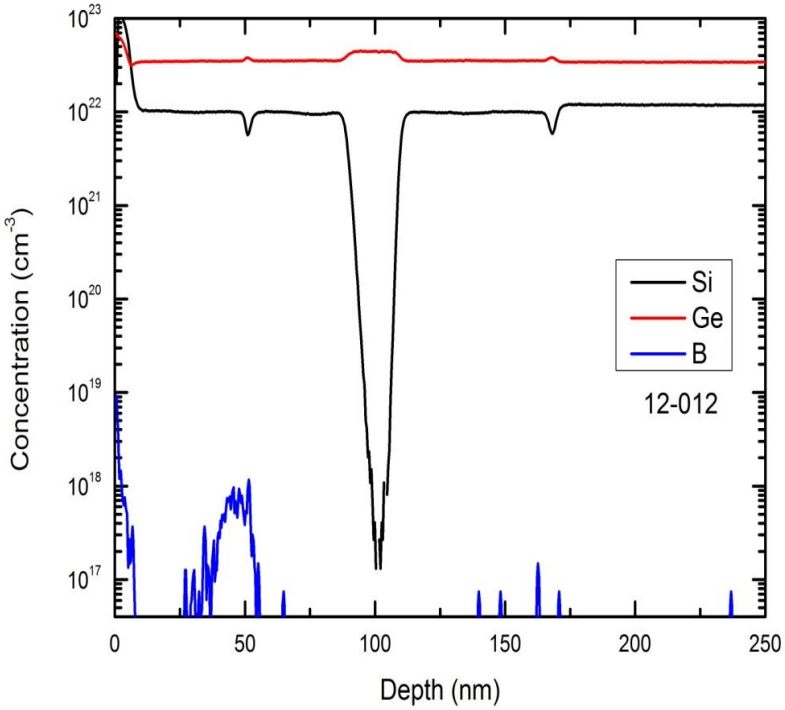

Figure 5.14 SIMS depth profile for Si, Ge and B from the normal structure (12-012) using an O_2^+ primary beam.

Sample	Doping ($\times 10^{18} cm^{-3}$)	Doping layer (nm)	Ge channel (±2nm)	Spacer layer (nm)
11-289	1.4	13±1	20	26±1
12-010	1.2	14±2	21	27±1
12-011	0.73	17±2	20	15±2
12-012	0.59	15±2	18	34±2
12-013	0.54	17±2	20	56±2

Table 5.1 Normal structure samples parameters extracted from SIMS depth profile

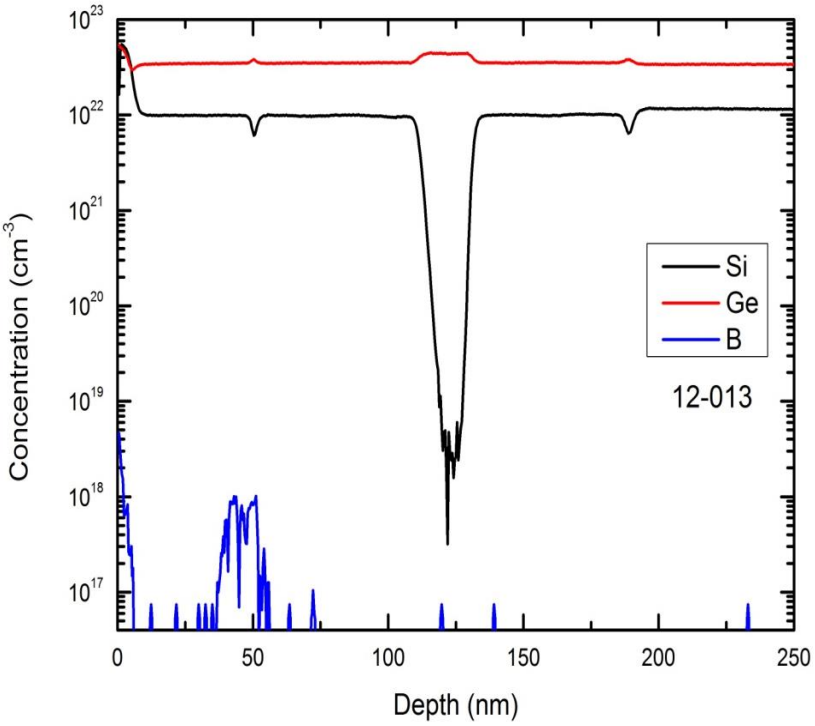

Figure 5.15 SIMS depth profile for Si, Ge and B from the normal structure (12-013) using an O_2^+ primary beam.

5.4 Electrical characterization of normal structure sGe QWs

The highest hole mobility recorded in the literature was obtained from sample 11-289 [84] and so it receives most attention in this study. Resistivity and Hall effect measurements were performed using a lock-in amplifier operating at a frequency of 13 Hz for each sample with a normal structure at temperatures from 12 K to 300 K. Three different kinds of device were used: square Van der Pauw with InGa contacts, VdP with Al contacts, and Hall bars (for sample 11-289 only). All the measurements were performed in the dark with excitation currents between 0.2 and 2μA applied along the devices, in both forward and reverse perpendicular magnetic fields with the field of 200 mT and 600 mT.

For sample 11-289 at the low sheet density of 2.60×10^{11} cm^{-2}, an extremely high hole mobility of 9.62×10^{5} $cm^2/V\,s$ was observed at 10 K, for the VdP device with InGa contacts (Figure 5.16). The resistivity and Hall coefficients were 25 Ω/sq and 2400 m^2/C, respectively, at the lowest temperature. It might be expected that even at low temperature this kind of device would have a high contribution of parallel conduction layers, but the saturation behaviour of mobility and sheet density below 40 K confirms the behaviour as that of carriers in a quantum well and shows the other parallel conducting layers must be frozen out. However, above 50 K there is a rapid increase in carrier density of two orders of magnitude, which is due to parallel conduction and is accompanied by a decrease in mobility.

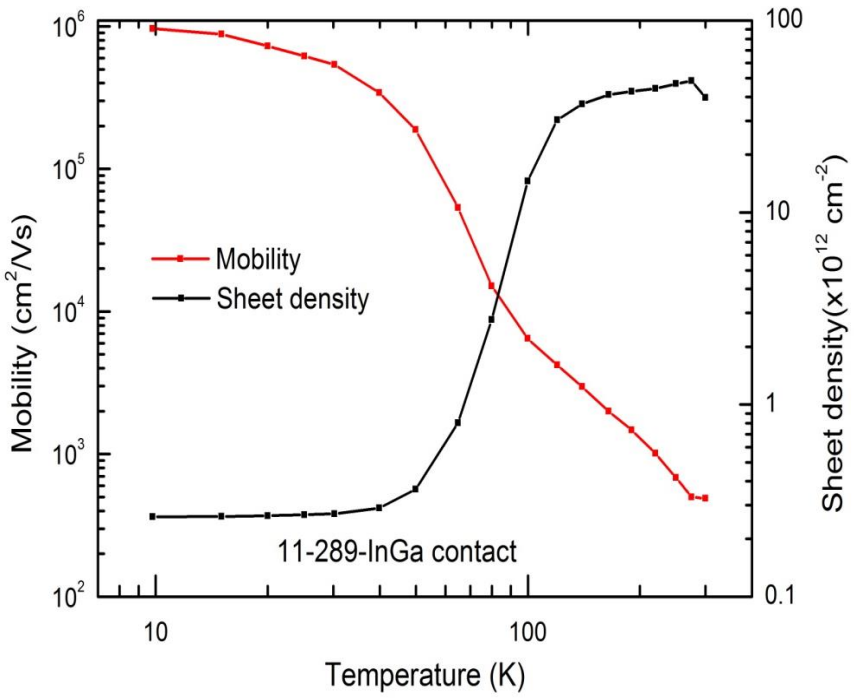

Figure 5.16 Mobility and sheet density as function of temperature for sample 11-289, measured on a Van der Pauw square with InGa contacts

Next, a Van der Pauw square with Al contacts was fabricated as mentioned in chapter 3 and used to measure the resistivity and Hall mobility. The result was more optimistic with a higher mobility of 1.14×10^{6} cm^2/V s at a carrier sheet density of 3.00×10^{11} cm^{-2} at 12 K, as shown in Figure 5.17. This hole mobility is nearly an order of magnitude higher than any previously reported [2, 64, 85], such as the 120,000 cm^2/Vs reported by Isella *et al.* [17] for a Ge hole gas of density 8×10^{11} cm^{-2}. From the structural analysis of the material and mobility modelling based on the relaxation time approximation (see below), we attribute this result to the combination of a high purity Ge channel and a very low background impurity level that is achieved from the reduced-pressure chemical vapour deposition growth method.

In general (see section 2.2 and the simulations below) the low temperature mobility peak occurs at the point where the contributions balance from background impurities, for which

the mobility increases with carrier density due to improved screening, and remote impurity or interface roughness scattering for which the mobility reduces as the carrier density increases due to the larger Fermi wave-vector. By reducing the background impurity levels it has been possible to push the mobility peak to lower hole density in these samples than for the material grown by LEPE-CVD and hence increase the peak mobility value [8, 20, 64]. It is also notable that this mobility exceeds the psychologically important threshold of one million cm^2/Vs. In GaAs based heterostructures this was the point where electron correlation effects such as the fractional quantum Hall effect started to be seen in the 1980's [86].

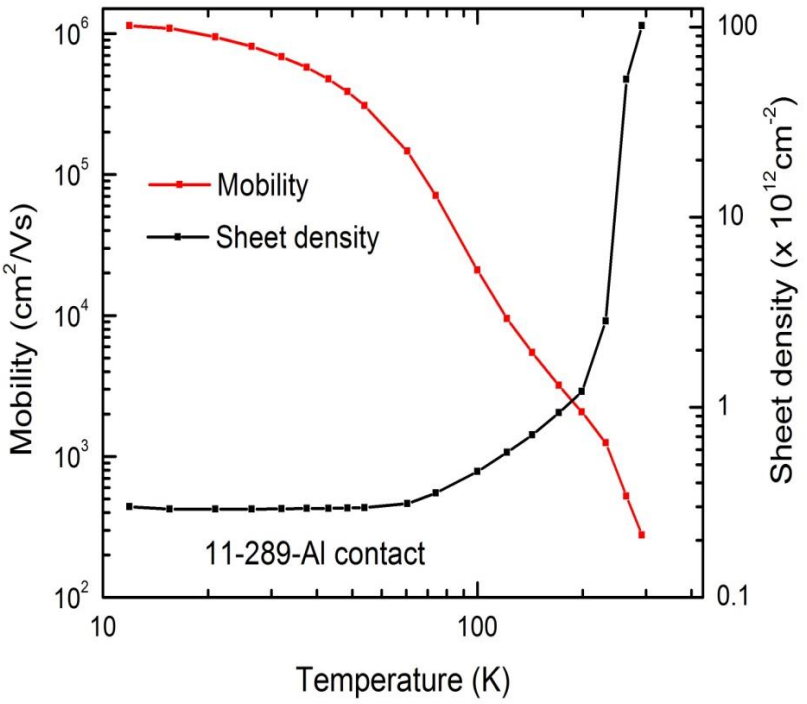

Figure 5.17 Mobility and sheet density as function of temperature for Van der Pauw square with Al contact.

Finally, low-field Hall effect measurements were carried out using a Hall Bar with Al contacts and the measurements extended down to 4 K. Figure 5.18 presents a hole mobility of 1.27×10^6 $cm^2/V.s$ at a carrier sheet density of 2.83×10^{11} cm^{-2} at 4 K, while at 10 K it is 1.01×10^6 $cm^2/V.s$ at a carrier sheet density of 2.84×10^{11} cm^{-2} (consistent with the previous

device types). In this case, the mobility did not saturate, which means it could still increase by reducing the temperature further. The resistivity at 4K was 16.76 Ohm/sq and the Hall coefficient was 2207 m^2/C. The remarkable purity of the channel as observed by SIMS, with a Si concentration in the centre of the strained Ge channels was less than 0.01 at.%, the high quality of the structure seen by TEM imaging, as well as the low level of background impurities, such as oxygen and carbon, all account for the extremely high hole mobility of sample 11-289.

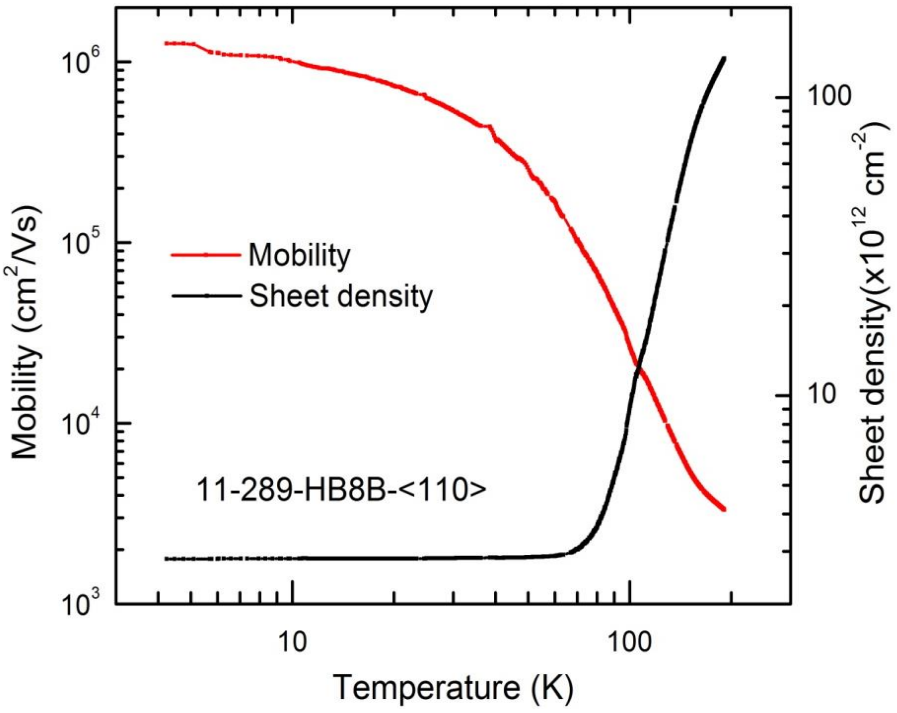

Figure 5.18 Mobility and sheet density as function of temperature for Hall bar in [110] orientation of the sample 11-289.

The Hall mobility and carrier sheet density of the 2DHG in the strained Ge channel was also determined for four more samples with different spacer thicknesses. Mobilities for samples 12-010, 12-011, 12-012, and 12-013 were 2.12 - 3.27×10^4 cm^2/Vs at sheet densities of 1.90 -

5.87 $\times 10^{11}$ cm^{-2} as shown in Figure 5.19 to Figure 5.22. All the results are summarised in Table 5.2

The first sample was 12-010 that was planned to be same as sample 11-289 with the same structure parameters. However, the high levels of O and C accounted for a mobility that is 33 times lower than for sample 11-289, even with the same strain and structure parameters. It is clear from the other samples that by increasing the spacer thickness the sheet density is reduced; the lowest sheet density of 1.90×10^{11} cm^{-2} is reached at a spacer thickness of 56±2 nm. The hole mobility peaked at 3.27×10^{4} cm^2/Vs at a sheet density of 2.62×10^{11} cm^{-2} for sample 12-012 at 12 K and reduced again for higher densities due to the effect of increased interface roughness scattering, as will be shown in the theoretical simulation in section 5.5.

Sample	Resistivity(Ω/sq)	R_H (m^2/C)	p_s ($\times10^{11}cm^{-2}$)	Mobility ($\times10^4$ cm^2/Vs)
12-010	612	1852	3.65	2.79
12-011	502	1153	5.87	2.12
12-012	729	2586	2.62	3.27
12-013	1087	3556	1.90	3.02
11-289	22	2400	2.60	96.2

Table 5.2 Resistivity and Hall measurement results for normal structure with high O and C level measured from VdP squares with InGa contacts, including values for 11-289 from a similar VdP device.

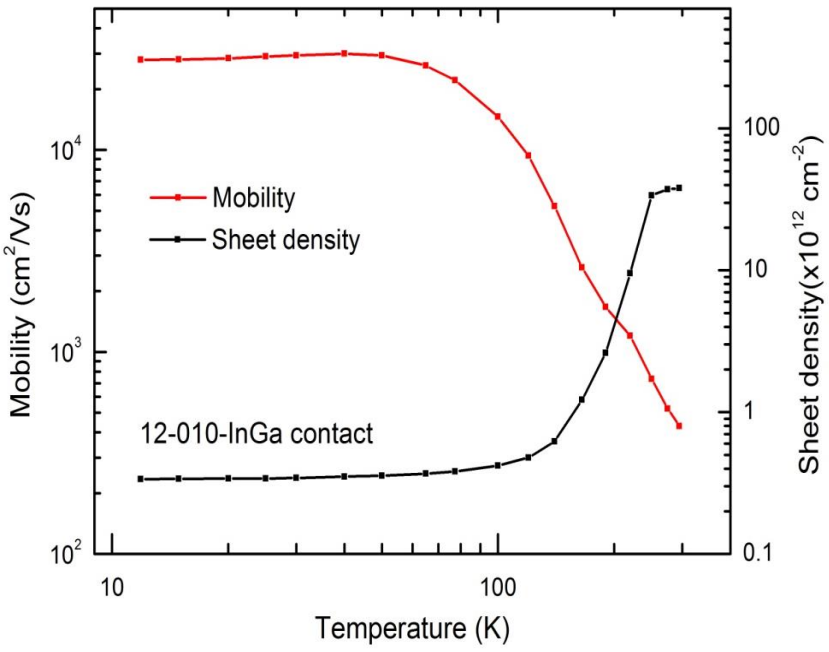

Figure 5.19 Mobility and sheet density as function of temperature for Van der Pauw square with InGa contact sample 12-010.

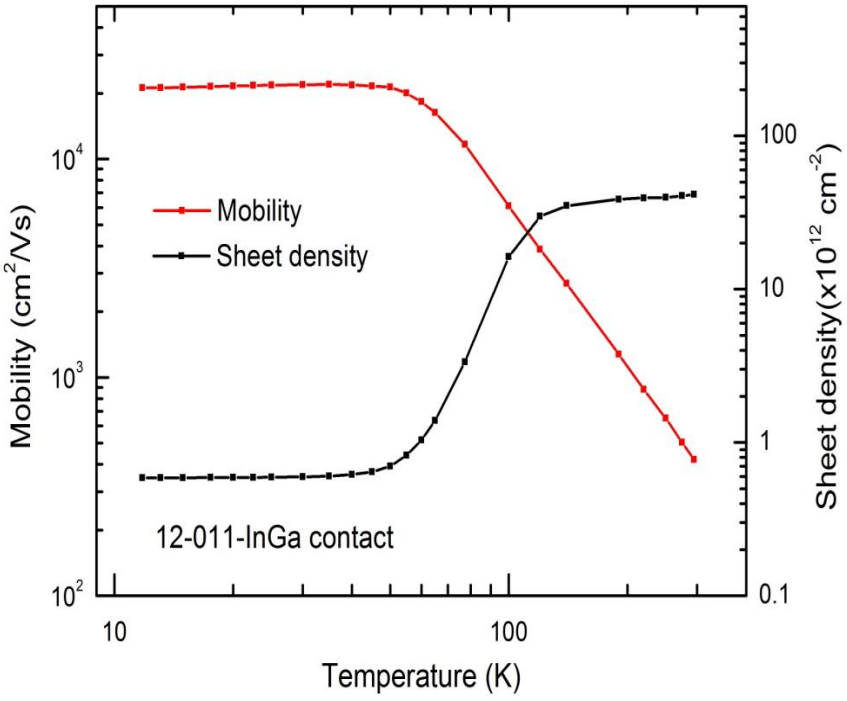

Figure 5.20 Mobility and sheet density as function of temperature for Van der Pauw square with InGa contact sample 12-011

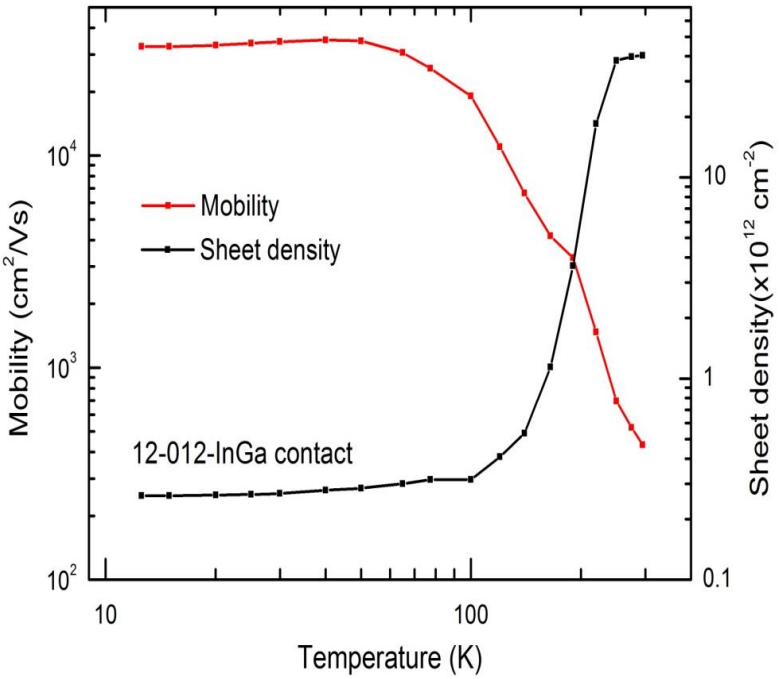

Figure 5.21 Mobility and sheet density as function of temperature for Van der Pauw square with InGa contact sample 12-012

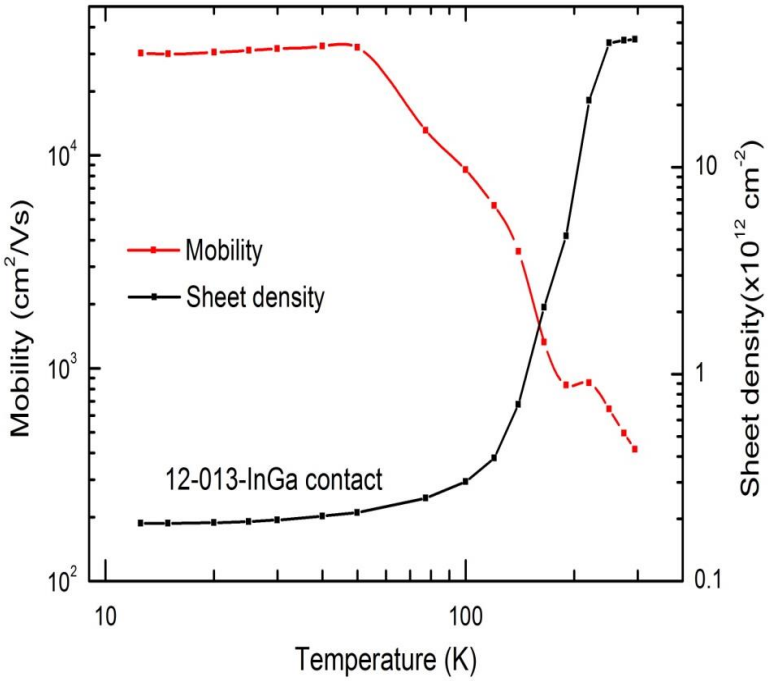

Figure 5.22 Mobility and sheet density as function of temperature for Van der Pauw square with InGa contact sample 12-013

5.5 Anisotropy study of normal structures:

The anisotropy ratio (*A*) for sample 11-289 was 1.02 which is significantly lower than for the inverted structures. The reason for this may be the much lower sheet density of 3×10^{11} cm^{-2} at low temperature. Figure 5.23 shows the behaviour of the anisotropy ratio with sheet density of the entire strained Ge sample. It clearly shows that the anisotropy ratio increases with increasing sheet density for samples that have similar channel thicknesses and growth temperature.

The mobility difference between the two orientations [110] (labelled 90DEG) and $[\bar{1}10]$ (labelled 0DEG) increased significantly as the temperature was reduced for the inverted structure samples. However, for this normal structure there is essentially no anisotropy at any temperature, as illustrated in Figure 5.24. Resistivity as well shows no significant change in both orientations at temperature range 12 K to 300 K Figure 5.25.

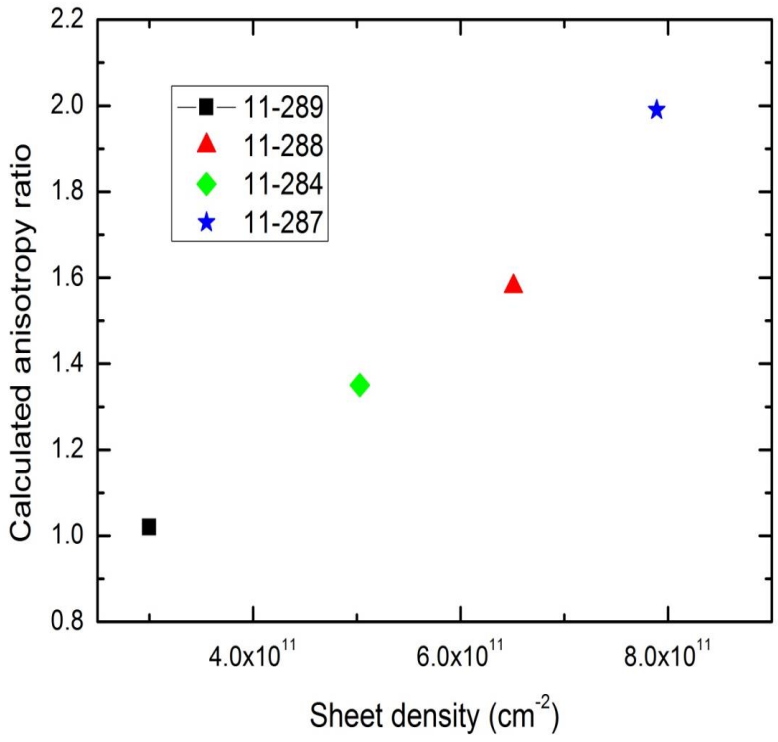

Figure 5.23 Anisotropy ratio for sGe quantum well as function of sheet density

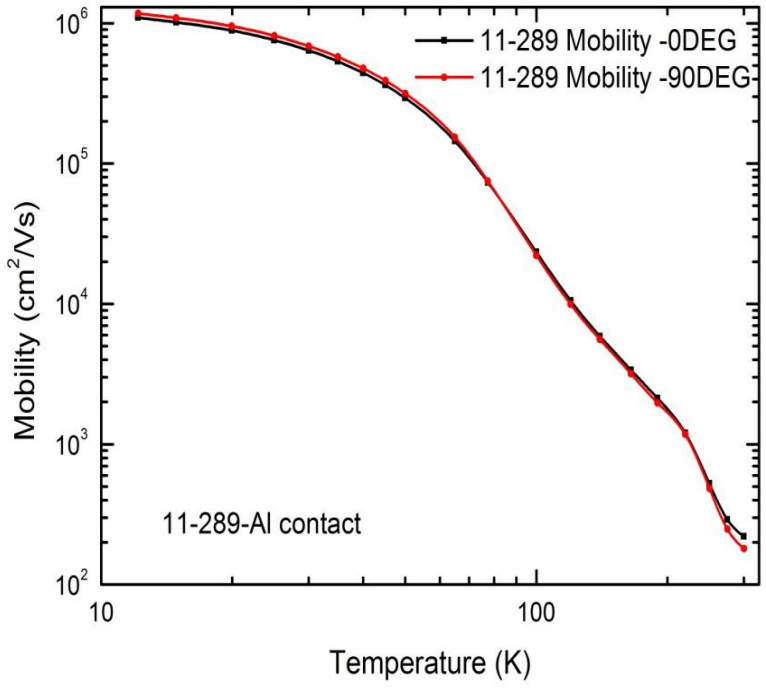

Figure 5.24 Mobility and sheet density as function of temperature for two orientation $[110]$ and $[\bar{1}10]$.

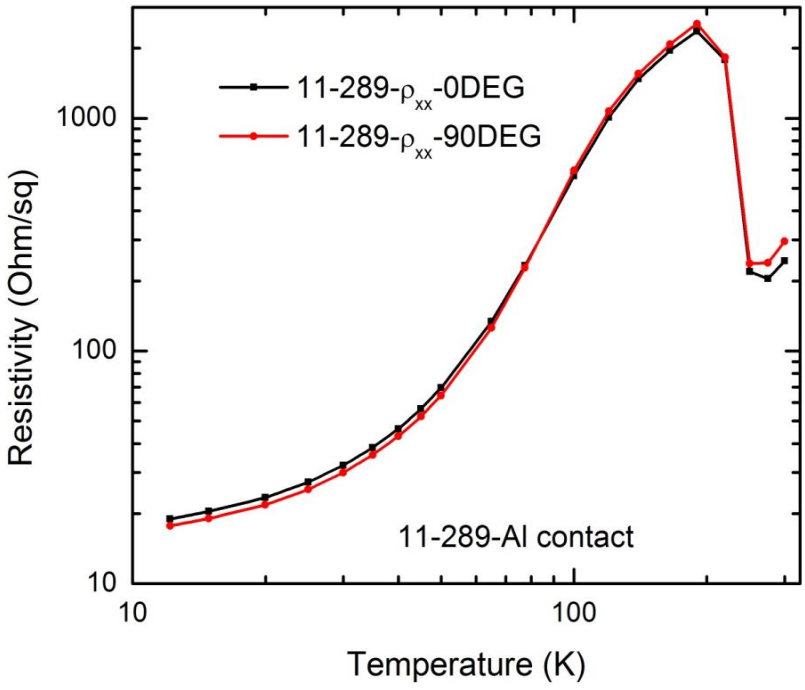

Figure 5.25 Resistivity and Hall coefficient as function of temperature for two orientation $[110]$ and $[\bar{1}10]$.

5.6 Scattering simulation of normal structure:

Following the same procedure as described in section 4.4 for the inverted structures, the mobility has been matched to a simulation that accounts for background and remote impurities together with interface roughness. Unfortunately, there was just one sample available as a normal structure with low O and C concentration, which means the fitting cannot be fully constrained. However, interface roughness could be excluded, due to the high quality structure that is seen in the XTEM images, and remote impurity scattering can be simulated using the boron density and spacer thickness measured by SIMS, so the only free parameter remaining is the background impurity density. The mobility simulation at low temperature is illustrated in Figure 5.26 (a) which shows the measured mobility close to the sweet spot where background and remote impurity limited scattering cross. If interface roughness is included in the simulation (Figure 5.26 (b)) it shows almost no effect on the mobility with interface roughness parameter values extract as λ= 30 nm and Δ= 0.14 nm.

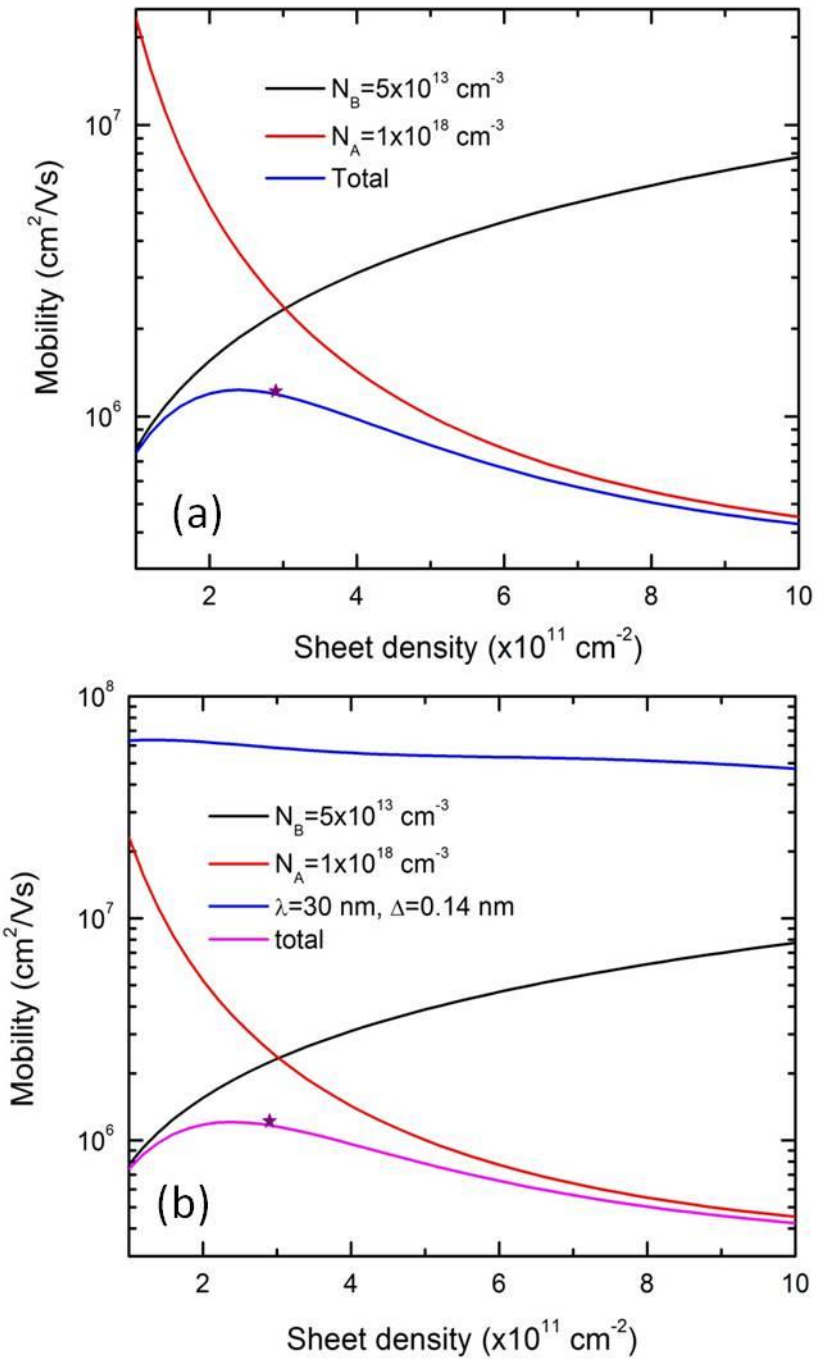

Figure 5.26 Scattering limited mobility simulation for 11-289 with low level of C and O, (a) with only impurity scattering and (b) with interface roughness included at a level where it does not reduce the overall mobility.

In the case of the lower mobility samples with high C and O levels, the drop in mobility towards the lowest hole density allows the background impurity to be fitted with a density of 2×10^{15} cm^{-3}, which is 4 times higher than in the previous simulation. The remote impurity density was taken as the average measured by SIMS and is similar magnitude to the previous simulation, but this time has negligible effect on the overall mobility. The fall-off in mobility towards higher hole density is now dominated by interface roughness and fitting the simulation to the experimental data gives a roughness height of 1.68 nm and period length of 4 nm. The simulation in Figure 5.27 generally provides a good fit to the experimental data (presented as stars) and shows that the mobility is limited by background impurities up to a sheet density of 3×10^{11} cm^{-2}, and as the sheet density increases interface roughness has a higher impact than other scattering.

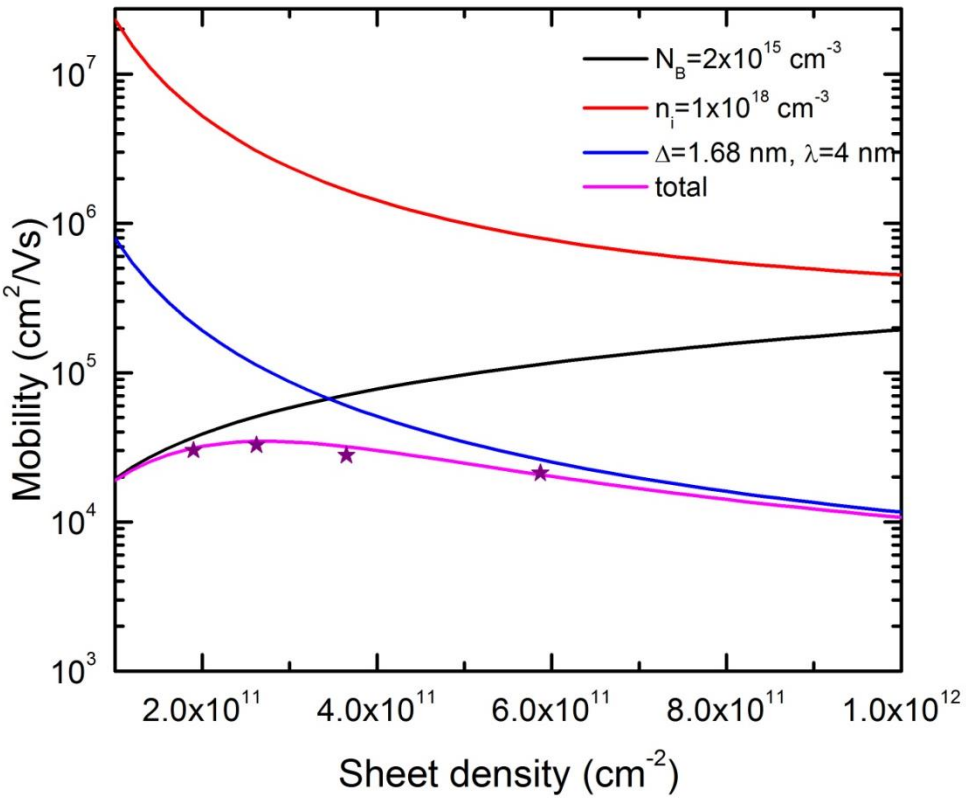

Figure 5.27 Scattering limited mobility simulation for normal structure with high level of carbon and oxygen.

5.7 Nextnano^3 simulations of the valence-band edge and hole concentration for normal structure:

This section presents a Nextnano^3 simulation for the valance band edge and hole concentration in the normal structure (11-289), using the effective mass approximation. The simulation was carried out for this sample at different temperatures with average doping concentration of 1.4×10^{18} cm^{-3}, doping distributed as illustrated by uleSIMS in doping layer ,while it is assumed to be just 3×10^{18} cm^{-3} in Si cap that is lower than the value presented in SIMS image (5×10^{19} cm^{-3}), and Ge concentration of 0.79 applied for all SiGe layers. Figure 5.28 and Figure 5.29 represent the heavy hole band edge and the hole concentration of sample 11-289 at 4 K and 50 K, respectively. In each case, carriers in the parallel conduction layers are frozen out and only the hole concentration in the quantum well is presented in the figures. The sheet density at each temperature calculated using this simulation is illustrated in Table 5.3. At 50 K the simulated sheet density by Nextnano^3 is 10% lower than the measured sheet density. This might be due to a small difference in Ge concentration in the SiGe alloy layers, which would lead to a different valance band offset and hence a different sheet density. However, at higher temperatures there is a significant difference between the simulated and experimental values of sheet density, which is due to the presence of carriers in the parallel conducting layers and will be discussed in the next section.

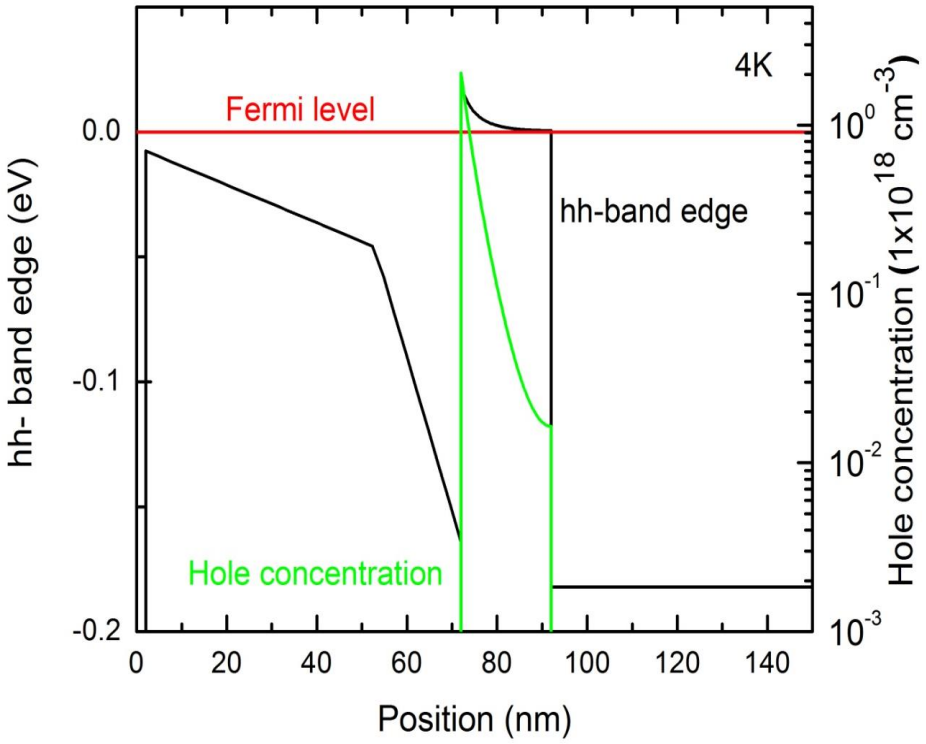

Figure 5.28 Heavy hole band edge simulation for the sample 11-289 using nextnano[3]

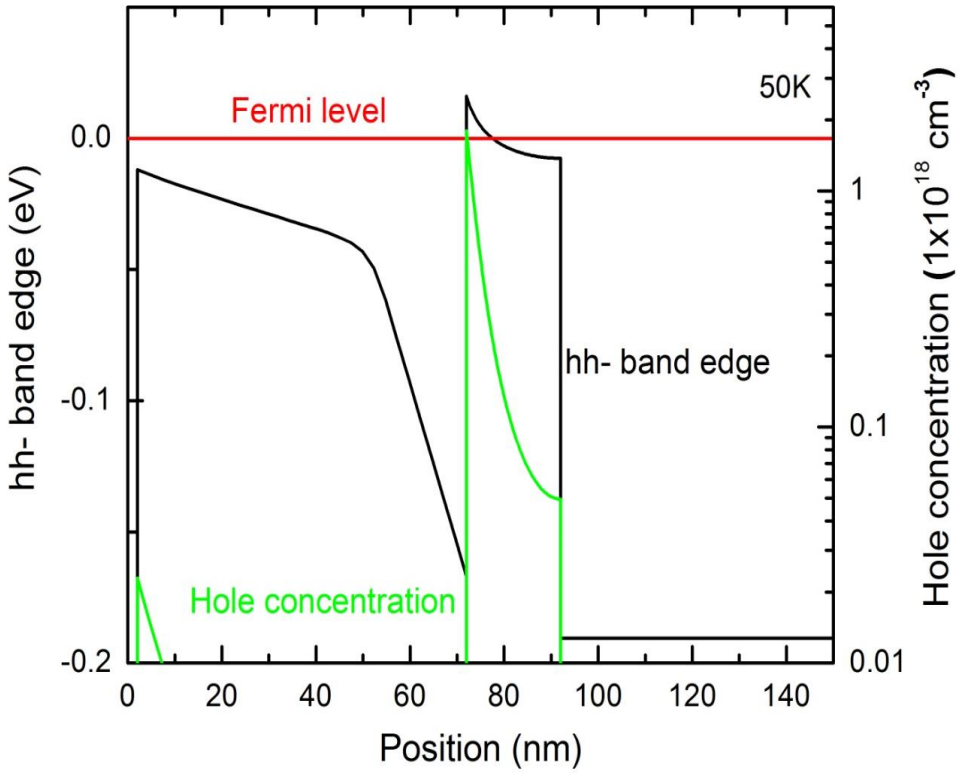

Figure 5.29 Nextnano3 simulation for normal configuration at 50K

5.8 Room temperature mobility and sheet density extraction and simulations:

Hole mobilities at room temperature (RT) have been studied for sample 11-289 using standard Van der Pauw resistivity and Hall effect measurements taken over a range of magnetic field and temperatures covering $-14\ \mathrm{T} < B < +14\ \mathrm{T}$ and $1.5\ \mathrm{K} < T < 300\ \mathrm{K}$, respectively, as shown in Figure 5.30. This high magnetic field range allowed the room temperature two dimensional hole gas mobility to be extracted from the total resistivity using maximum entropy-mobility spectrum analysis (ME-MSA)[66] and Bryan's algorithm mobility spectrum (BAMS) analysis [87]. Although data from Hall bars showed the highest mobility at 12 K for this sample, the ME-MSA and BAMS analysis had to be carried out using the square Van der Pauw sample because of the current leakage around the Hall bar mesa at higher temperature.

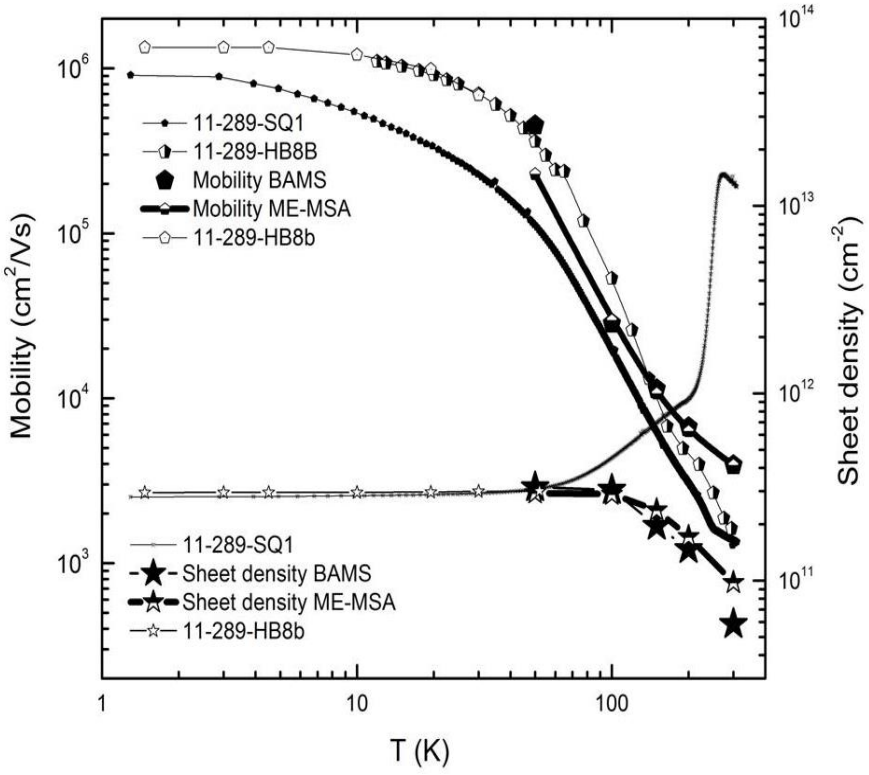

Figure 5.30 Hall mobility and carrier sheet density of the Van der Pauw square (11-289-SQ1) and the Hall Bar (11-289-HB8B). Samples compared to ME-MSA and BAMS results.

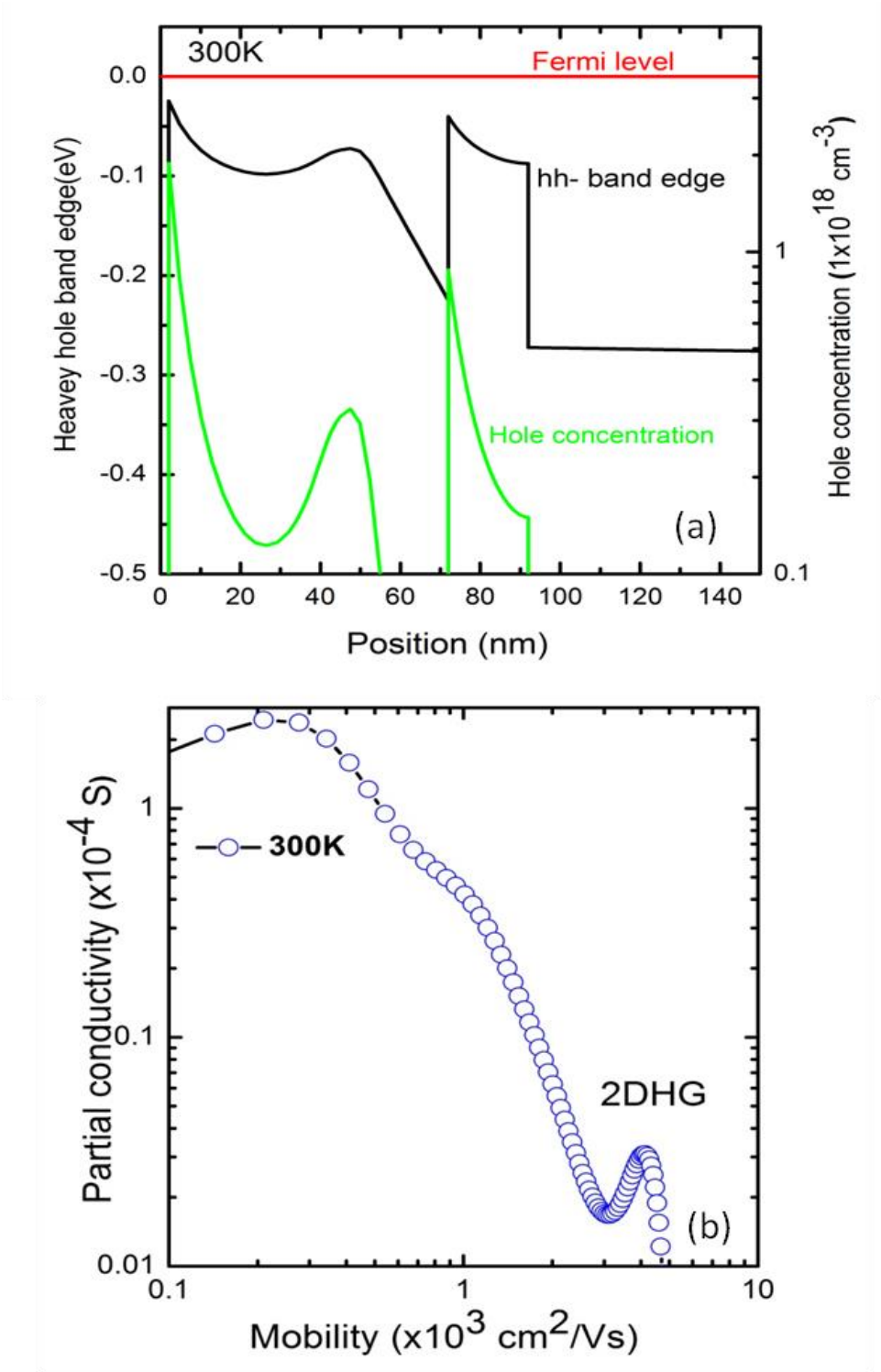

Figure 5.31 (a) Band edge and sheet density simulation at 300K for normal configuration, (b) ME-MSA simulation for normal structure (11-289-SQ1) at 300K.

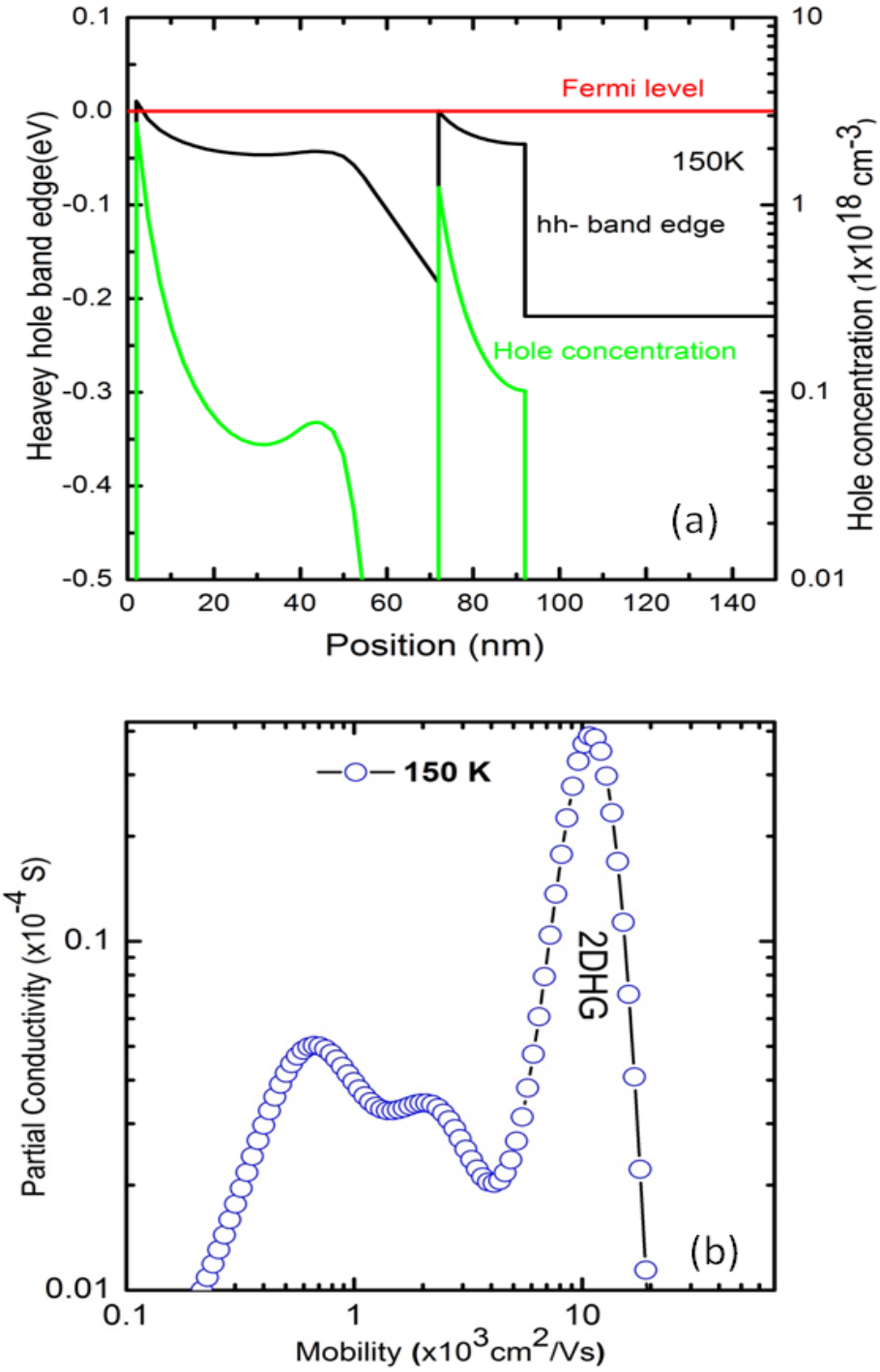

Figure 5.32 (a) Nextnano3 simulation for heavy hole band edge and sheet density at 150K. (b) ME-MSA simulation for mobility, conductivity and sheet density at 150K.

The raw Hall mobility measured for sample 11-289 at 300 K in this particular experiment was 1347 cm^2/Vs, while the combined layer sheet density (i.e. all conducting layers contributing to the mobility not just the carriers in the channel) was 1.27×10^{13} cm^{-2}. As at low temperature, this room temperature mobility is considerably higher than that measured for the inverted structures.

Using ME-MSA [88] the drift mobility and sheet density were extracted for the sGe channel from 50 K up to 300 K, in 50 K intervals. For each temperature a simulation was also made using Nextnano^3. Figure 5.31 and Figure 5.32 shows the results for 300 K and 150K respectively. Three hole mobility peaks are clearly visible for this structure. These peaks represent the hole concentration within the various layers which include the 2DHG Ge channel, the 13 nm B supply layer with an average doping concentration of 1.4×10^{18} cm^{-3} and holes in the 2 nm Si cap due to a boron spike at the surface, which are expected to have a much lower mobility. At 300 K, a ME-MSA mobility in the QW of $(3.9 \pm 0.4) \times10^3$ cm^2/Vs was determined with a hole density of 9.8×10^{10} cm^{-2}, which is the highest room temperature drift mobility published to date [4, 22, 62, 89-93]. However, given the low sheet density, the channel represents only 2-4% of the overall sample conductivity when all the parallel layers are considered. Moreover, this room temperature channel carrier density is lower than the measured Hall sheet density at low temperature where all parallel conduction is frozen out. A possible explanation is that at room temperature the Fermi level moves away from the Ge valence band as a result of strong ionization of the boron impurities [69, 85, 94], as seen in Figure 5.32 (a).

The 2 dimensional hole gas (2DHG) mobility in the sGe QW was also extracted from the magnetoresistance data (Figure 5.33 at 300 K and Figure 5.36 (a) at 100 K) using a different methodology, namely the Bryan's algorithm mobility spectrum (BAMS) technique. The room temperature mobility spectrum obtained from BAMS is shown in Figure 5.34 where again

three channels are identified and the channel mobility is once again determined to be almost 4000 $cm^2V^{-1}s^{-1}$. The carrier density is found to be lower using this technique (5.9×10^{10} cm^{-2}) and therefore the sample conduction at room temperature is again dominated by two low-mobility peaks with the channel only accounting for ~1%. In Figure 5.30 the line calculated from the mobility spectrum using both methods can be seen to agree very well with the square experimental data points.

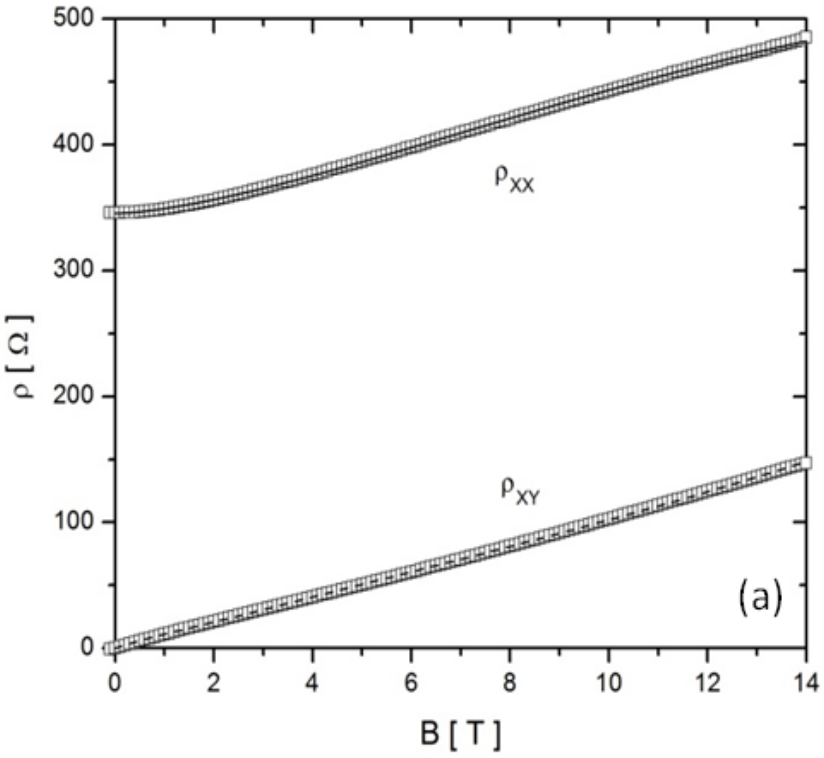

Figure 5.33 Magnetoresistance ρ_{xx} and Hall resistance R_{xy} at 300 K for 11-289.

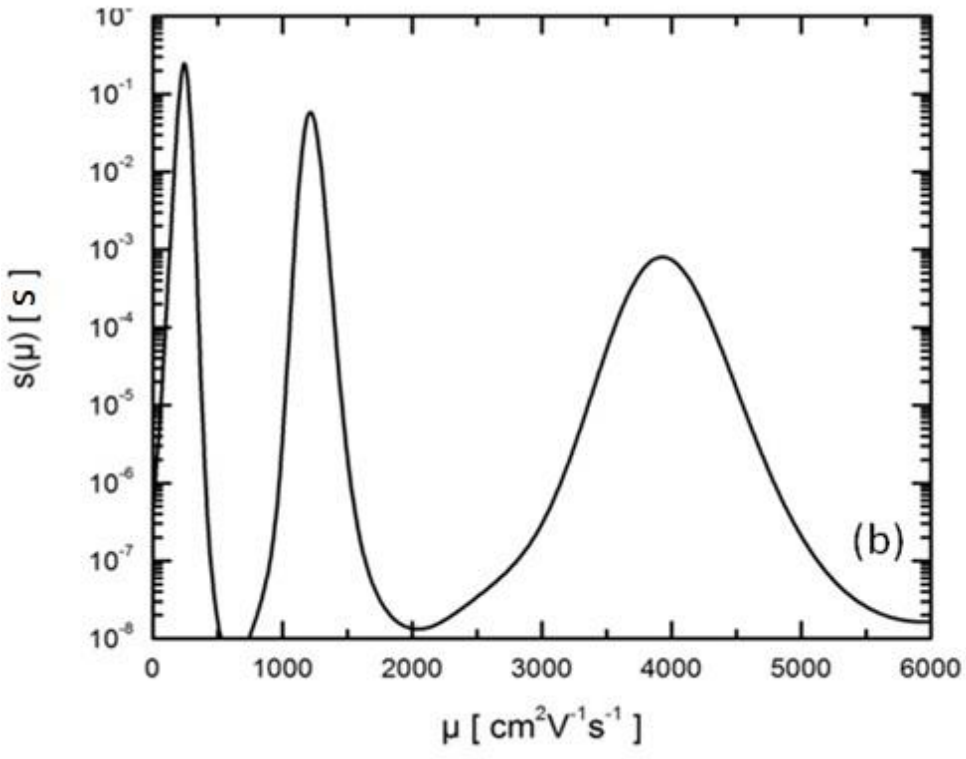

Figure 5.34 Mobility spectrum simulation at 300 K using BAMS for 11-289-SQ1.

As the temperature is reduced the relative importance of the QW increased Figure 5.32(a), shows how at 150 K the number of ionised donors reduces and the Fermi energy approaches the edge of the valance band in the QW. At 100 K the BAMS analysis in Figure 5.35 (b) shows that the sGe QW mobility increases to 28,400 $cm^2V^{-1}s^{-1}$ at a carrier density of 3.1×10^{11} cm^{-2}. At this temperature the parallel conduction begins to freeze out, so the channel now represents ~80% of the total conductivity.

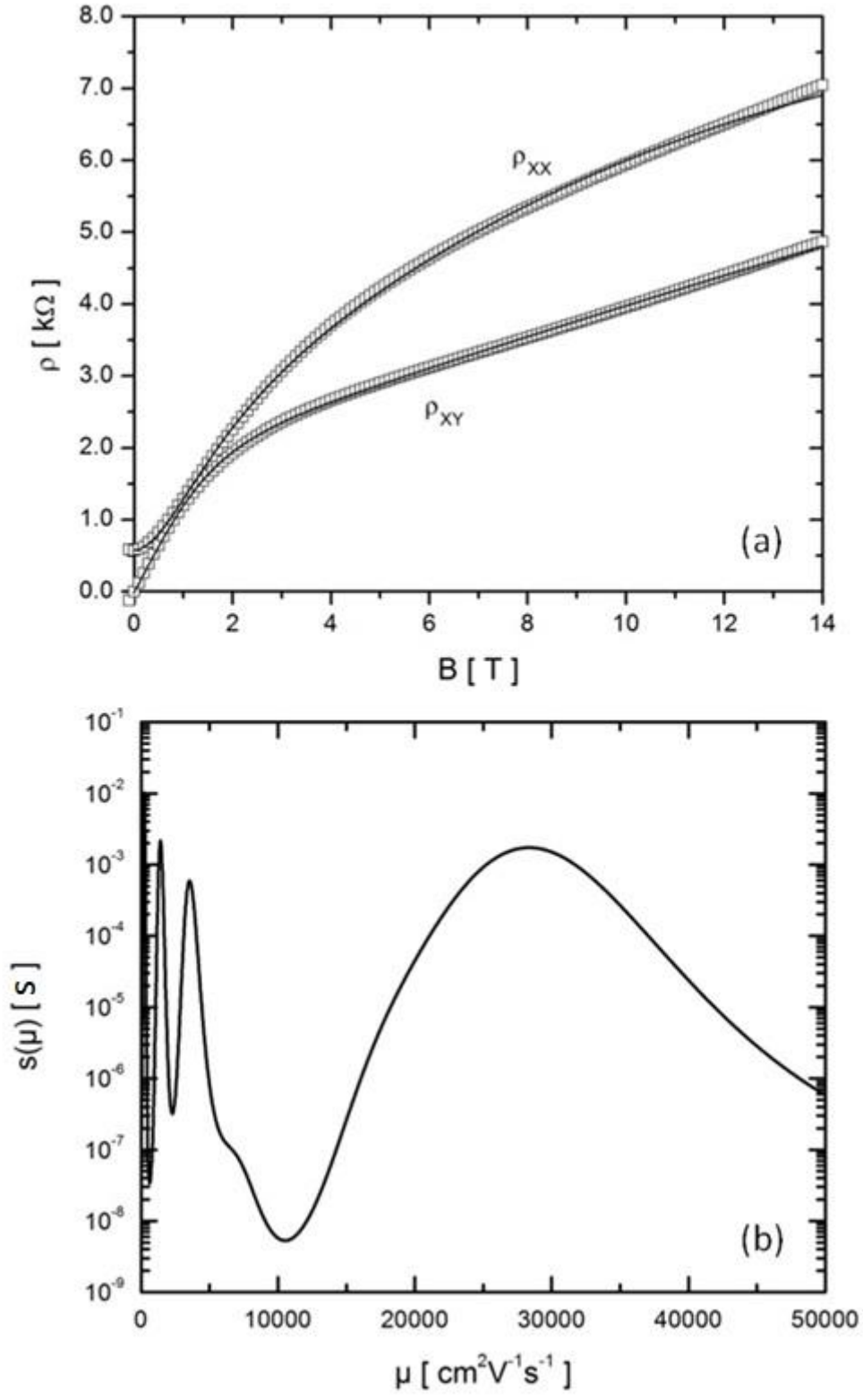

Figure 5.35 (a) Magnetoresistance ρ_{xx} and Hall resistance ρ_{xy} as function of magnetic field B at 100 K, comparing data (squares) and the fit obtained by a forward-transform of the extracted mobility spectrum, for normal structure 11-289-SQ1 (b) Mobility spectrum simulation at 300 K using BAMS for 11-289-SQ1.

Temperature (K)	p_s Nextnano^3 ($\times 10^{11}$ cm^{-2})	p_s BAMS ($\times 10^{11}$ cm^{-2})	p_s ME-MSA ($\times 10^{11}$ cm^{-2})	μ BAMS ($\times 10^4$ cm^2/Vs)	μ ME-MSA ($\times 10^4$ cm^2/Vs)
50	2.63	3.15	2.93	45 ± 15	23 ± 5
100	2.26	3.05	2.88	2.8 ± 0.4	3.0 ± 0.4
150	2.03	1.96	2.38	1.1 ± 0.1	1.1 ± 0.3
200	1.86	1.47	1.71	0.67 ± 0.04	0.63 ± 0.13
300	1.52	0.59	0.98	0.39 ± 0.02	0.39 ± 0.04

Table 5.3 Mobility and sheet density results extracted using ME-MSA and BAMS and sheet density from Nextnano^3

These QW mobility and sheet density values calculated by the two mobility spectrum techniques are given in Table 5.3 for each temperature, where they can be compared to the results of the Nextnano^3 simulations. Mobility spectrum values are also shown Figure 5.30 alongside the measured Hall effect data, and are found to be extremely comparable in the region where conduction is expected to be dominated by the QW channel.

5.9 Summary

This chapter has shown that normal structure of modulated doped sGe quantum well has a high hole mobility of 1.1×10^{6} cm^2/Vs at a sheet density of 3×10^{11} cm^{-2} at 12 K, which is comparable with the highest reported electron mobility for a strained Si channel [82, 95, 96] Structural characterisation confirms a pure Ge channel (Si is < 0.01at%) as well as high quality structure with low interface roughness (rms of 2.0±0.2 nm) which are believed to be important reasons for the high mobility samples.

Simulation for the scattering limited mobility has shown a low background impurity density of 5×10^{13} cm^{-3} for the high mobility sample. However, in samples with a high concentration of O and C, the level of background impurities required in the simulation increased by 4 times. Interface roughness for these samples, of 1.68 nm rms, was also 3 times higher than the lattice constant of Ge, while it is just one monolayer height (0.14 nm) for sample 11-289. Finally, the highest room temperature hole mobility of $(3.9\pm0.4)\times10^{3}$ cm^2/Vs at a sheet density of 0.98×10^{11} cm^{-2} is calculated from sample 11-289 using ME-MSA and $(3.9\pm0.2)\times10^{3}$ cm^2/Vs at a sheet density of 0.59×10^{11} cm^{-2} calculated by BAMS.

6 Magnetotransport of holes in pure sGe heterostructure in high magnetic fields

6.1 Introduction:

Magnetotransport properties of the two dimensional hole gas in strained germanium heterostructures is performed on three samples in this chapter: the normal structure sample 11-289 and two inverted structures samples 11-284 and 11-285. An extremely high hole mobility has been observed in each case, so this chapter will help understand the reason behind that, as well as using Shubnikov de Haas (SdH) oscillations to evaluate the hole effective mass and the actual scattering mechanisms affecting the mobility, for both normal and inverted structures.

6.2 SdH oscillations and QHE effect for inverted sGe samples:

Measurements were initially carried out at Warwick University on Hall bars of sample 11-284 HB5 and 11-289-HB2, with a current of 100 nA. Unfortunately, these samples were not well fabricated and exhibited high geometric effects with mixing of ρ_{xx} and ρ_{xy} components, leading to overshoot in the Hall resistance. Details of these measurement artefacts are not within the subject of this thesis. Therefore, the measurements were repeated for the two samples, with other Hall bars, at the Centre of Low Temperature Physics, Institute of Experimental Physics SAS, Kosice Slovakia, and International Laboratory of High Magnetic Fields and Low Temperatures, Wroclaw Poland, while sample 11-285-HB1 was measured at Warwick by the author.

6.2.1 Sample 11-284

Magnetotransport measurements of ρ_{xx} and ρ_{xy} for sample 11-284HB4b, which is orientated along [110], are shown for temperatures 100 mK–1.5 K in Figure 6.1 Mobility and sheet

density are extracted from the slope of the Hall voltage, as well as the mean free path and transport time for the holes at different temperatures, and are presented in Table 6.1. The Hall voltage shows two slopes which refers to two type of carriers in the channel. The zero-field mobility of lowest magnetic field (B<0.1T) was 5.13×10^5 cm^2/Vs at a sheet density of 5.1×10^{11} cm^{-2}at 100 mK, while the zero-field mobility at the higher magnetic field and at the same temperature was 3.99×10^5 cm^2/Vs at a sheet density of 6.56×10^{11} cm^{-2}.The high mobility is a result of the long time between scattering events, 15 ps, and corresponding long carrier mean free path which reached 5.33 μm at 100 mK.

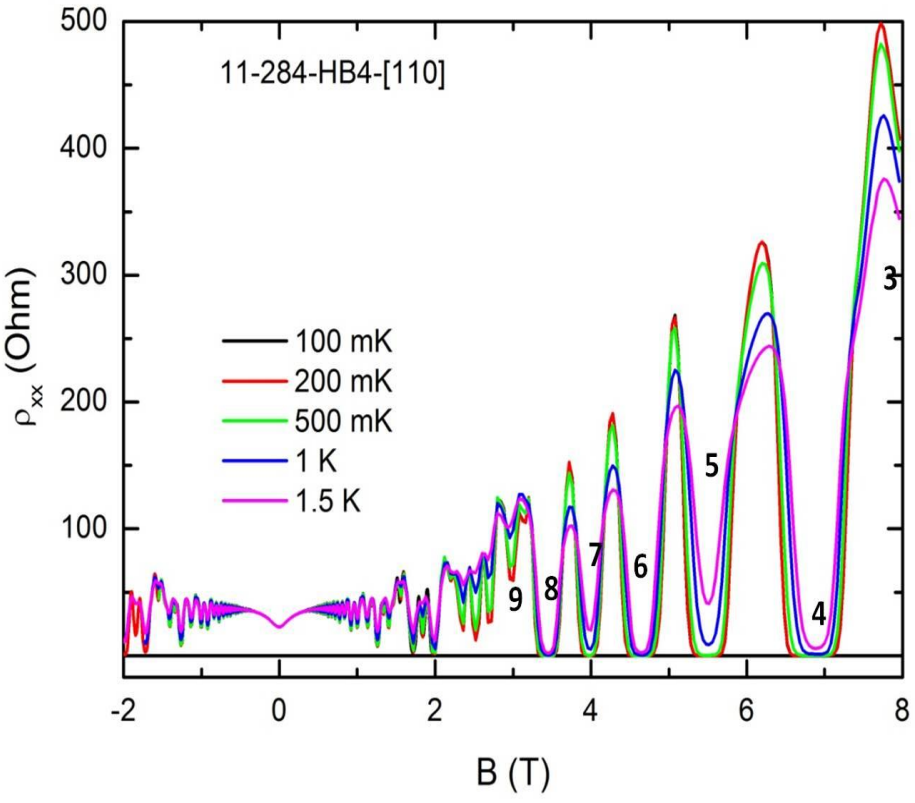

Figure 6.1SdH oscillations for the sample 11-284-HB4 in the [110] orientation at different temperatures and magnetic fields.

T K	ρ_{xx} Ohm/sq	p_{sHall} $\times 10^{11}$ cm^{-2}	P_{SdH} $\times 10^{11}$ cm^{-2}	p_{sFFT} $\times 10^{11}$ cm^{-2}	μ_1 $\times 10^5$ cm^2/Vs	l_m μm	τ_t ps	k_F $\times 10^8 m^{-1}$
0.1	23.87	6.56 5.14	4.88	4.89	3.99 5.1	5.33 6.03	15.9 20.3	2.03 1.79
0.2	23.87	6.61 5.19	4.89	4.94	3.96 5.03	5.31 6.08	15.8 20.7	2.04 1.80
1.0	23.88	6.63 5.08	4.83	4.88	3.95 5.15	5.30 6.05	15.7 20.4	2.04 1.79
1.5	24.00	6.61 5.24	4.84	4.88	3.94 4.96	5.28 5.92	15.7 19.7	2.03 1.81

Table 6.1 Transport parameters for the sample 11-284-HB4-[110] at different temperatures. Hall and sheet density calculated from two different slope in Hall resistance.

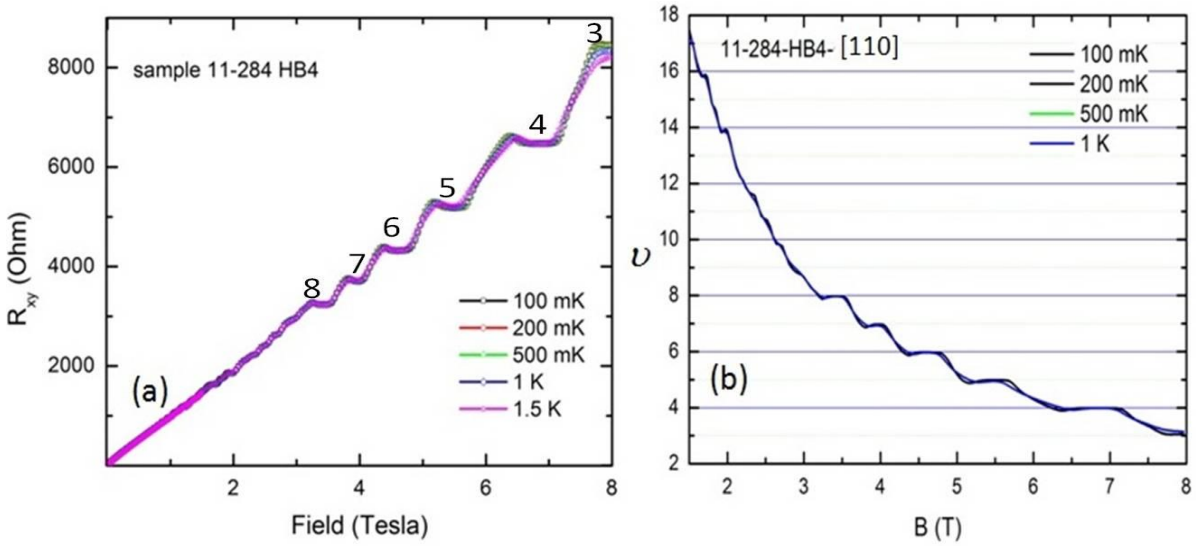

Figure 6.2 (a) Hall resistance vs magnetic field up to 8T at temperature 100 mK-1.5 K and, (b) Inverse Hall resistance scaled by h/e^2 that should yield IQHE plateaus at integer filling factor ν.

The density of the holes within the quantum well can also be found from the periodicity of the SdH oscillations. Looking initially at the Hall resistance shown in Figure 6.2 (a) for the temperatures from 100 mK to 1.5 K, there are very clear integer quantum Hall effect (IQHE) plateaus above 3 T to which filling factors can be assigned unambiguously, knowing the fundamental Klitzing constant of h/e^2 = 25,812.807449(86) Ω. This is done in Figure 6.2(b); it can be seen that the feature at the highest field measured here is at filling factor ν = 3, just above 8 T, which comes from a spin-splitting of the hole Landau levels; assignment of other filling factors follows naturally. From the periodicity a hole density of 4.88×10^{11}cm^{-2} is found.

The even integer features are more clearly defined, which can also be seen in Figure 6.1 where ν = 4, 6 & 8 show zero resistance states up to 1.5 K. The odd integer features correspond to smaller energy gaps in the Landau level spectrum, due to spin splitting, so whilst ν = 5 and 7 are also very clear, the higher odd integers are less distinct although they can be resolved as inflections in the Hall resistance and dips in the SdH to at least ν = 17.

Below 3 T the amplitude of the SdH oscillations follows a more complex pattern, with beating preserved across the ranges of temperatures which suggests there are two types of carriers present.

A Hall bar of sample 11-284-HB4 was also fabricated with $[010]$ orientation and measured to evaluate the difference in the transport properties between orientations Figure 6.3 presents the SdH oscillations and Hall resistance at magnetic fields $-0.8T \le B \le 3.5T$ and for temperatures from 90 mK to 1.5 K. The Hall mobility and sheet density extracted from this measurement are shown in Table 6.2 as well as other parameters. Almost the same parameters were extracted from this direction as for the $[110]$ orientation, and the same beating seen, which indicates no significant anisotropy between them. This was not expected

as an obvious anisotropy in resistance was observed between $[110]$ and $[\bar{1}10]$ in Chapter 4. The conclusion from Chapter 4 was that the anisotropy was due to differences in interface roughness in the two perpendicular directions, so it is possible that these two pieces of Hall bar did not have a significant difference due to variations across the wafer.

T K	ρ_{xx} Ohm/sq	p_{sHall} $\times 10^{11}$ cm^{-2}	p_{sSdH} $\times 10^{11}$ cm^{-2}	p_{sFFT} $\times 10^{11}$ cm^{-2}	μ $\times 10^{5}$ cm^2/Vs	l_m μm	τ_t ps	k_F $\times 10^8\ m^{-2}$
0.09	23.85	6.45 5.16	4.76	4.88	4.06 5.08	5.38 6.04	15.0 18.8	2.01 1.8
0.25	23.89	6.23 5.12	4.78	4.81	4.19 5.11	5.46 6.03	15.5 18.9	1.98 1.79
1	23.9	6.12 5.27	4.75	4.9	4.27 4.95	5.51 5.93	15.8 18.3	1.96 1.82
1.5	24	6.23 5. 54	4.75	4.9	4.18 4.77	5.44 5.80	15.4 17.6	1.98 1.85

Table 6.2 Transport parameters for the sample 11-284-HB4-$[010]$ 1-8 at different temperatures.

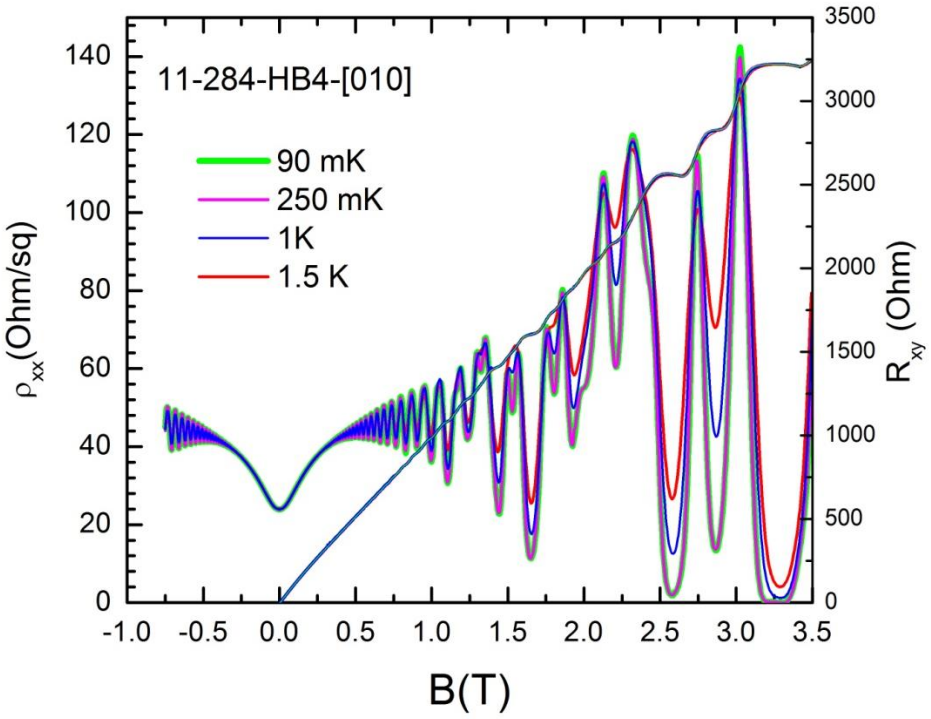

Figure 6.3 SdH oscillation for the sample 11-284-HB4 in [010] orientation at different temperatures and magnetic field.

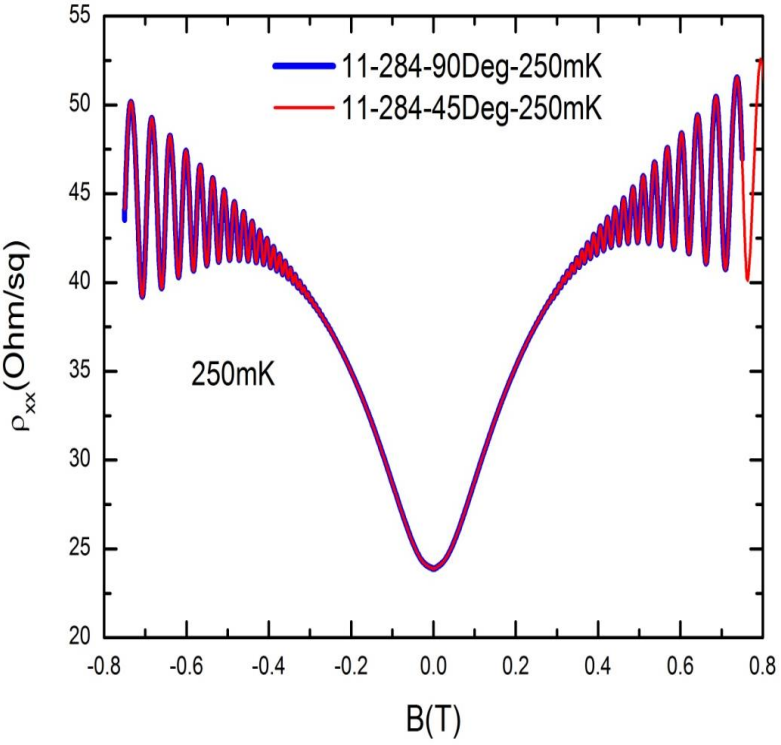

Figure 6.4 SdH Oscillation for both [110] and [010] orientations at -0.8T<*B*<0.8T at 250 mK

Oscillations in the low magnetic field range of -0.8T<T<0.8T are illustrated in Figure 6.4 for both orientation $[110]$ and $[010]$ at 250 mK, which very clearly confirms there is no difference between the orientations. The positive magnetoresistance presented in Figure 6.4 is due to two types of carrier contributing to the transport in this field range, which would also account for the SdH beating seen between 1 T and 3 T [97, 98]. A Fourier transform of this data, between 0.3 T and 0.9 T is presented in Figure 6.5, which shows just one subband with a sheet density 4.89×10^{11} cm^{-2} together with a harmonic at double the frequency due to non-sinusoidal oscillations. This is significantly lower density than found from the slope of the Hall resistance, which suggests there may be a second pocket of lower mobility carriers occupied at the top interface of the quantum well, as shown in the simulation of Figure 4.56.

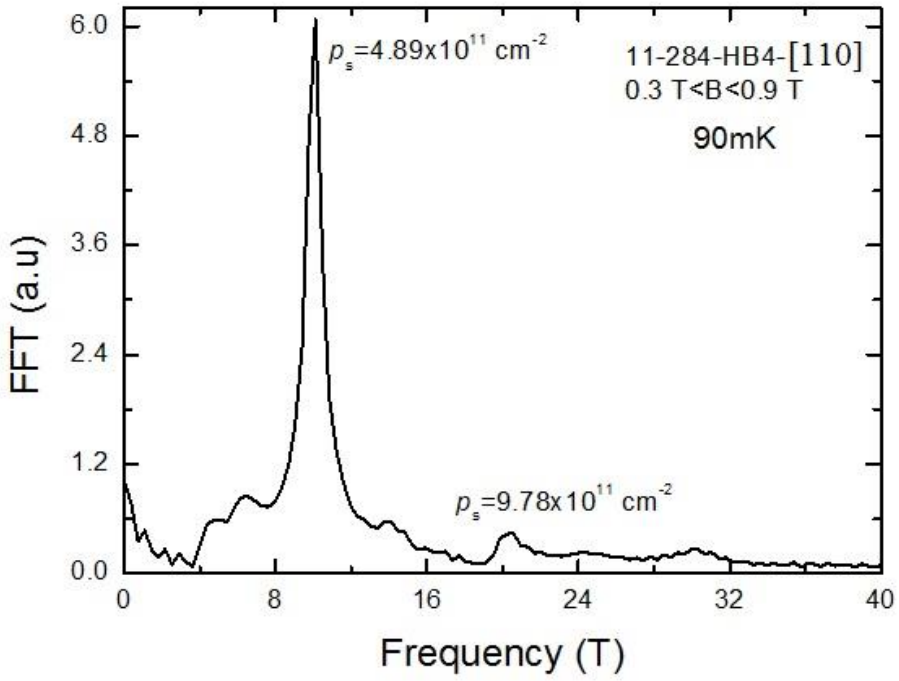

Figure 6.5 Fast Fourier transform of the magnetoresistance of the sample 11-284-HB6 at $[110]$ orientation at magnetic field 0.3 T<B<0.9 T at 90 mK.

6.2.2 Sample 11-285

Magnetotransport measurement of ρ_{xx} and R_{xy} were performed for sample 11-285-HB1[110] at range of temperatures from 300 mK to 15 K, and magnetic fields up to 11 T for few temperatures and -3T <B< 3T for others to analyse the effective mass. The SdH oscillations at the lowest temperature started from 0.4 T, with beating of the amplitude observed at temperatures up to 1K. The Hall mobility and sheet density for 0.3 K, and more parameters, are presented in Table 6.3, which shows a mean free path of 6.11 μm and Fermi wave length of $1.83\times10^{8}\,m^{-2}$ at 300 mK that was 1 to 2 % higher than mean free path and Fermi wave length in sample 11-284.

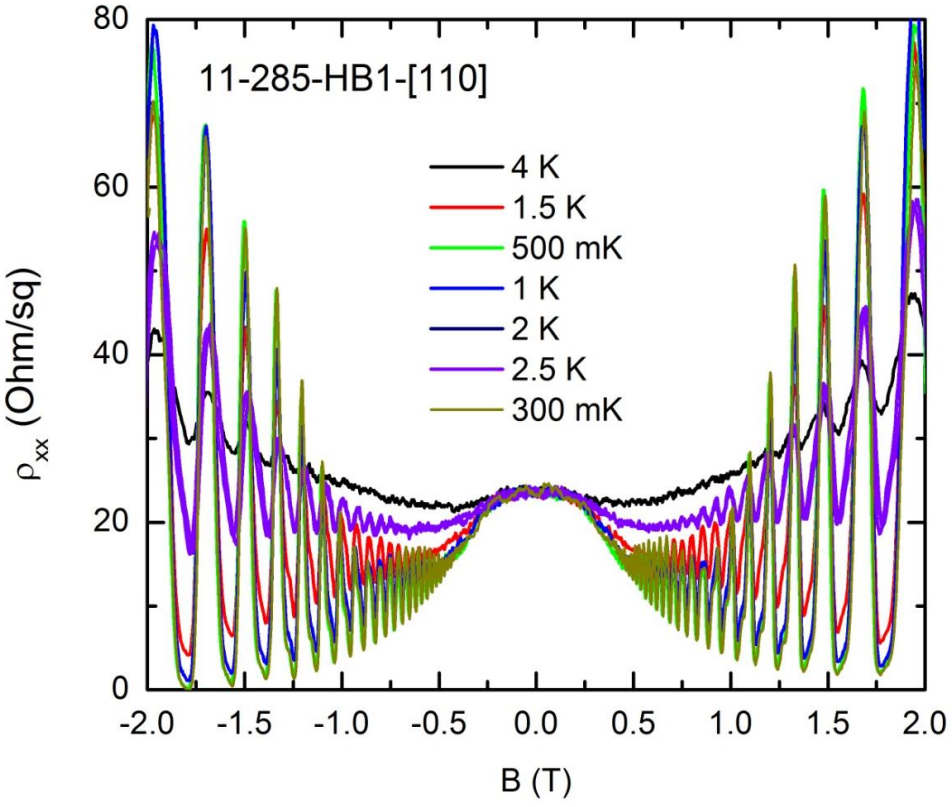

Figure 6.6 SdH oscillation for the sample 11-285-HB1at [110] degree at temperature range from 300 mK to 4K with applied magnetic field -2T<B<2T.

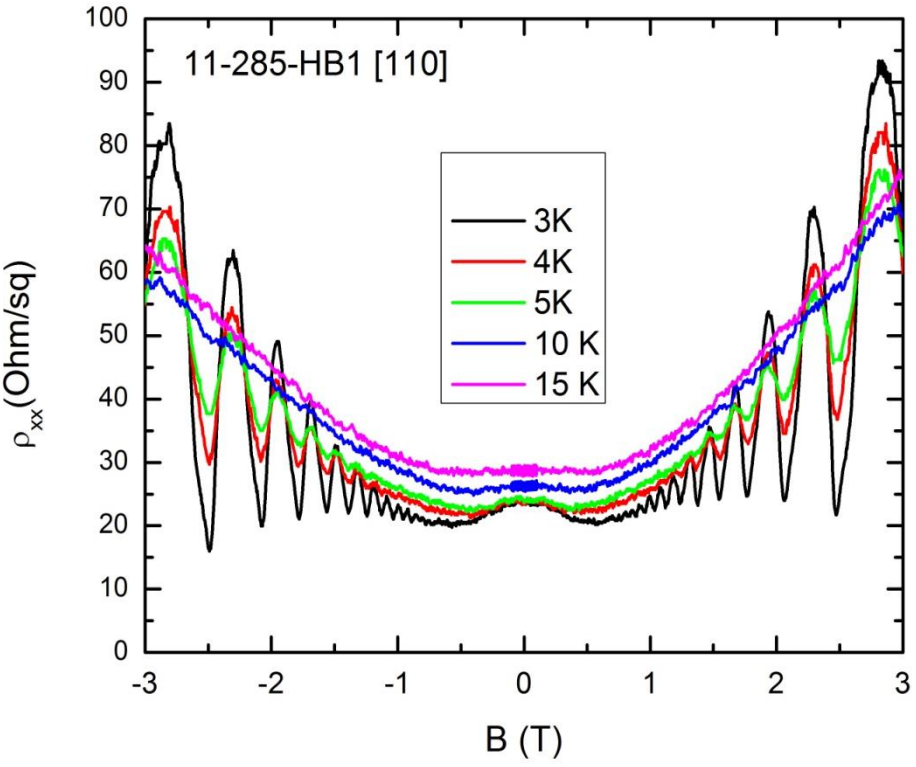

Figure 6.7 SdH oscillation for the sample 11-285-HB1at [110] degree at temperature range from 3K to 15K with applied magnetic field -3T<B<3T..

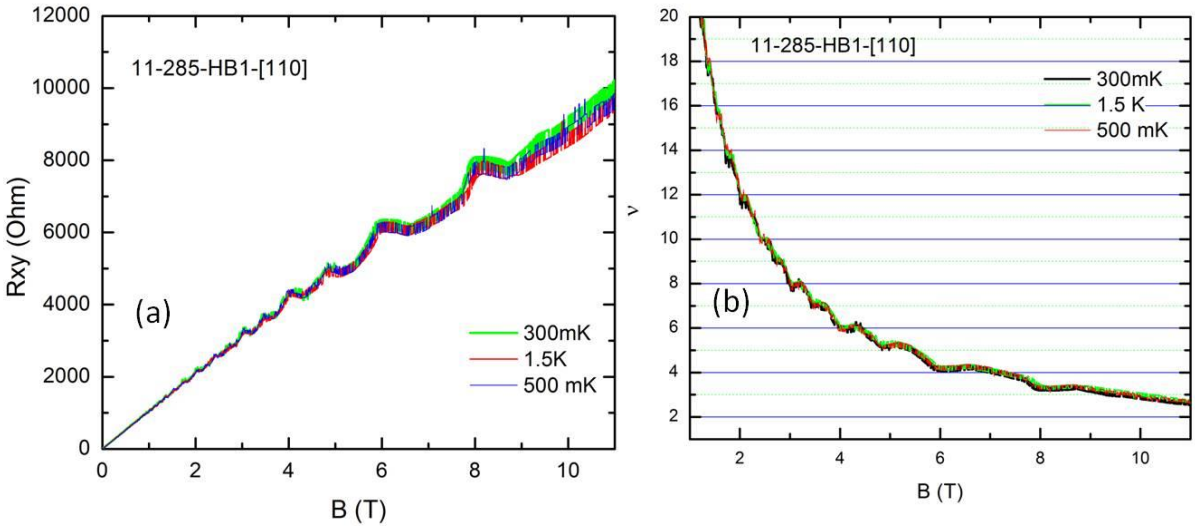

Figure 6.8 (a) Hall resistance vs magnetic field up to 11T at temperature 300 mK-1.5 K. and (b) filling factor as function of magnetic field ends at ν =3.

ρ_{xx}	p_{sHall}	p_{SdH}	p_{sFFT}	μ	l_m	τ_t	k_F
Ω/sq	$\times 10^{11}$ cm^{-2}	$\times 10^{11}$ cm^{-2}	$\times 10^{11}$ cm^{-2}	$\times 10^{5}$ cm^2/Vs	μm	ps	$\times 10^{8}\, m^{-2}$
23.17	6.02	5.98	6.02	4.48	5.73	16.0	1.94

Table 6.3 Transport parameters for the sample 11-285-HB1-[110] at 0.3 K.

The Hall resistance shows plateaus when the magnetoresistance is vanishing in the integer quantum Hall effect in magnetic fields up to 11 T. Clear plateaus are again observed at ν=3, 4, 5, 6,….etc. as shown in Figure 6.8 although they are not perfectly flat as in 11-284 which shows there is a slight geometry problem with this Hall bar which mixes in part of the diagonal component.

The SdH oscillations of Figure 6.6 correspond to spin splitting in the lowest HH subband. It disappears as the temperature increases and is not observed for 1.5 K and higher temperatures. A FFT analysis of the SdH oscillations for this sample at 300 mK and magnetic fields up to 2 T is inset in Figure 6.9. It shows peaks f_1 and f_2 relating to densities of holes in the two spin-split states of sheet density $p_1 = 2.95\times10^{11} cm^{-2}$ and $p_2 = 3.19\times10^{11} cm^{-2}$; a third peak at f_3 corresponds to the total density $p_t = 6.02\times10^{11} cm^{-2}$. Another small peak is observed in the FFT analysis at $f_1 + f_3$, which is an artefact of the transform. The carrier imbalance $\Delta p = (p_2 - p_1)/p_t$ is 4% indicating a surprisingly weak Rashba coefficient, which arises from the symmetry of the quantum well [99-101]. The spin precession (β) is given by the following equation [102, 103]

$$\beta = \frac{\Delta p \hbar^2}{m^*}\sqrt{\frac{\pi}{2(p_t - \Delta p)}} \tag{4.1}$$

For our case β = 4.8x10^{-12} eV.m which is significantly small compared to other reports in heterostructures [104]. This result is supported by the idea that the high doping observed in the Si cap may have affected the symmetry of the quantum well. This will have resulted in a double side doped structure instead of single side doping, which also means that the symmetry in the quantum well for each sample will depend on the concentration of the boron on both sides.

The zero-field spin-splitting energy can be calculated from the difference in densities, using the equation:

$$\Delta E = \frac{2\pi\hbar^2(\Delta p)}{m^*} \tag{4.2}$$

This yields 1.83 meV, which is almost in agreement with the spin-splitting energy difference at zero magnetic field calculated from $\Delta = 2\beta k_F$ which is 1.87 meV.

Further information on spin-splitting in this sample could be obtained by increasing the sheet density with illumination, or using gated Hall bar; this could be studied as future work. Similarly, the negative magnetoresistance observed at low temperatures in the range of weak magnetic fields before the SdH oscillations begin could be further investigated.

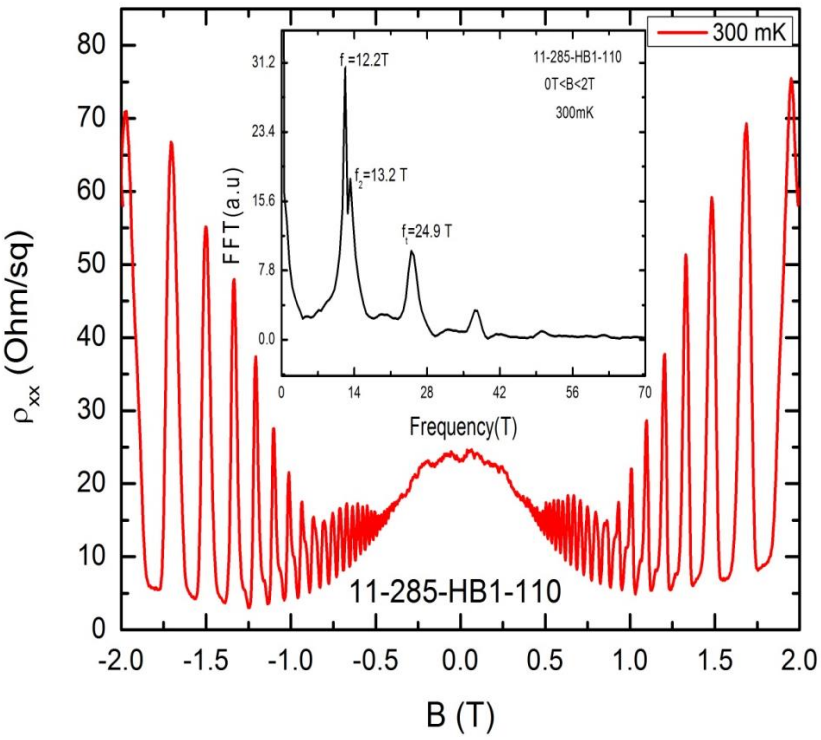

Figure 6.9 Magnetoresistance vs magnetic field with FFT analysis at 300 mK.

6.3 SdH oscillations and QHE effect for normal sGe sample:

Magnetotransport measurements of ρ_{xx} and ρ_{xy} have been performed at temperatures from 0.5 K to 52 K for sample 11-289 with a [110] orientation, see Figure 6.10. An extremely high mobility of 1.34×10^{6} cm^2/Vs at sheet density of 2.9×10^{11} cm^{-2} has been calculated at 0.5 K. Table 6.4 shows the various parameters for other temperatures as well. The SdH oscillations extend to below 0.4 T, again indicating a high quality sample. The position of the integer quantum Hall effect can be seen in the Figure 6.11 for the lowest temperatures. However, the IQHE plateaus do not appear flat, especially at higher field because of sample geometry issues. The feature at 5.8 T corresponds to $\nu = 2$ (Figure 6.12).

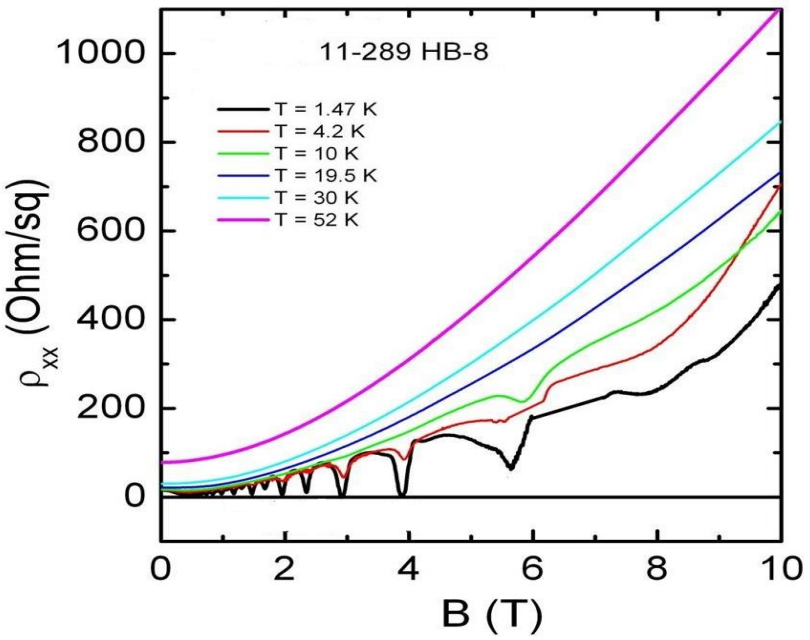

Figure 6.10 SdH oscillations for sample 11-289-HB8 at [110] between 1.47 K and 52 K

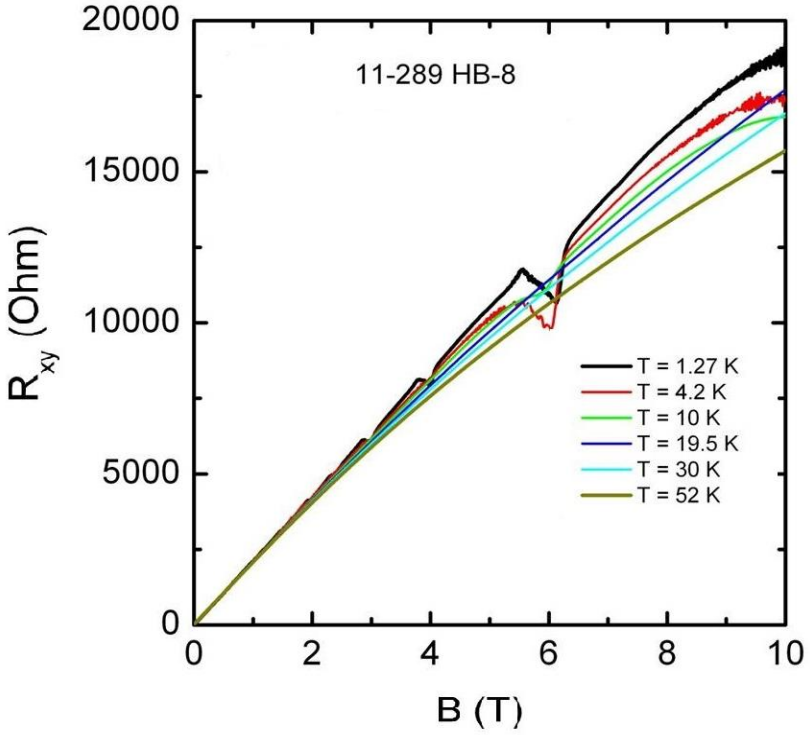

Figure 6.11 Hall resistance vs magnetic field with range of temperatures 1.27 K- 52 K.

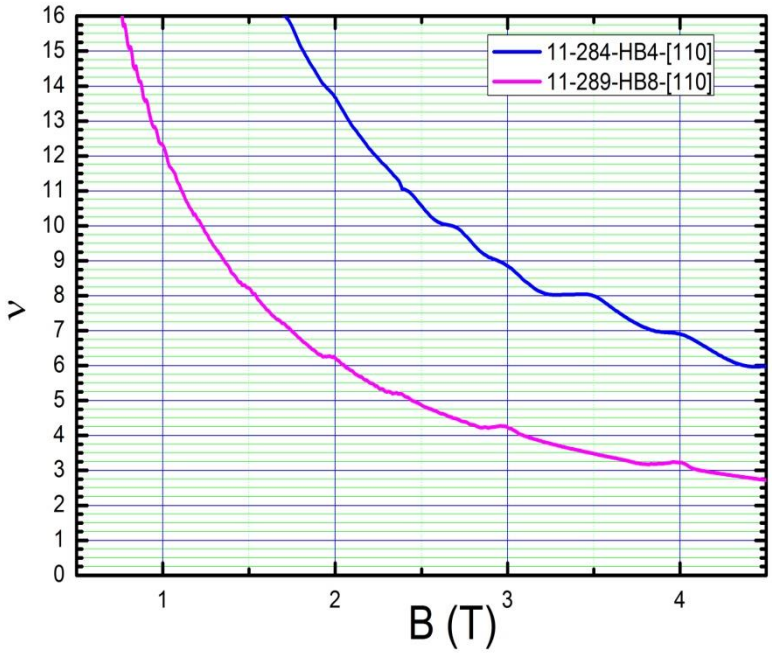

Figure 6.12 Filling factor for samples 11-289-HB8-[110] and 11-284-HB4-[110]

T K	p_s $\times 10^{11}cm^{-2}$	μ $\times 10^{6}$ cm^2/Vs	τ_t ps	l_m μm
1.47	2.94	1.34	48.0	12.05
3	2.95	1.34	47.6	11.98
4.5	2.95	1.34	47.6	11.98
10	2.95	1.21	43.3	10.83
19.5	2.96	0.98	35.0	8.88
30	2.99	0.68	24.3	6.21
52	3.00	0.26	9.0	2.35

Table 6.4 Transport parameters for sample 11-289-HB8-[110] at different temperatures.

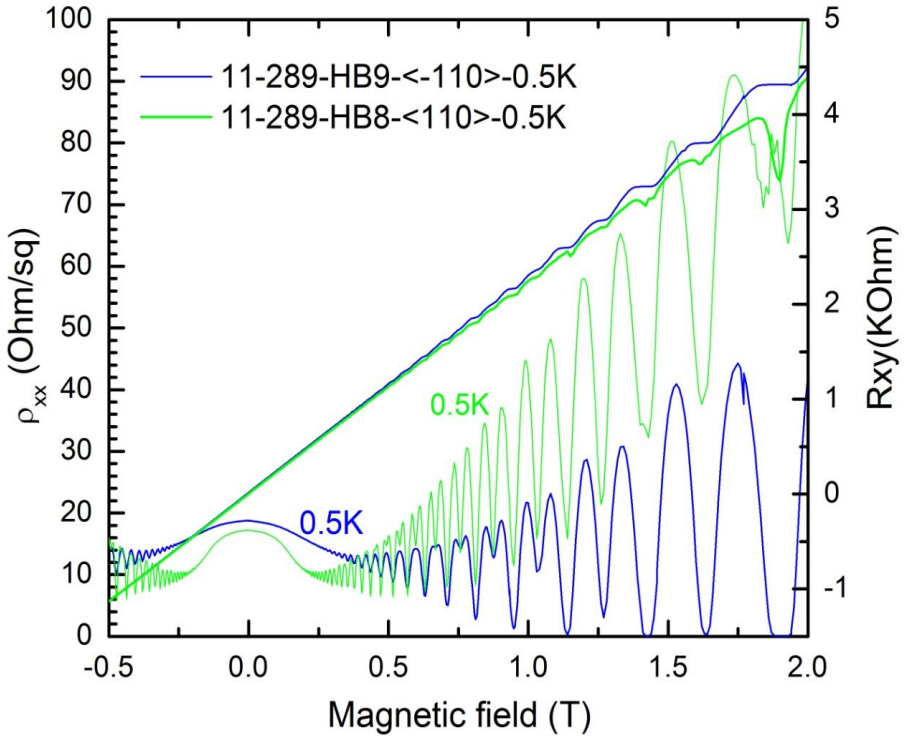

Figure 6.13 SdH oscillation and quantum Hall resistance for both orientations and at 0.5 K.

Hall bars in two orientations were measured at 500 mK: [110] for Hall bar 8 and [$\bar{1}$10] for Hall bar 9, as illustrated in Figure 6.13 which shows clear differences between them. Hall Bar 9 ([$\bar{1}$10] orientation) for shows better quality data, with flat quantum Hall plateaus and zero-resistance minima for ρ_{xx}; however, for Hall Bar 8 ([110] orientation) there is a lower zero-field resistance, the SdH oscillations start at lower magnetic field, and spin-splitting of the SdH oscillations is resolved at lower fields. All of these point to a higher mobility in this orientation. From these data (in Table 6.5) the anisotropy ratio for ρ_{xx} at 500 mK is calculated to be 1.09 which almost similar to the one obtained by Greek cross and square VdP samples in Chapter 5 at higher temperatures. It should be noted that the hole density for HB8 is 10% higher and that could also lead to higher mobility in the range of lower sheet density ($< 3\times10^{11}$ cm^{-2}).

Sample	μ ($\times 10^6$ cm^2/Vs)	$p_{s\ Hall}$ ($\times 10^{11}$ cm^{-2})	$p_{s\ SdH}$ ($\times 10^{11}$ cm^{-2})	$\rho_{xx0}(\Omega/sq)$
11-289-HB9-$[\bar{1}10]$	1.22	2.74	2.74	18.7
11-289-HB8-[110]	1.34	2.94	2.72	16.2

Table 6.5 Transport parameters for sample 11-289-HB8-[110] and 11-289-HB8-$[\bar{1}10]$ at 0.5 K.

FFT analysis was also executed on the low field oscillations to define the sheet density for both orientations. Firstly, the [110] orientation data was analysed Figure 6.14 at magnetic fields 0.18 T < B < 0.4 T, A single clear peak is observed for a sheet density of 2.72×10^{11}cm^{-2} showing single subband occupation for this sample. The second peak occurring at $2p_s$ (5.43×10^{11} cm^{-2}) is an artefact of the FFT. Sheet density of 2.74×10^{11} cm^{-2} obtained from the perpendicular orientation $[\bar{1}10]$ in Figure 6.15.

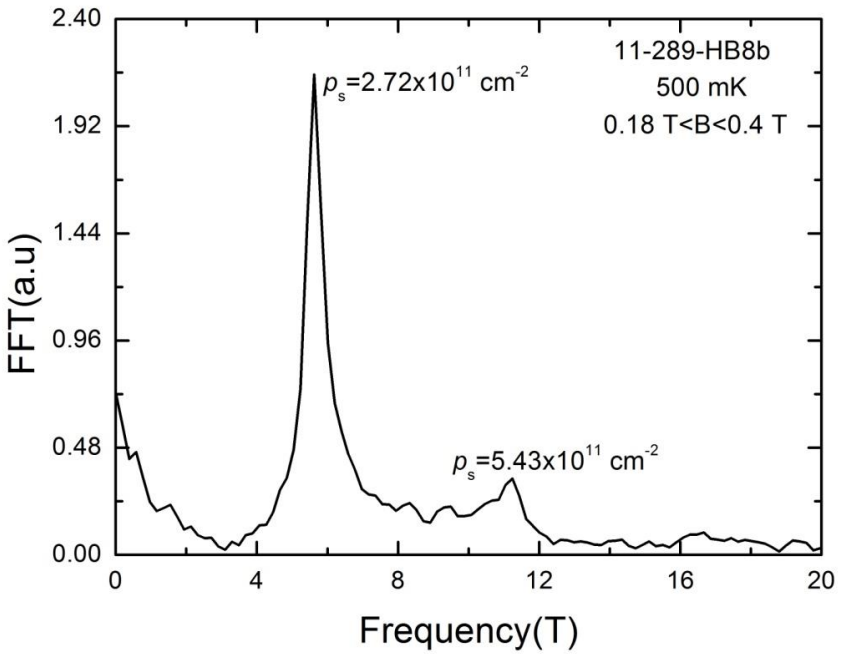

Figure 6.14 FFT analysis of SdH oscillation vs frequency for the sample 11-289-HB8 –[110] orientation.

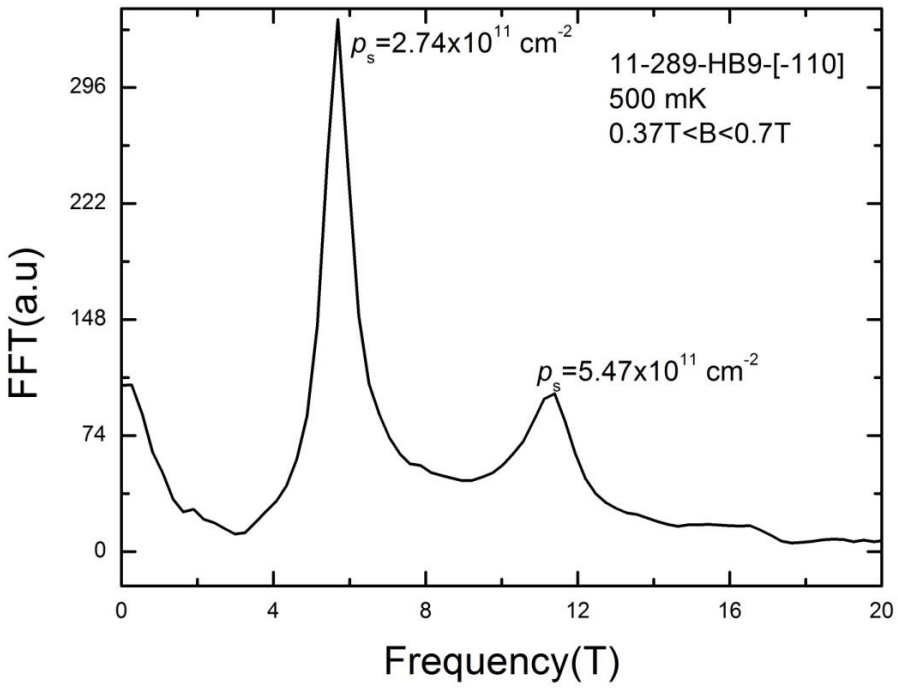

Figure 6.15 FFT analysis of SdH oscillation vs frequency for the sample 11-289-HB9 -$[\bar{1}10]$ orientation

A giant negative magnetoresistance was again observed in the normal structure sGe at low temperatures up to 4.2 K according to the high mobility and one subband occupation.

6.4 Observation of Fractional Quantum Hall Effect in sGe:

Beyond the integer quantum Hall effect, very high mobility samples can show evidence of features at fractional filling factor. This has been studied in great detail for GaAs/GaAlAs heterostructures [86, 105] and also for electrons in Si [106, 107], but not previously observed in Ge. The lowest temperature data in Figure 6.12 shows some indication of features at magnetic fields above those of filling factor 2. It was difficult to get proper data at high magnetic field due to current leakage in the Hall bar devices used to measure magnetoresistance at high magnetic fields. For that reason, square Van der Pauw samples were measured to get more accurate data. Room temperature magnetotransport measurement

was also performed on sample 11-289-SQ1, which was used in the mobility spectrum analysis illustrated in chapter 5.

Sample 11-289-SQ1 was measured at magnetic fields up to 16 T and temperatures down to 20 mK, as shown in Figure 6.16 . The hole mobility was 1.1×10^{6} cm^2/Vs at sheet density of 2.77×10^{11} cm^{-2} at this temperature. Beyond showing very clear integer quantum Hall effect plateaux, there are obvious indications of fractional effects between ν = 1 and 2 as well as weaker indications between ν = 2 and 3. Specifically, zero-resistance states are observed for ν = 4/3 & 5/3 with accompanying Hall plateaux at the correct resistance. The weaker features seen include ν = 7/5 & 8/5 and in the next Landau level 7/3 & 8/3. This represents the first observation of fractional quantum Hall effect in germanium.

Unfortunately, there is no time for more analysis to the quantum Hall resistance in the period of this thesis, and more work should be continued on these, or similar, samples.

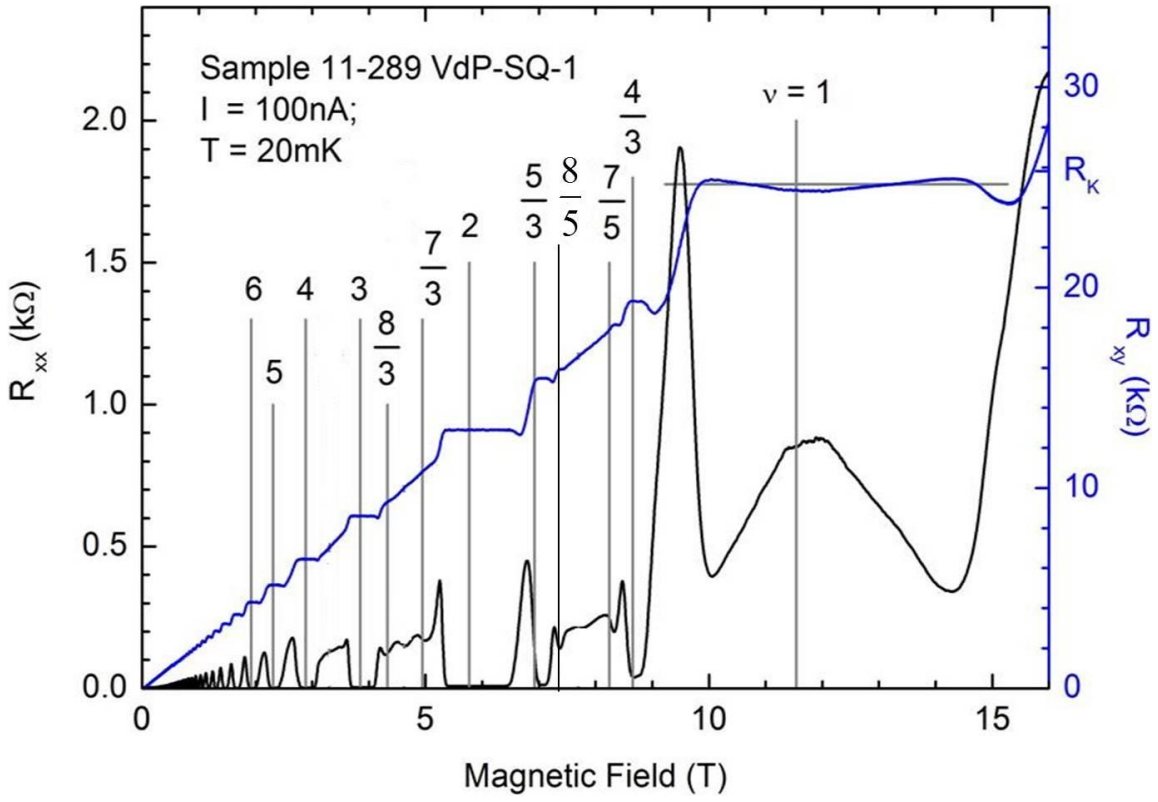

Figure 6.16 SdH oscillation and fractional quantum Hall effect for sample 11-289 square Van der Pauw.

6.5 Effective mass and Dingle ratio extraction:

Strain splits the heavy and light hole bands, changing their shape (*E-k* dispersion) which accounts for the reduction in hole effective mass that improves the mobility of the carriers. For that reason, extracting the hole effective mass for these samples is significant. By measuring the temperature dependence of SdH oscillations at low magnetic field a lot of parameters, including the effective mass as well as the sheet density and Dingle ratio α, can be extracted following the procedure set out in section 2.4. Magnetotransport measurements of ρ_{xx} and R_{xy} were therefore made over a range of temperatures for all the samples previously analysed, to understand the reason for the high mobility reported as well as the reason for differences in the transport properties between these samples. Only SdH oscillations that appeared sinusoidal were included in the analysis, which meant restricting the analysis to sufficiently low magnetic fields.

Firstly, sample 11-284-HB4 was analysed for Hall bars with the current directed in two orientations: [110] and [010]. The effective mass and Dingle ratio were found to be almost the same for both orientations: the effective mass (m^*) was $0.070\pm0.002\ m_0$ and $\alpha = 33$ for [110], while $m^* = 0.065\pm0.002\ m_0$ and $\alpha = 39$ for the [010] orientation, as seen from the Figure 6.17 and Figure 6.18, respectively. The Dingle plots in these figures illustrate a straight line that intercepts the y-axis at 4 (appearing at ln(4)=1.39 on the log scale), which is compatible with the standard theory [43]. A small deviation from the simple theory is observed and it is related to beating in the SdH oscillation those results from two types of carrier being present. Similar effective mass and α values were extracted for sample 11-285, the other inverted structure (see Figure 6.19). The effective mass of $0.063\pm0.003\ m_0$ is the lowest value published so far for a sGe quantum well. Some dispersion appeared due to zero-field spin splitting for sample 11-285, but the Dingle ratio is almost the same as for 11-284.

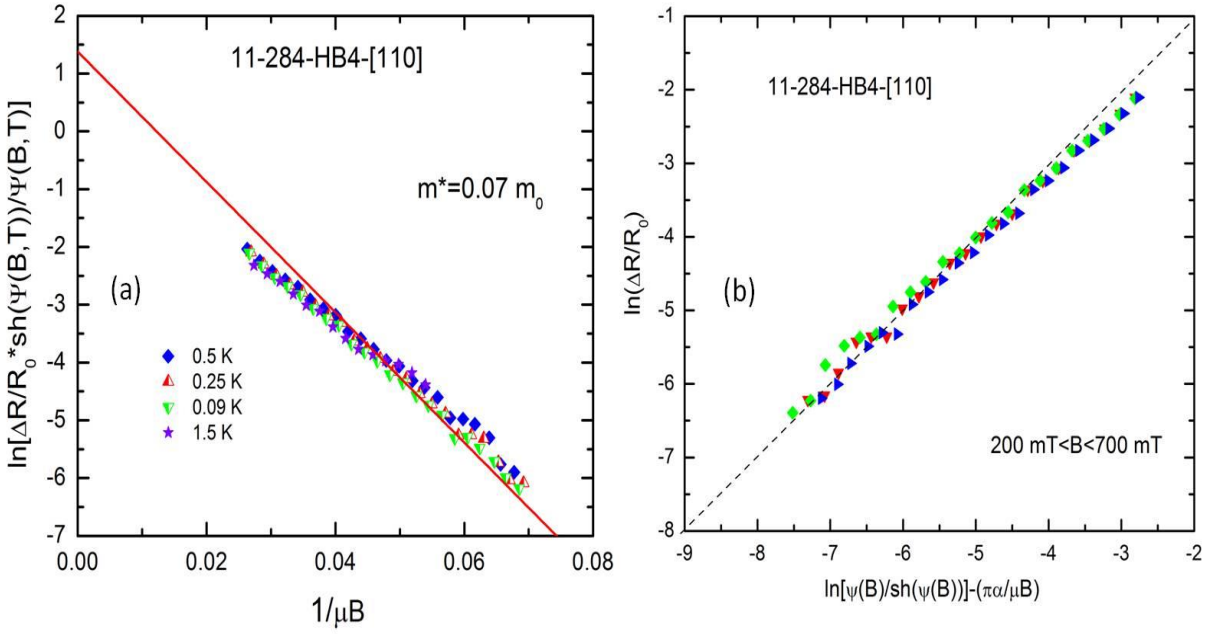

Figure 6.17 Dingle plot and α extraction curve for sample 11-284-HB4-[110]..

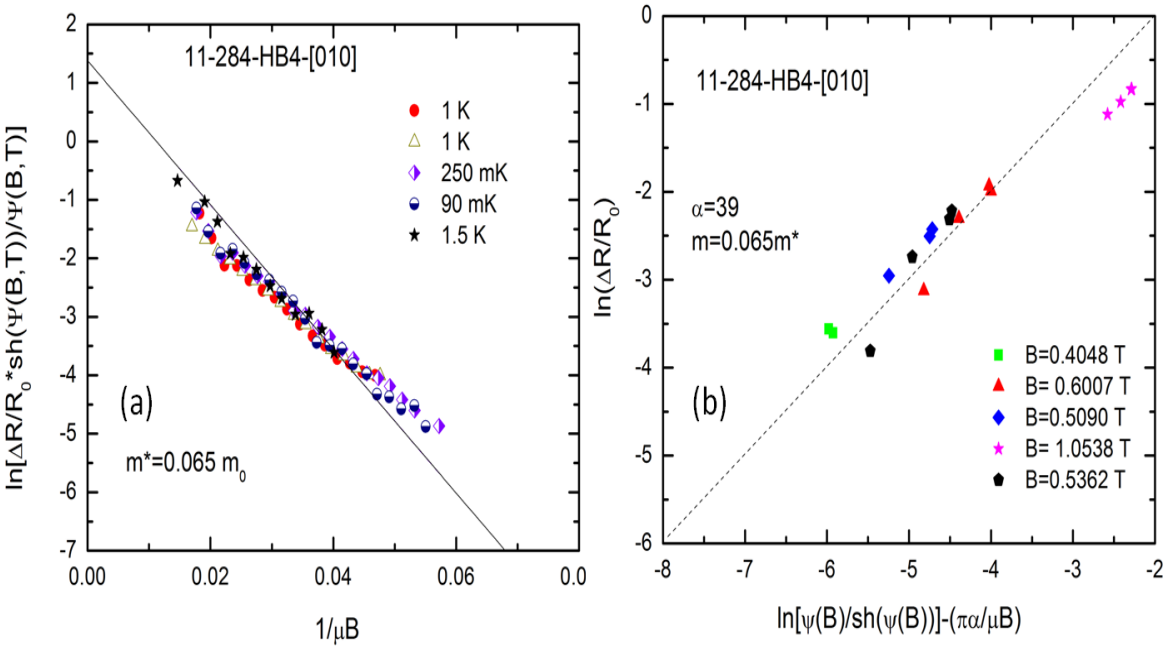

Figure 6.18 Dingle plot and α extraction curve for sample 11-284-HB4-[010].

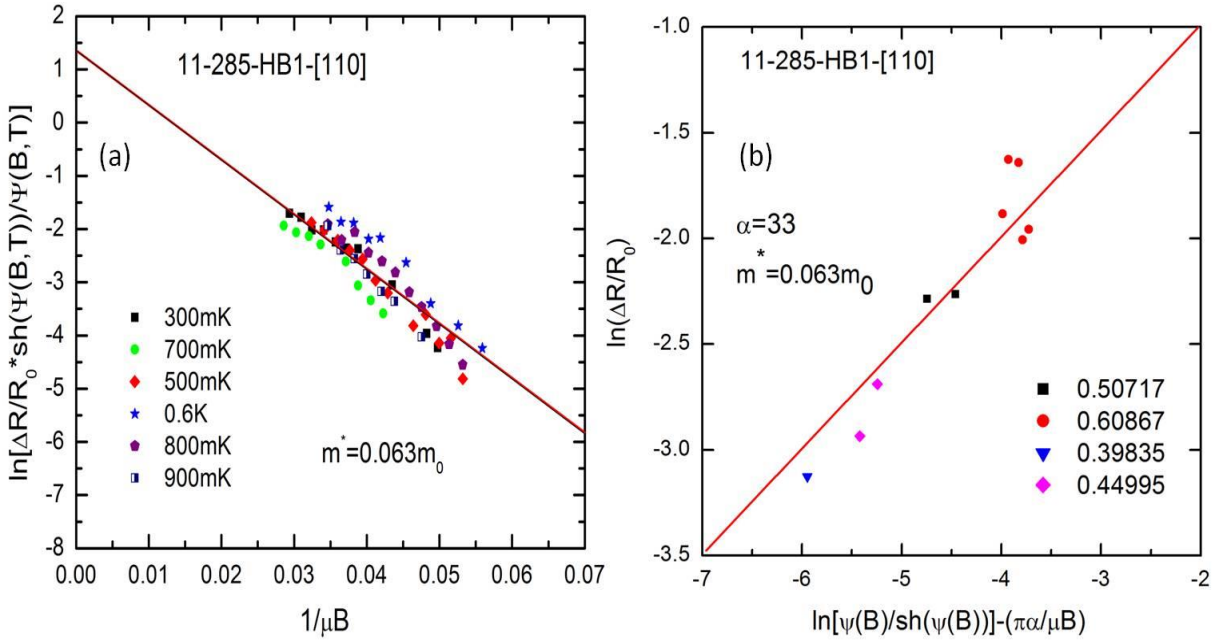

Figure 6.19 Dingle plot and α extraction curve for sample 11-285-HB1-[110].

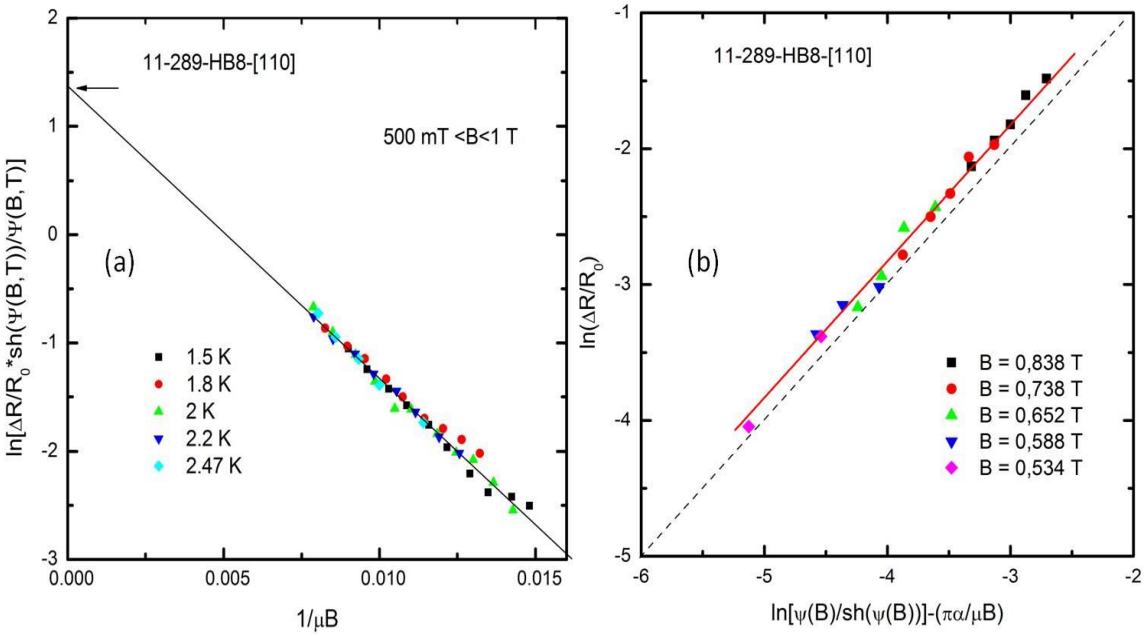

Figure 6.20 Dingle plot and α extraction curve for sample 11-289-HB8-[110].

For the normal structure sample 11-289 a similar low effective mass was extracted to the previously mentioned inverted structures. The Dingle plot for sample 11-289 in Figure 6.20 illustrates a straight line intercept with the y-axis at 4 that is compatible with the theory [108], and relates to homogeneous broadening of the Landau levels. However, the Dingle ratio, at $\alpha = 78$, is much greater than in the other samples.

Sample number	m*	α
11-284-HB4-[110]	0.070±0.002	33
11-284-HB4-[010]	0.065±0.002	39
11-285-HB1-[110]	0.063±0.003	33
11-289-HB8-[110]	0.063±0.001	78

Table 6.6: Dingle ratio and hole effective mass extracted from SdH oscillations

The Dingle ratio and effective mass for each sample are summarised in Table 6.6. These effective mass values are extremely low for holes in Ge [7, 109, 110] The Dingle ratios are similarly very high, which indicates that small angle scattering is dominant. This only happens when scattering from background impurities has been eliminated in comparison to long range scattering from remote ionised impurities and is also due to the purity of the Ge channel that is not contaminated with Si atoms. The Dingle ratios are almost the same for 11-284 and 11-285 which shows they have a similar distribution of dopants and impurities. Sample 11-289 could be expected to also have a similar level of background impurities coming from the overall cleanliness of the epitaxy system as it was grown in the same batch, but the much higher Dingle ratio suggests that there are fewer background impurities in the

channel than for 11-284 or 11-285. The 'normal' doping structure of sample 11-289, with the dopant layer grown after the channel, avoids any chance of dopants introduced during the growth process from getting into the channel, which could happen with segregation in the 'inverted' doping structures where the dopant layer is grown before the channel. Together, the low m^*, reduction in the background scattering, and the high quality of structures that reduces interface roughness significantly can account for the high mobility reported in these samples compared to previous studies.

6.6 Summary

Significant properties for three samples are reported in this chapter, which presents two inverted samples with two types of carriers as illustrated by their SdH oscillations. Analysis of these oscillations by FFT shows one peak (one subband occupation) and no presence of zero field spin splitting, which supported the idea that the reason of beating is due to two pockets of sheet density presented in the Ge channel of the sample 11-284. Sample 11-285 FFT analysis illustrates zero field spin splitting that accounts of the beating in the oscillation; however, further analysis indicated a weak Rashba effect even with one subband occupation, which means this asymmetry is very week and also supported the idea of two pockets of carriers in the channel. Finally, the normal structure (11-289) shows no beating and is a clear case of only one subband occupation.

The low effective mass of (0.070±0.002) m_0 for sample 11-284, 0.063±0.003 m_0 for sample 11-285, and (0.063±0.001) m_0 for sample 11-289 is one reason that accounts for the high mobility reported in these samples. Moreover, the high Dingle ratio of 33 for samples 11-284 and 11-285, and 78 for sample 11-289 demonstrates that remote impurity scattering is the limited scattering mechanism for the mobility and indicates a significant reduction to the interface roughness and background impurity scattering.

7 Conclusion and Further Work

7.1 Conclusion

In this research, transport properties of strained Ge quantum wells have been investigated by different techniques for a range of samples. The most significant result was the extremely high hole mobilities observed for all the samples and especially for the normal structure sample 11-289, which presented a hole mobility of 1.34×10^{6} cm^2/Vs at a sheet density of 2.94×10^{11} cm^{-2} at 0.5 K. A considerable room temperature mobility of $(3.9\pm0.4)\times10^{3}$ cm^2/Vs from carriers in the Ge quantum well of this sample at a sheet density of 0.98×10^{11} cm^{-2} was the highest mobility recorded in literature so far.

The reasons behind this result are due to the high purity of Ge channel, which was confirmed to contain only 0.01 at% of Si, as well as the high quality structure with very low interface roughness scattering and low background impurity scattering. Scattering simulation has confirmed that background impurity scattering is the limited parameters for mobility at low sheet density and at higher sheet density remote impurities or interface roughness scattering could be the limited parameters depending on the quality of the sample. For the normal structure remote impurities dominate at high sheet density, while for the inverted structures, with anisotropy properties, interface roughness is significant as sheet density increased.

The sample growth parameters were varied to assist the study of the transport properties of holes in Ge quantum wells, such as channel thickness, spacer thickness, doping concentration and growth temperature. Hall measurement results show that an increased sheet density reduces the mobility according to an increase in the effect of interface roughness especially for the $[\bar{1}10]$ orientation, which affected the average mobility for Van der Pauw devices. The channel thickness did not affect mobility, as observed in $[110]$ oriented Hall bar samples with

between 20 nm and 15 nm channel thicknesses. This underlines the high quality structure with low interface roughness.

Further, a significant measured mobility and resistivity anisotropy has been reported in this thesis for sGe quantum wells. The reason for the mobility anisotropy is believed to be due to the off-cut angle of the Si substrate. Simulation for the mobility at both orientations [$\bar{1}$10] and [110] was performed, which showed a pronounced increase for the anisotropy by increasing sheet density. For the higher mobility [110] orientation, the total mobility was found to be dominated by the interface roughness scattering component having a height of the roughness of Δ=0.28 nm and roughness period λ of 7 nm, while for the lower mobility [$\bar{1}$10] orientation the interface roughness height was Δ=0.42 nm with a period of λ= 4 nm and this has the effect of significantly reducing the hole mobility.

Magnetotransport measurements illustrated a high Dingle ratio of 78 for the normal structure and 33 for the inverted structure in [110] orientation, while it is 39 in the [010] orientation. The hole effective mass was 0.063 m_0, 0.063 m_0, and 0.07 m_0 for samples 11-289, 11-285, 11-284, respectively, which are the lowest reported up to date. All the samples have one subband occupation as revealed by FFT analysis as well as simulated by Nextnano[3] program. However, sample 11-285 and 11-284 contain two types of carriers, which is different from the normal structure sample 11-289. Zero-field spin splitting was observed in the 15 nm channel thickness samples with a small Rashba effect, since the sheet density imbalance shows a very small value of 4%, which means the quantum well is quite symmetric. This in fact agrees with the assumption that the high doping in the Si cap affects the symmetry of the channel and two pockets of holes appeared in the quantum well.

In conclusion, it has been proven by this study that Ge is a promising material in MODFET devices with high hole mobility, and more improvement to the characterization is possible especially in terms of spintronics.

7.2 Further work

This work is almost concentrated on the highest mobility samples of normal and inverted structures, more samples could be investigated in high magnetic field to be sure about the transport properties of the carriers and more parameters should be taken in consideration in future such as:

1. In terms of spintronics devices, samples with smaller channel thicknesses should be investigated in order to get single subband occupation, also reducing the doping in the Si cap should be taken in consideration to ensure quantum well asymmetry.
2. A small increase to the concentration of Ge in this structure up to 85% may increase the valance band offset, which would reduce the sheet density and allow study of the effect of the reduction of sheet density on mobility and effective mass of holes in the Ge channel.
3. Gated devices would give more opportunities to get full information from the same samples, so it is significant to understand the priority of making these devices.
4. Hall bar devices should be fabricated on all the samples in different orientation for more understanding of the reason for the anisotropy in this structure and get more accurate details, or van der Pauw squares with 8 contacts which would allow for more accuracy in the result.

5. Magnetic field in different angle and parallel magnetic field allows to get more information about these samples especially sample 11-285.

6. Normal structure with different spacer thicknesses or different doping to get variable sheet density may give opportunity to get higher mobility than that reported in this study.

7. More investigation for FQHE on the normal structure is needed for the sample 11-289, so higher magnetic field than 16 T with lower temperature than 300 mK.

8. Inverted structure with higher sheet density should investigated as well as that by lower the spacer thickness less than 10 nm or increase the doping > 4×10^{18} cm^{-2}.

9. Negative magnetoresistance in samples 11-285 and 11-289 should take more attention in the future

8 Bibliography

1. Sawano, K., et al., *Compressive strain dependence of hole mobility in strained Ge channels.* Applied Physics Letters, 2005. **87**(19).
2. Rossner, B., et al., *Scattering mechanisms in high-mobility strained Ge channels.* Applied Physics Letters, 2004. **84**(16): p. 3058-3060.
3. Xie, Y.H., et al., *Very high mobility two-dimensional hole gas in Si/Ge_xSi_{1-x}/Ge structures grown by molecular beam epitaxy.* Applied Physics Letters, 1993. **63**(16): p. 2263-2264.
4. Madhavi, S., V. Venkataraman, and Y.H. Xie, *High room-temperature hole mobility in modulation-doped heterostructures.* Journal of Applied Physics, 2001. **89**(4): p. 2497-2499.
5. Myronov, M., K. Sawano, and Y. Shiraki, *Enhancement of hole mobility and carrier density in Ge quantum well of SiGe heterostructure via implementation of double-side modulation doping.* Applied Physics Letters, 2006. **88**(25): p. -.
6. Irisawa, T., et al., *Channel width dependence of mobility in Ge channel modulation-doped structures.* Japanese Journal of Applied Physics Part 1-Regular Papers Short Notes & Review Papers, 2001. **40**(4B): p. 2694-2696.
7. Irisawa, T., et al., *Hole density dependence of effective mass, mobility and transport time in strained Ge channel modulation-doped heterostructures.* Applied Physics Letters, 2003. **82**(9): p. 1425-1427.
8. von Kanel, H., et al., *Very high hole mobilities in modulation-doped Ge quantum wells grown by low-energy plasma enhanced chemical vapor deposition.* Applied Physics Letters, 2002. **80**(16): p. 2922-2924.
9. Myronov, M., et al., *Temperature dependence of transport properties of high mobility holes in Ge quantum wells.* Journal of Applied Physics, 2005. **97**(8).
10. Sze, S.M., *Physics of Semiconductor Devices*. 2nd ed. 1981, New York: Wiley.
11. Schaffler, F., *High-mobility Si and Ge structures.* Semiconductor Science and Technology, 1997. **12**(12): p. 1515-1549.
12. Ma, J.-L., et al., *Valence band structure and hole effective mass of uniaxial stressed Germanium.* Journal of Computational Electronics, 2011. **10**(4): p. 388-393.
13. Parsons, J., *Relaxation of Strained Silicon on Virtual Substrates.* PhD Thesis, University of Warwick., 2007.
14. People, R., et al., *Modulation doping in GexSi1−x/Si strained layer heterostructures.* Applied Physics Letters, 1984. **45**(11): p. 1231-1233.
15. Ueno, T., T. Irisawa, and Y. Shiraki, *p-type Ge channel modulation doped heterostructures with very high room-temperature mobilities.* Physica E: Low-dimensional Systems and Nanostructures, 2000. **7**(3–4): p. 790-794.
16. Bean, J.C., *Silicon molecular beam epitaxy: 1984–1986.* Journal of Crystal Growth, 1987. **81**(1–4): p. 411-420.
17. Isella, G., et al., *Low-energy plasma-enhanced chemical vapor deposition for strained Si and Ge heterostructures and devices.* Solid-State Electronics, 2004. **48**(8): p. 1317-1323.
18. Li, J.H., et al., *Relaxed Si0.7Ge0.3 layers grown on low-temperature Si buffers with low threading dislocation density.* Applied Physics Letters, 1997. **71**(21): p. 3132-3134.

19. Irisawa, T., et al., *Thermal stability of Ge channel modulation doped structures.* Journal of Crystal Growth, 2001. **227**: p. 796-800.
20. Bollani, M., et al., *Compressively strained Ge channels on relaxed SiGe buffer layers.* Materials Science and Engineering: B, 2003. **101**(1–3): p. 102-105.
21. Myronov, M., et al., *Control of epilayer thickness during epitaxial growth of high Ge content strained Ge/SiGe multilayers by RP-CVD.* Journal of Crystal Growth, 2011. **318**(1): p. 337-340.
22. Morris, R.J.H., et al., *High conductance Ge p-channel heterostructures realized by hybrid epitaxial growth.* Semiconductor Science and Technology, 2004. **19**(10): p. L106-L109.
23. Schroder, D.K., *Semiconductor material and device characterization.* John Wiley & Sons, Inc., Hoboken, New Jersey, 2006.
24. Pauw, L.J.V.d., *A Method of measuring the resistivity and Hall coefficent on limellae of arbitrary shape.* Phillips Res Repts, 1958. **20**: p. 220.
25. Bierwagen, O., et al., *Mobility and carrier density in materials with anisotropic conductivity revealed by van der Pauw measurements.* Physical Review B, 2004. **70**(16): p. 165307.
26. Martin, N., J. Sauget, and T. Nyberg, *Anisotropic electrical resistivity during annealing of oriented columnar titanium films.* Materials Letters, 2013. **105**(0): p. 20-23.
27. Szmulowicz, F., *Calculation of optical- and acoustic-phonon—limited conductivity and Hall mobilities for p-type silicon and germanium.* Physical Review B, 1983. **28**(10): p. 5943-5963.
28. Ottaviani, G., et al., *Hole drift velocity in high-purity Ge between 8 and 220 °K.* Journal of Applied Physics, 1973. **44**(6): p. 2917-2918.
29. Emeleus, C.J., et al., *Scattering mechanisms affecting hole transport in remote-doped Si/SiGe heterostructures.* Journal of Applied Physics, 1993. **73**(8): p. 3852-3856.
30. Pearson, G.L. and J. Bardeen, *Electrical Properties of Pure Silicon and Silicon Alloys Containing Boron and Phosphorus.* Physical Review, 1949. **75**(5): p. 865-883.
31. Ando, T., A.B. Fowler, and F. Stern, *Electronic properties of two-dimensional systems.* Reviews of Modern Physics, 1982. **54**(2): p. 437-672.
32. Stern, F. and W.E. Howard, *Properties of Semiconductor Surface Inversion Layers in the Electric Quantum Limit.* Physical Review, 1967. **163**(3): p. 816-835.
33. Gold, A. and V.T. Dolgopolov, *Temperature dependence of the conductivity for the two-dimensional electron gas: Analytical results for low temperatures.* Physical Review B, 1986. **33**(2): p. 1076-1084.
34. Gold, A., *Scattering time and single-particle relaxation time in a disordered two-dimensional electron gas.* Physical Review B, 1988. **38**(15): p. 10798-10811.
35. Lee, J., H.N. Spector, and V.K. Arora, *Impurity scattering limited mobility in a quantum well heterojunction.* Journal of Applied Physics, 1983. **54**(12): p. 6995-7004.
36. Lee, K., et al., *Low field mobility of 2-d electron gas in modulation doped $Al_xGa_{1-x}As/GaAs$ layers* Journal of Applied Physics, 1983. **54**(11): p. 6432-6438.
37. Hess, K., *Impurity and phonon scattering in layered structures.* Applied Physics Letters, 1979. **35**(7): p. 484-486.
38. Gold, A., *Electronic transport properties of a two-dimensional electron gas in a silicon quantum-well structure at low temperature.* Physical Review B, 1987. **35**(2): p. 723-733.
39. Markus, Y., et al., *Anisotropic mobility and roughness scattering in a 2D electron gas.* Semiconductor Science and Technology, 1994. **9**(7): p. 1297.

40. Monroe, D., et al., *Comparison of mobility-limiting mechanisms in high-mobility $Si_{1-x}Ge_x$ heterostructures.* Journal of Vacuum Science & Technology B, 1993. **11**(4): p. 1731-1737.
41. http://www.nextnano.de/nextnano3/.
42. P. Blood, a.a.J.W.O., *The electrical characterization of semiconductors: majority carriers and electron states.* Academic Press, 1992.
43. Isihara, A. and L. Smrcka, *Density and magnetic field dependences of the conductivity of two-dimensional electron systems.* Journal of Physics C: Solid State Physics, 1986. **19**(34): p. 6777.
44. Whall, T.E., et al., *Effective mass and quantum lifetime in a $Si/Si_{0.87}Ge_{0.13}/Si$ two-dimensional hole gas.* Applied Physics Letters, 1994. **64**(3): p. 357-359.
45. Whall, T.E., et al., *Hole effective mass in remote doped $Si/Si_{1-x}Ge_x$ quantum wells with $0.05 \leq x \leq 0.3$.* Applied Physics Letters, 1994. **65**(26): p. 3362-3364.
46. Coleridge, P.T., et al., *Effective masses in high-mobility 2D electron gas structures.* Surface Science, 1996. **361–362**(0): p. 560-563.
47. B. A. Piot, et al., *Quantum Hall ferromagnet at high filling factors: A magnetic-field-induced Stoner transition.* PHYSICAL REVIEW B, 2005. **72**: p. 245325.
48. C.Weisbuch and a.B. Vinter, *Quantum semiconductor stuctures.* Academic Press, 1991.
49. Winkler, R., *Spin–Orbit Coupling Effects in Two-Dimensional Electron and Hole Systems.* Springer-Verlag Berlin Heidelberg, 2003. **volume 191 of Springer Tracts in Modern Physics**.
50. Berkutov, I.B., et al., *Magnetotransport studies of SiGe-based p-type heterostructures: Problems with the determination of effective mass.* Low Temperature Physics, 2012. **38**(12): p. 1145-1152.
51. Berkutov, I.B., et al., *Magnetotransport studies of SiGe-based p-type heterostructures: Problems of the effective mass determination.* Fizika Nizkikh Temperatur, 2012. **38**(12): p. 1455-1463.
52. Paul, D.J., et al., *Low temperature characterization of modulation doped SiGe grown on bonded silicon-on-insulator.* Applied Physics Letters, 1996. **69**(18): p. 2704-2706.
53. Coleridge, P.T., R. Stoner, and R. Fletcher, *Low-field transport coefficients in $GaAs/Ga_{1-x}Al_xAs$ heterostructures.* Physical Review B, 1989. **39**(2): p. 1120-1124.
54. Coleridge, P.T., *Small-angle scattering in two-dimensional electron gases.* Physical Review B, 1991. **44**(8): p. 3793-3801.
55. Laikhtman, B., M. Heiblum, and U. Meirav, *Effect of high unintentional doping in AlGaAs barriers on scattering times in accumulation layers.* Applied Physics Letters, 1990. **57**(15): p. 1557-1559.
56. Fang, F.F., T.P. Smith Iii, and S.L. Wright, *Landau-level broadening and scattering time in modulation doped GaAs/AlGaAs heterostructures.* Surface Science, 1988. **196**(1–3): p. 310-315.
57. Komnik, Y.F., et al., *Quantum effects in hole-type Si/SiGe heterojunctions.* Low Temperature Physics, 2000. **26**(8): p. 609-614.
58. Protasov, D.Y., et al., *Electron scattering in AlGaN/GaN heterostructures with a two-dimensional electron gas.* Semiconductors, 2013. **47**(1): p. 33-44.
59. Tanaka, T., et al., *Upper limit of two-dimensional hole gas mobility in strained Ge/SiGe heterostructures.* Applied Physics Letters, 2012. **100**(22): p. -.
60. Tanaka, T., et al., *Experimental and theoretical analysis of the temperature dependence of the two-dimensional electron mobility in a strained Si quantum well.* Journal of Applied Physics, 2012. **111**(7): p. -.

61. Myronov, M., et al., *Observation of pronounced effect of compressive strain on room-temperature transport properties of two-dimensional hole gas in a strained Ge quantum well.* Applied Physics Express, 2008. **1**(5): p. 3.
62. Myronov, M., et al., *Extremely high room-temperature two-dimensional hole gas mobility in Ge/$Si_{0.33}Ge_{0.67}$/Si(001) p-type modulation-doped heterostructures.* Applied Physics Letters, 2002. **80**(17): p. 3117-3119.
63. Myronov, M., K. Sawano, and Y. Shiraki, *Enhancement of hole conductance in the Ge quantum well of a SiGe heterostructure via realization of double-side modulation doping.* Semiconductor Science and Technology, 2007. **22**(1): p. S63.
64. von Kanel, H., et al., *High mobility SiGe hetero structures fabricated by low-energy plasma-enhanced chemical vapor deposition.* Microelectronic Engineering, 2004. **76**(1-4): p. 279-284.
65. Höck, G., et al., *Carrier mobilities in modulation doped $Si_{1-x}Ge_x$ heterostructures with respect to FET applications.* Thin Solid Films, 1998. **336**(1–2): p. 141-144.
66. Kiatgamolchai, S., et al., *Mobility spectrum computational analysis using a maximum entropy approach.* Physical Review E, 2002. **66**(3): p. 036705.
67. Jaynes, E.T., *Information Theory and Statistical Mechanics.* Physical Review, 1957. **106**(4): p. 620-630.
68. Beck, W.A. and J.R. Anderson, *Determination of electrical transport properties using a novel magnetic field-dependent Hall technique.* Journal of Applied Physics, 1987. **62**(2): p. 541-554.
69. Myronov, M., et al., *High Quality Strained Ge Epilayers on a $Si_{0.2}Ge_{0.8}$/Ge/Si(100) Global Strain-Tuning Platform.* Electrochemical and Solid State Letters, 2010. **13**(11): p. H388-H390.
70. Shah, V.A., et al., *Reverse graded relaxed buffers for high Ge content SiGe virtual substrates.* Applied Physics Letters, 2008. **93**(19).
71. Shah, V.A., et al., *Reverse graded SiGe/Ge/Si buffers for high-composition virtual substrates.* Journal of Applied Physics, 2010. **107**(6).
72. Mitard, J., et al., *High Hole Mobility in 65 nm Strained Ge p-Channel Field Effect Transistors with HfO2 Gate Dielectric.* Japanese Journal of Applied Physics, 2011. **50**(4).
73. Dobbie, A., et al., *Thermal Stability of Thin Compressively Strained Ge Surface Channels Grown on Relaxed $Si_{0.2}Ge_{0.8}$ Reverse-Graded Buffers.* Journal of the Electrochemical Society, 2012. **159**(5): p. H490-H496.
74. Morris, R.J.H., et al., *Overcoming Low Ge Ionization and Erosion Rate Variation for Quantitative Ultralow Energy Secondary Ion Mass Spectrometry Depth Profiles of $Si_{1-x}Ge_x$/Ge Quantum Well Structures.* Analytical Chemistry, 2012. **84**(5): p. 2292-2298.
75. Birkholz, M., *Thin film analysis by X-ray scattering.* Wiley-VCH John Wiley distributor,
Weinheim Chichester, 2006.
76. Ishikawa, Y., et al., *Strain-induced enhancement of near-infrared absorption in Ge epitaxial layers grown on Si substrate.* Journal of Applied Physics, 2005. **98**(1).
77. Mironov, O.A., et al., *Cyclotron resonance of extremely conductive 2D holes in high Ge content strained heterostructures.* Journal of Low Temperature Physics, 2010. **159**(1-2): p. 216-221.
78. Savin, A.M., et al., *Mobility anisotropy of two-dimensional hole gases in (001)GaAs/$Al_{0.5}Ga_{0.5}As$ heterostructures and the influence of uniaxial compression.* Semiconductor Science and Technology, 1999. **14**(7): p. 632.

79. Neumann, R., K. Brunner, and G. Abstreiter, *Hole transport in SiGe channels on step-bunched vicinal Si surfaces.* Physica E: Low-dimensional Systems and Nanostructures, 2002. **13**(2–4): p. 986-989.
80. Neumann, R., et al., *Self-assembled growth and magnetotransport investigations on strained Si/SiGe multilayers on vicinal (113)-Si surfaces.* Thin Solid Films, 2000. **380**(1–2): p. 124-126.
81. Lichtenberger, H., et al., *Ordering of self-assembled islands on vicinal Si(001) substrates.* Journal of Crystal Growth, 2005. **278**(1–4): p. 78-82.
82. Huang, S.-H., et al., *Mobility enhancement of strained Si by optimized SiGe/Si/SiGe structures.* Applied Physics Letters, 2012. **101**(4): p. 042111.
83. Luo, Y., et al., *Strong Electro-Absorption in GeSi Epitaxy on Silicon-on-Insulator (SOI).* Micromachines, 2012. **3**(2): p. 345-363.
84. Dobbie, A., et al., *Ultra-high hole mobility exceeding one million in a strained germanium quantum well.* Applied Physics Letters, 2012. **101**(17): p. 172108.
85. Rossner, B., et al., *2-D hole gas with two-subband occupation in a strained Ge channel: Scattering mechanisms.* Thin Solid Films, 2006. **508**(1-2): p. 351-354.
86. Chang, A.M., et al., *Fractional quantum Hall effect at low temperatures.* Physical Review B, 1983. **28**(10): p. 6133-6136.
87. Chrastina, D., J.P. Hague, and D.R. Leadley, *Application of Bryan's algorithm to the mobility spectrum analysis of semiconductor devices.* Journal of Applied Physics, 2003. **94**(10): p. 6583-6590.
88. S. Kiatgamolchai, et al., *Mobility spectrum computational analysis using a maximum entropy approach.* physical Review E, 2002. **66**: p. 036705.
89. Irisawa, T., et al., *Growth of SiGe/Ge/SiGe heterostructures with ultrahigh hole mobility and their device application.* Journal of Crystal Growth, 2003. **251**(1–4): p. 670-675.
90. Irisawa, T., et al., *Ultrahigh room-temperature hole Hall and effective mobility in $Si_{0.3}Ge_{0.7}$/Ge/$Si_{0.3}Ge_{0.7}$ heterostructures.* Applied Physics Letters, 2002. **81**(5): p. 847-849.
91. Myronov, M., et al., *Enhancement of room-temperature 2DHG conductivity in narrow and strained double-sides modulation doped Ge quantum well.* Thin Solid Films, 2008. **517**(1): p. 359-361.
92. Myronov, M., et al., *Observation of two-dimensional hole gas with mobility and carrier density exceeding those of two-dimensional electron gas at room temperature in the SiGe heterostructures.* Applied Physics Letters, 2007. **91**(8): p. -.
93. Myronov, M., D.R. Leadley, and Y. Shiraki, *High mobility holes in a strained Ge quantum well grown on a thin and relaxed $Si_{0.4}Ge_{0.6}$/LT-$Si_{0.4}Ge_{0.6}$/Si(001) virtual substrate.* Applied Physics Letters, 2009. **94**(9): p. 3.
94. Dobbie, A., et al., *Thermal Stability of Thin Compressively Strained Ge Surface Channels Grown on Relaxed $Si_{0.2}Ge_{0.8}$ Reverse-Graded Buffers.* Journal of The Electrochemical Society, 2012. **159**(5): p. H490-H496.
95. Lu, T.M., et al., *Upper limit of two-dimensional electron density in enhancement-mode Si/SiGe heterostructure field-effect transistors.* Applied Physics Letters, 2011. **99**(15): p. 153510.
96. Lu, T.M., et al., *Observation of two-dimensional electron gas in a Si quantum well with mobility of 1.6x10(6) cm(2)/V s.* Applied Physics Letters, 2009. **94**(18): p. 3.
97. Gilbertson, A.M., et al., *Zero-field spin splitting and spin-dependent broadening in high-mobility asymmetric quantum well heterostructures heterostructures,* Physical Review B, 2009. **79**(23): p. 235333.

98. Minkov, G.M., et al., *Two-dimensional semimetal in a wide HgTe quantum well: Magnetotransport and energy spectrum.* Physical Review B, 2013. **88**(15): p. 155306.
99. Eisenstein, J.P., et al., *Effect of Inversion Symmetry on the Band Structure of Semiconductor Heterostructures.* Physical Review Letters, 1984. **53**(27): p. 2579-2582.
100. Gerl, C., et al., *Carbon-doped symmetric GaAs/AlGaAs quantum wells with hole mobilities beyond* $10^6 cm^2/V\,s$. Applied Physics Letters, 2005. **86**(25): p. 252105.
101. Hirmer, M., *High-mobility two-dimensional hole gases in III-V semiconductor heterostructures: growth and transport properties.* PhD Thesis in Physics , University at Regensburg, 2012.
102. Engels, G., et al., *Experimental and theoretical approach to spin splitting in modulation-doped As/InP quantum wells for* $B \rightarrow 0$. Physical Review B, 1997. **55**(4): p. R1958-R1961.
103. Žutić, I., J. Fabian, and S. Das Sarma, *Spintronics: Fundamentals and applications.* Reviews of Modern Physics, 2004. **76**(2): p. 323-410.
104. Cho, K.S., et al., *Zero-field spin splitting in modulation-doped* $Al_xGa_{1-x}N/GaN$ *two-dimensional electron systems.* Applied Physics Letters, 2005. **86**(22): p. -.
105. Tsui, D.C., H.L. Stormer, and A.C. Gossard, *Two-Dimensional Magnetotransport in the Extreme Quantum Limit.* Physical Review Letters, 1982. **48**(22): p. 1559-1562.
106. Nelson, S.F., et al., *Observation of the fractional quantum Hall effect in Si/SiGe heterostructures.* Applied Physics Letters, 1992. **61**(1): p. 64-66.
107. Lu, T.M., et al., *Fractional quantum Hall effect of two-dimensional electrons in high-mobility Si/SiGe field-effect transistors.* Physical Review B, 2012. **85**(12): p. 121307.
108. A. Isihara and L. Smrcka, *Density and magnetic field dependences of the conductivity of two-dimensional electron systems.* J. Phys. C: Solid State Phys, 1986. **19**: p. 6777.
109. Rößner, B., G. Isella, and H.v. Känel, *Effective mass in remotely doped Ge quantum wells.* Applied Physics Letters, 2003. **82**(5): p. 754-756.
110. Komnik, Y.F., et al., *Features of the Shubnikov–de Haas oscillations of the conductivity of a high-mobility two-dimensional hole gas in a SiGe/Ge/SiGe quantum well.* Low Temperature Physics, 2006. **32**(1): p. 82-85.